# IRON LOSSES IN BRUSHLESS PERMANENT MAGNET DC MACHINES

**KAIS ATALLAH**

A thesis submitted for the degree of Doctor of Philosophy

in the Department of Electronic and Electrical Engineering,

University of Sheffield,

April, 1993

## ABSTRACT

A closed-loop computer-controlled single-sheet test system has been developed to characterise lamination materials and to measure the iron loss density under any specified flux density waveform. The system has been used to validate predictions from a recently developed theoretical model for the calculation of the excess loss component associated with domain wall movement, under flux density waveforms typical of those encountered in the stator core of brushless permanent magnet dc motors. In addition, an improved expression for the calculation of the iron loss density component, from measured $\vec{H}$ and $\vec{B}$ vectors, due to rotation in non-purely rotating flux conditions, has been derived.

A simple analytical model from which the airgap flux density and spread of magnet working points can be determined and which accounts for the effects of curvature for radial-field permanent magnet machines has been developed and validated. The model has been coupled to an analytical technique for the prediction of the open-circuit flux density waveforms in different regions of the stator core, and has subsequently been employed for the prediction of the open-circuit iron loss.

In order to predict the iron loss under any specified load condition, a technique which couples a brushless dc drive system simulation to a series of magnetostatic finite element analyses corresponding to discrete instants in a commutation cycle has been developed. It enables the prediction of the local flux density waveforms throughout the stator core under any operating condition, and has been employed to predict the local iron loss density distribution and the total iron loss and their variation with both the load and the commutation strategy. Finally, the theoretical findings have been validated against measurements on a representative low power brushless drive system.

## ACKNOWLEDGEMENTS

I should like to extend my sincere thanks to everyone who contributed to making this thesis possible, in particular :

- My supervisor, Professor D. Howe, for his continuous encouragement, advice, and ideas throughout the project.

- Dr Z. Q. Zhu, for his encouragement and invaluable discussions.

- All members of electrical machines and drives group at Sheffield, for their help and humour. In particular, Mr N. Schofield for lending equipment.

- Algerian and British governments for the joint grant.

- Finally my parents and wife for their continued love and consistent encouragement.

# LIST OF SYMBOLS

a = Parameter characterising an elliptic flux density loci.

A = Pry and Bean excess eddy current loss factor.

$A_n$ = Area of the $n^{th}$finite element.

$a_n$, $b_n$ = Fourier coefficients.

$\vec{B}$ = Flux density.

$B_m$, $B_{max}$ = Maximum flux density.

$b_o$ = Slot opening.

$B_r$ = Remanence.

$B_{tmax}$ = Maximum flux density in the tooth body.

$B_{tr}$ = Maximum radial flux density in region 1 of the tooth tip.

$B_{t\theta}$ = Maximum circumferential flux density in region 1 of the tooth tip.

$B_{t2}$ = Maximum flux density in region 2 of the tooth tip.

$B_{yc}$ = Flux density in the stator back-iron section with adjacent tooth axis coinciding with a magnet pole transition.

$B_{ymax}$ = Maximum flux density in the stator back-iron.

$C_n$ = Percentage of the $n^{th}$ harmonic to the fundamental.

d = Lamination width.

$\vec{E}$ = Electric field.

$e_a$, $e_b$, $e_c$ = Induced emfs in phases A, B and C.

$e_{bs}$ = Induced emf in the B-search coil.

$e_h$ =Voltage drop across the precision resistor.

$\vec{e_r}$, $\vec{e\theta}$ = Unit vectors in polar coordinates.

f = Frequency.

g = Airgap length.

g' = Effective airgap length.

$G_{mo}$ = Eddy current damping factor of an active magnetic object.

$G_w$ = Eddy current damping factor of $180^0$ moving wall.

$\vec{H}$ = Magnetic field.

$H_e$ = Eddy current counter field.

$h_m$ = Magnet height.

I = RMS current in the stator winding.

$i_a$, $i_b$, $i_c$ = Instantaneous currents in phases A, B and C.

$\vec{i}, \vec{j}, \vec{k}$ = Unit vectors in rectangular coordinates.

j = Complex operator.

$\vec{J}$ = Current density.

$k_c$ = Classical eddy current loss constant.

$k_e$ = Excess eddy current loss constant.

$k_h$ = Hysteresis loss constant.

L = Lamination width.

$l_e$ = Effective magnetic path length of the single-sheet tester.

$L_p$ = Phase self inductance.

$l_{stk}$ = Stator stack length.

$l_t$ = Length of the intersection line between regions 1 and 2 of the tooth tip.

$\vec{M}$ = Magnetization.

$M_s$ = Saturation magnetization.

$M_p$ = Mutual inductance between two phases.

$\hat{n}$ = Effective number of simultaneously active magnetic objects.

N = Number of intervals per period in a piece-wise linear waveform.

$N_{bs}$ = Number of turns of the B search coil.

$N_{bts}$ = Number of bits.

$N_e$ = Number of elements in the finite element mesh.

$N_m$ = Number of turns of the single-sheet tester magnetising winding.

$N_{mlp}$ = Number of minor loops.

$n_{mo}$ = Number of simultaneously active magnetic objects.

$N_p$ = Number of rotor positions.

$N_s$ = Number of slots.

$N_{sp}$ = Number of samples per cycle.

$N_{st}$ = Number of stairs per period in a periodic staircase waveform.

$n_w$ = Number of simultaneously active domain walls.

p = Number of pole pairs.

$\vec{P}$ = Poynting vector.

$P_a$ = Iron loss density component due to alternating components.

$P_c$ = Iron loss density component due to classical eddy classical eddy currents.

$P_{c\_t}$ = Classical eddy current loss component in the tooth body.

$P_{c\_ttp1}$ = Classical eddy current loss component in region 1 of the tooth body.

$P_{c\_ttp2}$ = Classical eddy current loss component in region 2 of the tooth body.

$P_{c\_y}$ = Classical eddy current loss component in the back-iron.

$P_e$ = Iron loss density component due to excess eddy currents.

$P_{e\_t}$ = Excess eddy current loss component in the tooth body.

$P_{e\_ttp1}$ =Excess eddy current loss component in region 1 of the tooth tip.

$P_{e\_ttp2}$ = Excess eddy current loss component in region 2 of the tooth tip.

$P_{e\_y}$ = Excess eddy current loss component in the back-iron.

$P_h$ = Iron loss density component due to hysteresis.

$P_{h\_t}$ = Hysteresis loss component in the tooth body.

$P_{h\_ttp1}$ = Hysteresis loss component in region 1 of the tooth body.

$P_{h\_ttp2}$ =Hysteresis loss component in region 2 of the tooth body.

$P_{h\_y}$ = Hysteresis loss component in the stator back-iron.

$P_r$ = Iron loss density component due to rotation or rotational power loss.

$P_t$ = Total iron loss density.

$r, \theta$ = Polar coordinates.

R = Stator winding resistance.

$R_h$ = Resistance of the precision resistor.

$R_m$ = Rotor bore radius.

$R_r$ = Rotor hub radius.

$R_s$ = Stator bore radius.

S = Lamination cross-sectional area.

t = Time.

T = Period.

$T_d$ = Duration of the transition between tooth body flux of one polarity to the other.

thd = Total harmonic distorsion.

$T_t$ = Duration of the transition between region 2 of a tooth tip flux of one polarity to the other.

U = Voltage staircase/digitized waveform.

$U_{da}$ = Maximum voltage which can be generated by the D/A converter.

$U_k$ = DC voltage of one stair/step.

$U_m$ = Maximum voltage of staircase/digitized waveform.

v = Domain wall velocity.

$V_o$ = Parameter relating the effective number of simultaneously active magnetic objects to the eddy current counter field.

$V_t$ = Volume of the tooth body.

$V_{ttp1}$ = Volume of region 1 of the tooth tip.

$V_{ttp2}$ = Volume of region 2 of the tooth tip.

$V_{yk}$ = Volume of the stator back-iron.

$W_t$ = Width of the tooth body.

$W_{yk}$ = Width of the stator back-iron.

x, y, z = Rectangular coordinates.

$x_o$ = Optimum ratio of the rotor bore radius to the rotor hub radius.

$\alpha$ = Angle of lag between $\vec{H}$ and $\vec{B}$.

$\alpha_c$ = Commutation angle.

$\alpha_{ma}$ = Relative position of the permanent magnet field with respect to the armature field.

$\alpha_h$ = Hysteresis loss constant.

$\alpha_p$ = Pole arc to pole pitch ratio.

$\alpha_{pa}$ = Pole-arc.

$\beta$ = Parameter characterising the effect of slotting on the airgap flux density distribution.

$\delta$ = Mass density.

$\gamma$ = Delay of the commutation event from the zero-crossing of the induced emf.

$\mu$ = Permeability.

$\mu_o$ = Permeability of free space.

$\mu_r$ = Relative permeability.

$\kappa$ = Parameter characterising an eight interval piece-wise linear waveform.

$\Phi$ = Magnetic scalar potential.

$\varphi_p$ = Flux per pole.

$\varphi_{t2}$ = Maximum flux entering region 2 of a tooth tip.

$\varphi_{tm}$ = Tooth body flux when adjacent slot opening coincides with a magnet pole transition.

$\varphi_{tmax}$ = Maximum flux in the tooth body.

$\dot{\varphi}_w$ = Flux rate contribution from a moving domain wall.

$\varphi_{yc}$ = Flux in the stator back-iron section with adjacent tooth axis coinciding with a magnet pole transition.

$\varphi_{ymax}$ = Maximum flux in the stator back-iron.

$\omega$ = Angular frequency.

$\omega_r$ = Rotor speed.

$\tau$ = Parameter characterising a trapezoidal waveform.

$\tau_t$ = Slot pitch.

**Subscripts**

$r, \theta$ = Radial and circumferential components.

x, y, z = x, y and z components.

I = Airgap region.

II = Magnet and interpole airspaces.

# CONTENTS

## CHAPTER 1
## INTRODUCTION

## CHAPTER 2
## MEASUREMENT OF IRON LOSSES IN ELECTRICAL STEEL LAMINATIONS

## CHAPTER 3
## PREDICTION OF THE IRON LOSS DENSITY IN ELECTRICAL STEEL LAMINATIONS



## CHAPTER 4
## PREDICTION OF THE FLUX DENSITY WAVEFORMS IN THE STATOR CORE OF BRUSHLESS DC MACHINES

## CHAPTER 5
## PREDICTION OF IRON LOSSES IN THE STATOR CORE OF BRUSHLESS DC MACHINES

## CHAPTER 6
## CONCLUSIONS

# CHAPTER 1

# INTRODUCTION

## 1-1) Introduction

In the United Kingdom, iron losses in electric motors amount to approximately $5 \times 10^9$ kWhr per annum [1]. These losses, half of which are produced in industrial 3-phase induction motors, cost the user £150 millions pa. Although reductions to these loss figures can be achieved, for example, by the use of better grades of electrical steel, the resulting increase in the initial capital cost represents a major obstacle. However, the use of lower loss grades of electrical steel is certainly economically justified, if the real cost is considered to include the capitalised running cost over the expected life time of the machine. Indeed, it is estimated that for most motors in the 5-125 hp range operating for 500 to 1000 hours/year it would be economical to use a better grade of electrical steels [1]. In addition, alternative drive formats, in particular those based on permanent magnets, are emerging which offer the potential for further efficiency improvements.

Permanent magnets are cost-effective and energy efficient components of numerous types of electrical machine. For example, stepper motors, line-start synchronous motors, and brushless dc motors. Nevertheless, the brushless dc format is arguably the most prominant for a wide spectrum of applications. However, their optimal utilisation requires attention to many aspects related to the machine design and performance. In this respect the calculation of iron losses, which may account for a significant component of the total loss, is particularly challenging since it requires an accurate prediction of the temporal and spatial distribution of the flux density and the corresponding iron loss density distribution.

Efficiency opportunities, through for example, the use of improved electrical steel laminations and/or more sophisticated control strategies, can be quantified at the design stage on an application by application basis only if the iron loss calculation can account for the interaction between the machine and the system by which it is controlled. This thesis describes research which has been undertaken on the prediction of iron losses in brushless permanent magnet dc drives. Therefore, it focuses on two facets of the iron loss prediction problem in electrical machines, viz the prediction of the spatial and temporal distribution of the flux density, and the calculation of the corresponding iron loss density distribution, which are equally challenging.

In this chapter, the most significant advances related to the measurement and prediction of iron losses in electrical steel laminations and electrical machines are first reviewed. The main features of the research to be described in the remainder of the thesis are then highlighted.

## 1-2) Soft ferromagnetic materials

Soft magnetic materials are essential constituents of nearly every electromechanical device, as they perform the crucial task of concentrating and shaping magnetic flux. The continued development of better materials has resulted both in improved efficiencies of key building blocks of present technology, viz motors, generators, transformers, inductors, and sensors, and in novel devices and applications [2].

### 1-2-1) A brief excursion into atomic physics

In order to understand the cause of ferromagnetism the nature of the atom must first be considered. At its centre there is a nucleus around which electrons orbit in a complicated manner. Since the nucleus only has a small magnetic contribution, it is justified to consider only the orbiting electrons. Each electron possesses an electric

charge, and, as a result of its rotation around itself, it has a magnetic spin moment. The effect of a vast number of such electron magnets, summed under prescribed conditions and in a specific way, represents ferromagnetism. In addition to its spin moment, each electron possesses a magnetic orbital moment moment caused by its rotation around the nucleus.

In an atom having a large number of electrons, there are very strict laws governing the magnitude and direction of the individual contributions. The tendency is for the contributions to either wholly or partially cancel out, so that frequently there is no resultant magnetic moment associated with a single atom, whilst in some cases it results from only a few electrons. The number of electrons which are effective in contributing to the atomic magnetic moment is called the Bohr magneton number.

Even though the existence of the atomic magnetic moment represents the fundamental cause of any type of magnetism, eg. ferromagnetism, anti-ferromagnetism etc, it is the effect of the coupling forces between the atomic magnetic moments that determines the type of magnetism. In the case of ferromagnetism, these forces cause the atomic magnetic moments to arrange themselves parallel, resulting in an intrinsic magnetization, or saturation magnetization, whose magnitude is dependent on the number of atoms per unit volume and more strongly on the Bohr magneton number, see Table (1.1).

Table (1.1) Bohr magneton numbers and saturation magnetizations for the primary soft ferromagnetic metals.

| Element | Number of electrons per atom | Bohr magneton number | Saturation magnetization (T) |
|---|---|---|---|
| Iron | 26 | 2.218 | 2.16 |
| Cobalt | 27 | 1.714 | 1.8 |
| Nickel | 28 | 0.604 | 0.61 |

In reality, the ideal case of perfectly parallel atomic magnetic moments in ferromagnetic materials occurs only at very low temperatures. At higher temperatures the atomic magnetic moments make jittery movements about the field direction, which increase with increasing temperature, up to a value $T_C$ called the Curie temperature, where the thermal agitation overcomes the effect of the coupling forces, and the material loses its ferromagnetic properties. Fig (1.1) shows a typical variation of the intrinsic magnetization with temperature.

### 1-2-2) Magnetic domains and domain walls

The coupling forces in ferromagnetic materials are generally so powerful that the atomic magnets at room temperature are almost entirely parallel-aligned. This does not, however, occur generally throughout the body, but only within certain regions. In adjacent regions, there is still alignment but the atomic magnets lie in different directions, so that the mean magnetic moment of the whole body is zero. These regions of large scale alignment of atomic magnetic moments are called magnetic domains.

The boundaries between the magnetic domains are called domain walls or Bloch walls ( after F. Bloch ). Such a wall is not only a boundary, it is more of a transition layer with its own system of laws. Its thickness may vary from several hundreds to a thousand atomic distances. The orientation of the atomic magnetic moments within the wall changes in a screw-like fashion from the direction of one domain to the other, Fig (1.2).

### 1-2-3) Elementary processes of magnetization

If a soft ferromagnetic core is introduced into a small magnetic field, the domain walls exhibit a slight displacement from their rest positions, and if the field is switched off

they return to their original positions. If, however, the field is allowed to rise more sharply, the domain boundaries wrench themeselves free from their rest positions under the influence of the field and can come to rest again only when they encounter major obstacles, which can be surmounted only when the magnetic field is increased further. These domain wall jumps are called "Barkhausen jumps". They are the cause of ferromagnetic hysteresis. It can happen that a domain will absorb one of its neighbours by a single jump, as those domains in which the spontaneous magnetization happens already to lie roughly in the direction of the lines of the magnetic field grow at the expense of the other domains.

Other elementary processes that occur during the magnetization of soft ferromagnetic material are the domain rotations, during which the atomic magnetic moments of a whole domain align themselves simultaneously in the direction of the applied field. These rotational processes, however, demand relatively high field strengths.

Although the magnetizing process is in fact supported by small rotations, with soft ferromagnetic metals it is accomplished at the start by wall displacements, and only when these are concluded, and preferred directions close to the field have been assumed throughout, does the final alignment in the field direction take place by domain rotations on further raising the field.

Table (1.2) summarises the different magnetizing processes and their properties, whilst Fig (1.3) shows a diagramatic representation of the different stages of magnetization of an initially demagnetized sample.

### 1-2-4) Different types of anisotropy

In soft ferromagnetic materials three types of anisotropies exist, viz

Table (1.2) Elementary magnetization processes.

| Magnetization process | Magnetic field strength | Reversibility |
|---|---|---|
| Slight wall displacements | Small | reversible |
| Barkhausen jumps | Medium | irreversible |
| Domain rotations | High | reversible |

a) Crystal anisotropy

b) Induced uniaxial anisotropy

c) Stress anisotropy

Crystal anisotropy is present mainly in materials characterised by a crystalline structure, and represents the tendancy of the intrinsic magnetization to lie in a specific direction inside the crystal or "grain". In isotropic crystalline materials, the easy axes of magnetization of the different crystals are randomly distributed over the body, resulting in a macroscopically isotropic material.

To overcome the effects of the random distribution of the crystals easy axes, in crystalline materials to be used in applications where only a unidirectional magnetization is needed, eg. transformer cores, a uniaxial anisotropy is induced by heat treatment of the material near its Curie temperature in the presence of a magnetic field. This results in a magnetization process along the induced easy axis which is dominated mainly by wall displacements, hence reducing the amount of energy necessary for magnetization by avoiding domain rotations.

Before defining stress inisotropy, it is necessary to highlight another feature of soft ferromagnetic materials, viz magnetostriction, which represents a change in material dimensions as a result of it being magnetized. Since magnetostriction is caused only by domain rotation processes, a perfectly grain-oriented material would not exhibit a

change in its dimension as a result of being magnetized. However, in practice imperfections in the structure often cause magnetostriction.

The inverse of magnetostriction results in the creation of uniaxial stress induced anisotropy. For example, for a material with positive magnetostriction in tension, the stress anisotropy would compete with the crystal anisotropy to align the magnetization along the stress direction. As such, the sensitivity of a particular material to stress is determined by its crystal anisotropy as well as the extent of domain rotation during its magnetization. Thus, non crystalline materials, such as metallic glasses, which are characterised by a liquid-like structure in which the atomic ordering does not exceed 2 to 3 atoms, and the crystal anisotropy is negligible, present a particular sensitivity to stress. For example, in typical metallic glasses for transformer applications, the magnetization is predominantly determined by stress effects beyond a stress level of about 2 MPa.

### 1-2-5) Heat treatments of soft ferromagnetic materials

Soft ferromagnetic materials are subjected to heat treatments for a variety of reasons:

a) To bring them after cold working into a state amenable for further working
b) To achieve desired magnetic properties

#### 1-2-5-1)Annealing heat treatments

In carrying out the annealing of soft ferromagnetic materials it is necessary that time, temperature and in many cases also the cooling conditions be accurately monitored and controlled. It is best carried out in electric resistance heating furnaces having automatic temperature control. Further, the annealing process should be carried out in a protective gas atmosphere to avoid scaling of the material. Generally, hydrogen is

preferred because it not only acts as a proctector, but also reacts with the metal to remove impurities. Annealing in ammonia gas or in a vacuum is also possible.

### 1-2-5-2) Final-annealing

There are several objectives for this annealing process, among which are :

a) The growth of a disturbance free structure from the crystal grains of the metal which were disturbed by the working.

b) Creation of the uniaxial anisotropy by orienting the crystallites in a specific manner.

After final annealing the material must be protected from subsequent mechanical stresses, even apparently minor ones.

### 1-2-5-3) Stress-relieving annealing

For an annealed material which has been subjected to mechanical overstresses, especially when it has been plastically deformed, the resultant magnetic damage can usually be almost entirely repaired by two to three hours annealing at 650-800$^{0}$ C in a near perfect annealing atmosphere. However, after very intensive stresses, the whole final annealing programme must be repeated.

## 1-2-6) Losses in soft ferromagnetic materials

When subjected to a time-varying magnetization, soft ferromagnetic materials exhibit two types of losses, viz

a) Hysteresis loss

b) Eddy current losses

Hysteresis loss is due to energy consuming changes in the domain structure caused by Barkhausen jumps during the magnetization process. Since, the duration of a Barkhausen jump is typically around 0.1 $\mu s$ the hysteresis loss per cycle is fairly independent of frequency, in the range of frequencies which soft ferromagnetic materials are normally used, and depends only on the number of jumps per cycle. In other words, in the absence of minor loops it is dependent only on the maximum magnetization. As regards the variation of the hysteresis loss with the peak magnetization, two typical flux conditions are distinguished, viz :

- Alternating flux conditions
- Rotating flux conditions

Under alternating flux conditions the magnetization is varied in magnitude and polarity whilst maintaining the same direction. Hence, increasing the magnetization necessarily leads to an increase of the number of Barkhausen jumps to cater for the magnetization swing, leading to an increase of the hysteresis loss.

Under rotating flux conditions, however, the magnetization is kept constant in magnitude whilst its direction is rotated. Under medium field strengths the change in the magnetization direction is still accomplished mainly by Barkhausen jumps. At higher field strengths, and because there is no magnetization swing, the magnetization rotation will be accomplished mainly by the reversible domain rotation process, which explains the drop in the hysteresis loss at relatively high magnetizations, until it vanishes at saturation. Fig (1.4) shows typical variations of the hysteresis loss under both alternating and rotating flux conditions.

The eddy current losses, however, represents the power loss due to the Joule effect caused by eddy currents induced by the rate of change of the flux density. They exist under time-varying flux conditions, but unlike the hysteresis loss, under rotating flux conditions they do not vanish at saturation.

Table (1.3) Major families of soft ferromagnetic materials [2].

| Category | Saturation $B_S$ (T) | Resistivity ( $\mu\Omega-m$ ) | Maximum permeability | Applications / Notes |
|---|---|---|---|---|
| I. Steels | | | | |
| low carbon steels | 2.1-2.2 | 0.4 | - | Cheap fractional hp motors |
| non-oriented Silicon steels | 2.0-2.1 | 0.24-0.5 | - | high efficiency motors |
| Grain-oriented Silicon steels | 2.0 | 0.45-0.48 | - | Power and distribution transformers |
| II. Nickel and Cobalt alloys | | | | |
| 40-50Ni | 1.6 | 0.48 | $150 \times 10^3$ | high permeability requirement applications |
| 70-80Ni | 1.1 | 0.55 | $150 \times 10^3$ | |
| 79Ni-4Mo | 0.8 | 0.58 | $10^6$ | highest permeability metallic material |
| 49Co-2V | 2.3 | 0.35 | $50 \times 10^3$ | Highest $B_S$ of commercial soft materials |
| III. Ferrites | | | | |
| MnZn | 0.5 | $2 \times 10^6$ | 6000 | Power supply inductors, HF transformers |
| NiZn | 0.35 | $10^{10}$ | 4000 | |

## 1-2-7) Major families of soft ferromagnetic materials

Table (1.3) summarises the major families of laminated soft ferromagnetic materials, their properties and their applications. Other types of soft ferromagnetic materials, such as the metallic glasses, viz amorphous alloys, are also available. However, athough characterised by relatively good magnetic performance, the difficulty of using such thin brittle materials makes them far from economically viable for many applications.

In addition, 6.5 % Silicon steel has excellent magnetic properties but present a poor ductility. Thus, commercial production of this material was not possible until 1988

Table (1.4) Comparison between 6.5 % Silicon steel and conventional Silicon steels [3].

| Material | Thickness (mm) | Core loss 1T/50Hz (W/kg) | Core loss 1T/400Hz (W/kg) | permea-bility | Magneto-striction |
|---|---|---|---|---|---|
| 6.5 % Silicon steel | 0.1 | 0.51 | 5.98 | 31000 | $0.2 \times 10^{-6}$ |
| | 0.3 | 0.49 | 10.0 | 40000 | |
| | 0.5 | 0.58 | 15.6 | 58000 | |
| 3.5 % Silicon steel | 0.5 | 1.36 | 27.1 | 7700 | $5.0 \times 10^{-6}$ |
| 3.2 % Grain oriented Silicon steel | 0.3 | 0.35 | 10.5 | 74000 | $1.3 \times 10^{-6}$ |

when the Japanese company NKK Corporation [3] developed a process for the commercial production of the material in sheet forms with thicknesses ranging from 0.1 to 0.5 mm and a with maximum width of 400 mm. Being characterised by low loss, high permeability and very low magnetostriction, 6.5 % Silicon steel has a promising future for a wide range of applications. Table (1.4) shows a comparison between the magnetic properties of the conventional Silicon steels and 6.5 % Silicon steel.

### 1-2-8) Operational environment

The capability of a soft ferromagnetic material to withstand mechanical and climatic stresses depends on the form in which the material is supplied, the alloy composition, and the strip thickness. Thus, the capability of a specific material cannot generally be specified. Further, the operating temperature could be an important parameter in some applications. In this respect the magnetic properties of Nickel alloys have a relatively higher sensitivity to temperature, because of their relatively lower Curie temperatures.

In applications which expose materials to high energy radiation, such as in nuclear reactors, new types of demands are placed on soft ferromagnetic materials. Indeed, two effects of primary importance arise, viz :

a) A change of magnetic properties due to irradiation

b) Induced radioactivity in the material

High energy radiation causes stresses and other inhomogeneities which prevent the displacement of the domain walls as well as initiating rearrangement processes in alloys characterised by uniaxial anisotropy. Both effects alter the coercivity, remanence and the shape of the hysteresis loop.

In addition to affecting the magnetic properties, high energy radiation also induces radioactivity in soft ferromagnetic materials. Indeed, by the capture of thermal neutrons, in particular, some isotopes contained in the natural elements are excited into radioactive radiation. In this respect, *γ–radiation* which is hazardous to human beings, is determined by the activation constant of the basic element, which depends on the cross-sections of the capture reaction, the abundance of the isotope, and the product of the emission probability and the energy of the *γ–radiation* components arising, and the half life time of the isotope. Table (1.5) gives the activation constants and the half-lives of the *γ–emitters* for the primary soft ferromagnetic materials, from which it can be seen that Cobalt is by far the highest *γ–ray* emitter. Thus, Cobalt alloys should be avoided or used with caution in radioactive environments.

Table (1.5) Activation constants and half-lives of primary soft ferromagnetic metals

| Element | Activation constant ($cm^2$.MeV/g) | Half life | Isotope |
|---|---|---|---|
| Iron (Fe) | $3.0 \times 10^{-5}$ | 47 days | $Fe^{59}$ |
| Nickel (Ni) | $1.7 \times 10^{-4}$ | 2.6 hours | $Ni^{65}$ |
| Cobalt (Co) | 0.85 | 5.3 years | $Co^{60}$ |

**1-3) Review of measurement of iron losses in electrical steel laminations**

The most important quantity for characterising the quality of electrical steel laminations is the iron loss density. The Epstein frame, with double overlapping corners, was first proposed by Burgwin in 1936, as a means of measuring iron loss densities in electrical steel laminations under alternating flux conditions. It is characterised by a high degree of repeatability, and, given the great amount of experience which has been aquired on the measurement procedure, considerable knowledge of the correlation between the results which it provides and the losses in real devices now exists. However, this high correlation does not mean that it provides an exact value of the iron losses [4], the inhomogeneity caused by the overlapping corners in the magnetic circuit of the Epstein frame being a major cause of errors. Therefore, new experimental techniques are becoming more popular, in particular single sheet or strip testers (SSTs). These are preferred to the Epstein square for two basic reasons. Firstly, the sample preparation and its insertion into the test rig are easier, and secondly, they eliminate the errors which are present in the Epstein square.

Single-sheet/strip testers are used in three different configurations, viz the Ss-type, and the So-type, which differ only in the location of the H sense-coil, and the D-type, Fig (1.5). The D-type is preferred to the others for two main reasons, viz, it gives a better uniformity of the field strength along the length of the sheet [5], and the influence of the overhang length of the sample is negligible [6].

In the single-sheet tester, the magnetic field strength H can be sensed by one of two methods. The first is a direct sensing method, using so-called H-coils, as shown in the configuration of Fig (1.5). However, because in theory the field to be sensed is actually at the surface of the lamination sample, the distance between the sense-coil and the lamination can be a source of error. Indeed, the field strength has been found to be linearily dependant on the distance, and an improved method using a double

H-coil has been proposed [7]. However, the risk of errors by using search coils is great for two reasons. The first is concerned with the calibration of the coil area-turns, the error of which enters linearily into the loss calculation. Secondly, the coil is a very sensitive sensor which is prone to pick-up from surrounding magnetic sources. Furthermore, because the induced coil voltage is proportional to dH/dt, an intermediate integration is necessary to obtain H, which may create an additional source of error, especially if analogue integrators are used.

Another method of measuring H is based on the determination of the effective magnetic path length and a knowledge of the applied mmf. Indeed, the error in measuring iron loss densities by assuming the effective magnetic path of the sheet simply to be its inner length, $l_e$ in Fig (1.5), has been found to be negligible [6]. The main advantage of this method is that no integration is required, the field strength being determined directly from the measured magnetising current, which avoids all the practical problems associated with the H-coil method. The corresponding flux density, however, must still be sensed by means of a search coil tightly wound around the lamination sample, to provide an induced voltage signal proportional to dB/dt.

Rotational fluxes also occur in electrical machines in addition to alternating fluxes. For example, they occur at the T-joints of transformer cores and in the core-back of rotating machines, and can contribute significantly to the total iron loss. Since early this century the problem of measuring iron losses under purely rotating flux conditions has been studied by many investigators. The first measurement method which was proposed to measure the rotational hysteresis loss [8] was the torque magnetometer method, in which disc shaped samples were rotated at very low speed so as to avoid the generation of eddy currents. However, this method was abandoned for two reasons [9]. Firstly, it was difficult to magnetise the discs with a homogeneous magnetisation because residual domains always remain non-magnetised at the edges. Secondly, in materials having a degree of anisotropy the magnetisation could not be kept constant at any angle from the easy axis, giving rise to unknown alternating components.

Therefore, Kaplan [10] subsequently replaced the disc by a cross-shaped sample having magnetising windings on the orthogonal legs. The magnetic field components in the mutually perpendicular directions were measured by means of small iron yoke devices which served as magnetic potential probes, and the flux density components were measured by means of pick-up tips, via the drop voltage due to eddy currents. However, because the small yoke devices could influence the magnetisation process, they were subsequently replaced by air-cored coils [11], whilst the flux densities were measured by means of coils threaded through small holes drilled in the central region of the sample, with laminated yokes carrying the magnetising windings being added to carry the flux between the legs [12].

Brix et al [13] proposed a new configuration, in which the sample was square shaped, and an airgap was introduced between the sample and the yokes so as to produce a better flux pattern in the region of interest. This also eased insertion of the sample.

Having established the rotating flux conditions, thermal methods based on the determination of the rate of change of temperature of the sample [14] by means of a thermocouple or thermistor have also been used to determine the iron loss. However, iron loss measurements based on the measurement of the orthogonal flux density and field strength components is considered to be the most convenient, since, apart from giving the total loss, it enables other quantities to be derived, especially under non-purely rotating flux conditions, such as the component of the total loss caused by the rotating flux component alone. However, problems still exist, and quite contradictory results have been published concerning the formulae from which the total loss, and the rotational components are calculated [11,15,16,17,18]. This will be discussed later in detail in Chapter 2.

**1-4) Review of the prediction of iron losses in electrical steel laminations**

It is usual to separate iron losses into two main categories, viz quasi-static losses, or hysteresis losses, and dynamic losses. The hysteresis loss per cycle is equal to the area of the hysteresis loop. Hence, any model which is capable of predicting magnetic hysteresis would be capable of predicting this component of loss. In the first and the only model, proposed by F. Preisach [19], the macroscopic hysteresis loop is seen as the superposition of a large number of elementary rectangular loops, with reversal fields $H^+$ and $H^-$ characterised by a distribution function $p(H^+,H^-)$. As such the change in magnetisation M due to a change of the magnetic field from $H_i \rightarrow H_o$ is given by

$$\Delta M = 2 \langle M_S \rangle \int_{H_i}^{H_o} \int_{H_i}^{H^+} p(H^+,H^-)\, dH^+\, dH^- \qquad (1.1)$$

and the area of a hysteresis loop having extremums $H_i$ and $H_o$, is given by:

$$P_h = 2 \langle M_S \rangle f \int_{H_i}^{H_o} \int_{H_i}^{H^+} p(H^+,H^-)\,(H^+ - H^-)\, dH^+\, dH^- \qquad (1.2)$$

where $\langle M_S \rangle$ represents the height of the elementary Preisach loops. In grain oriented materials it equals the saturation magnetisation $M_S$, whilst in isotropic materials and because of the random orientation of the crystallites, $\langle M_S \rangle \approx 0.85\, M_S$.

One of the properties of this representation is the congruency, which means that all hysteresis loops, major or minor, which correspond to the same magnetic field extremums are congruent. However, in soft ferromagnetic materials this is not necessarily the case, as the height of a minor loop depends not only on the extremum fields but also on the average magnetisation [20,21], Fig (1.6). Furthermore, the distribution function $p(H^+,H^-)$ is generally unknown, even though Bertotti [22,23,24] suggested that the distribution function $p(H^+,H^-)$ can be decomposed as

$p(H^+,H^-) = f(H^+)f(-H^-)$, and that the function f (H) could be approximated by a Lorentzien function:

$$f(H) = \frac{K}{1 + \left(\frac{H}{H_m} - \frac{1}{2}\right)^2} \tag{1.3}$$

where K is a normalisation constant and $H_m$ is the distribution width. Whilst very good results have been reported concerning the hysteresis loss prediction in the case of 3% SiFe steels, this can by no means be generalised as similar analyses carried out on different types of sheet steels have not yielded the same degree of accuracy. As a consequence, hysteresis loss prediction still has to be done empirically. In practice, however, this does not present a major problem because in the absence of minor loops the hysteresis loss per cycle does depend only on the maximum flux density.

As concerns the dynamic loss the first model proposed for its prediction is the classical eddy current model which assumes a uniform magnetisation throughout the lamination cross-section. However, experiments show that the dynamic losses predicted by this model are usually far from accurate, and there is always a so-called excess dynamic loss. Therefore, although this model provides relevant information about the effects of certain parameters, for example the lamination thickness, the fact that it completely disregards the existence of the domain structure in ferromagnetic materials is the major cause of its failure. In 1959 Pry and Bean [25] presented a model which took into account the existence of the domain structure. They divided the lamination into domains of rectangular cross-sections with alternate polarisation. If 2L is the domain width with zero overall magnetisation, this model predicts an excess loss for L>d ( case of grain oriented SiFe ) characterised by the following factor:

$$A = \frac{(P_e + P_c)}{P_c} \approx 3.26\frac{L}{d} \tag{1.4}$$

where d is the lamination thickness. Since $\frac{P_c}{f}$ varies linearly with frequency, this factor shows that the dependence of the excess loss per cycle on frequency is also linear. However, in practice its dependence on frequency is far from linear [26]. As regards the materials characterised by a fine domain structure, such as non-oriented materials, the model predicts negligible excess loss. However, experiments show that excess loss exists both in oriented and non-oriented materials. This model failed because its overall interpretation was only based on the concept of domain wall spacing. Indeed, two other concepts which characterise the Bloch wall bahaviour have a high contribution to the loss process in soft ferromagnetic materials. These are the number of simultaneously active walls contributing to the total flux rate and the enhanced eddy current overlap due to wall proximity [26]. Whilst the increase in the number of simultaneously active walls tends to cause a decrease in excess loss, domain wall proximity effects tend to cause an increase, which may explain the existence of the excess loss in materials with fine domain structure.

A recent model has been proposed by G. Bertotti [27,28,29,30,31], in which the loss calculation is reduced to a statistical problem. In this model the magnetisation rate is described as a sequence of random elementary jumps, each of which corresponds to a localised and sudden wall displacement. It is written as follows:

$$\frac{dM}{dt}(r,t) = \sum_{i=1}^{n} \dot{m}(r,t,r_i,t_i) \tag{1.5}$$

where n is the number of jumps, and $\dot{m}(r,t,r_i,t_i)$ is the contribution of the jump i at position $r_i$ and time $t_i$.

In this model the shape of the jump is not dealt with because of its effect on the hysteresis loss rather than on the dynamic losses in which its effect on the instantaneous magnetisation rate is most important. To cater for the effect of domain wall proximity, the model introduces a new concept, which is the idea of magnetic objects (MOs). An (MO) is a group of Bloch walls behaving in a very correlated

fashion in a certain region of the sample, and which contribute to the magnetisation change in clusters. The effect of the whole group is modelled in a compact form, namely the above mentioned (MO). This new concept reduces the number of highly correlated walls into a number of independant magnetic objects (MOs).

As regards the rotational losses, the same components exist, viz hysteresis, classical eddy current, and excess or " anomalous " losses. However, in practice high fields tend to cause a coherent rotation of the magnetisation, which reduces the irreversible processes due to Barkhausen jumps, and explains the variation of the hysteresis losses with the magnitude of the rotating flux density which tend to decrease above a certain value until it completely vanishes at the saturation flux density. This explanation is further strengthened by experimental work [9], which shows that not only is the hysteresis loss reduced but also the excess loss which is also related to Barkhausen jumps. However, only experimental investigations are available and no model for predicting the rotational losses has yet been proposed.

## 1-5) Parameters affecting iron losses in electrical steel laminations

As reviewed in section 1-2, the magnetic properties and losses of soft ferromagnetic materials are affected by several parameters, the most important in electrical machines being stress and temperature. However, whilst temperature is generally related to the operating condition, stress is generally induced during the fabrication process. Other effects, such as welding also affect the magnetic performance of built cores.

### 1-5-1) Effects of stress

Stress affects iron losses in different ways. For example, compressive stress tends to increase the losses [32], whilst tensile stress tends to decrease them up to a certain level when the effect is reversed. In most electrical machines, a significant radial

compressive stress is caused by the pressure imposed by shrink fitting the outer frame onto the stator [33], which induces a complicated local stress distribution throughout the stator core which is primarily dependent on the mechanical properties of the laminations as well as their geometry. Of course, in interior stator/exterior rotor machine topologies such a stress is not likely to occur. Other types of stress can also be inflicted axially, during the adjustment of the stacking factor of the lamination stacks during assembly, for example [34].

Further, magnetic damage at lamination edges may also be prominent [34,35], as the stamping process induces a stress zone at the edge, Fig (1.7), whose depth is controlled only by the manufacturing process. As such, the sharper the punching tool the less damage occurs. However, in order to minimise this effect the laminations should be subjected to a stress relieving annealing, despite the extra cost of such a process step.

Other methods for cutting laminations albeit normally for pre-production prototypes are also used, eg laser cutting and electro-discharge machining. However, no reports on the extent of damage which they may cause to the magnetic properties are available.

After being stacked, core laminations are sometimes welded. As welding is accompanied by the formation of a zone of metal fusion with a clearily pronouced nonequilibrium structure and a recrystallized zone a depth of several millimeters, it affects the magnetic properties of the soft ferromagnetic materials, resulting in an increase of coercivity in the weld zone [36], and hence an increase in iron losses [37].

### 1-5-2) Effects of temperature

Temperature also affects iron losses in different ways. Firstly, the most common effect is an increase of the material resistivity, resulting in a decrease of the eddy current loss

component. Indeed, an investigation [38] as to the effects on temperature on iron losses in a Coblt alloy, which is characterised by a relatively high Curie temperature, $T_C = 920^o\ C$, showed that an increase in temperature up to $200^o\ C$, resulted in a decrease of the total iron losses, which points to the fact that temperature effects in this case are more or less limited to the resistivity. Because of their relatively higher saturation magnetization, about 2.3 T, Cobalt alloys are used in rotating machines when the power-to-weight ratio is a critical factor, such as in aerospace applications. Since magnetic steels, viz low Carbon and Silicon steels, are also characterised by high Curie temperatures, over $700^o\ C$, in the range of operating temperatures generally encountered, temperature effects would also be limited in practice to the resistivity of the materials.

### 1-5-3) Effects of the electrical steel laminations grade

Changing the grade of material from which a machine core is built can result in a dramatic change in the performance of the machine, especially as far as efficiency is concerned. However, whilst this may result in an increase of the initial cost, in applications where efficiency is a key performance factor, such as battery-fed devices, this may be unavoidable. In this respect, a study made by Takada et al [39], on the effect of using the newly developed 6.5 % Silicon steel for the core of electrical machines showed a dramatic reduction in the iron loss. Table (1.6) and (1.7) show a comparison between the iron loss for different core materials for an 1800 rpm, 8-pole brushless dc micro-motor for an audio-visual machine and a 2-pole, 0.4 kW, 200 V,

Table (1.6) Effect of using 6.5 % Silicon steel on iron losses of brushless dc micro-motor [39].

| Material | Iron loss (W) |
|---|---|
| 3.5 % Silicon steel | 0.102 |
| 6.5 % Silicon steel | 0.067 |

Table (1.7) Effect of using 6.5 % Silicon steel on iron losses of a high speed induction motor [39].

| Type of supply | No load and iron losses (W) | 0.5 mm, 6.5 % Silicon steel | 0.5 mm, 3.5 % Silicon steel | Amorphous alloy |
|---|---|---|---|---|
| Sinusoidal supply | No load loss | 39.0 | 53.0 | 38.0 |
| | Iron loss | 22.0 | 34.3 | 20.9 |
| Non sinusoidal supply | No load loss | 45.0 | 67.0 | 48.9 |
| | Iron loss | 27.2 | 47.5 | 29.7 |

360 Hz high-speed induction motor, respectively. From such results two conclusions can be drawn. Firstly, changing the grade of material can lead to a dramatic change in iron losses, and secondly 6.5 % Silicon steel has a promising future.

## 1-6) Measurement of iron losses in electrical machines

Efficiency is one of the most important performance characteristics of any energy conversion device. Whilst all energy conversion processes exhibit losses, be they primary or secondary, the electromechanical energy conversion process is one of the most efficient. However, the design of energy efficient machines requires a thorough knowledge of the different losses which exist in a particular design, which can only be achieved through direct measurement and/or accurate prediction techniques.

Electrical machines exhibit different types of losses, which can be summarised as follows:

a) Copper losses, due to the joule effect in the windings ($I^2 R$)

b) Losses in the ferromagnetic core of the machine, or iron losses, which are due to time-varying fluxes.

c) Mechanical losses, due to windage and friction.

Their proportions vary with the type and power rating of the machine, as well as the operating condition.

In theory, the total loss of an electrical machine can be obtained by measuring the input and the output power simultaneously. However, it is ironic that the more efficient the machine the less reliable is this method, since experimental errors in the measurement of the input and the output powers can induce an untolerable error in the loss. For eaxmple, a machine having an efficiency of 90%, but with input and output powers measured with an error of 2% would lead to an error of 14% in the determined loss. Therefore, other methods, such as the calorimetric method, for the direct measurement of the total or component losses, either through their cause or their effect, are often preferred.

### 1-6-1) Loss separation in electrical machines

The copper losses depend on the current in the windings as well as their resistances, which in turn is dependant on the winding temperature rise. However, in most machines, a steady state copper loss measurement can be easily achieved through a single measurement of the steady state RMS winding currents, whilst the winding resistances are measured immediatly after switching off the machine. Of course, this would not be possible for machines with unaccessible windings, such as the rotor bars in squirrel cage induction machines.

The mechanical losses can be measured when the machine is unexcited, as these are dependent only on the speed of rotation. However, whilst this is quite easy with wound-field machines, for permanent magnet excited machines it is difficult to separate the open-circuit iron losses from the mechanical losses. One possibility, however, is to temporarily replace the magnets with non-magnetic components having the same geometry and the same weight, so as to produce the same windage loss and the same friction loss in the bearings.

Unlike the copper and mechanical losses, the iron losses cannot be determined directly since there is no condition when they are the only loss component. As such, they have

always to be separated from another loss component, no matter whether the machine is operated on open-circuit or on load. On open-circuit they have to be separated from the mechanical losses, whilst on-load they have to be separated from both copper and mechanical losses. Hence, a high degree of acccuracy has to be achieved in measuring both the total loss and the other loss components if an acceptable error in the iron losses is to be achieved.

## 1-7) Prediction of iron losses in electrical machines

The prediction of iron losses in electrical machines has always been, and will be for some time, limited to accounting for the effect of design parameters whilst assuming ideal manufacturing conditions. Altough, rules for handling and processing electrical steel laminations during the manufacture of machines in order to achieve conditions close to the ideal exist the cost of implementing such procedures has always been the major obstacle. Furthermore, as far as the magnetic properties of the laminations are concerned these can vary dramatically from the first stage of a manufacturing process to the last as well as with the quality of the process. For example, Figs (1.8) and (1.9) show the variation of the extent of the damage incurred at the edge of stamped laminations with the sharpness of the cutting tool [35].

The prediction of iron losses in electrical machines, even assuming ideal manufacturing conditions, has always been a two-fold problem, determining firstly the cause, namely the temporal and spatial flux density distribution throughout the core, and secondly the effect, namely the iron loss density distribution throughout the core.

### 1-7-1) Conventional approach

The conventional approach has been based on determining the average flux density in specific regions of the core, generally the stator teeth and back-iron, and assuming that

the flux density exhibits a sinusoidal temporal variation so that a corresponding iron loss density can be attributed to the different regions, either directly from manufacturer's iron loss data or calculated from classical expressions for the iron loss density under sinusoidal flux densities [40]. However, even though this pragmatic approach may be acceptable in classical ac machine formats, in which the flux density waveforms are essentially sinusoidal, if only an approximate estimate is required, this is not the case for most formats of permanent magnet excited machines, since the magnets generally induce flux density waveforms which are essentially non-sinusoidal. Indeed, they are often closer to having a trapezoidal waveform rather than a fundamental sinusoid. As such, a more refined method for predicting the flux density waveforms is required [41].

### 1-7-2) Impact of numerical techniques

With the availability of computer workstations, more and more computing power is available to machine designers, who can now use numerical techniques such as the finite element method for field calculations. Besides being accurate, finite element analysis provides localised information of the field, so that most of the assumptions regarding the flux density distribution in the conventional method for iron loss calculation can be avoided. Furthermore, when finite element analysis is coupled to a drive system simulation accurate information on the field distribution under any specific operating condition can be obtained. Indeed, numerous investigators have exploited these possibilities, no-load iron losses being computed for salient-pole alternators [42], iron losses being shown to increase in permanent magnet brushed dc motors when controlled by chopping circuits [43], the effects of stator flux density waveform harmonics in buried magnet permanent magnet synchronous motors being quantified [44], the prediction of stator no load iron loss and the improvement in efficiency as a result of changing the stator core material of induction motors has been attempted [45,46].

Studies on laminations [47] tested under flux density waveforms similar to those which would exist in inverter supplied induction motors have shown that not all types of inverter necessarily cause an increase of iron loss. For example, whilst a substantial increase has been reported for the case of a PWM inverter, no substantial increase has been observed for the case of a six-step inverter. However, whilst such studies on laminations may provide a guideline, a sensible estimation of the effect of such inverters can be achieved only in the context of the complex electromagnetic nature of the machines, either by experiment on real prototypes or by using numerical analysis techniques which couple the drive system simulation to the field calculation.

## 1-8) Discussion

As will be evident in the foregoing review, the calculation of the iron loss in electrical machines is characterised by several problem, the most fundamental of which concerns the prediction of the magnetic power loss in the electrical steel laminations. To date a unifying model, which enables the prediction of the magnetic power loss under any flux condition, has yet to be proposed, and an examination of current research in this particular area suggests that it is unlikely that a model of such a nature will be proposed in the near future. Therefore, given the nature of the problem and the ever growing need for a more accurate estimation of the iron losses in electromagnetic devices, researchers in the field have tended to undertake semi-empirical approaches, which are guaranteed to yield results, rather then attempt to solve the problem from its fundamental base, bearing in mind that, over the years, many researchers have tried and failed. Furthermore, the sensitivity of the properties of soft ferromagnetic materials to mechanical conditions, such as stress, in real devices adds to the complexity of the problem. However, from the engineer's point of view this does not matter too much, in as much as an estimation of the actual iron loss in a particular design and/or operating condition is still possible. However, a greater awareness of the fundamental problems which exist would provide the designers with the possibility of

undertaking a more sensible design methodology as well as avoiding assumptions based on oversimplified analysis. An accurate knowledge of the temporal and spatial flux density distribution is a necessary condition, and any improvement in this area will have a direct benefit. However, this is far from being the only requirement since the accuracy of the prediction of the temporal and spatial field distribution throughout the core is very much dependent on the modelling of the soft ferromagnetic materials. Nevertheless, even in the most sophisticated techniques for the field calculation, soft ferromagnetic components in the magnetic circuit are often assumed to be loss-less, and the relationship between the magnetic field strength and the flux density is approximated simply by the initial dc magnetization curve. Whilst this simplified modelling of soft ferromagnetic materials would not affect the accuracy of certain performance parameters, such as total flux per pole etc, other parameters such as the local flux density waveforms throughout the core will be more affected.

As concerns manufacturing conditions, these are quite impossible to include since they can vary dramatically from one manufacturer to another. However, whilst many investigators have investigated their effects from tests performed under laboratory controlled conditions [32,33,34,48,49,50,51,52,53], their results can be used only to assess the influence of manufacturing parameters, without being able to yield quantitative data.

In the subsequent chapters of this thesis, the following facets of the investigation are described:

Chapter 2: A description is given of closed-loop computer-controlled single-sheet testers which have been developed for the measurement of iron losses in electrical steel laminations, under alternating flux conditions. Ambiguities related to the calculation of the iron loss from the measured $\vec{H}$ and $\vec{B}$ vectors are clarified, and an expression for the calculation of that portion of loss due to rotation in non-purely rotating flux conditions is derived. Finally, a description

of a computer-controlled system which has been developed for the characterisation of electrical steel laminations under dc conditions is included.

Chapter 3: The most recent techniques for the prediction of the iron loss density in electrical steel laminations are described, and predictions are validated against measurements carried out on the single-sheet testers, for flux density waveforms typical of those encountered in permanent magnet brushless dc motors.

Chapter 4: A simple analytical technique for the prediction of the flux density waveforms throughout the stator core of permanent magnet brushless dc machines on open-circuit is presented. In the analysis special emphasis is given to curvature effects on the airgap flux density in radial-field machine topologies. A simple analytical model which caters for the effect of curvature is presented, and predictions are compared to those obtained from more sophisticated models and experiments.

Further, a numerical technique which couples the simulation of a brushless dc drive system to magnetostatic finite element analyses, for predicting the temporal and spatial flux density distribution throughout the stator core is described.

Comparisons of flux density waveforms in various regions of the stator core as predicted by both analytical and numerical techniques are made with measurements carried out on a prototype brushless dc motor.

Chapter 5: A comparison is made between predicted and measured iron losses, on both open-circuit and on-load condition, for the same prototype motor. The method of measurement is described, and the effect of the load condition and commutation strategy on the total iron losses

and the iron loss density distribution throughout the stator core is analysed.

Chapter 6: Conclusions on the various aspects of the research which has been carried out are presented.

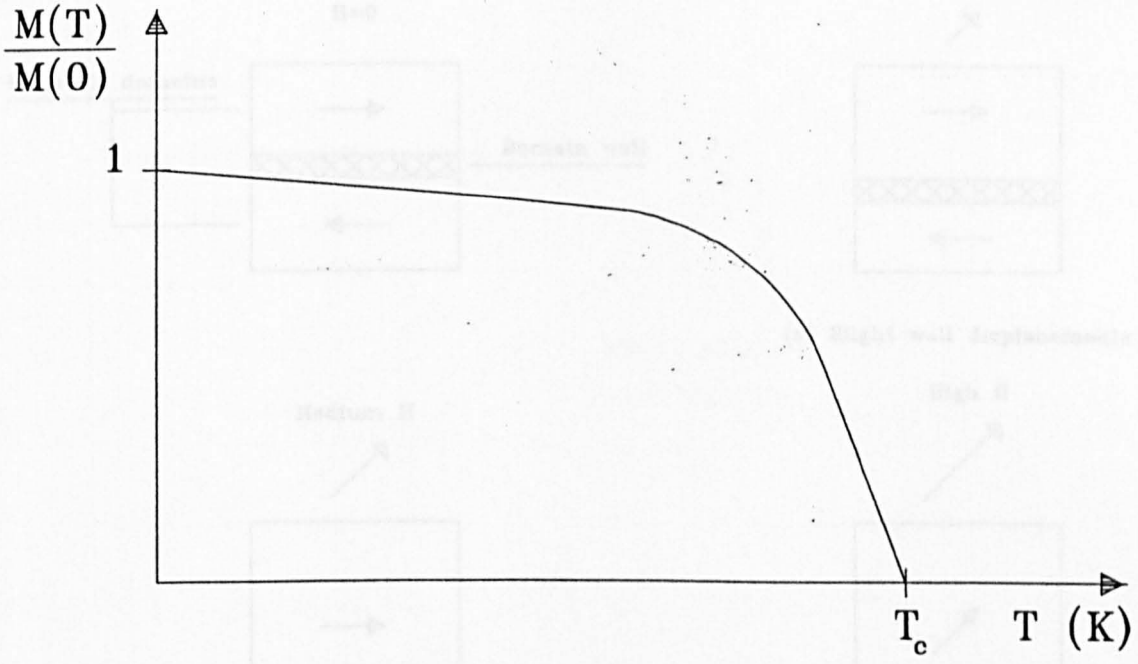


Fig (1.1) Typical variation of the intrinsic magnetization with temperature.

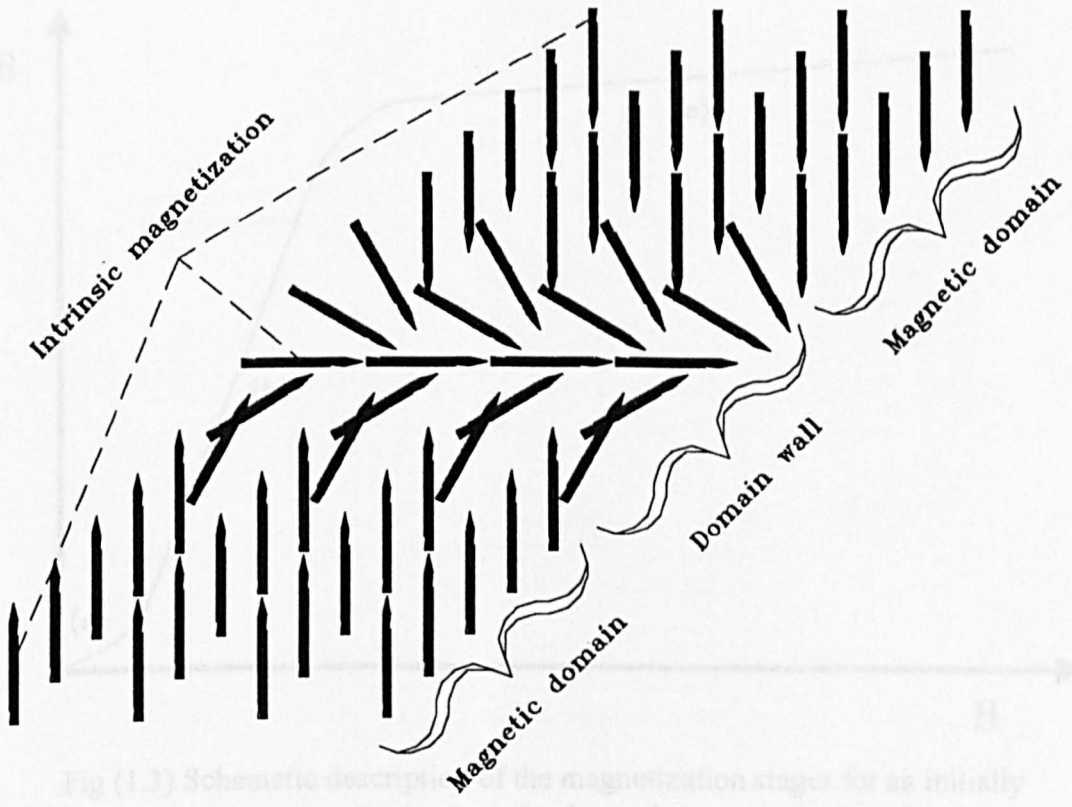


Fig (1.2) Change in the intrinsic magnetization direction in domain wall.

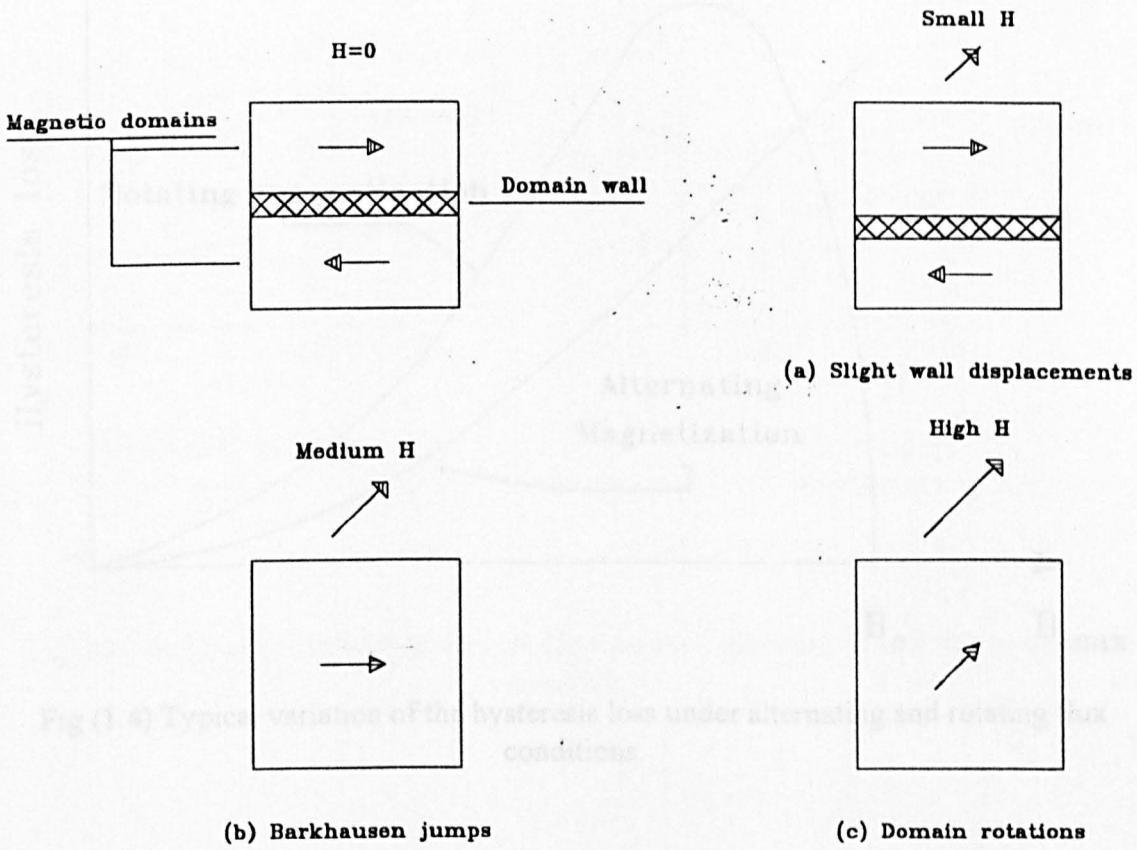


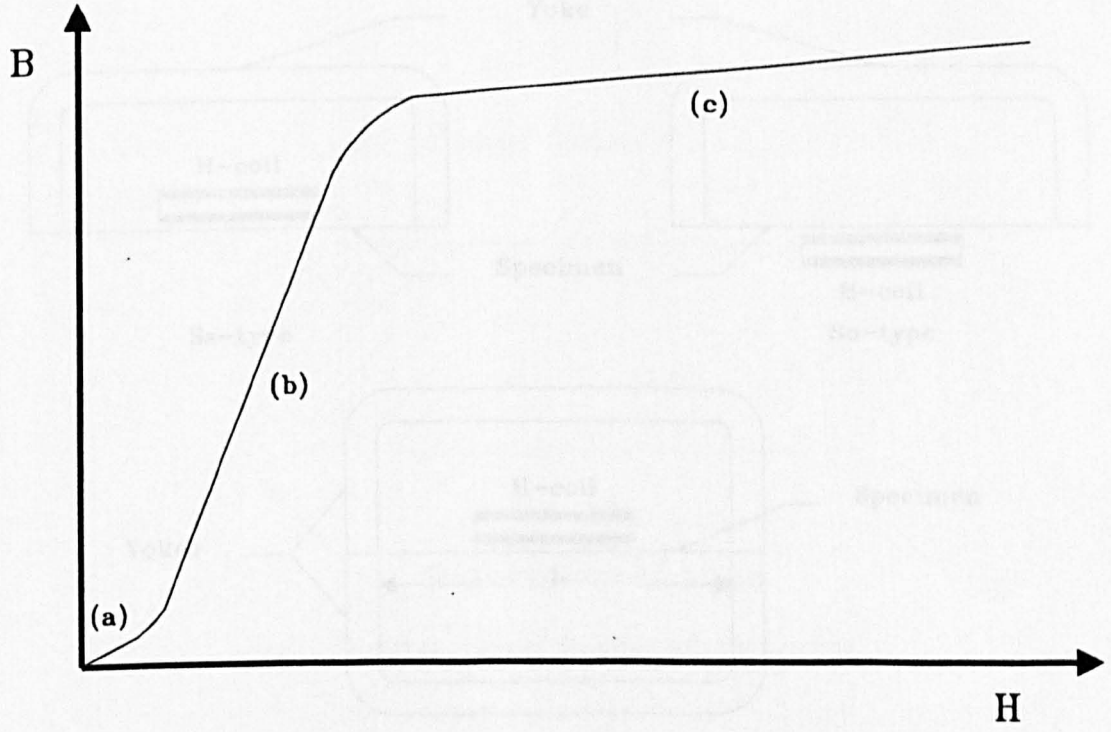


Fig (1.3) Schematic description of the magnetization stages for an initially demagnetized sample.

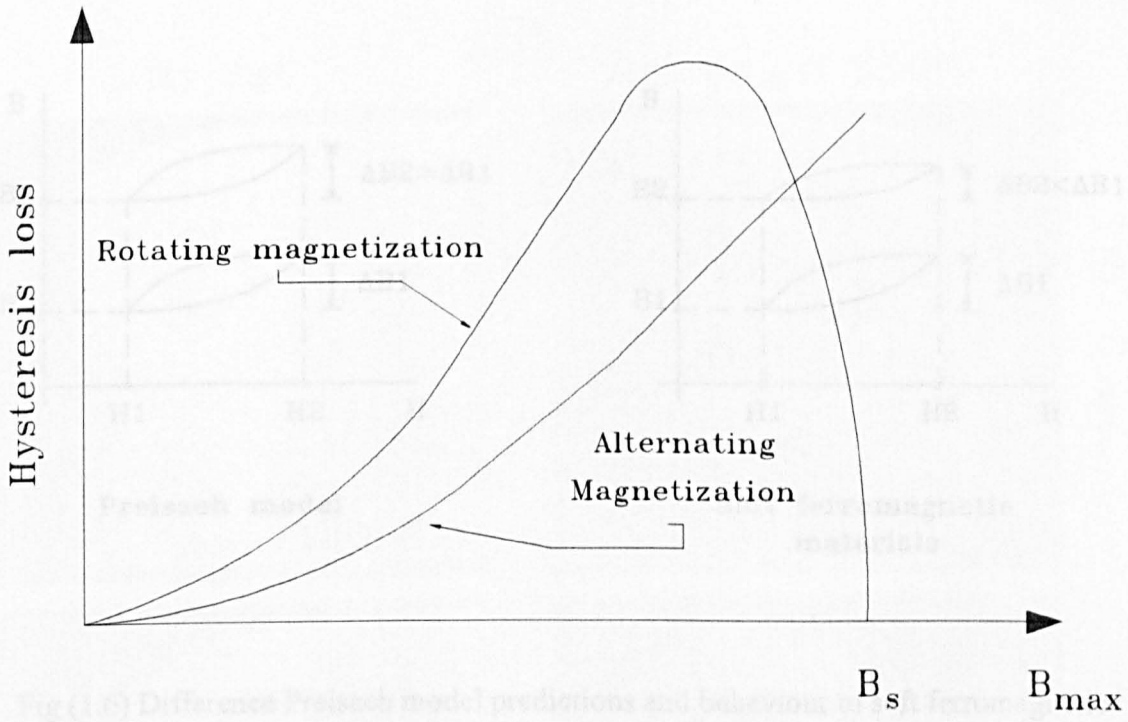


Fig (1.4) Typical variation of the hysteresis loss under alternating and rotating flux conditions.

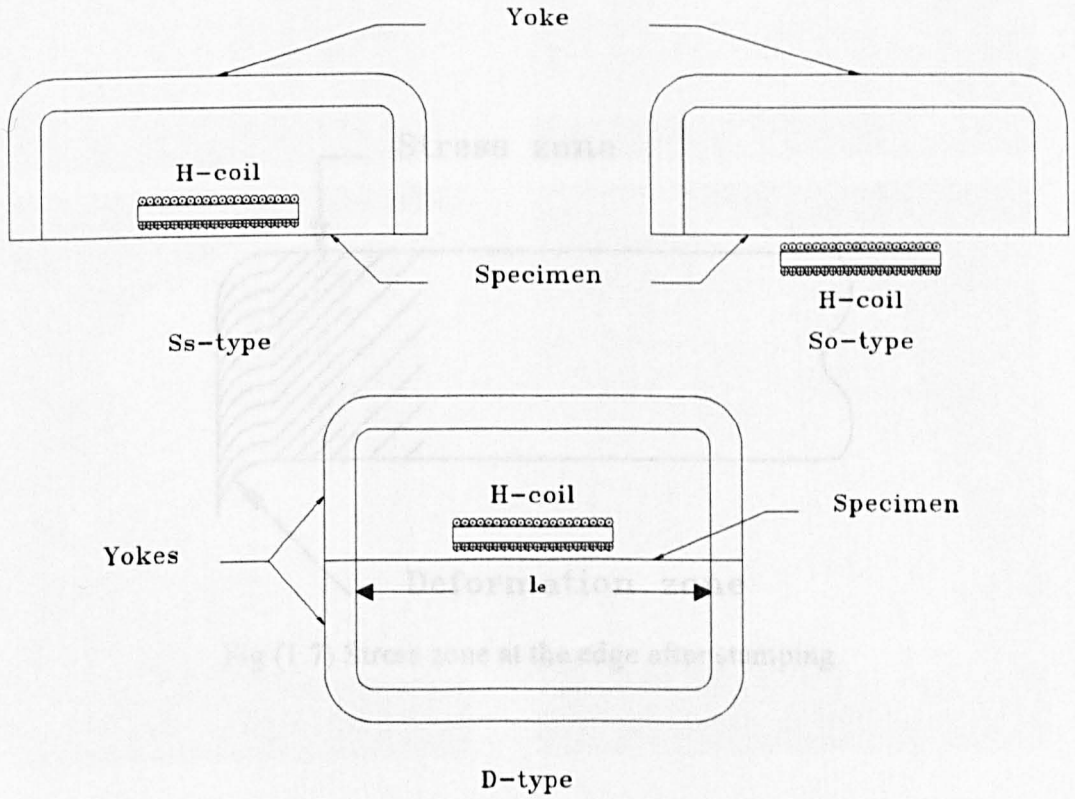


Fig (1.5) Different magnetic circuits for the alternating flux single-sheet tester.

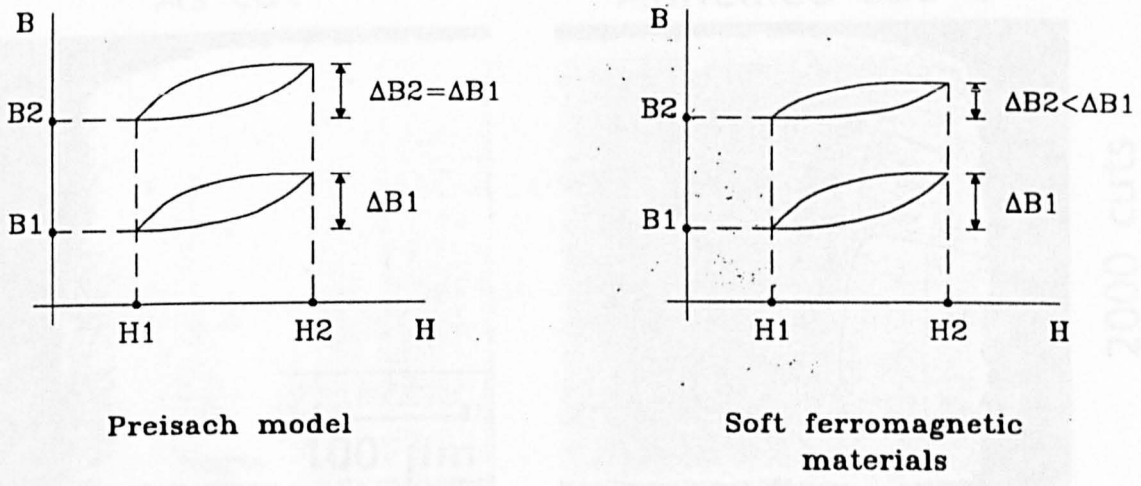


Fig (1.6) Difference Preisach model predictions and behaviour of soft ferromagnetic materials.

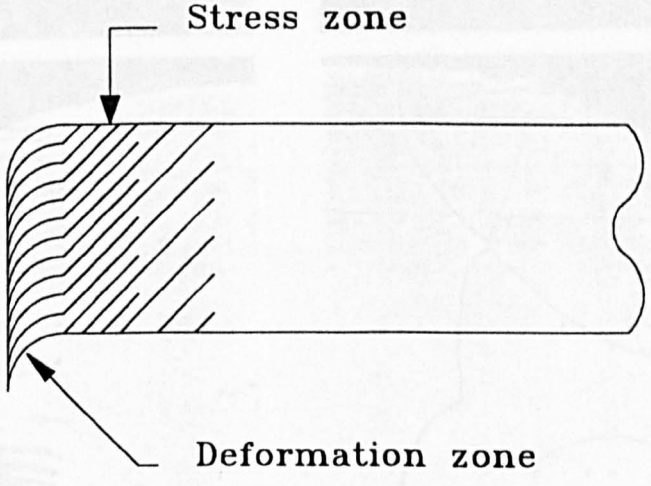


Fig (1.7) Stress zone at the edge after stamping.

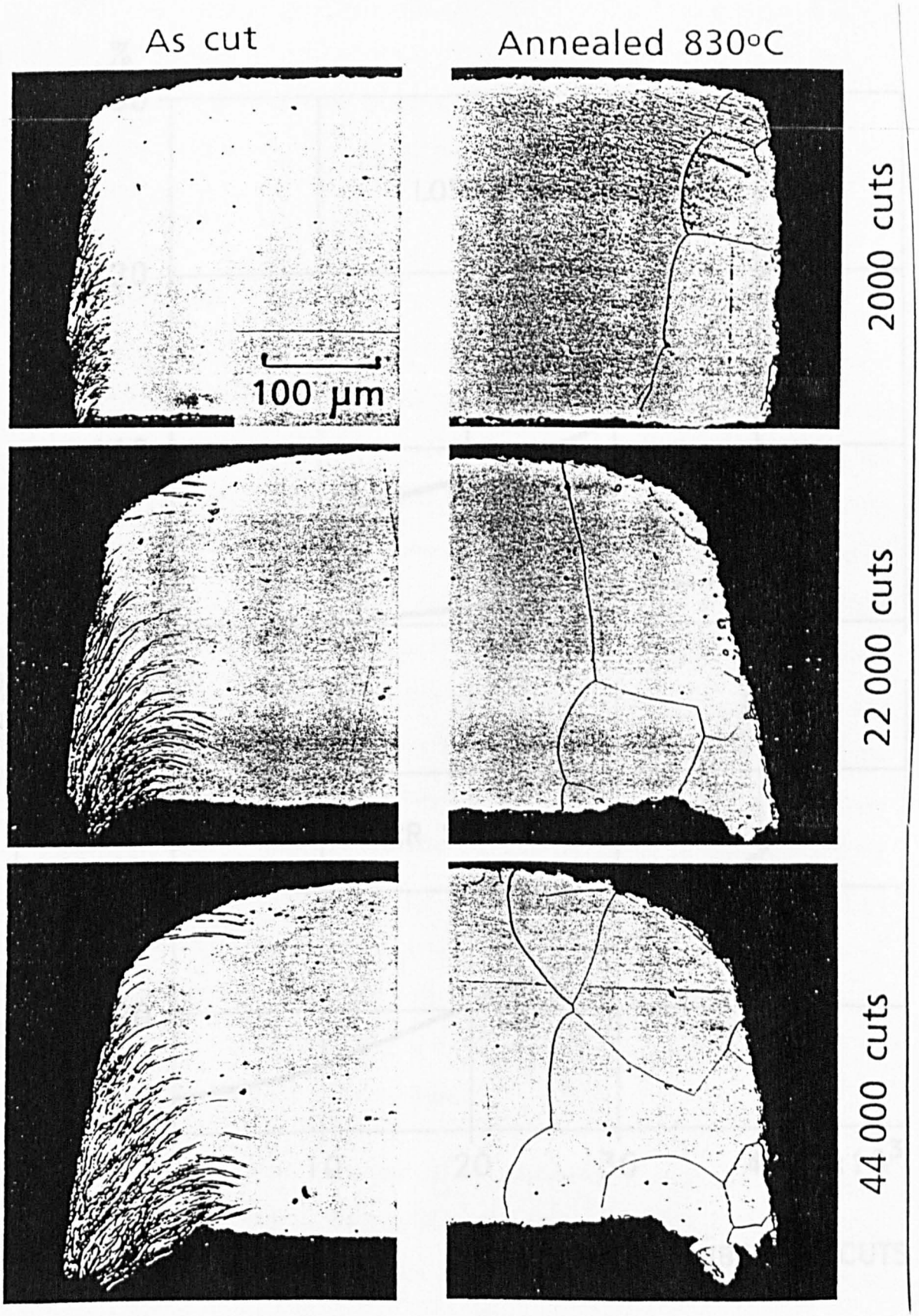


Fig (1.8) Sections through cut edge in grain-oriented SURA M-5 as cut and after stress relief annealing [36].

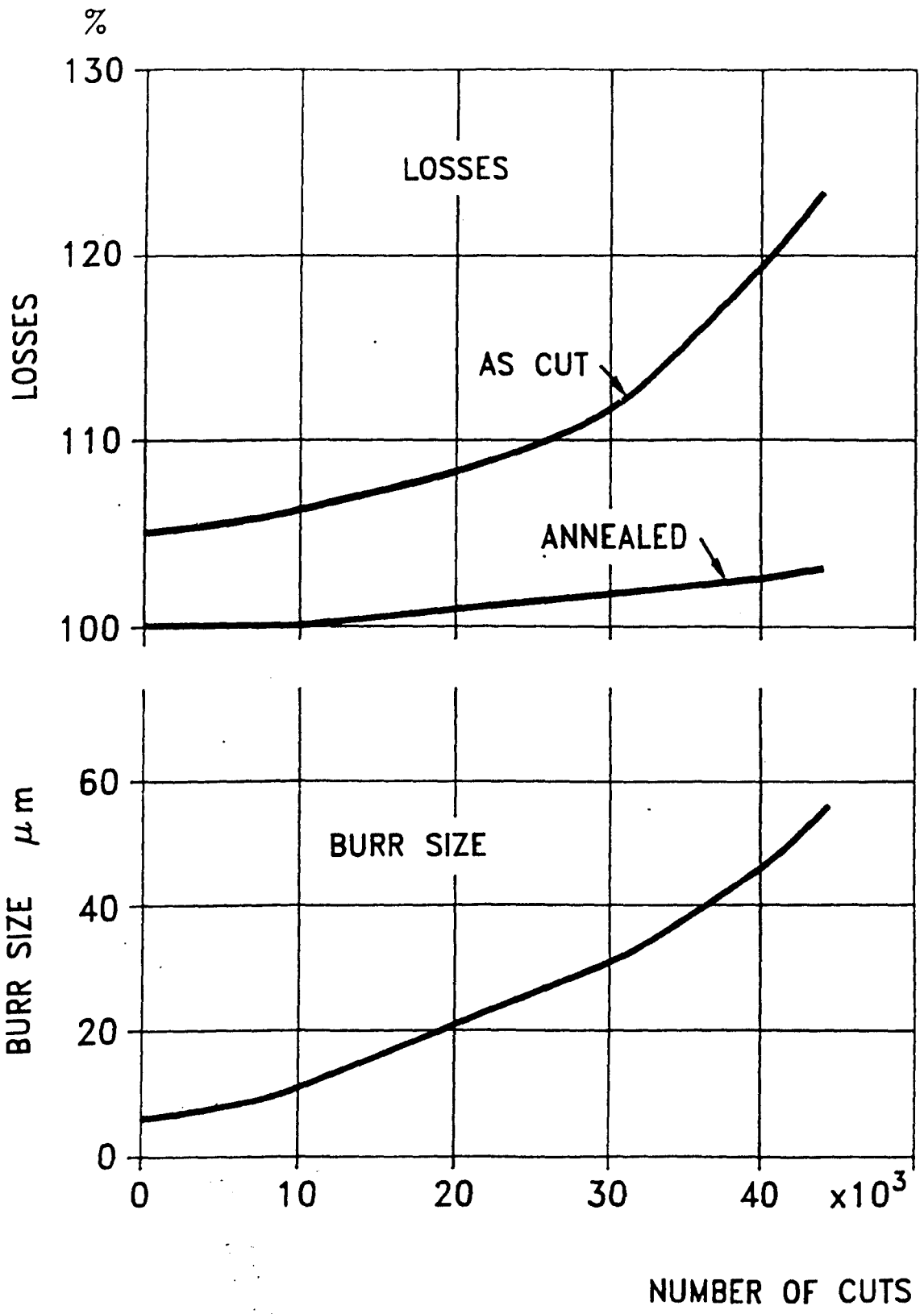


Fig (1.9) Variation of relative iron losses and burr size in grain-oriented SURA M-5 as cut and after stress relief annealing with the number of cuts [36].

# CHAPTER 2

# MEASUREMENT OF IRON LOSSES IN ELECTRICAL STEEL LAMINATIONS.

## 2.1) Introduction

Arguably the most important parameter for characterising the quality of electrical steel laminations is the iron loss density, which depends on the excitation frequency, the flux density waveform, and the flux conditions, which may vary from purely alternating to purely rotating. However, the data provided by electrical steel manufacturers is generally limited to alternating flux conditions and sinusoidal flux density waveforms at fundamental supply system frequencies most applied, viz 50 or 60 Hz. In most electrical machines, flux conditions generally vary greatly from one location in the core to another, whilst local flux density waveforms often deviate substantially from a fundamental sinusoid, particularily in controlled drive systems operating from power electronic converters. For these reasons, the characterisation of electrical steel laminations under conditions which mimic those encountered in practice is necessary if power loss involved during the energy conversion is to be predicted to an acceptable accuracy without resorting to the application of empirical iron loss factors, and the suitability of a particular grade of material for a specific application is to be assessed with confidence.

Systems which have been developed for the measurement of the iron loss under alternating controlled flux conditions will be described in this chapter. Further, for the case of non-purely rotating flux conditions, ambiguities related to the calculation of the magnetic power loss from measured $\vec{H}$ and $\vec{B}$ vectors, will be clarified, and

expressions for the calculation of the iron loss contributions from alternating and rotating flux components will be derived.

## 2.2) Single-sheet iron loss test system

Fig (2.1) shows schematic diagram of a closed-loop computer-controlled test system which has been developed for the measurement of the power loss in electrical steel laminations, under alternating flux conditions. It enables the measurement of power loss under any pre-specified flux density waveform and up to a fundamental frequency of 300 Hz. This limit is primarily set by the hardware specifications, namely the 100 KHz maximum sampling frequency of the analog to digital converters ICs, and can be easily overcome by the use of faster components, without substantial alterations to the original design. The systems, Fig (2.2), comprise the following elements:

- An 80286 personal computer.
- 1 programmable waveform generators.
- 2 digital recorders.
- A 2-channel linear power amplifier.
- Amplification and feed-back control circuits.
- Magnetic circuit for imposing alternating flux conditions.

### 2.2.1) Waveform generator and digital recorders

A system consisting of 4 modules, viz: a waveform generator, 2 digital recorders and a peripheral interface, have been constructed. For flexibility reasons, the modules have been designed separate in housing and operation. And can be interfaced to any IBM compatible personal computer by a 3 I/O ports universal peripheral interface. Fig (2.3) shows a functional block diagram of the system, the main features being as follows:

i) Controllable by any IBM compatible personal computer.

ii) In the run mode it operates under the control of an external TTL clock, with all the hardware control procedures effected on board. This feature makes the frequency of waveform generation and sampling limited only by the hardware specifications and not by the language used for the control software or the speed of the computer.

iii)Specifically designed for periodic waveform generation and sampling, as such only 512 Bytes of memory is needed for each waveform generation or sampling modules.

When effecting measurement under a periodic flux waveform, controlled by a personal computer, the control software should implement the following procedure:

- Set all the modules to the read/write mode.
- Load the waveform arrays to the memory cells of the waveform generators.
- Set all the modules to the run mode.
- Allow a steady-state condition to be reached.
- Set all the modules to the read/write mode.
- Read the measured data arrays from the digital recorders.
- Convert and post-process the measured data.

#### 2.2.1.1) Programmable waveform generator

The waveform generator generates a periodic 256 step staircase function, which is loaded into on-board memory cells, and then periodically fed into a 12-Bit digital to analog (D/A) converter. The frequency of the analog output is controlled by an external TTL clock driving an 8-Bit counter which generates the memory cell addresses. The relationship between the TTL clock frequency $f_{clock}$ and the analog output frequency $f$ is given by:

$$f_{clock} = 256 \times f \tag{1.1}$$

Periodic staircase functions include a large number of higher harmonics. A periodic staircase function can be described as:

$$U(\theta) = U_k, \quad \text{for } (k-1)\frac{2\pi}{N_{st}} \le \theta < k\frac{2\pi}{N_{st}} \tag{2.2}$$

where $N_{st}$ is the number of stairs per period and $U_k$ is the dc voltage of one stair. For stairs of equal length the Fourier spectrum of the periodic staircase function can be expressed as:

$$a_n = \frac{2}{\pi n}\sin(\frac{n\pi}{N_{st}})\sum_{k=1}^{N_{st}} U_k \cos(n(2k-1)\frac{\pi}{N_{st}}) \tag{2.3a}$$

$$b_n = \frac{2}{\pi n}\sin(\frac{n\pi}{N_{st}})\sum_{k=1}^{N_{st}} U_k \sin(n(2k-1)\frac{\pi}{N_{st}}) \tag{2.3b}$$

In the case of a sinusoidal waveform generated by an $N_{bts}$ Bit digital to analog converter $U_k$ is given by:

$$U_k = U_m \sin(\frac{2\pi}{N_{st}}(k-m)) \tag{2.4}$$

where

$$m = \begin{cases} 1 & \text{for } |U_m \sin(\frac{2\pi}{N_{st}}k) - U_{k-1}| < \frac{U_{da}}{2^{N_{bts}}} \\ 0 & \text{for } |U_m \sin(\frac{2\pi}{N_{st}}k) - U_{k-1}| \ge \frac{U_{da}}{2^{N_{bts}}} \end{cases} \tag{2.5}$$

where $U_m$ and $U_{da}$ are the maximum voltage of the generated waveform and the maximum voltage that can be generated by the D/A converter. Table (2.1) shows the effect of the D/A converter resolution on the higher harmonics in a sinusoidal waveform approximated by a staircase function.The total harmonic distortion is calculated as:

$$thd = \sqrt{\sum_{2}^{\infty} C_n^2} \tag{2.6}$$

where $C_n$ is the percentage of the $n^{th}$ harmonic to the fundamental. The harmonic content of the alternating voltage for the control of the power amplifier for iron loss measurements under sinusoidal flux density waveforms should not exceed 0.2% [54]. A 256 step staircase function generator, equipped with a 12-Bit D/A converter, fulfills this condition for a wide range of the ratio $U_m/U_{da}$.

### 2.2.1.2) Digital recorders

These modules perform the digitization of periodic analog waveforms. The digitization is achieved by a 12-Bit analog to digital (A/D) converter. 256 samples are stored, and periodically updated, in on-board memory cells. The sampling frequency is controlled by the same external clock, driving the counter which generates the memory addresses, at the rate of 1 sample per clock cycle.

A digitized periodic waveform is only known for a finite number of instants per cycle. For equi-spaced samples it can be described as:

$$U(\theta) = U_k \quad \text{for } \theta = \frac{2\pi}{N_{sp}}(k-1) \tag{2.7}$$

where $N_{sp}$ is the number of samples per cycle. For equi-spaced samples the Fourier spectrum, for $n \leq N_{sp}/2$, of a periodic discrete function is given by:

$$a_n = Real\left(\sum_{k=1}^{N_{sp}} U_k \times z^n\right) \tag{2.8a}$$

Table (2.1) Computer total harmonic distortion for different D/A converter resolutions. (The calculation is performed taking account of up to the $1000^{th}$ harmonic)

| $\frac{U_m}{U_{da}}$ | thd | | | | |
|---|---|---|---|---|---|
| | $N_{bts} = 8$ | $N_{bts} = 9$ | $N_{bts} = 12$ | $N_{bts} = 14$ | $N_{bts} = 16$ |
| 0.25 | 0.769 | 0.41 | $2.09 \times 10^{-2}$ | $2.44 \times 10^{-3}$ | $3.53 \times 10^{-4}$ |
| 0.5 | 0.417 | 0.18 | $7.83 \times 10^{-3}$ | $6.61 \times 10^{-4}$ | $1.11 \times 10^{-4}$ |
| 0.75 | 0.268 | $9.74 \times 10^{-2}$ | $4.13 \times 10^{-3}$ | $6.71 \times 10^{-4}$ | $1.11 \times 10^{-4}$ |
| 1.0 | 0.181 | $6.70 \times 10^{-2}$ | $2.44 \times 10^{-3}$ | $3.53 \times 10^{-4}$ | $1.3 \times 10^{-6}$ |

$$b_n = Imag\left(\sum_{k=1}^{N_{sp}} U_k \times z^n\right) \tag{2.8b}$$

where the complex variable z is given by:

$$z = \cos\left(\frac{2\pi}{N_{sp}}(k-1)\right) + j\sin\left(\frac{2\pi}{N_{sp}}(k-1)\right) \tag{2.9}$$

where $j^2 = -1$. Digital sampling is also affected by the resolution of the A/D converter. Similar analysis to that performed for the periodic staircase functions shows that 256 samples per cycle carried out by a 12-Bit A/D converter are sufficient for an accurate reconstruction of periodic waveforms similar to those encountered in iron loss measurements.

### 2.2.2) Magnetic circuits and $\vec{H}$ and $\vec{B}$ sensing.

In Chapter I it was argued that the D-type single-sheet/strip-tester has the best characteristics, in that it combines accuracy, simplicity of the test sample, and ease of magnetic field sensing. Fig (2.4) shows the dimensions of the magnetic circuit. The magnetic yokes are made of 0.3 mm thick laminations of high quality grain-oriented steel (M5).

The flux density derivative $dB/dt$ is measured using a search coil wound tightly around the lamination in order to minimise the effect of air flux. The relationship between the voltage induced in the search coil and $dB/dt$ is given by:

$$\frac{dB}{dt} = \frac{e_{bs}}{N_{bs} S} \tag{2.10}$$

where $e_{bs}$ is the search coil induced voltage.

$N_{bs}$ is the number of turns of the search coil.

$S$ is the lamination sample cross-section area.

The magnetic field strength H is deduced by using a precision resistor $R_h$ connected in series with the magnetising winding. Assuming that the effective magnetic path length is the inner length of the sample, the field strength is given by:

$$H = \frac{N_m}{l_e R_h} e_h \tag{2.11}$$

where $N_m$ is the number of turns of the magnetising windings.

$l_e$ is the effective magnetic path length.

$R_h$ is the resistance of the precision resistor.

$e_h$ is the voltage drop across the precision resistor.

### 2.2.3) Closed loop control

Soft ferromagnetic materials are characterised by having a non-linear B-H characteristic under both dc and ac flux conditions. Under dc flux conditions, however, the shape of the B-H hysteresis loop is dependant only on the maximum flux density, whilst under ac conditions it also depends on the excitation frequency as well as the magnetic field waveform. However, under the application of a specified magnetic field waveform the flux density waveform is virtually unpredictible, whilst both the hysteresis and eddy current components of iron loss are dependant on the flux density. Since, any comprehensive measurement system should be capable of imposing the cause, if the effect is to be thoroughly investigated, a feed-back control system has been designed and implemented which allows the iron loss measurement to be carried out under a pre-specified flux density waveform.

In practice, however, the control of the flux density B is achieved through the control of its derivative dB/dt for two main reasons:

i) The sensing search coil provides a signal proportional to dB/dt. Hence the direct control of B would necessarily lead to intermediate integration, with all the attendant practical problems, such as offset drifts.

ii) Closed-loop control can never be perfect, since it is always subject to practical limitations. However, whilst a sucessful reduction of unwanted distortion in the dB/dt waveform guarantees that at least the same success has been achieved in the B waveform, the reverse is not true. As a consequence, unwanted distortion in a periodic flux density waveform is always more pronouced in its derivative.

Fig (2.5) shows a schematic diagram of the closed-loop control. It will be seen that a variable cut-off frequency first order low pass filter has been added to overcome the effect of sub-resonance phenomena associated with non-linear systems. Under closed-loop, these cause the system to oscillate, besides the specified frequency, at frequencies many times higher. Since the degree of non-linearity in electrical steel laminations depends on the grade of material, the maximum flux density, the specified frequency and the flux density waveform, it is quite impossible to set a standard value for the cut-off frequency of the filter, and hence it has to be manually adjusted to create the required measurement conditions.

Fig (2.6) and (2.7) show examples of measured dB/dt waveforms together with their Fourier spectrums, for specified sinusoidal B waveforms of amplitudes 1.5 T and 1.7 T respectively. Where it will be noted that, under pre-specified sinusoidal B waveforms, total harmonic distorsion as low as 0.7% in dB/dt waveform can be achieved for relatively high maximum flux densities.

## 2.4 ) Iron loss calculation from measured $\vec{H}$ and $\vec{B}$.

The calculation of the total iron loss from measured values of $\vec{H}$ and $\vec{B}$ is still subject to considerable controversy, especially under rotating flux conditions, for which only experimental investigations are available, and the lack of rigorous theoretical analysis has lead to some confusion, as well as paradoxical conclusions, being drawn, as will be discussed later. For this reason, in the following section expressions for the

calculation of the total iron loss from measured $\vec{H}$ and $\vec{B}$ vectors are derived from the fundamental theory of electromagnetic fields.

### 2.4.1) Total iron loss calculation

The power transferred electromagnetically from a volume to its environment is given by the flux of the Poynting vector through the enclosing surface. The Poynting vector is defined as:

$$\vec{P} = \vec{E} \times \vec{H} \tag{2.12}$$

where $\vec{E}$ is the electric field

$\vec{H}$ is the magnetic field

The power transferred from the external system to the volume enclosed by the surface is:

$$P_t = -\iint_{surface} \vec{P}.\vec{n}\, ds \tag{2.13}$$

where $\vec{n}$ is the unit vector normal to the surface.

The divergence theorem yields

$$P_t = -\iint_{surface} \vec{P}.\vec{n}\, ds = -\iiint_{V} div(\vec{P})\, dv \tag{2.14}$$

where V is the volume contained by the enclosing surface.

Further,

$$div(\vec{P}) = div(\vec{E} \times \vec{H}) = \vec{H}.\, curl\, \vec{E} - \vec{E}.\, curl\, \vec{H} \tag{2.15}$$

and from Maxwell equations,

$$curl\, \vec{E} = -\frac{\partial \vec{B}}{\partial t} \tag{2.16}$$

where $\vec{B_l}$ is the local flux density. From equations (2.15) and (2.16), the electromagnetic power density is given by:

$$w = -div(\vec{P}) = \vec{H}.\frac{\partial \vec{B_l}}{\partial t} + \vec{E}.curl\,\vec{H} \tag{2.17}$$

In the iron loss measurement for both rotating and alternating flux conditions, the applied magnetic field $\vec{H}$ is generated by the magnetising windings and is assumed to be uniform over the cross-section of the lamination. Hence, its curl operator vanishes and equation (2.17) becomes:

$$w = \vec{H}.\frac{\partial \vec{B_l}}{\partial t} \tag{2.18}$$

and spatial averaging leads to:

$$\overline{w} = \frac{1}{S}\int_S \vec{H}.\frac{\partial \vec{B_l}}{dt}\,ds = \vec{H}.\frac{d\vec{B}}{dt} \tag{2.19}$$

where $\vec{B}$ is the average flux density in the lamination.

Alternating flux conditions

In this case the flux is unidirectional and the average power loss density becomes:

$$\overline{w} = H\frac{dB}{dt} \tag{2.20}$$

Time averaging over a cycle yields:

$$P_t = \frac{1}{T}\int_T H\frac{dB}{dt}\,dt \tag{2.21}$$

where T is the period

Rotating flux conditions

In this case the flux has two orthogonal components, and using the properties of the dot product the average power density becomes:

$$\overline{w} = H_x \frac{dB_x}{dt} + H_y \frac{dBy}{dt} \tag{2.22}$$

where $H_x$ and $H_y$ are the components of $\vec{H}$ in the x and y directions respectively. $B_x$ and $B_y$ are the components of $\vec{B}$ in the x and y directions respectively.

Again time averaging over a cycle yields

$$P_t = \frac{1}{T}\int_T \left( H_x \frac{dB_x}{dt} + H_y \frac{dB_y}{dt} \right) dt \tag{2.23}$$

In the above analysis, only the applied magnetic field, which represents the primary source of power, has been considered. However, whilst this may still be open to argument, a good agreement between the field sensing, using equation (2.23), and the initial rate of rise of temperature loss measuring methods has been reported [55].

An alternative expression for the total loss calculation, which has been considered to be equivalent to equation (2.23) [11], is as follows:

$$P_r = \frac{\omega}{T}\int_T (\vec{H} \times \vec{B})_z \, dt \tag{2.24}$$

where $(\vec{H} \times \vec{B})_z$ is the component of the vector $(\vec{H} \times \vec{B})$ on the z direction, which is also the instantaneous torque caused by the rotation of the field .

Experimental investigations [15], however, have shown that these expressions give the same results only for the case of a pure rotating flux condition. Indeed, as will be shown later, equations (2.23) and (2.24) are mathematically equivalent only for the case of a pure rotating flux condition. However, as derived previously, equation (2.23) should give the total loss under any flux condition. Hence, an issue which requires resolving is the loss which equation (2.24) represents.

Equation (2.24) has been attributed by certain investigators as being the true rotational power loss [16,17], namely the component of loss due to rotation in non-purely rotating flux conditions, because it provides the power loss caused by the loss torque

which is a consequence of the angle of lag between the vectors $\vec{H}$ and $\vec{B}$. The existence of the angle of lag between the two vectors is certainly a characteristic of rotating flux conditions, and the component of loss that it causes can be a good measure of the effect of rotation. However, equation (2.24) is certainly not correct. This is supported by experimental results, given by the same investigators, which show that in the case of grain oriented materials the loss given by equation (2.24) when the flux density is not purely rotating is higher than that given by equation (2.23). Which lead them to conclude that the power loss given by equation (2.23) does not represent the total loss, being just the sum of the losses due to the flux components in the x and y directions, whilst equation (2.23) still provides the power loss component due to rotation. In reality the contrary is true. To resolve this controversy, an expression for the portion of loss due to rotation, ie rotational loss, is derived, and the paradox is clarified.

### 2.4.2) Calculation of the iron loss component due to rotation, or rotational loss, due to non-purely rotating flux conditions

In polar coordinates $\frac{d\vec{B}}{dt}$ is given by:

$$\frac{d\vec{B}}{dt} = |\vec{B}|\frac{d\theta}{dt}\vec{e_\theta} + \frac{d|\vec{B}|}{dt}\vec{e_r} \tag{2.25}$$

where $\vec{e_\theta}$ and $\vec{e_r}$ are the unit vectors in the circumferential and radial directions respectively. In rectangular coordinates they are given by:

$$\vec{e_r} = \cos\theta\,\vec{i} + \sin\theta\,\vec{j} \tag{2.26a}$$

$$\vec{e_\theta} = -\sin\theta\,\vec{i} + \cos\theta\,\vec{j} \tag{2.26b}$$

where $\vec{i}$ and $\vec{j}$ are the unit vectors in the x and y directions respectively, as shown in Fig (2.8).

Furthermore , $\vec{H}$ can be expressed as:

$$\vec{H} = |\vec{H}| \cos(\alpha+\theta)\,\vec{i} + |\vec{H}| \sin(\alpha+\theta)\,\vec{j} \tag{2.27}$$

where $\alpha$ is the angle of lag between $\vec{H}$ and $\vec{B}$.

From equations (2.25), (2.26), and (2.27), the power density $\vec{H}.\frac{d\vec{B}}{dt}$ is rewritten as:

$$\vec{H}.\frac{d\vec{B}}{dt} = \frac{d\theta}{dt}|\vec{H}||\vec{B}| \sin\alpha + |\vec{H}|\frac{d|\vec{B}|}{dt}\cos\alpha \tag{2.28}$$

which can also be written as:

$$\vec{H}.\frac{d\vec{B}}{dt} = \frac{d\theta}{dt}(\vec{H}\times\vec{B})_z + |\vec{H}|\frac{d|\vec{B}|}{dt}\cos\alpha \tag{2.29}$$

From equation (2.29) the rotational power loss is given by:

$$P_r = \frac{1}{T}\int_T \frac{d\theta}{dt}(\vec{H}\times\vec{B})_z\,dt \tag{2.30}$$

and the power loss due to alternating flux components is given by:

$$P_a = \frac{1}{T}\int_T |\vec{H}|\frac{d|\vec{B}|}{dt}\cos\alpha\,dt \tag{2.31}$$

### 2.4.3) Effect of the instantaneous angular speed of the flux density vector $\vec{B}$

The difference between expressions (2.24) and (2.30) for the rotational power loss calculation is the instantaneous angular speed of the rotation of the flux density vector $\frac{d\theta}{dt}$, which has been wrongly assumed to be $\omega = 2\pi f$. Indeed, under non-purely rotating flux density, and even if the x and y components are purely sinusoidal, although the average rotational speed is $\omega$ the instantaneous speed is not. To clarify this consider a flux density vector having x and y components as follows:

$$B_x = B_m \sin(\omega t) \tag{2.32a}$$

$$B_y = a\,B_m \cos(\omega t) \tag{2.32b}$$

where $0 \leq a \leq 1$. a=1 corresponds to a pure rotating flux density, and a=0 corresponds to a pure alternating flux density. From equations (2.32a) and (2.32b),

$$\theta = arctg\left(\frac{B_y}{B_x}\right) = arctg\left(a\ tg\left(\omega t\right)\right) \tag{2.33}$$

leading to,

$$\frac{d\theta}{dt} = \frac{a\,\omega}{\cos^2\left(\omega t\right) + a^2 \sin^2\left(\omega t\right)} \tag{2.34}$$

Fig (2.9) shows flux density loci for different values of a, whilst Fig (2.10) shows the variation of the per unit instantaneous angular speed $\frac{1}{\omega}\frac{d\theta}{dt}$ over a cycle for different values of the ratio a, where it will be noted that under non-purely rotating flux density conditions the instantaneous angular speed of the flux density vector is not constant over a cycle but can vary substantially.

Furthermore, under purely rotating flux conditions, the magnitude of the flux density is constant, leading to:

$$\frac{d\left|\vec{B}\right|}{dt} = 0 \tag{2.35}$$

whilst from equation (2.34), for a=1, the instantaneous angular speed is constant and is given by:

$$\frac{d\theta}{dt} = \omega \tag{2.36}$$

From equations (2.30), (2.31), (2.35), and (2.36):

$$P_a = 0 \tag{2.37}$$

and

$$P_t = P_r = \frac{\omega}{T}\int_T \left(\vec{H} \times \vec{B}\right)_z dt = \frac{1}{T}\int_T \vec{H} \cdot \frac{d\vec{B}}{dt} dt \tag{2.38}$$

which proves the mathematical equivalence of equations (2.23) and (2.24) for purely rotating flux conditions only.

## 2.5) D C conditions

The characterisation of soft ferromagnetic materials under dc flux conditions is also very important, because it gives a direct indication of the potential magnetic performance of the material, which is often diluted by dynamic effects under ac flux conditions. Furthermore, the prediction of the power loss usually requires its separation into its fundamental components, viz, hysteresis and eddy current losses, which are linked to the magnetic and electric properties of the material. A computer-controlled system for the characterisation of soft ferromagnetic materials under dc conditions has been developed. Among other things, the system enables the measurement of the hysteresis loss as well as the initial dc magnetisation curve. Fig (2.11) shows a schematic diagram of the system, which comprises the following elements.

- An 80286 personal computer.
- A linear power amplifier.
- An integrating fluxmeter.
- 14 Bit, 16 channels A/D, 2 channels D/A converters card.
- Magnetic circuit.

### 2.5.1) Sample demagnetisation.

The magnetisation in a ferromagnetic material is a function of its past history as well as the level of the magnetic field strength. In other words, a knowledge of the magnetic field strength alone is insufficient for a complete characterisation of the magnetisation. For this reason, before effecting any measurement the initial conditions have to be known if the experiment is to have any relevence.

For the above reason, the lamination sample are demagnetised before each measurement. This is achieved by initially subjecting the sample to a high magnetic field strength, above 5000 A/m, and then periodically reversing the magnetic field whilst gradually decreasing its magnitude to zero.

### 2.5.2) Measurement of the hysteresis loss and the initial magnetisation curve.

The initial magnetisation curve is the B-H characterestic of a sample when it is gradually magnetised from a fully demagnetised state. Due to symmetry, the tips of a family of dc hysteresis loops, for each of which the enclosed area represents the hysteresis loss per cycle, is the initial magnetisation curve. Hence, the measurement of the initial magnetisation curve as well as the hysteresis loss can be undertaken simultanously. In the current investigation the magnetic circuit as well as the lamination samples are identical to those used for the alternating flux iron loss measurement. However, ring shaped lamination samples can also be used for the measurement without altering the control software.

## 2.6) Conclusions

In this chapter systems for measuring iron losses in electrical steel laminations under both alternating and rotating flux conditions have been described. Ambiguities related to the calculation of the total iron loss under rotating flux conditions from measured $\vec{H}$ and $\vec{B}$ have been clarified, and an expression for the calculation of the portion of loss due to rotation under non-purely rotating flux conditions has been derived. In addition, procedures for measuring the initial dc magnetisation characteristic and the hysteresis component of iron loss have been presented.

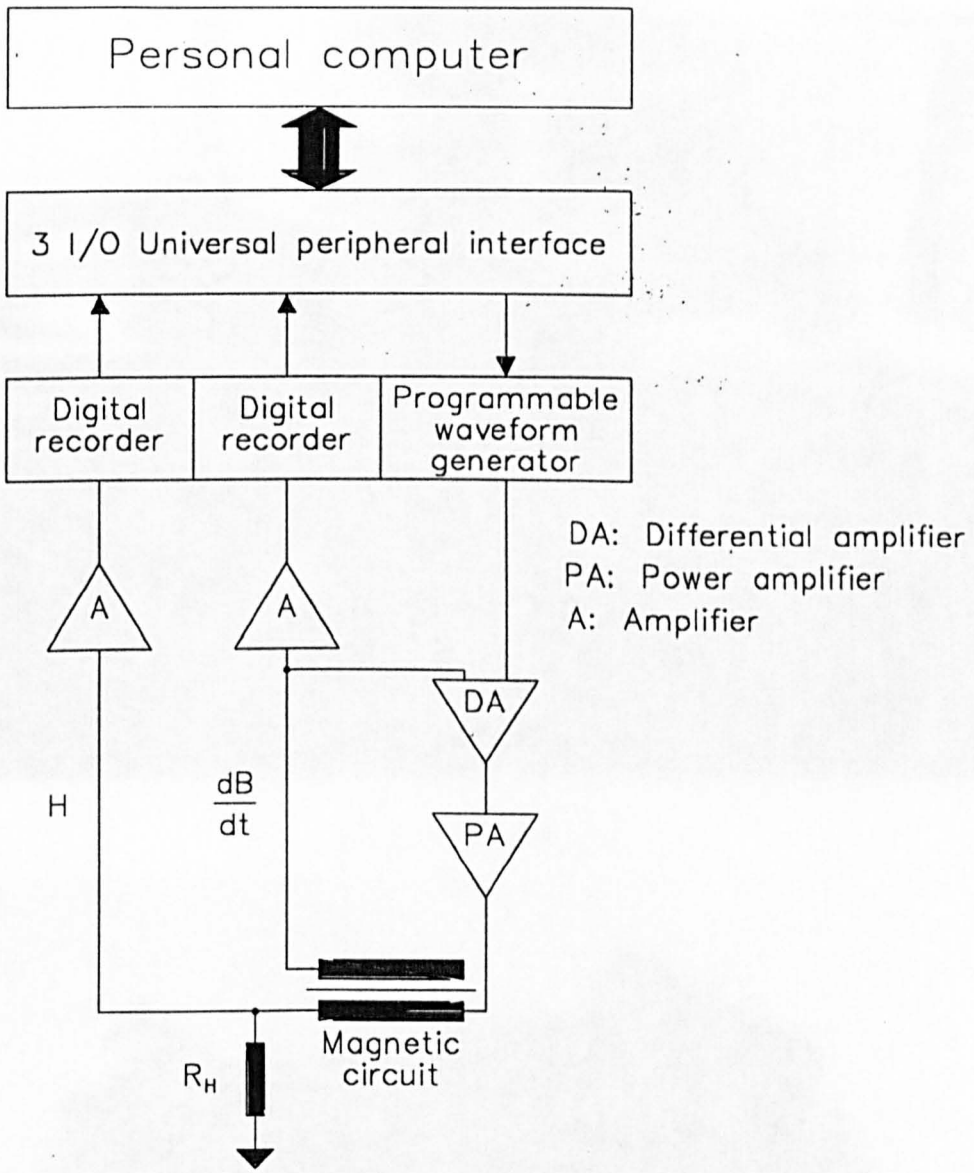


Fig (2.1) Schematic of iron loss measurement system under alternating flux condition.

(a) Connected system.

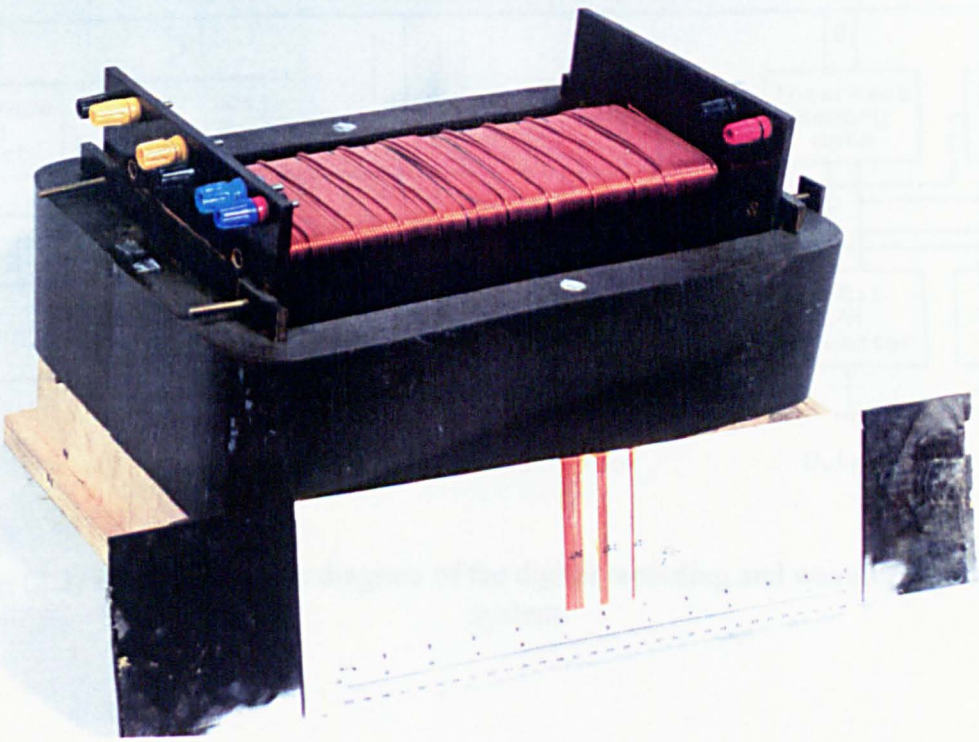

(b) Magnetic circuit.

Fig (2.2) Single-sheet test system for measurement of magnetic power loss in electrical steel laminations.

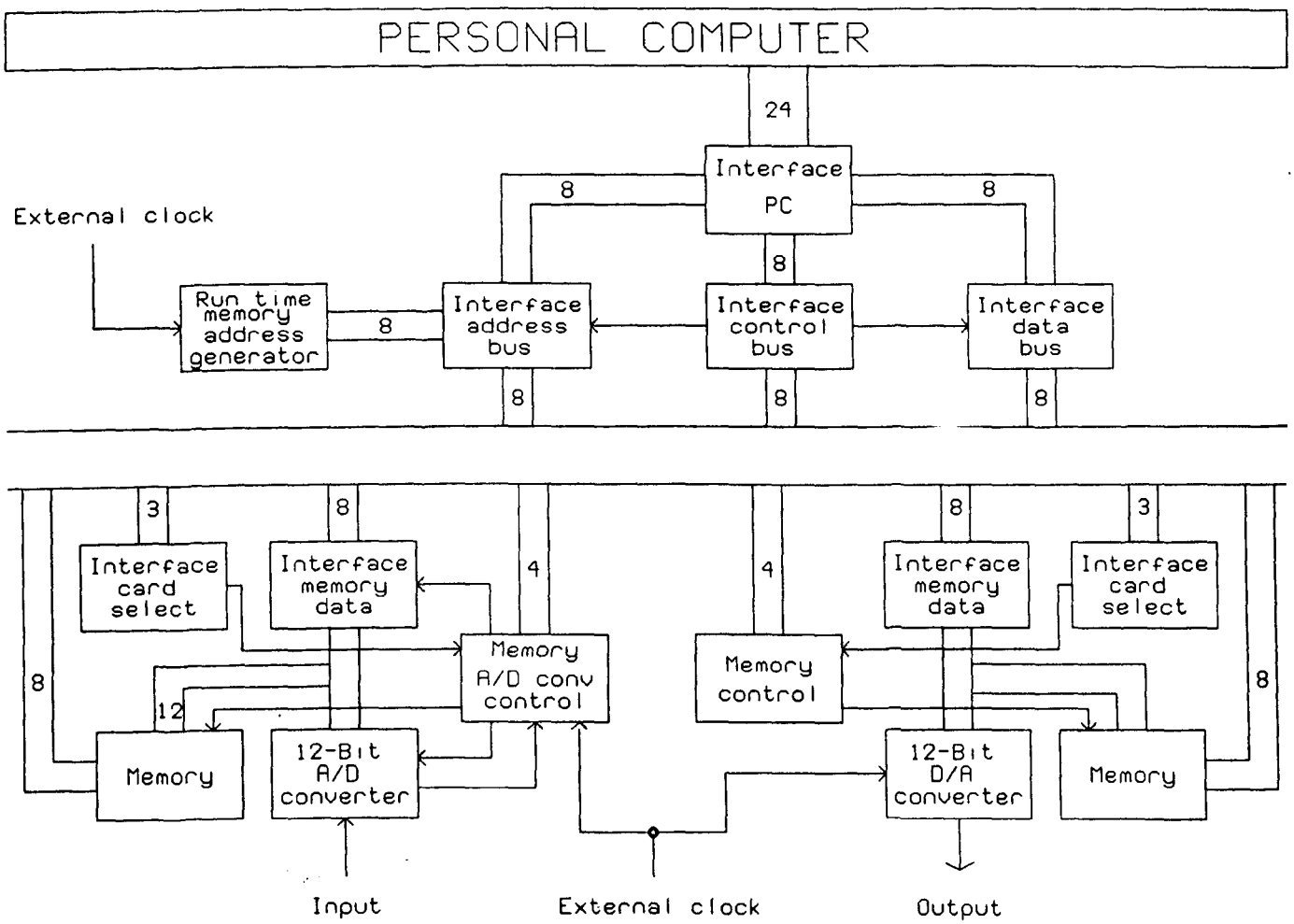


Fig (2.3) Functional block diagram of the digital recording and waveform generation system.

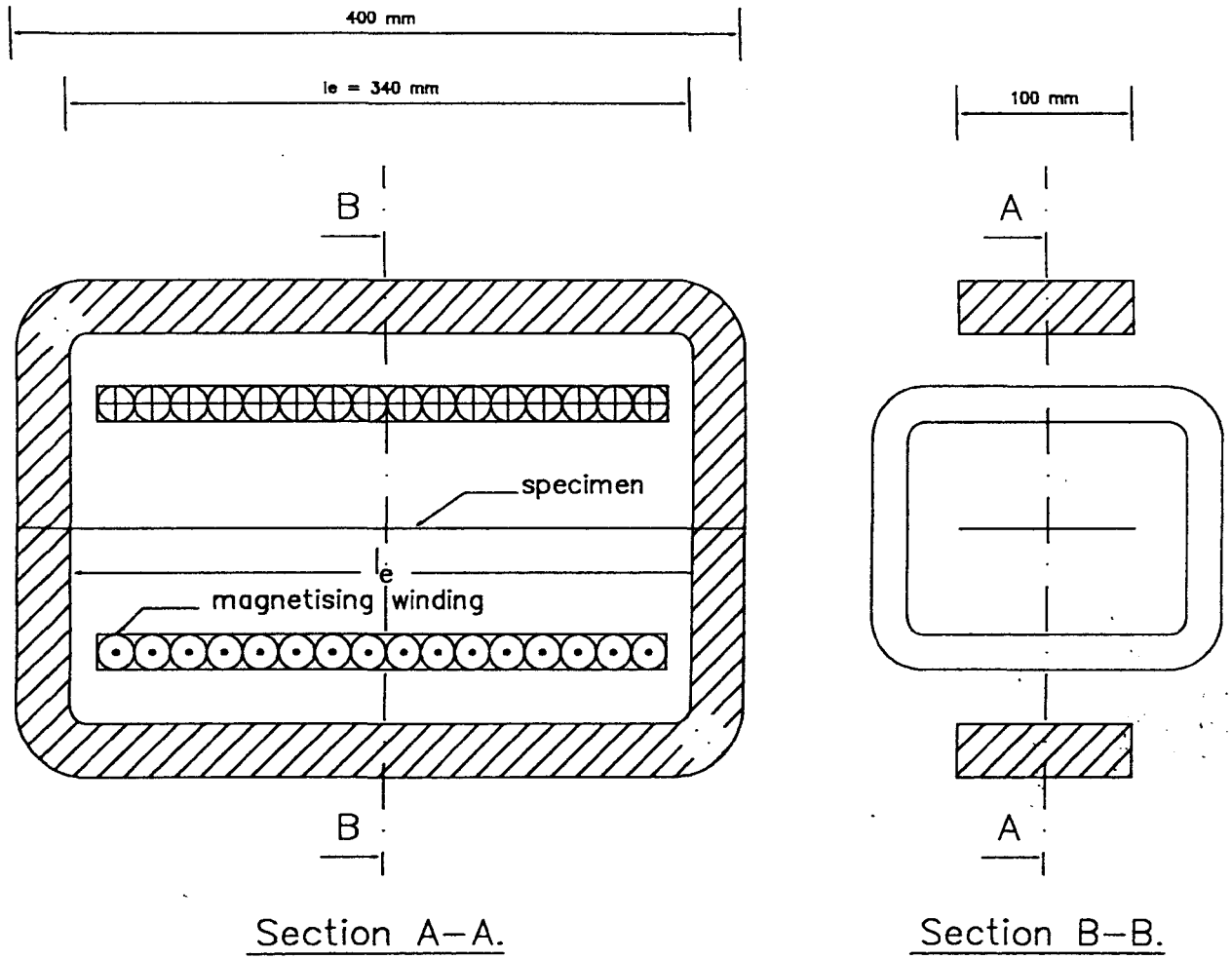


Fig (2.4) Magnetic circuit of single-sheet test rig for alternating flux conditions.

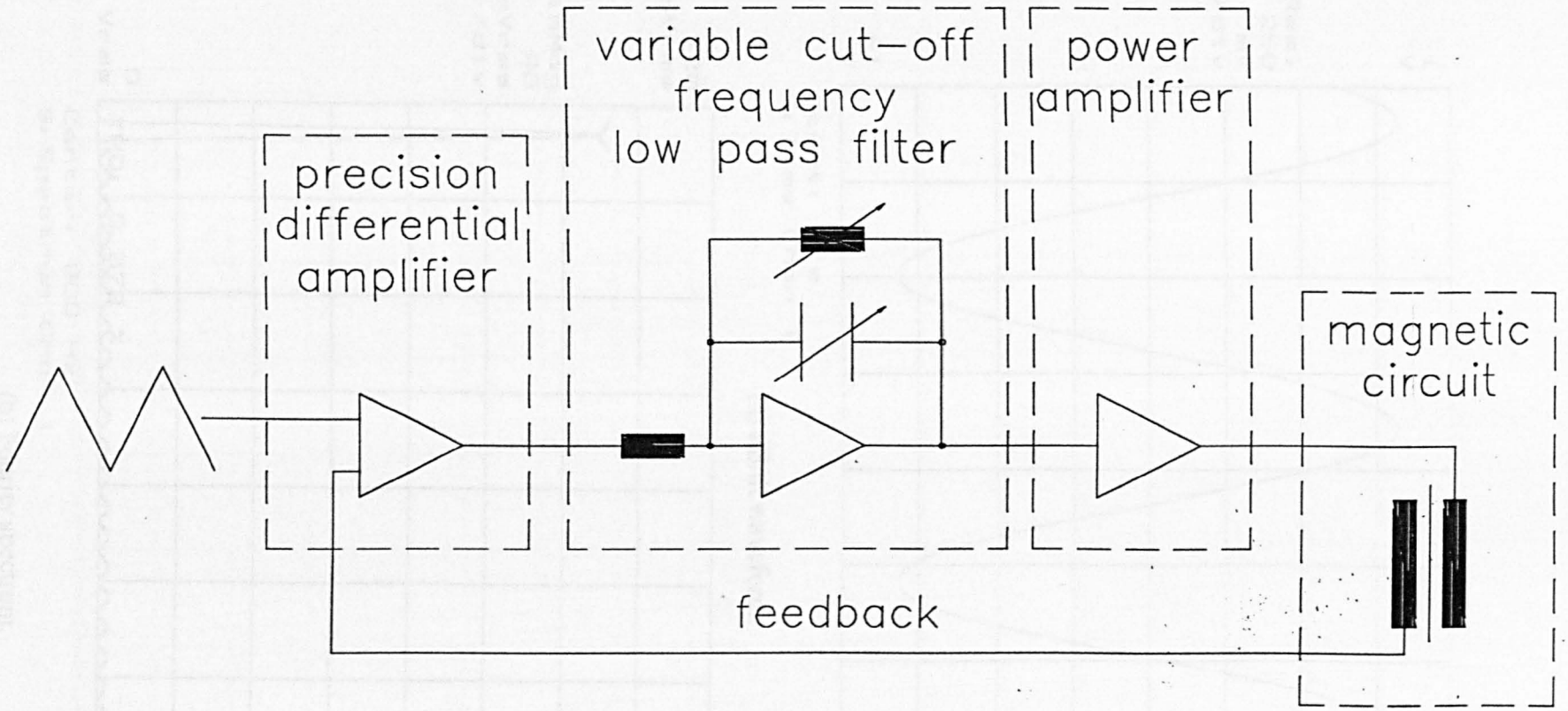


Fig (2.5) Schematic of closed-loop control system.

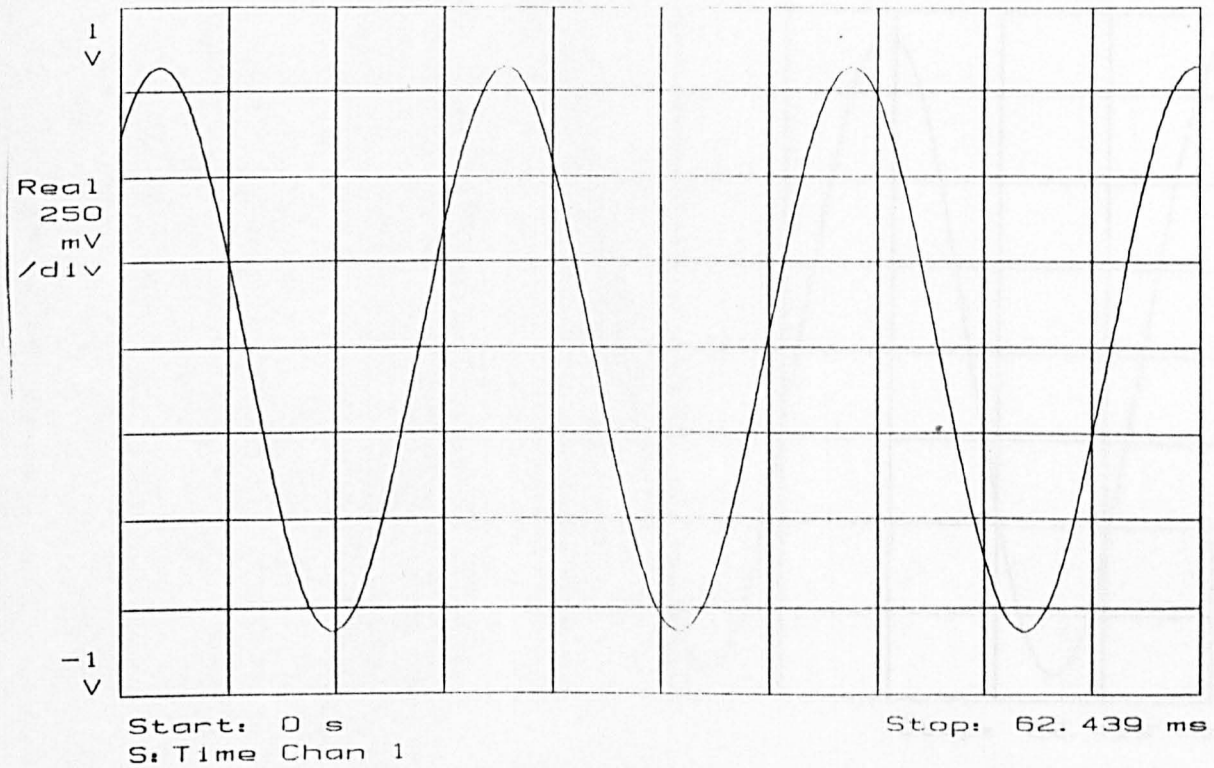


(a) dB/dt waveform.

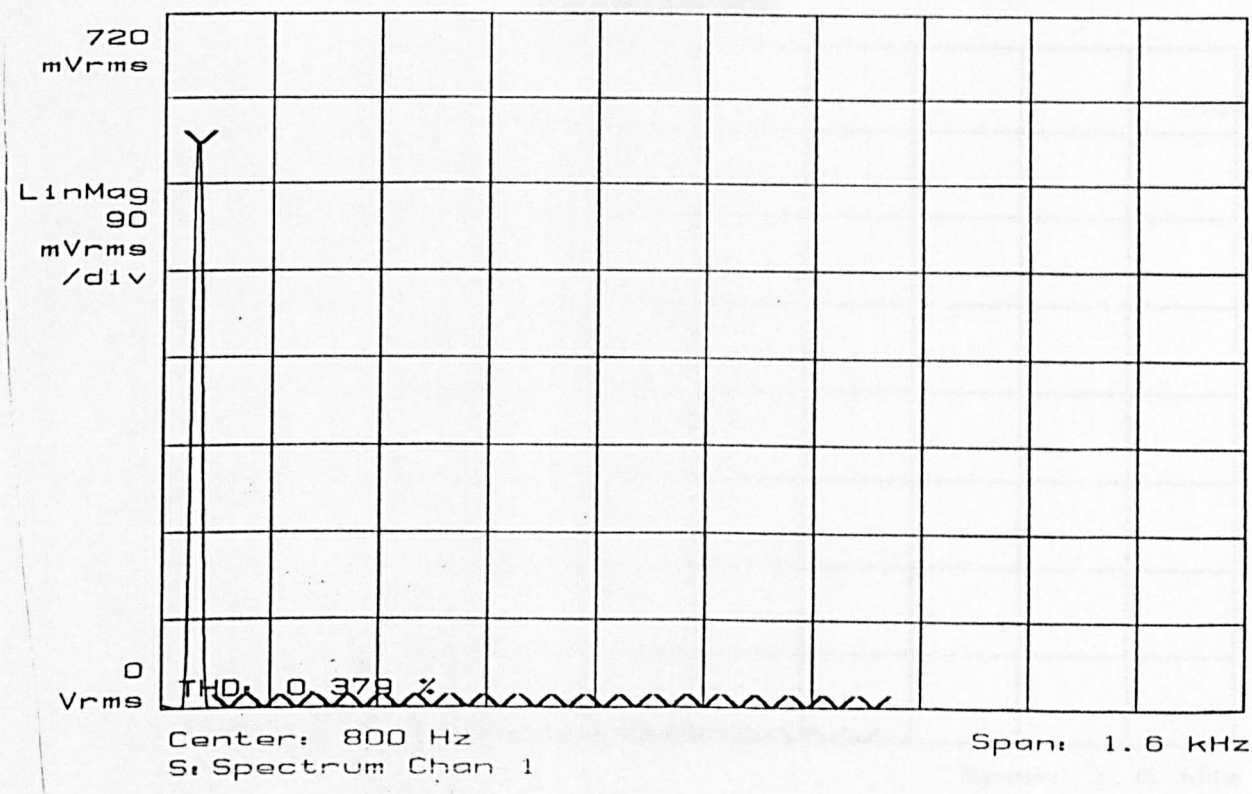


(b) Fourier spectrum.

Fig (2.6) Measured dB/dt waveform and Fourier spectrum for a pre-specified sinusoidal flux density waveform ($B_{max}$ = 1.5 *T*).

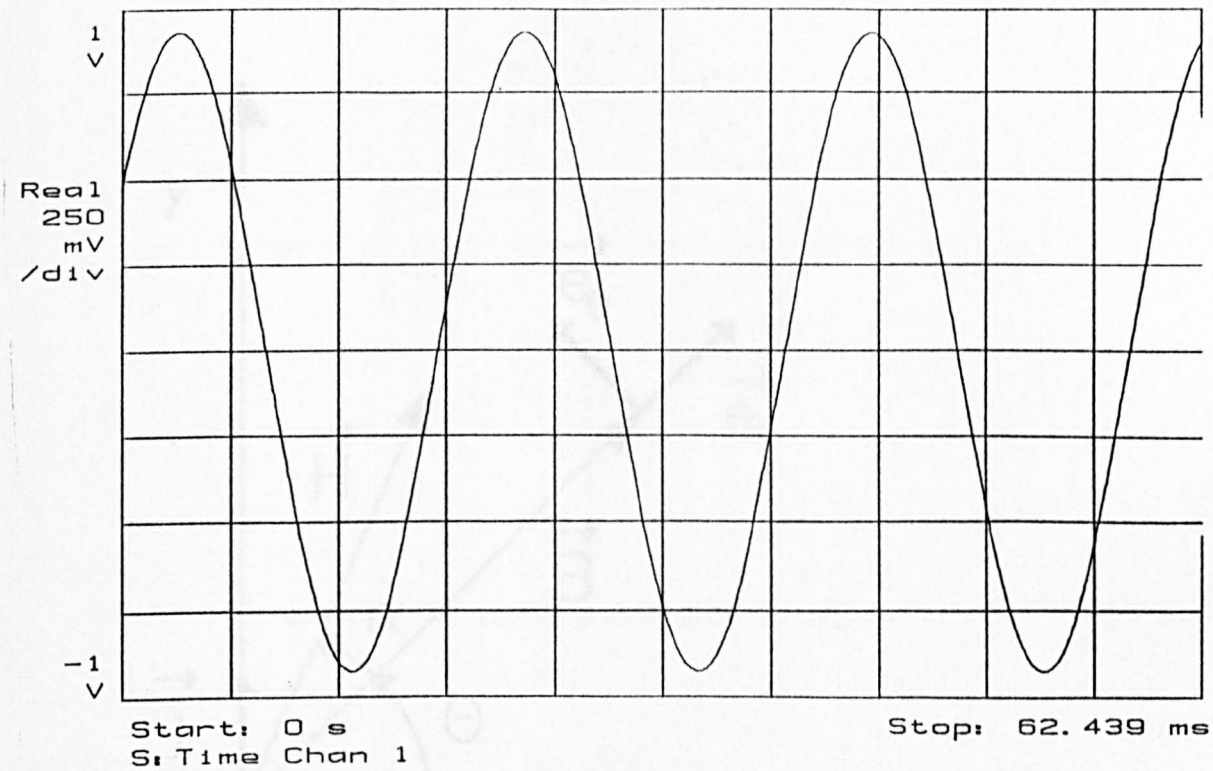


(a) dB/dt waveform.

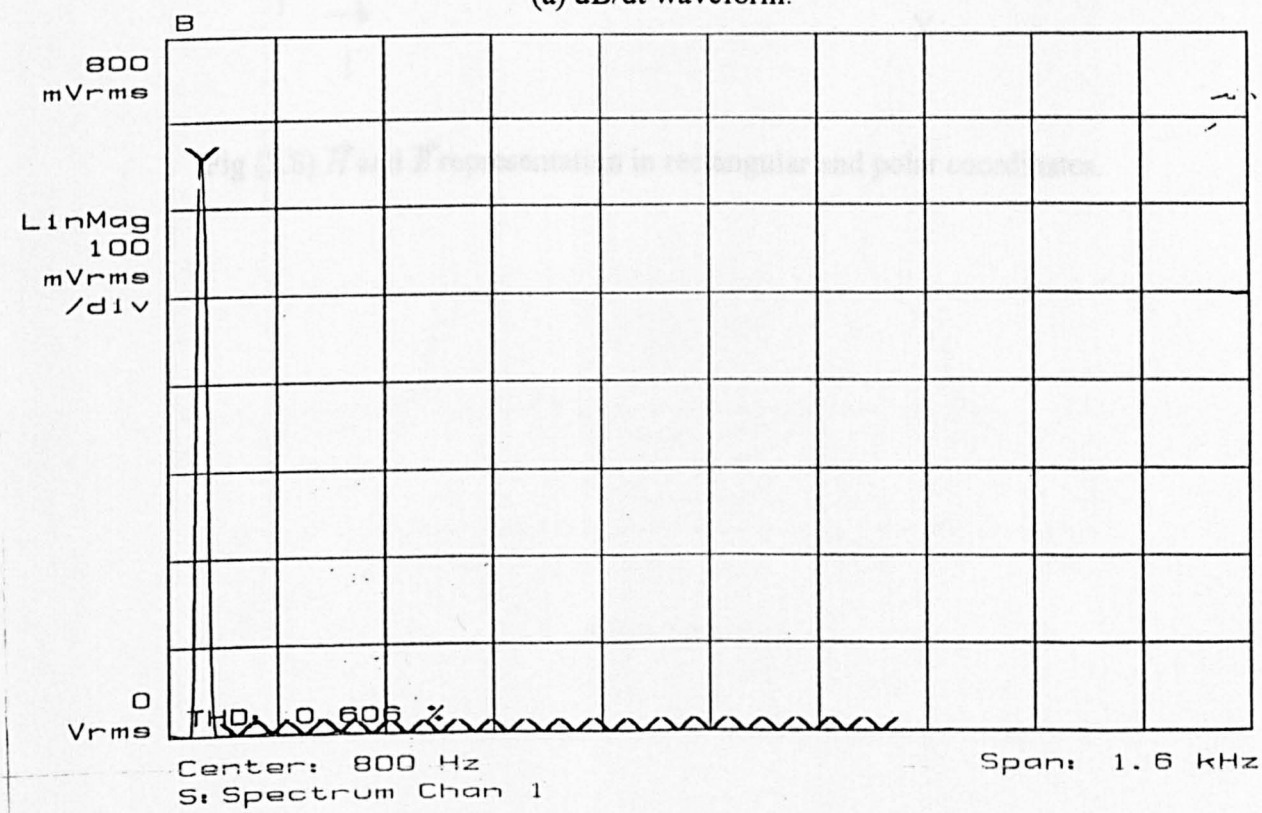


(b) Fourier spectrum.

Fig (2.7) Measured dB/dt waveform and Fourier spectrum for pre-specified sinusoidal flux density waveform ($B_{max}$ = 1.7 $T$).

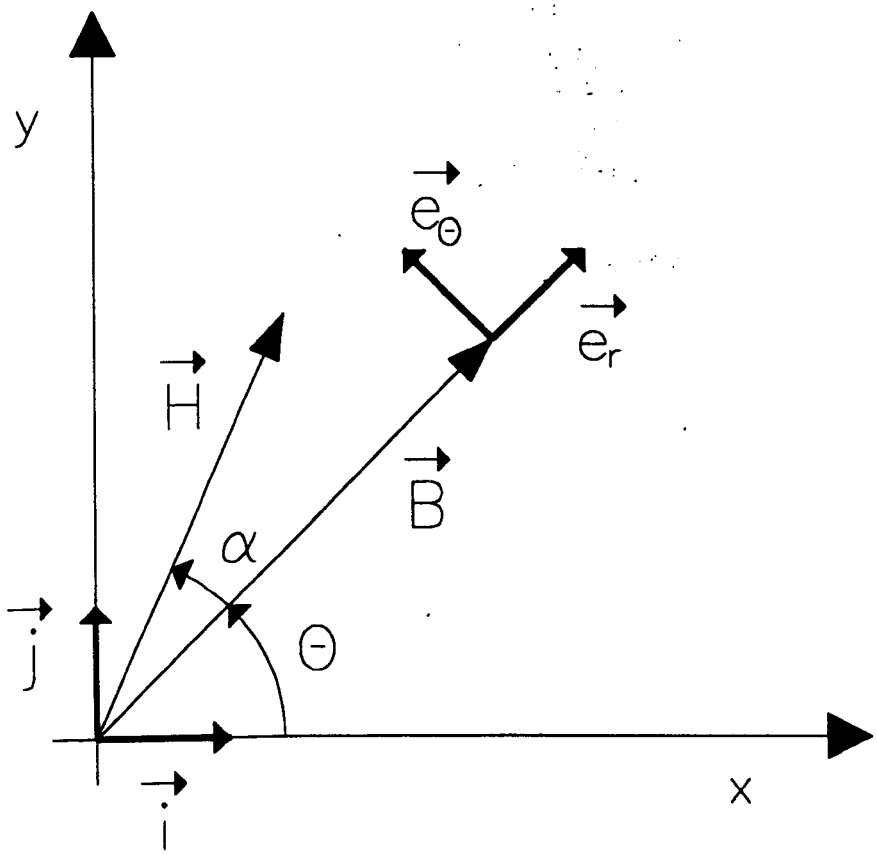


Fig (2.8) $\vec{H}$ and $\vec{B}$ representation in rectangular and polar coordinates.

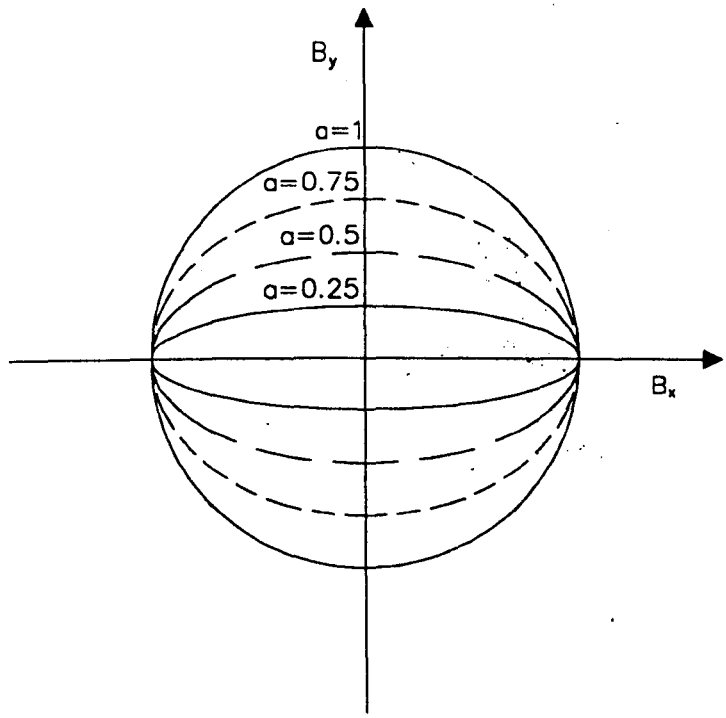


Fig (2.9) Flux density loci for different values of a.

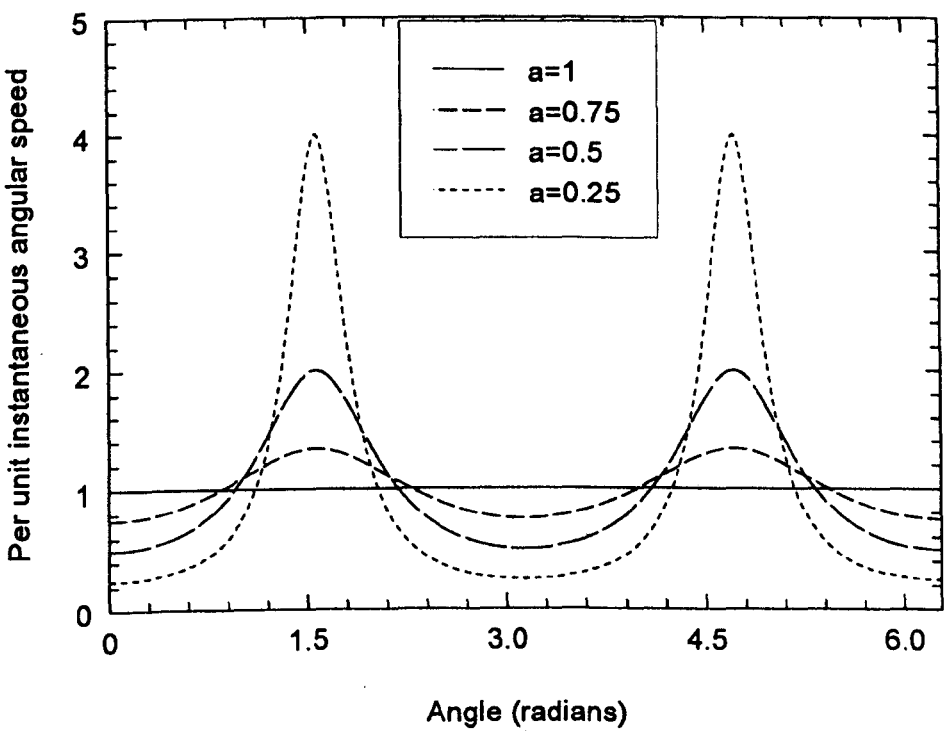


Fig (2.10) Instantaneous angular speed for different flux density loci.

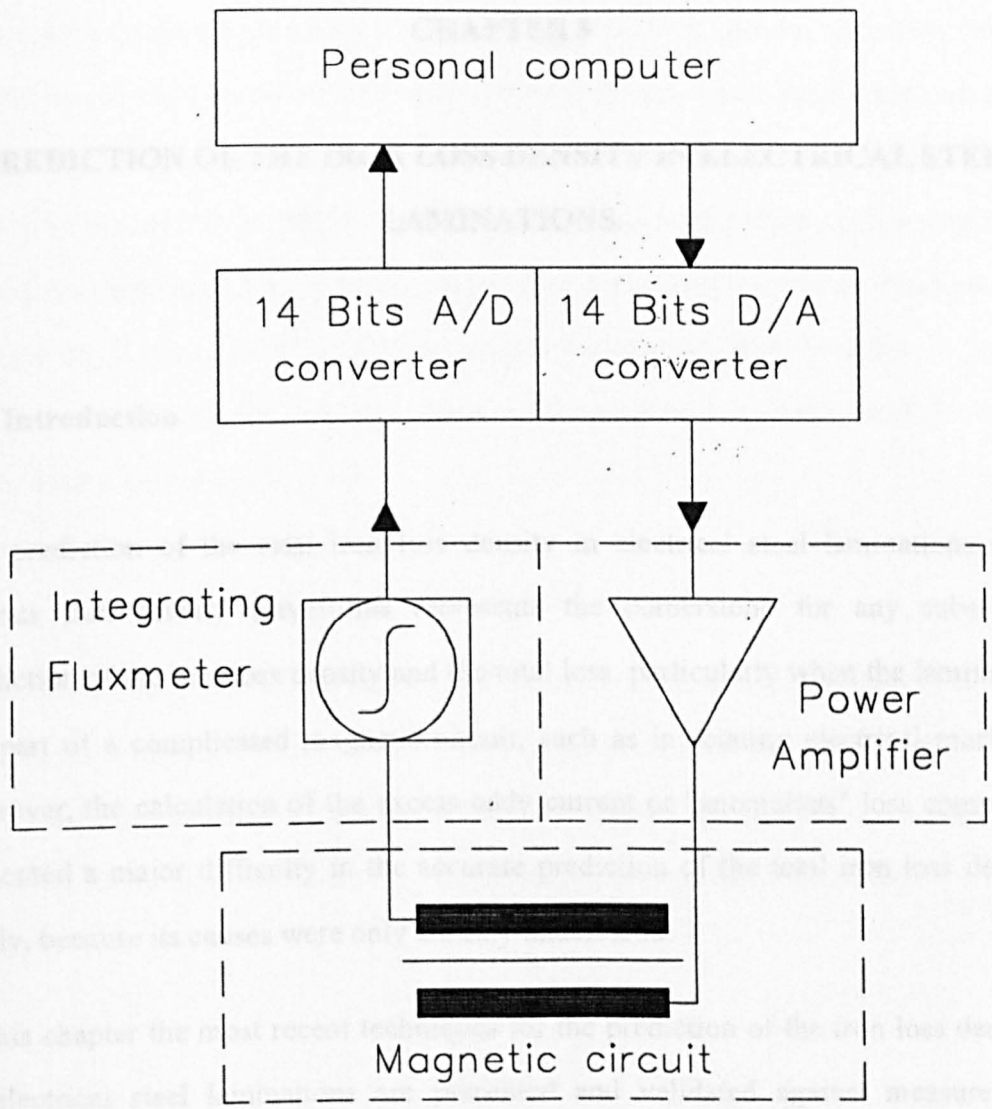


Fig (2.11) Schematic of electrical steel laminations characterisation under DC alternating condition.

# CHAPTER 3

# PREDICTION OF THE IRON LOSS DENSITY IN ELECTRICAL STEEL LAMINATIONS.

## 3.1) Introduction

The prediction of the total iron loss density in electrical steel laminations under various flux density waveforms represents the cornerstone for any subsequent prediction of the iron loss density and the total loss, particularly when the laminations are part of a complicated magnetic circuit, such as in rotating electrical machines. However, the calculation of the excess eddy current or "anomalous" loss component presented a major difficulty in the accurate prediction of the total iron loss density, partly, because its causes were only broadly understood.

In this chapter the most recent techniques for the prediction of the iron loss densities in electrical steel laminations are presented and validated against measurements carried out on samples of non-oriented electrical steel laminations under flux density waveforms similar to those encountered in the stator core of permanent magnet brushless dc motors.

## 3.2) Prediction of the hysteresis loss

The hysteresis loss is due to irreversible changes in the domain structure, namely Barkhausen jumps, which are very localised in time and space. The loss is the difference in potential energy before and after each jump. It is important to note that it is independant of the dissipation mechanism, as this only influences the duration of the jump [26]. As a consequence the hysteresis loss per cycle is fairly independant of the

magnetising frequency, and only depends on the maximum flux density, when the flux density waveform does not cause minor hysteresis loops. When minor hysteresis loops occur, their area has to be added to the area of the major loop to determine the total hysteresis loss per cycle [56]. However, in practice the calculation of this component of iron loss does not ususally present a problem, and a single experimental hysteresis loss per cycle data, covering a wide range of maximum flux densities, is usually sufficient. In general, the following empirical expression provides a good fit to such experimental data [41]:

$$P_h = k_h f B_m^{\alpha_h} \tag{3.1}$$

where $k_h$ and $\alpha$ are constants determined by fitting the above equation to a set of experimental data, preferably covering a wide range of peak inductions, and $f$ and $B_m$ are the frequency and the peak induction respectively. In cases where $N_{mlp}$ minor hysteresis loops occur, the following empirical correction can be used [56]:

$$P_h = K(B_m) \times P_h(B_m) \tag{3.2}$$

where

$$K(B_m) = 1 + \frac{0.65}{B_m} \sum_{i=1}^{N_{mlp}} \Delta B_i \tag{3.3}$$

$\Delta B_i$ being the change in flux density during the excursion around a minor loop.

### 3.3) Prediction of the dynamic loss

The natural action of an applied field, which is uniform in space, is to induce a homogeneous magnetisation over the lamination cross-section. In materials with no structural inhomogeneities, this is exactly what happens, and the dynamic loss is equal to the classical eddy current loss. However, in soft ferromagnetic materials the magnetisation can only proceed easily as a correspondence of Bloch walls which

separate different magnetic domains. This results in the the magnetisation changing coherently inside a characteristic region, which , in turn, results in eddy currents concentrating above the average around the active region, which gives rise to the excess or the "anomalous" loss . In this respect, two extreme cases can be distinguished, viz

a) Magnetically oriented materials, where the average Bloch wall spacing is larger than the lamination thickness, the correlation region coincides with a single wall.

b) Non-oriented materials, which are characterised by a fine domain structure leading to a strong interaction between the neighbouring Bloch walls. In this case, the magnetisation change involves a highly correlated motion of a great number of wall segments in a limited region of the sample.

As a consequence, Bertotti [30,31] introduced the new concept of a magnetic object (MO), which correponds to a group of neighbouring walls so strongly correlated, that they can be treated as a whole. The structural and dynamic properties of the (MOs) are different in different materials, ranging between the ones for a single wall to ones for a cluster of walls, as the average wall spacing decreases. Furthermore, the (MOs) are employed in the context of the following assumptions:

i) All the (MOs) are identical.

ii) The (MOs) are randomly distributed.

iii)The average eddy current distribution due to all the active (MOs) is identical to that of a homogeneous medium.

From the above reasoning the eddy current loss can be separated into two components, viz, the power loss due to the average eddy current distribution, and which can be calculated by the classical model assuming a homogeneous medium, and the power loss due to the extra concentration of eddy currents around the active (MOs).

### 3.3.1) Prediction of eddy current losses by the classical model

The classical model is based on the assumption of a smooth distribution of the magnetisation over the cross-section of the lamination. In other words, it neglects the existence of the domain structure.

Given $d << L$ in a practical lamination, and the flux density $\vec{B}$ vector is along the z direction, as shown in Fig (3.1), the induced electric field $\vec{E}$ has no component along z and its component along y is negligible in the major part of the lamination cross-section, ie

$$\vec{B} = 0\,\vec{i} + 0\,\vec{j} + B\,\vec{k} \tag{3.4}$$

and

$$\vec{E} = E_x\,\vec{i} + 0\,\vec{j} + 0\,\vec{k} \tag{3.5}$$

where $\vec{i}, \vec{j},$ and $\vec{k}$ are the unit vectors in the x, y, and z coordinate directions respectively. Furthermore, $\vec{E}$ and $\vec{B}$ are related by the following Maxwell equation:

$$curl\,\vec{E} = -\frac{\partial \vec{B}}{\partial t} \tag{3.6}$$

From equations (3.4), (3.5) and (3.6):

$$\frac{\partial E_x}{\partial y} = \frac{\partial B_z}{\partial t} \tag{3.7}$$

In the range of frequencies where skin effect is negligible, $\vec{B}$ is almost constant throughout the cross-section of the lamination. Therefore, from equation (3.7):

$$E_x = \left(\frac{dB_z}{dt}\right) y + c \tag{3.8}$$

where c is an integration constant, which can be determined as follows.

In the practical range of frequencies the continuity equation is reduced to:

$$div\,\vec{J} = 0 \tag{3.9}$$

where $\vec{J}$ is the eddy current density, and which is related to the electric field by:

$$\vec{J} = \sigma \vec{E} \tag{3.10}$$

where $\sigma$ is the electric conductivity of the lamination. From equations (3.9) and (3.10):

$$div\,\vec{E} = 0 \tag{3.11}$$

Hence, the eddy current and the induced electric field force lines are closed. In addition, a force line at $y = y_o$ reverses direction at $x = \pm \infty$ and returns at $y = -y_o$. Therefore, the symmetry requires that:

$$E_x \mid_{y = y_o} = - E_x \mid_{y = -y_o} \tag{3.12}$$

From equations (3.8) and (3.12) the intgrating constant is derived as c = 0.

The local eddy current power loss density is given by:

$$p_c(t) = \sigma E_x^2 \tag{3.13}$$

and space averaging leads to:

$$\overline{p_c}(t) = \frac{1}{d}\int_{-d/2}^{d/2} p_c(t)\,dy \tag{3.14}$$

From equations (3.8) and (3.13):

$$\overline{p_c}(t) = \frac{\sigma d^2}{12}\left(\frac{dB}{dt}\right)^2 \quad (W/m^3) \tag{3.15}$$

and averaging over a cycle:

$$P_c = \frac{\sigma d^2}{12\,\delta}\frac{1}{T}\int_T \left(\frac{dB}{dt}\right)^2 dt \quad (W/kg) \tag{3.16}$$

where $T$ and $\delta$ are the period and the mass density respectively. Furthermore, in the case of a sinusoidally time-varying flux density:

$$P_c = \frac{\sigma d^2 \pi^2}{6 \delta} f^2 B_{max}^2 \tag{3.17}$$

where $B_{max}$ and $f$ are the maximum flux density and the frequency respectively.

### 3.3.2) Prediction of the excess or " anomalous " loss by Bertotti's model

Firstly, is considered the case of a plane, $180^o$ domain wall, moving at the velocity v. Besides the applied field and the coercive counter field, the moving wall also experiences an eddy current counter field, due to its own movement. According to the results of Williams et al [58], it is given by:

$$H_e = \frac{8 M_s \sigma d}{\pi^3} \left( \sum_{odd\ n} \frac{1}{n^3} \right) v = \sigma G_w \dot{\varphi}_w \tag{3.18}$$

where $\dot{\varphi}_w$ is the flux rate provided by the moving wall, $M_s$ is the saturation magnetisation, and the dimensonless parameter $G_w$ given by:

$$G_w = \frac{4}{\pi^3} \left( \sum_{odd\ n} \frac{1}{n^3} \right) \approx 0.136 \tag{3.19}$$

which measures the damping effect of the eddy current pattern which surrounds the wall, and is obtained from Maxwell's equations, with assumptions made on the shape of the wall as well as the geometry of the sample cross-section.

In the case of $n_w$ simultaneously active uncorrelated walls, and imposing the requirements that the flux rate due to the $n_w$ moving walls must be equal to the imposed average flux rate,

$$n_w \dot{\varphi}_w = S \frac{dB}{dt} \tag{3.20}$$

where S is the cross-sectional area and B is the average flux density. From equations (3.18) and (3.20),

$$H_e = \frac{\sigma G_w S}{n_w} \frac{dB}{dt} \tag{3.21}$$

and

$$P_e = \frac{\sigma G_w S}{n_w} \left(\frac{dB}{dt}\right)^2 \tag{3.22}$$

In the above equation the excess loss is inversely proportional to the number of simultaneously active walls $n_w$. Therefore, if $n_w$ tends to infinity the excess loss vanishes. This can be interpreted by the fact that the greater the number of walls contributing to the total flux change the smoother is the distribution of the magnetisation in the cross-section of the lamination.

By analogy with the former case, but in this case with the wall replaced by a magnetic object, which at a limit can coincide with a wall, the same formulae can be derived, viz

$$H_e = \frac{\sigma G_{mo} S}{n_{mo}} \frac{dB}{dt} \tag{3.23}$$

and

$$P_e = \frac{\sigma G_{mo} S}{n_{mo}} \left(\frac{dB}{dt}\right)^2 \tag{3.24}$$

where $G_{mo}$ is a damping factor dependant on the shape and the internal structure of the magnetic object, and $n_{mo}$ is the number of active magnetic objects. All the information on the structural and dynamic characteristics of the magnetic objects is included in the ratio $\frac{G_{mo}}{n_{mo}}$. In order to unify the mathematical formulation a new parameter is introduced:

$$\hat{n} = n_{mo} \frac{G_w}{G_{mo}} \tag{3.25}$$

$\hat{n}$ could be interpreted as the effective number of magnetic objects. In terms of the above defined parameter a general expression governing the excess field and loss is derived, viz

$$H_e = \frac{\sigma G_w S}{\hat{n}} \frac{dB}{dt} \tag{3.26}$$

and

$$P_e = \frac{\sigma G_w S}{\hat{n}} \left( \frac{dB}{dt} \right)^2 \tag{3.27}$$

The above two equations show that if the function $\hat{n} = f( H_e )$ is known the excess loss could be calculated for any frequency, when the skin effect is negligible, and for any flux density waveform.

Bertotti [31,59] found experimentally that in many iron-based materials $\hat{n} = f( H_e )$ follows a simple linear law:

$$\hat{n} = \hat{n}_o + \frac{H_e}{V_o} \tag{3.28}$$

where $V_o$ is a parameter determined experimentally. Further equation (3.38) can be reduced to

$$\hat{n} \approx \frac{H_e}{V_o} \tag{3.29}$$

in non-oriented materials, above a frequency of few Hz. From equations (3.26), (3.27) and (3.29) an expression for the excess loss is derived as:

$$p_e = \sqrt{\sigma G_w S V_o} \left| \frac{dB}{dt} \right|^{\frac{3}{2}} \tag{3.30}$$

Averaging over a cycle, leads to

$$P_e = \frac{\sqrt{\sigma G_w S V_o}}{T} \int_T \left| \frac{dB}{dt} \right|^{\frac{3}{2}} dt \tag{3.31}$$

which becomes

$$P_e = 8.67 \sqrt{\sigma G_w S V_o} f^{3/2} B_m^{3/2} \quad (3.32)$$

for a sinusoidal flux density waveform.

In equations (3.31) and (3.32) the only unknown variable is the field $V_o$, which can be determined experimentally. It is worth mentioning that the field $V_o$ exhibits a dependence on the maximum induction for certain materials [31,59].

### 3.4) Experimental validation

To validate the theoretical analysis given in the previous sections, three lamination samples S1, S2 and S3, for which information is given in Table (3.1), have been considered. The samples were chosen on the basis of their wide use for the laminations of stator cores.

#### 3.4.1) Determination of the laminations constants

##### 3.4.1.1) Hysteresis loss constants

The hysteresis loss constants have been derived directly from a set of hysteresis loss data, covering a range of flux densities, which have been fitted to equation (3.1). Fig (3.2) shows an example of measured dc hysteresis loops for sample S2, whilst Figs

Table (3.1) General specifications of the samples S1, S2 and S3.

| Sample | Commercial name | Heat treatment | Sample thickness (mm) |
|---|---|---|---|
| S1 | Newcor 660 | non-annealed | 0.5 |
| S2 | Losil 450 | annealed | 0.5 |
| S3 | Transil 300 | annealed | 0.35 |

(3.3), (3.4) and (3.5) show hysteresis loss data for the samples S1, S2 and S3 respectively, where it will be noted that equation (3.1) provides a very good fit to experimental data for S1 and S2, but not for S3 as the exponent $\alpha$ is an increasing function of the maximum flux density. To overcome this problem a correction to equation (3.1) is suggested, viz

$$P_h = k_h f B_m^{\alpha_h} \tag{3.33}$$

where

$$\alpha_h = \alpha_{h1} B_m^2 + \alpha_{h2} \tag{3.34}$$

Fig (3.5) shows the very good fit provided by equation (3.33) for S3. Table (3.2) gives the hysteresis constants for S1, S2 and S3.

As the hysteresis loss is only dependant on the maximum flux density when the flux density waveform does not induce minor loops, in practice a single set of experimental hysteresis loss per cycle data for a reasonable range of flux densities can be fitted to a cubic spline to enable the accurate computation of the hysteresis loss for any frequency and flux density waveform.

### 3.4.1.2) Excess or " anomalous " loss constant

In theory, the excess loss constant $k_e = \frac{\sqrt{\sigma G_w S V_o}}{\delta}$ can be determined from a single value of the total iron loss density measured at a given frequency and amplitude for a sinusoidally time-varying flux density, ie from

Table (3.2) Hysteresis loss constants.

| Sample | $k_h$ | $\alpha_{h1}$ | $\alpha_{h2}$ |
|---|---|---|---|
| S1 | $1.49 \times 10^{-1}$ | 1.56 | 0.0 |
| S2 | $1.96 \times 10^{-2}$ | 1.58 | 0.0 |
| S3 | $1.55 \times 10^{-2}$ | 1.36 | $4.27 \times 10^{-1}$ |

$$k_e = \frac{P_t - P_h - \frac{\sigma d^2 \pi^2}{6\delta} B_m^2 f^2}{8.67\, B_m^{1.5} f^{1.5}} \tag{3.35}$$

However, it is then very sensitive to the accuracy to which $P_t$ and $P_h$ can be determined. Therefore, a preferred approach, which reduces the effect of experimental errors, is to fit experimental loss per cycle data, spanning a range of frequencies, to equation (3.36). For example, Fig (3.6) compares measured and curve fitted loss per cycle data for sample S2.

$$\frac{P_t}{f} = \frac{P_h}{f} + \frac{\sigma d^2 \pi^2}{6\delta} B_m^2 f + 8.67\, k_e\, B_m^{1.5} f^{0.5} \tag{3.36}$$

Figs (3.7), (3.8) and (3.9) show the variation of the constant $k_e$ with the maximum flux density for each of the samples. It will be noted that $k_e$ exhibits a negligible variation for S1, whilst for S2 and S3 it increases with the maximum flux density. At first, this was attributed to experimental errors. However, the similarity of the variation of $k_e$ for S2 and S3 as well as the possibility of such variation occuring as reported by Bertotti [31,59] tended to eliminate this possibility. Furthermore, the experimental error should be more pronouced in sample S1 because of its higher hysteresis loss component compared to its dynamic loss component. In practice an average value of $k_e$ could be used as an approximation. Alternatively, however, a more accurate approach is to obtain a set of values for $k_e$ for a reasonable range of maximum flux densities to which a cubic spline curve fit is performed to enable the computation of the excess loss for any flux density waveform, in a similar manner to the hysteresis loss component.

### 3.4.2) Validation of iron loss calculation

The experimentally derived constants under dc conditions for the hysteresis loss component and under ac sinusoidal flux density waveforms for the excess loss component can be used to compute the total iron loss density under flux density waveforms usually present in permanent magnet excited machines. From equations

(3.16) and (3.31) the eddy current loss component of the iron loss density due to a piece-wise linear flux density waveform composed of N intervals can be shown to be:

$$P_c = \frac{\sigma d^2}{24 \pi \delta} \omega^2 \sum_{i=1}^{N} \frac{\Delta B_i^2}{\Delta \theta_i} \tag{3.37}$$

whilst

$$P_e = \frac{k_e}{2 \pi} \omega^{1.5} \sum_{i=1}^{N} \frac{|\Delta B_i|^{1.5}}{\sqrt{\Delta \theta_i}} \tag{3.38}$$

where $\omega = 2 \pi f$, and f is the fundamental frequency, $\Delta B_i$ is the incremental change of flux density over interval i, and $\Delta \theta_i$ is the duration of the interval (elec rad). Trapezoidal flux density waveforms, typical of those which exist in the teeth of permanent magnet brushless dc motors, can be characterised by the parameter $\tau$ which determines the extent of the " flat-top ", where $\tau = 0\%$ corresponding to a rectangular waveform and $\tau = 100\%$ corresponds to a triangular waveform as shown in Fig (3.10). In terms of the parameter $\tau$, equations (3.37) and (3.38) can be transformed as follows:

$$P_c = \frac{\sigma d^2}{3 \pi^2 \delta} \omega^2 \frac{B_m^2}{\tau} \tag{3.39}$$

and

$$P_e = \frac{2 \sqrt{2}\, k_e}{\pi \sqrt{\pi}} \omega^{1.5} \frac{B_m^{1.5}}{\sqrt{\tau}} \tag{3.40}$$

Figs (3.11), (3.12) and (3.13) show a comparison between measured and computed iron loss densities for samples S1, S2 and S3 respectively, for a wide range of trapezoidal flux density waveforms.

Furthermore, Figs (3.14), (3.15) and (3.16) show a comparison between measured and computed iron loss densities for other piece-wise linear flux density waveforms, typical of those which exist in the stator yoke of brushless dc motors having 1/2 slot/pole/phase, and characterised by the parameter $\kappa$ as shown in Fig (3.17). Again, equations (3.37) and (3.38) can be transformed, this time in terms of $\kappa$ to give :

$$P_c = \frac{\sigma d^2}{2\pi^2 \delta} \omega^2 B_m^2 \left( 3\kappa^2 - 2\kappa + 1 \right) \tag{3.41}$$

and

$$P_e = \frac{2\sqrt{3}\, k_e}{\pi\sqrt{\pi}} \omega^{1.5} B_m^{1.5} \left( \sqrt{2}\, \kappa^{1.5} + (1-\kappa)^{1.5} \right) \tag{3.42}$$

### 3.4.3) Discussion

Apart from showing that good agreement can be obtained between computed and measured iron loss densities, the results presented in this section illustrate clearly the effect of the flux density waveform on the total iron loss density. The iron loss density can vary dramatically simply by varying the flux density waveform with the peak value kept constant. Since the hysteresis loss component would remain constant, the variation is caused entirely by a change in the eddy current loss component. Further, Tables (3.3) and (3.4) compare measured per unit iron loss densities under sinusoidal, triangular and trapezoidal flux density waveforms having a maximum flux density of

Table (3.3) Per unit iron loss densities at 50 Hz.

| Sample | Sinusoidal waveform | Triangular waveform | Trapezoidal waveform | | |
|---|---|---|---|---|---|
| | | | $\tau$ = 30 % | $\tau$ = 60 % | $\tau$ = 90 % |
| S1 | 1.0 | 0.97 | 1.20 | 1.035 | 0.985 |
| S2 | 1.0 | 0.93 | 1.63 | 1.14 | 0.95 |
| S3 | 1.0 | 0.966 | 1.25 | 1.07 | 0.981 |

Table (3.4) Per unit iron loss densities at 100 Hz.

| Sample | Sinusoidal waveform | Triangular waveform | Trapezoidal waveform | | |
|---|---|---|---|---|---|
| | | | $\tau$ = 30 % | $\tau$ = 60 % | $\tau$ = 90 % |
| S1 | 1.0 | 0.95 | 1.34 | 1.07 | 0.957 |
| S2 | 1.0 | 0.90 | 1.90 | 1.20 | 0.93 |
| S3 | 1.0 | 0.935 | 1.40 | 1.06 | 0.97 |

1.5 T, for 50 Hz and 100 Hz respectively. It will be seen that iron loss density data corresponding to sinusoidal flux density waveforms is generally inappropriate for predicting the iron loss of permanent magnet machines. Further, it will be noted that the iron loss density under a triangular flux density waveform is less than under a pure sinusoidal flux density waveform. This is due to the fact that a constant rate of change of flux density induces less eddy current loss, both classical and excess components. This can also be seen in Figs (3.14), (3.15) and (3.16) where the iron loss density variation exhibits a minimum at $\kappa = \frac{1}{3}$ which corresponds to a triangular flux density waveform.

The excess loss component, which has been usually neglected or poorly catered for can represent a substantial portion of the total iron loss density. Tables (3.5), (3.6) and (3.7) show the proportion of each loss density component in the total iron loss densities under sinusoidal, triangular and trapezoidal flux density waveforms having a peak flux density of 1.5 T, at 50 and 100 Hz, for samples S1, S2 and S3 respectively. It can be seen that in sample S1 the hysteresis loss component is predominent because the sample is not annealed, whilst the excess eddy current component is still important

Table (3.5) Iron loss density separation for Sample S1. ( $B_{max} = 1.5\ T$ )

| Flux density waveform | | Frequency (Hz) | Hysteresis loss (%) | Classical eddy current loss (%) | Excess eddy current loss (%) |
|---|---|---|---|---|---|
| Sinusoidal | | 50 | 86.1 | 10.68 | 3.21 |
| | | 100 | 76.85 | 19.08 | 4.06 |
| Triangular | | 50 | 88.09 | 8.86 | 3.03 |
| | | 100 | 80.0 | 16.1 | 3.89 |
| Trapezoidal | $\tau = 30\ \%$ | 50 | 71.51 | 23.9 | 4.5 |
| | | 100 | 56.82 | 38.12 | 5.05 |
| | $\tau = 60\ \%$ | 50 | 82.49 | 13.83 | 3.67 |
| | | 100 | 71.51 | 23.98 | 4.49 |
| | $\tau = 90\ \%$ | 50 | 87.09 | 9.73 | 3.16 |
| | | 100 | 78.43 | 17.53 | 4.03 |

Table (3.6) Iron loss density separation in sample S2. ( $B_{max}$ = 1.5 $T$ )

| Flux density waveform | | Frequency (Hz) | Hysteresis loss (%) | Classical eddy current loss (%) | Excess eddy current loss (%) |
|---|---|---|---|---|---|
| Sinusoidal | | 50 | 45.43 | 24.53 | 30.02 |
| | | 100 | 33.17 | 35.82 | 30.99 |
| Triangular | | 50 | 48.88 | 21.37 | 29.77 |
| | | 100 | 36.52 | 31.97 | 31.49 |
| Trapezoidal | $\tau$ = 30 % | 50 | 28.0 | 40.84 | 31.16 |
| | | 100 | 18.2 | 53.13 | 28.66 |
| | $\tau$ = 60 % | 50 | 39.73 | 28.98 | 31.27 |
| | | 100 | 27.99 | 40.84 | 31.16 |
| | $\tau$ = 90 % | 50 | 46.97 | 22.84 | 30.18 |
| | | 100 | 34.70 | 33.75 | 31.54 |

compared to the classical eddy current component. For the annealed samples S2 and S3, however, the excess eddy current loss component represents not only a substantial portion of the total iron loss density, but can be higher than the classical eddy current

Table (3.7) Iron loss density separation in sample S3. ( $B_{max}$ = 1.5 $T$ )

| Flux density waveform | | Frequency (Hz) | Hysteresis loss (%) | Classical eddy current loss (%) | Excess eddy current loss (%) |
|---|---|---|---|---|---|
| Sinusoidal | | 50 | 72.18 | 7.49 | 20.32 |
| | | 100 | 62.27 | 12.93 | 24.79 |
| Triangular | | 50 | 74.40 | 6.26 | 19.32 |
| | | 100 | 65.11 | 10.96 | 23.92 |
| Trapezoidal | $\tau$ = 30 % | 50 | 56.98 | 15.98 | 27.02 |
| | | 100 | 44.80 | 25.14 | 30.05 |
| | $\tau$ = 60 % | 50 | 67.76 | 9.50 | 22.72 |
| | | 100 | 56.98 | 15.98 | 27.02 |
| | $\tau$ = 90 % | 50 | 73.13 | 6.83 | 20.02 |
| | | 100 | 63.52 | 11.88 | 24.59 |

loss component. Thus, neglecting it or poorly modelling it would necessarily lead to a substantial error on the total iron loss density prediction.

### 3.5) Rotational loss

Rotating fields also exist in most electrical machines. However, to date a model for predicting the associated iron loss has yet to be presented. Nevertheless, experimental investigations [9] have shown that for low to medium induction levels a reasonable approximation is to add the losses associated with the corresponding orthogonal alternating flux density components.

Further, the calculation of the rotational loss in soft ferromagnetic materials introduces a problem as to which parameters have to be defined, ie the specification of parameters which yield a unique loss density. For example, under alternating flux conditions the peak flux density is not a parameter which fully specifies the flux conditions, since the same peak flux density can yield different iron loss densities. Similarly, the flux density loci, which to date represent the only way of characterising a rotating flux condition, cannot yield a unique total iron loss density. In addition, the instantaneous angular velocity of the flux density vector is a necessary parameter, as was shown in Chapter 2. Thus, only a flux condition defined by the flux density loci and the instantaneous angular velocity can yield a unique rotational iron loss density.

### 3.6) Conclusions

The excess or " anomalous " dynamic loss component has, until recently, presented a major obstacle in the way of accurately predicting iron loss densities in electrical steel sheets, and this has lead to the development of various empirical methods over the years, which were generally validated against flux density waveforms having a harmonic content similar to that caused by saturation in transformers and classical a.c

machines. However, even under those conditions they did not prove to be very reliable [56]. Bertotti's model, however, which takes into account the discrete nature of the magnetisation process, which is the cause of the excess loss, would clearly be expected to provide a more reliable solution. Indeed, the results for sinusoidal flux density waveforms with $3^{rd}$ harmonic distortion [50], as well as the results provided in the proceeding section for a wider range of flux density waveforms, for which very good agreement has been obtained between predictions and measurements, confirm the generalised nature of Bertotti's model. For the calculation of iron losses in permanent magnet machines, this presents a major step forward, since the rectangular magnet m.m.f naturally produces highly "distorted" flux density waveforms.

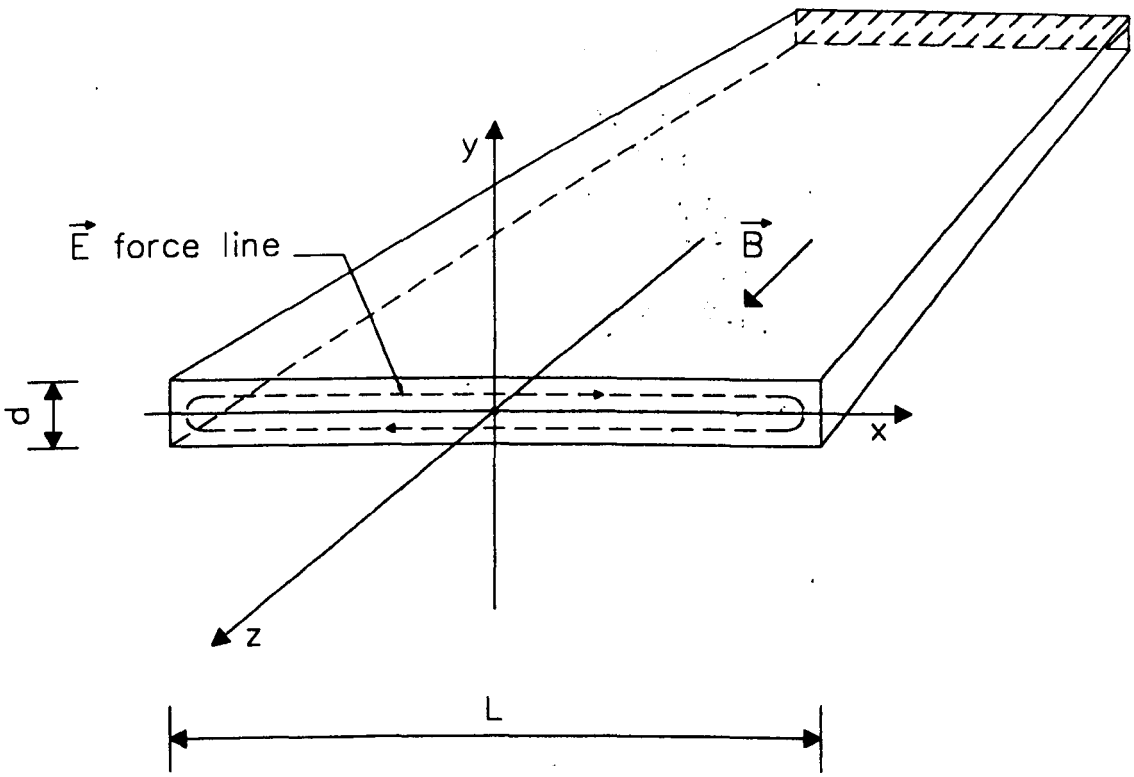


Fig (3.1) Classical model for eddy current loss calculation.

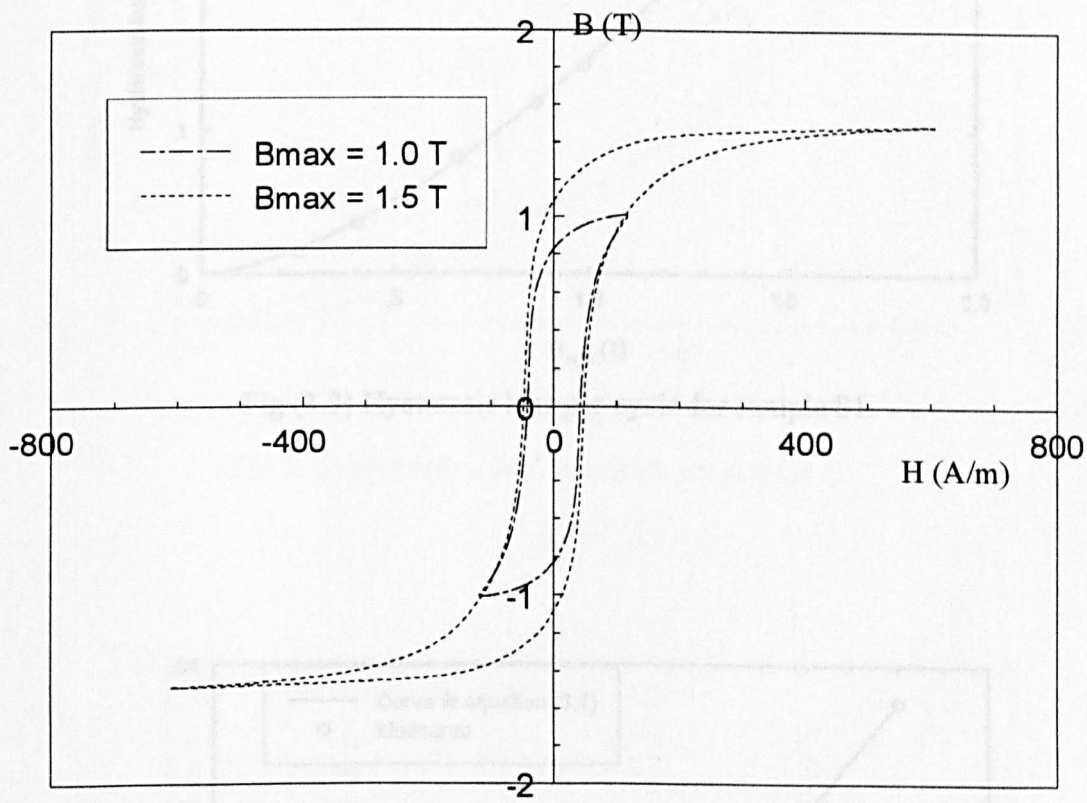


Fig (3.2) Measured dc hysteresis loops for sample S2.

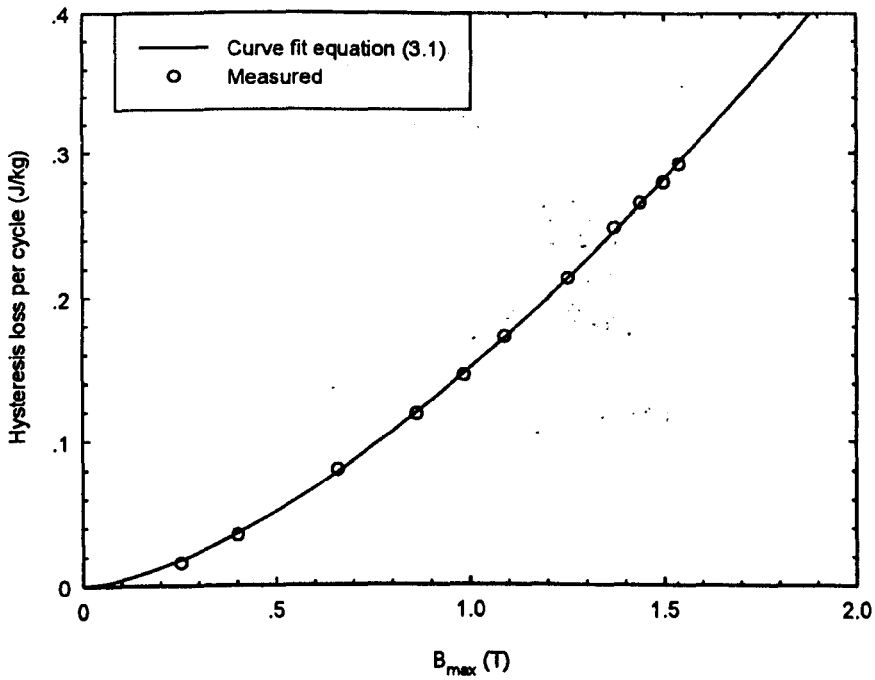


Fig (3.3) Hysteresis loss per cycle for sample S1.

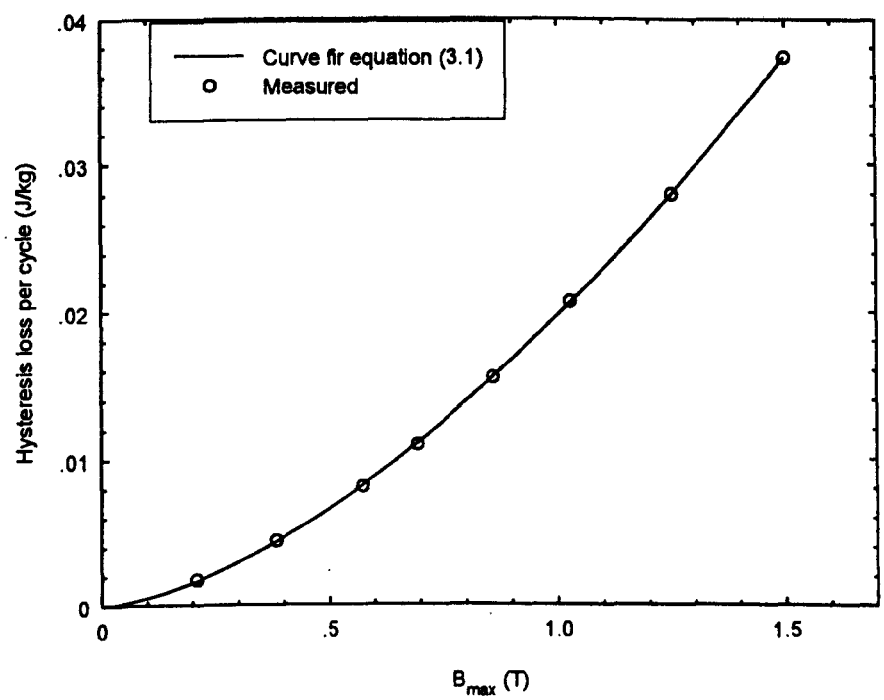


Fig (3.4) Hysteresis loss per cycle for sample S2.

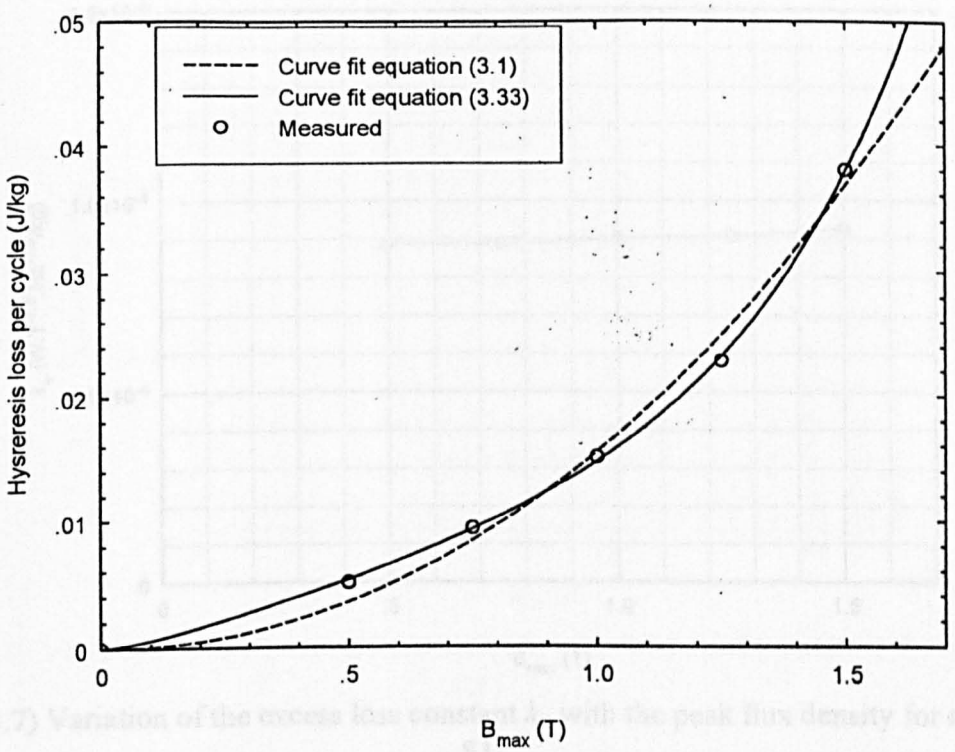


Fig (3.5) Hysteresis loss per cycle for sample S3.

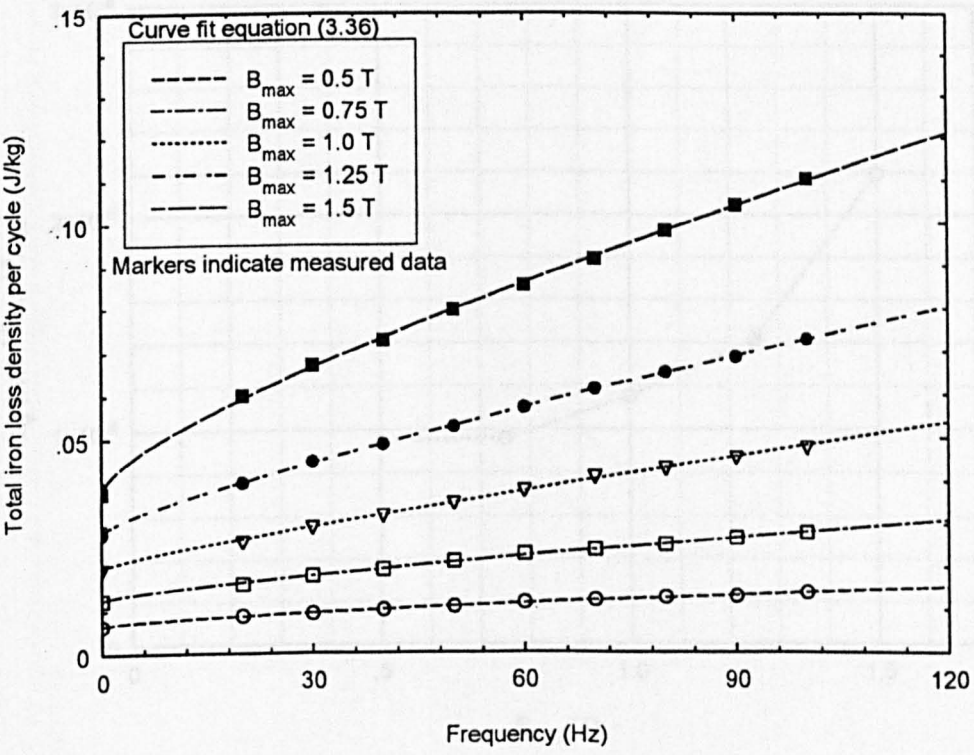


Fig (3.6) Variation of the total iron loss density per cycle for sample S2.

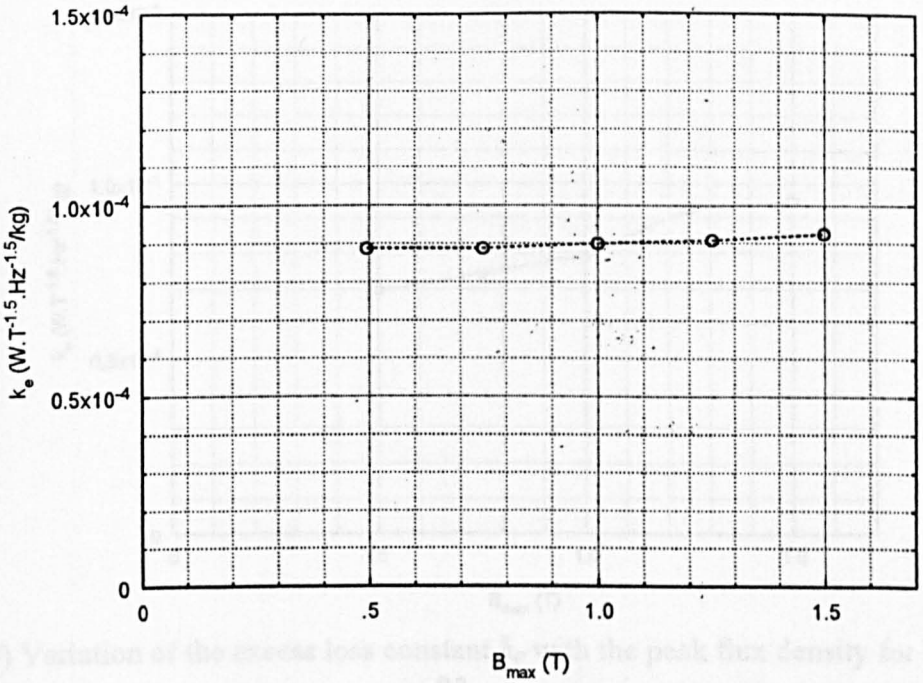


Fig (3.7) Variation of the excess loss constant $k_e$ with the peak flux density for sample S1.

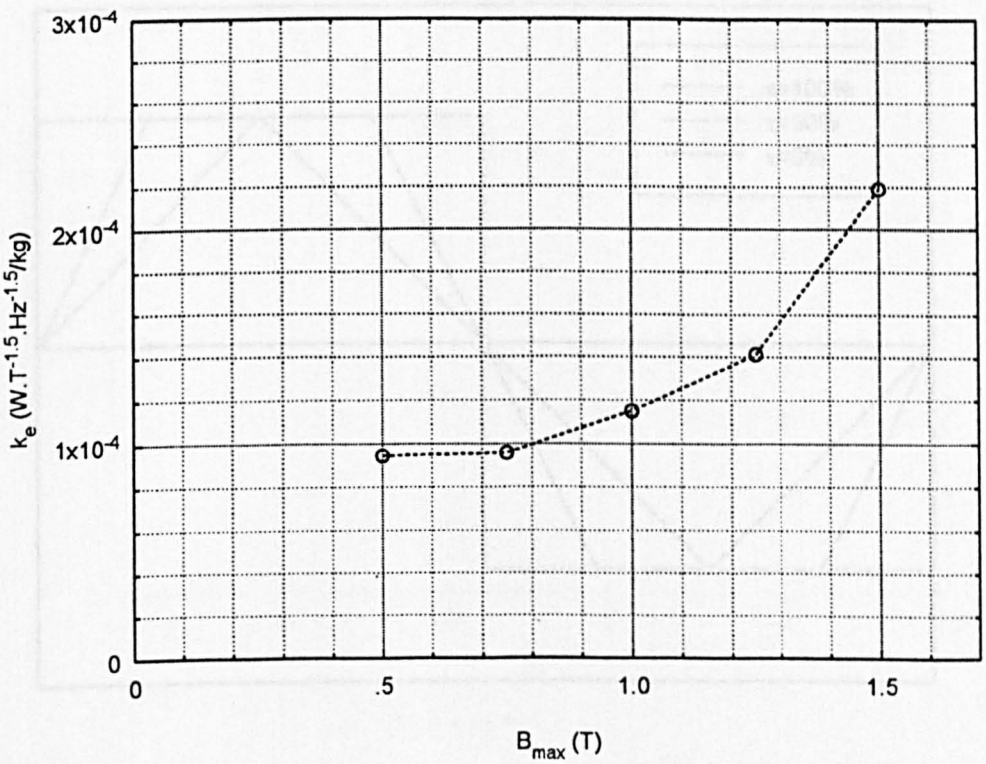


Fig (3.8) Variation of the excess loss constant $k_e$ with the peak flux density for sample S2.

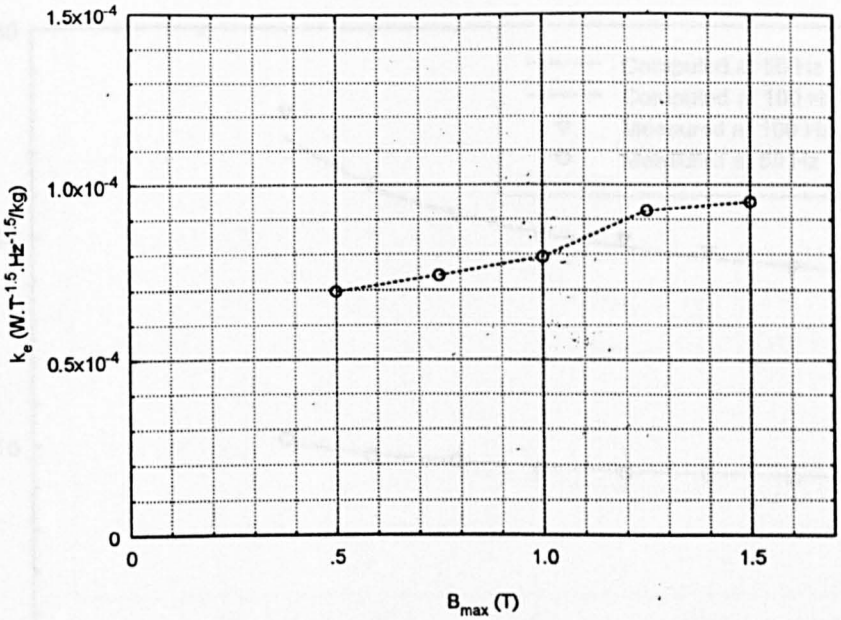


Fig (3.9) Variation of the excess loss constant $k_e$ with the peak flux density for sample S3.

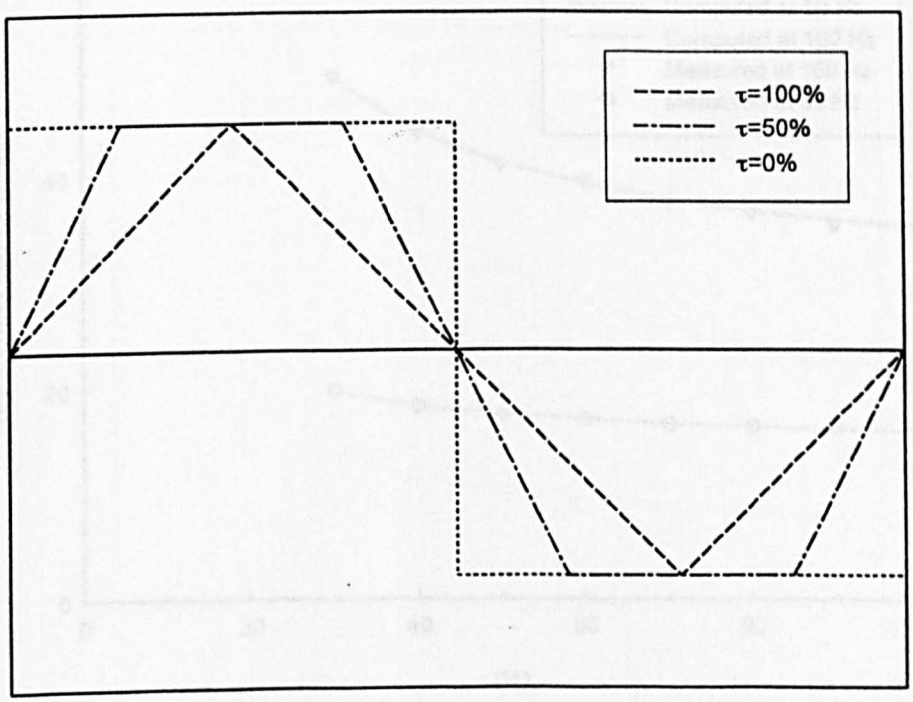


Fig (3.10) Examples of trapezoidal waveforms characterised by the parameter τ.

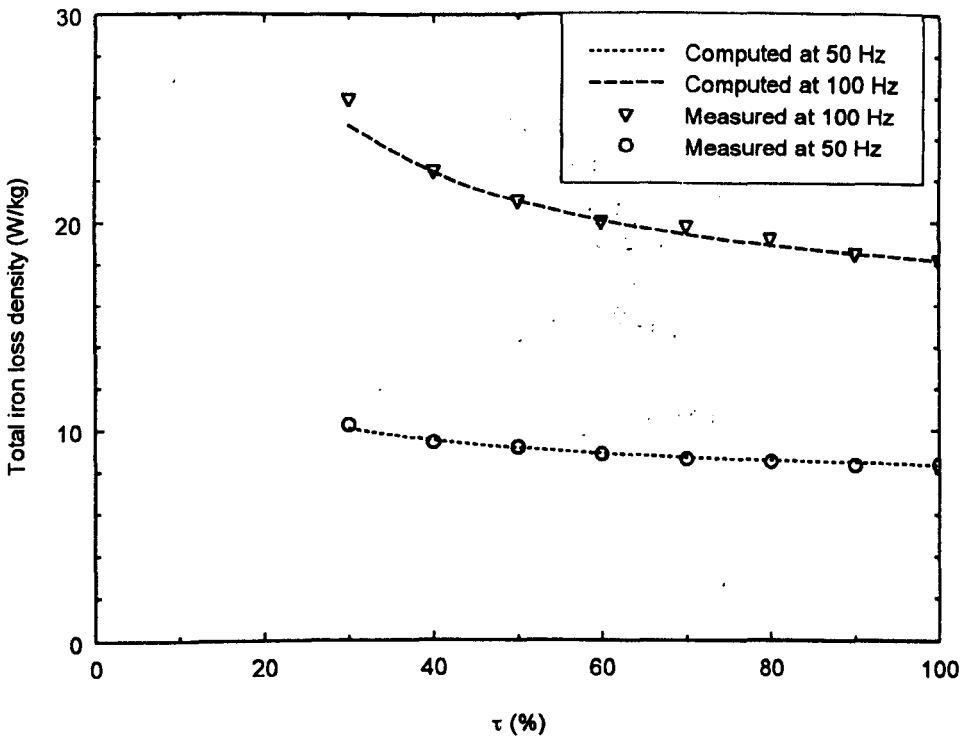


(a) $B_{máx} = 1.0\ T$

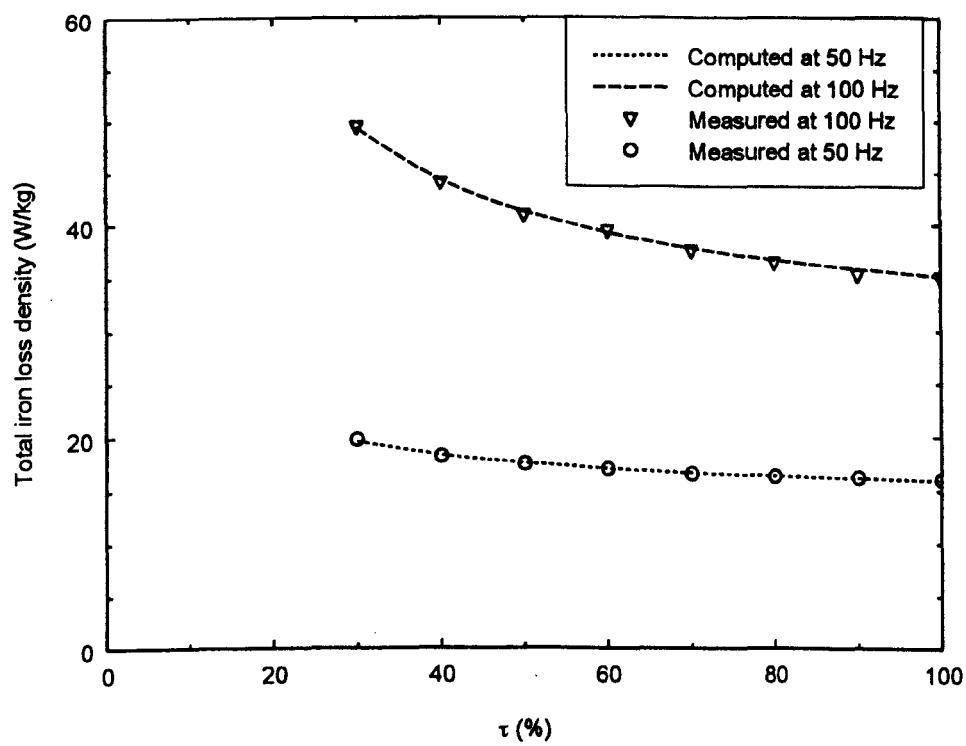


(b) $B_{max} = 1.5\ T$

Fig (3.11) Total iron loss density under trapezoidal flux density waveforms in sample S1.

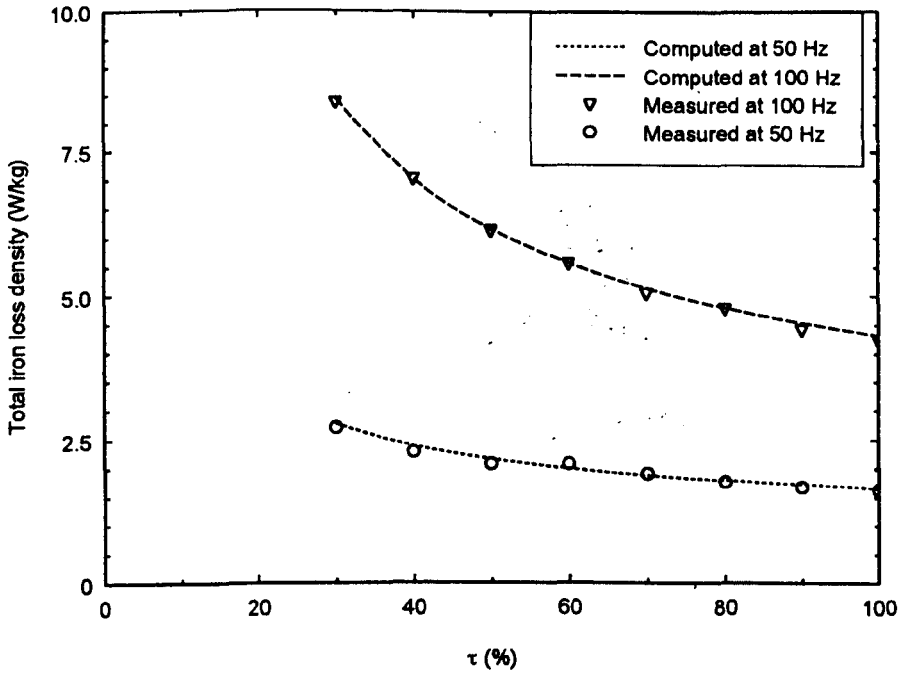


(a) $B_{max} = 1.0\ T$

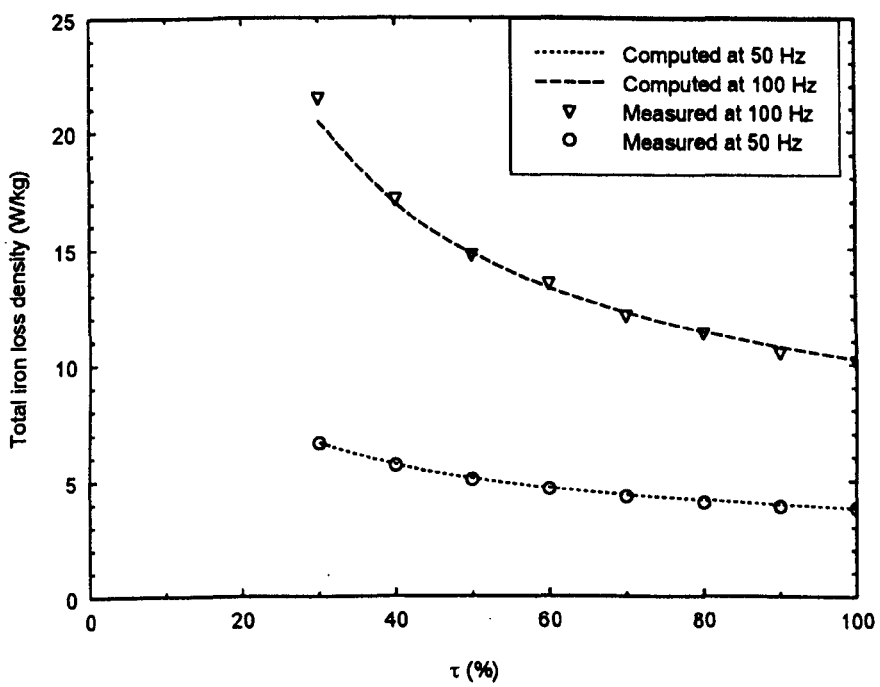


(b) $B_{max} = 1.5\ T$

Fig (3.12) Total iron loss density under trapezoidal flux density waveforms in sample S2.

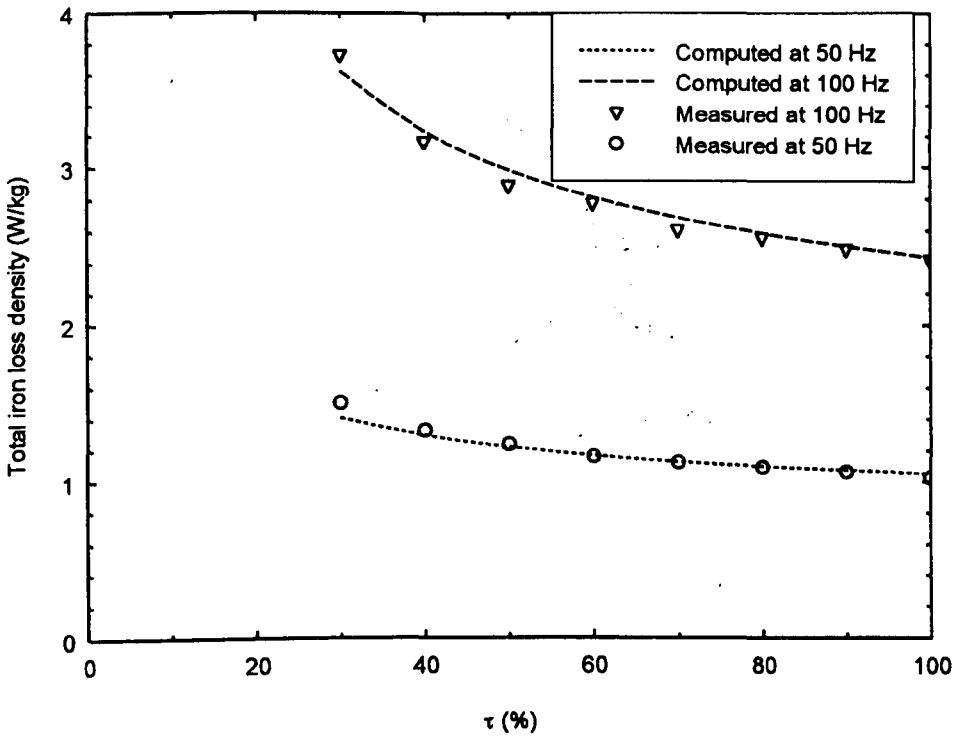


(a) $B_{max} = 1.0\ T$

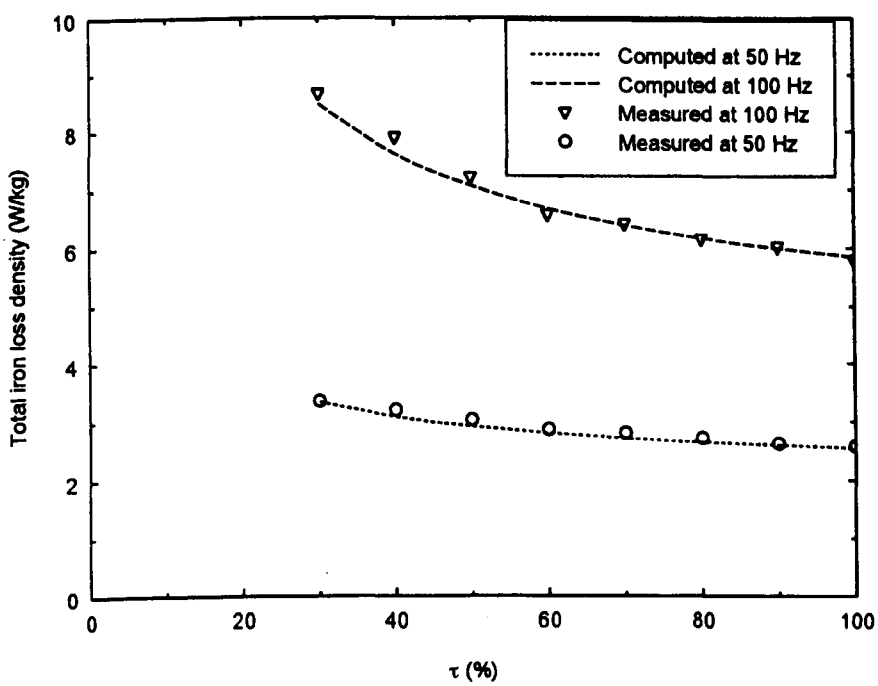


(b) $B_{max} = 1.5\ T$

Fig (3.13) Total iron loss density under trapezoidal flux density waveforms in sample S3.

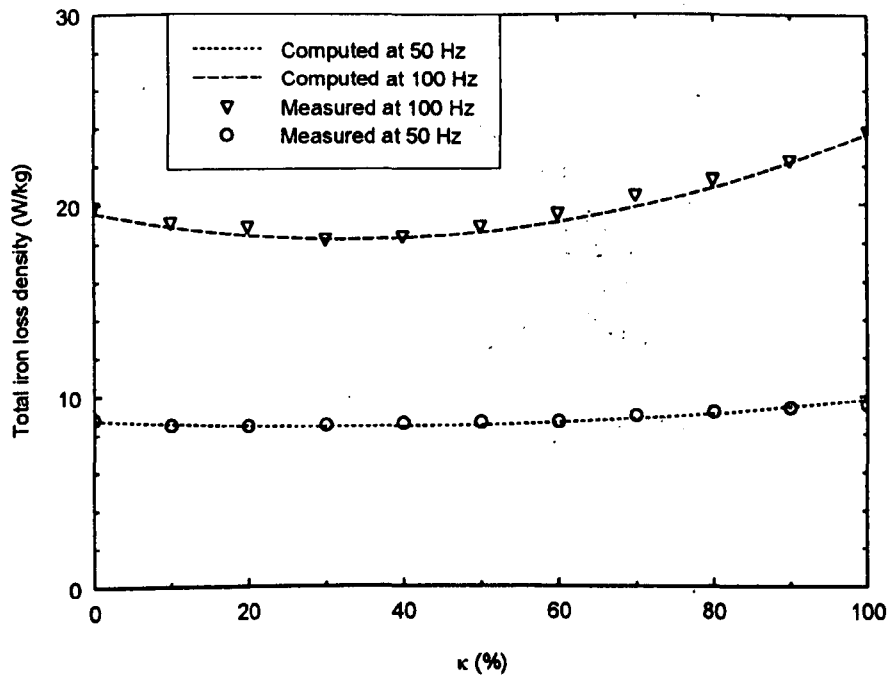


(a) $B_{max} = 1.0\ T$

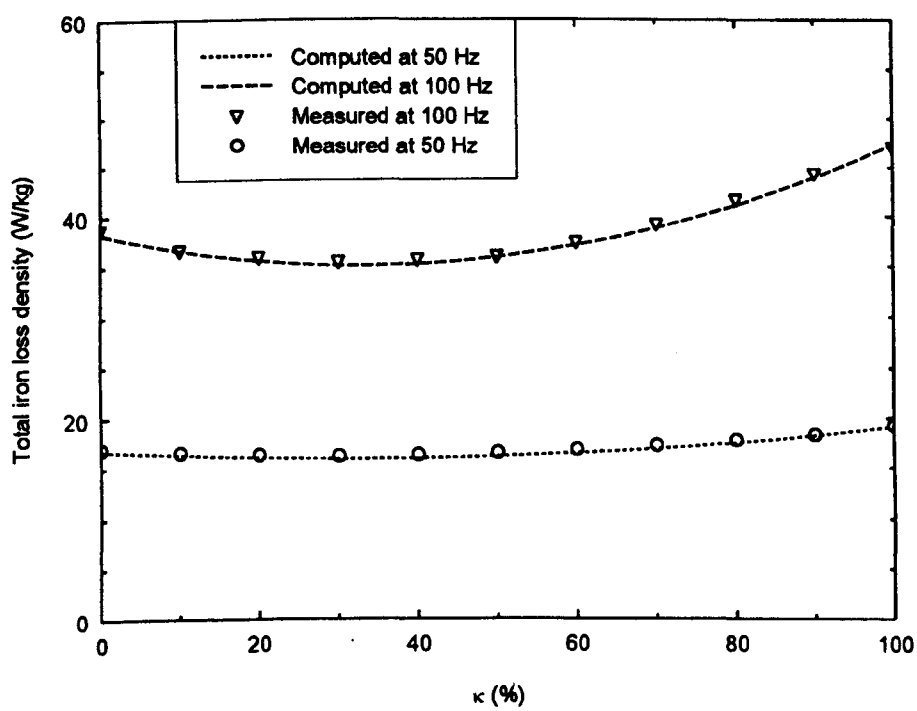


(b) $B_{max} = 1.5\ T$

Fig (3.14) Total iron loss density under piece-wise linear flux density waveforms for sample S1.

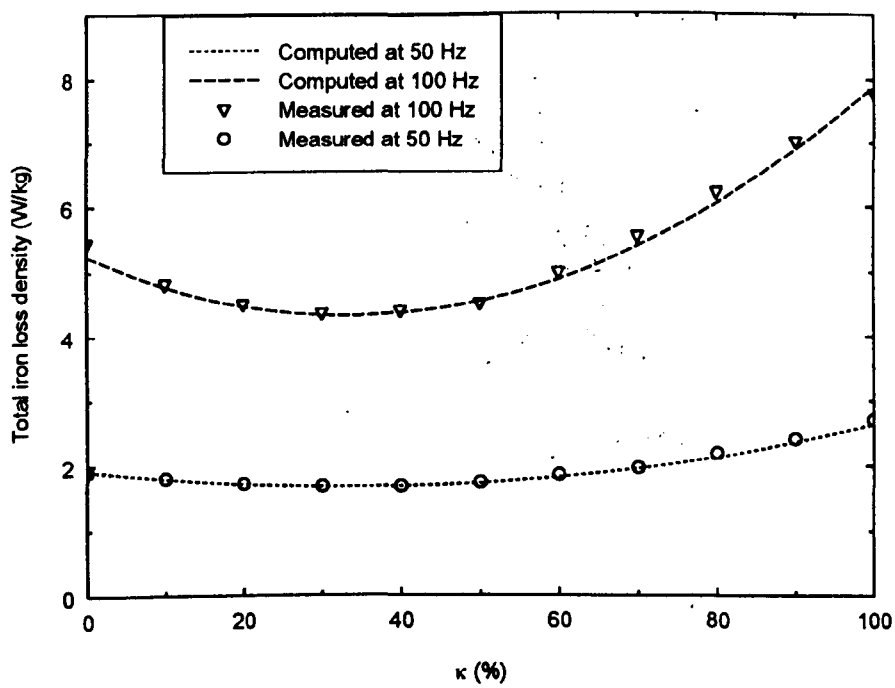


(a) $B_{max} = 1.0\ T$

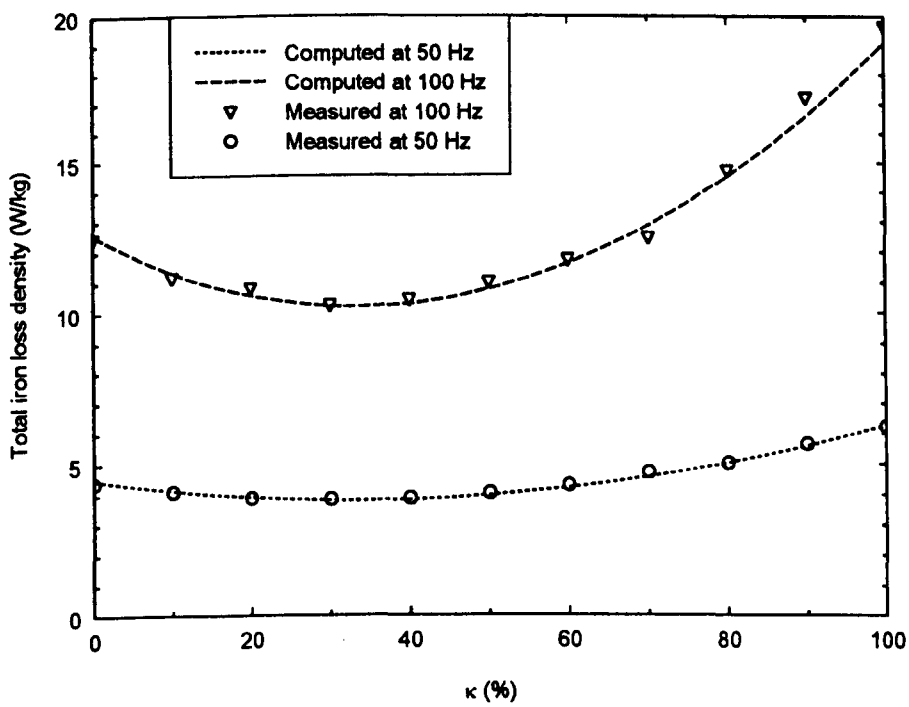


(b) $B_{max} = 1.5\ T$

Fig (3.15) Total iron loss density under piece-wise linear flux density waveforms for sample S2.

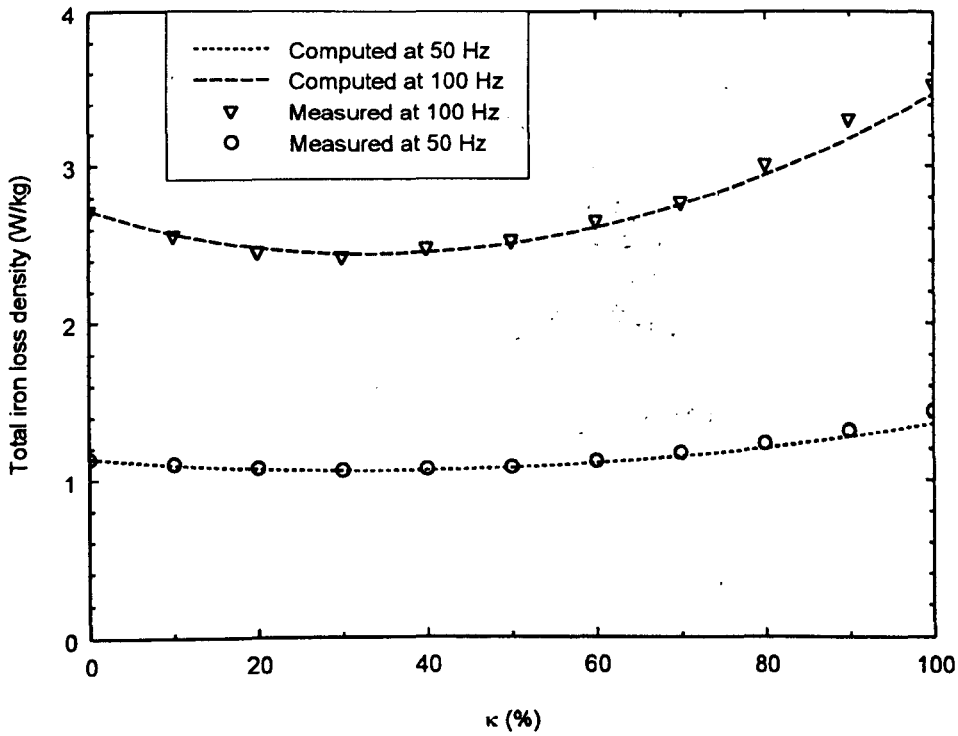


(a) $B_{max} = 1.0\ T$

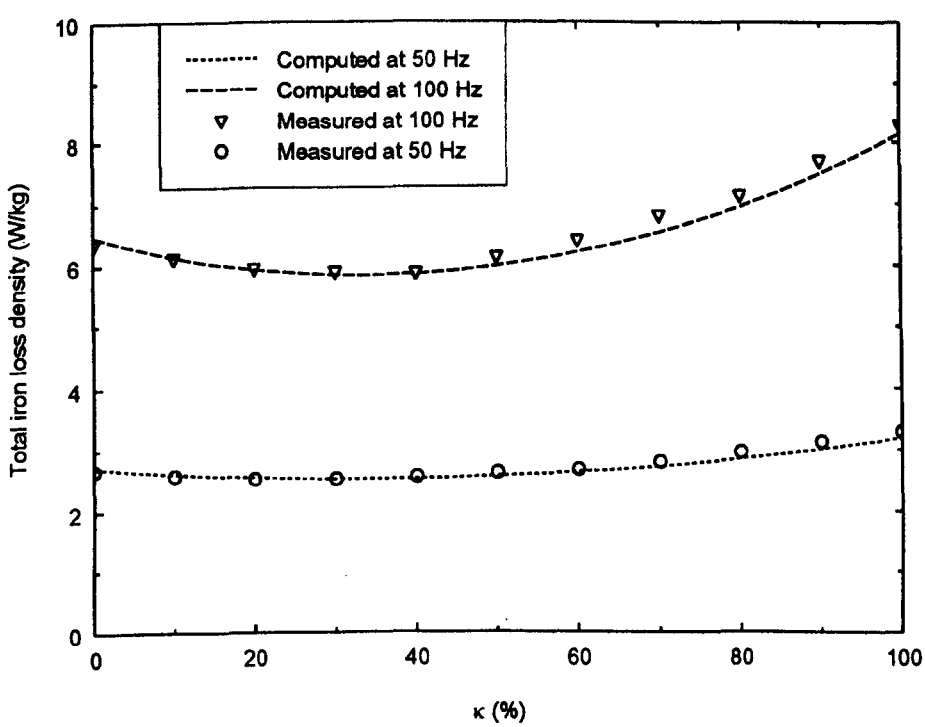


(b) $B_{max} = 1.5\ T$

Fig (3.16) Total iron loss density under piece-wise linear flux density waveforms for sample S3.

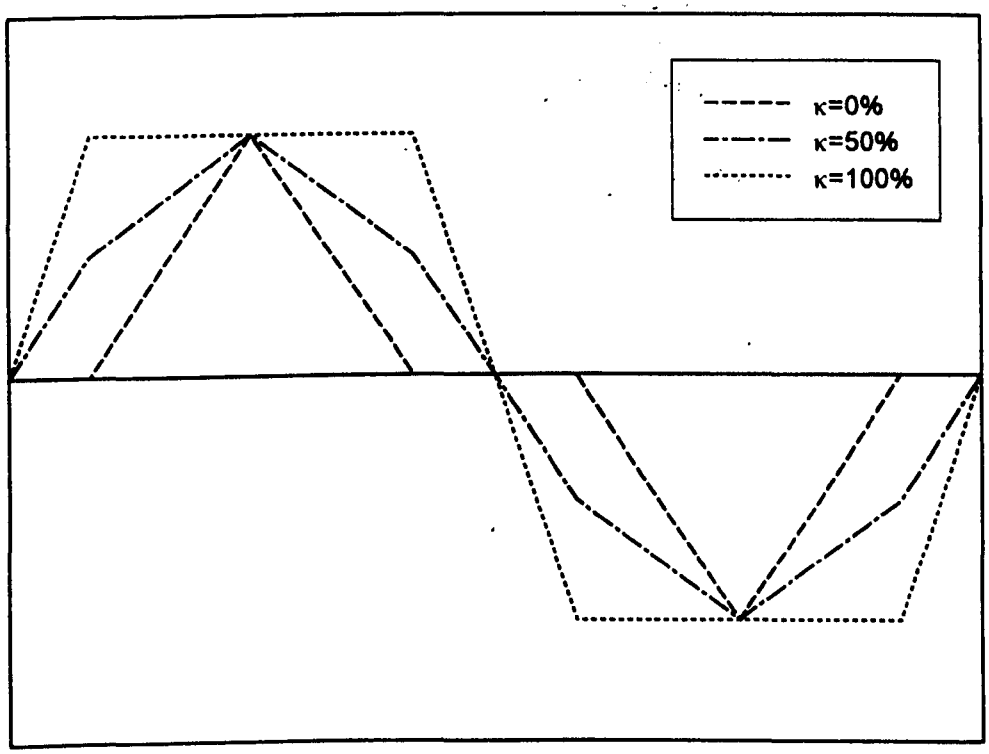


Fig (3.17) Examples of piece-wise linear waveforms characterised by the parameter κ.

# CHAPTER 4

# PREDICTION OF THE FLUX DENSITY WAVEFORMS IN THE STATOR CORE OF BRUSHLESS DC MACHINES.

## 4.1) INTRODUCTION

The calculation of the total iron loss requires a knowledge of the flux density waveform in different regions of the stator core. Whereas in classical a.c machines the flux density waveforms are essentially sinusoidal and only a knowledge of the peak flux density is required, in permanent magnet excited machines not only is the peak required but also the waveform, which is generally far from being sinusoidal.

The analytical prediction of the flux density waveforms in a permanent magnet machine on open-circuit is achieved by initially calculating the airgap flux density waveform and then deducing corresponding waveforms throughout the stator core. It builds on the technique reported in [41].

In this investigation, special attention is given to the airgap flux density waveform, and it will be shown that curvature effects, which are often neglected or poorly modelled, can cause significant errors to the prediction of the airgap flux density waveform. In this respect, a simple analytical model for the calculation of the magnet/airgap flux density taking account of curvature, is presented, and predictions are compared to those from more sophisticated techniques, both analytical and numerical, as well as with measurements.

The technique for predicting the stator core flux density waveforms, is applied to brushless dc motors having 1-slot/pole/phase, which usually carry "overlapping"

windings as well as to motors having 1/2-slot/pole/phase, which usually carry "non-overlapping" windings.

Much more detailed information on the temporal and spatial variation of the flux density distribution throughout the stator core, under both open-circuit and load conditions, can be derived from a series of 2-d magnetostatic finite element analyses as the rotor rotates 180°elec, with the instantaneous phase currents corresponding to each rotor position varying according to the specific operating condition of the drive. The series of field solutions is post-processed to obtain local flux density waveforms over the cross-section of the stator core. Predictions from such analyses are compared with analytical predictions for the open-circuit condition, and with measurements for the load condition.

## 4.2) Flux density waveforms on open-circuit

### 4.2.1) Prediction of flux density distribution in magnet/airgap region of slotless radial-field machines

In radial-field machine topologies, flux focusing can cause a significant spread of magnet working points. Thus, the usual analytical expression for the airgap flux density:

$$B_g = \frac{B_r}{1 + \mu_r \frac{g}{h_m}} \tag{4.1}$$

in which $B_r$, $\mu_r$, $g$ and $h_m$ are the remanence, the relative recoil permeability, the airgap length and the magnet thickness respectively, and which assumes a single magnet working point, can be considerably in error. In order to account for a spread of magnet working points, a simple model, designated A, is presented. The predictions of model A are compared to those of a more sophisticated analytical model, designated

B. Model A assumes negligible inter-pole leakage flux, but has the merit of leading to a simple analytical expression for the magnet/airgap flux density, whereas Model B caters for leakage flux. However, both models assume:

a. Radial magnetization.

b. Magnetization to saturation throughout the volume of the magnets.

c. Infinitely permeable stator and rotor cores.

d. Slotless magnetic circuit.

***Model A***

With reference to Fig (4.1), the flux per pole at any radius r between $R_r$ and $R_s$ is constant, i.e.

$$\varphi_p(r) = B(r)\, r\, \alpha_{pa} = Constant \tag{4.2}$$

where $\alpha_{pa}$ is the pole-arc. Hence, the flux density varies inversely with the radius:

$$B(r) = \frac{C}{r} \tag{4.3}$$

Applying Ampere's law:

$$\int_{R_r}^{R_s} H(r)\, dr = 0 \tag{4.4}$$

where

$$H(r) = \frac{1}{\mu_r \mu_o} \left( \frac{C}{r} - B_r \right) \tag{4.5a}$$

in the magnets, and

$$H(r) = \frac{C}{\mu_o r} \tag{4.5b}$$

in the airgap. Hence, the constant C can be determined from:

$$C = \frac{B_r\,(R_m - R_r)}{\mu_r \ln\left(\frac{R_s}{R_m}\right) + \ln\left(\frac{R_m}{R_r}\right)} \tag{4.6}$$

for both machine topologies shown in Fig (4.1). For the topology of Fig (4.1a) $R_m = R_r + h_m$ and $R_s = R_m + g$

$$B(r) = \frac{B_r\,h_m}{\mu_r \ln\left(1 + \frac{g}{R_m}\right) + \ln\left(1 + \frac{h_m}{R_r}\right)} \times \frac{1}{r} \tag{4.7a}$$

and for the topology of Fig (4.1b) $R_r = R_m + h_m$ and $R_m = R_s + g$

$$B(r) = \frac{B_r\,h_m}{\mu_r \ln\left(1 + \frac{g}{R_s}\right) + \ln\left(1 + \frac{h_m}{R_m}\right)} \times \frac{1}{r} \tag{4.7b}$$

***Model B***

In polar coordinates the magnetization $\vec{M}$ can be written as:

$$\vec{M} = M_r\,\vec{r} + M_\theta\,\vec{\theta} \tag{4.8a}$$

where

$$M_r = \sum_{odd\ n}^{\infty} M_n \cos(n\,p\,\theta) \text{ and } M_\theta = 0 \tag{4.8b}$$

with respect to the axis of a magnet pole, where p is the number of pole pairs, and

$$M_n = 2\frac{B_r}{\mu_o}\alpha_p \frac{\sin\left(\frac{n\,\pi\,\alpha_p}{2}\right)}{\frac{n\,\pi\,\alpha_p}{2}} \tag{4.9}$$

$\alpha_p$ is the pole-arc to pole-pitch ratio. Assuming uniformly radially magnetized magnets:

$$div\,\vec{M} = \frac{M_r}{r} + \frac{\partial M_r}{\partial r} + \frac{1}{r}\frac{\partial M_\theta}{\partial \theta} = \frac{M_r}{r} \tag{4.10}$$

and

$$\frac{\partial^2 \Phi_I}{\partial r^2} + \frac{1}{r}\frac{\partial \Phi_I}{\partial r} + \frac{1}{r^2}\frac{\partial^2 \Phi_I}{\partial \theta^2} = 0 \tag{4.11a}$$

in the airgap, and

$$\frac{\partial^2 \Phi_{II}}{\partial r^2} + \frac{1}{r}\frac{\partial \Phi_{II}}{\partial r} + \frac{1}{r^2}\frac{\partial^2 \Phi_{II}}{\partial \theta^2} = \frac{M_r}{r\,\mu_r} \tag{4.11b}$$

in the magnets and interpole airspaces, where the magnetic scalar potential functions $\Phi_I$ and $\Phi_{II}$ are related to the components of $\vec{H}$ by:

$$H_r = -\frac{\partial \Phi}{\partial r}\,,\; H_\theta = -\frac{1}{r}\frac{\partial \Phi}{\partial \theta} \tag{4.12}$$

and

$$B_{rI} = \mu_o H_{rI},\; B_{\theta I} = \mu_o H_{\theta I} \tag{4.13a}$$

$$B_{rII} = \mu_o \mu_r H_{rII} + \mu_o M_r\,,B_{\theta II} = \mu_o \mu_r H_{\theta II} + \mu_o M_\theta \tag{4.13b}$$

For both machine topologies shown in Fig (4.1) the general solutions of equations (4.11a) and (4.11b) are:

$$\Phi_I(r,\theta) = \sum_{odd\,n}^{\infty} \left( A_{nI} r^{np} + B_{nI} r^{-np} \right) \cos\left( n p\, \theta \right) \tag{4.14}$$

$$\Phi_{II}(r,\theta) = \sum_{odd\,n}^{\infty} \left( A_{nII} r^{np} + B_{nII} r^{-np} \right) \cos\left( n p\, \theta \right)$$

$$+ \sum_{odd\,n}^{\infty} \frac{M_n}{\mu_r \left(1 - (np)^2\right)} r \cos\left( n p\, \theta \right) \tag{4.15a}$$

for $np \neq 1$, and

$$\Phi_{II}(r,\theta) = \left( A_{1II} r + B_{1II} r^{-1} \right) \cos\left( \theta \right) + \frac{1}{2}\frac{M_1}{\mu_r} r \ln r \cos\left( \theta \right) \tag{4.15b}$$

for np = 1.

The boundary conditions are:

$$H_{\theta I}(R_s,\theta) = 0 \tag{4.16a}$$

$$H_{\theta II}(R_r,\theta) = 0 \tag{4.16b}$$

$$B_{rI}(R_m,\theta) = B_{rII}(R_m,\theta) \tag{4.16c}$$

$$H_{\theta I}(R_m,\theta) = H_{\theta II}(R_m,\theta) \tag{4.16d}$$

Hence, the complete solution for the magnetic field components in both the airgap and magnet regions can be deduced [61]. For example, the radial flux density distribution at the surface $r = R_s$ is:

$$B(R_s) = \sum_{odd\ n}^{\infty} \frac{2\,\mu_o\, M_n\, n\, p}{(np)^2 - 1}\left(\frac{R_s}{R_m}\right)^{np-1} \times \left[\frac{(np-1)\,R_m^{2np} + 2\,R_r^{np+1}\,R_m^{np-1} - (np+1)\,R_r^{2np}}{(\mu_r+1)\,[R_s^{2np} - R_m^{2np}] - (\mu_r-1)\,[R_m^{2np} - R_s^{2np}\,(\frac{R_r}{R_m})^{2np}]}\right] \cos(n\,p\,\theta) \tag{4.17a}$$

when $np \neq 1$, and

$$B(R_s) = \mu_o M_1 \left[\frac{(\frac{R_m}{R_s})^2 - (\frac{R_r}{R_s})^2 + (\frac{R_r}{R_s})^2 \ln(\frac{R_m}{R_r})^2}{(\mu_r+1)[1-(\frac{R_r}{R_s})^2] - (\mu_r-1)\,[(\frac{R_m}{R_s})^2 - (\frac{R_r}{R_m})^2]}\right] \cos(\theta) \tag{4.17b}$$

when np = 1.

### 4.2.2) OPTIMIZATION

In the machine topology shown in Fig (4.1a), having an airgap length g, the flux density at the surface $r = R_s$ exhibits a maximum value for a particular magnet thickness, which can be deduced from:

$$\frac{dB(R_s)}{dh_m} = 0 \tag{4.18}$$

where $B(R_s)$ can be obtained from equation (4.7a). From equations (4.7a) and (4.18):

$$x_o - \ln x_o = 1 + \mu_r \ln ( 1 + \frac{g}{R_m} ) \tag{4.19}$$

where $x_o = \frac{R_m}{R_r}$.

Although equation (4.19) can be easily solved numerically, there is no exact analytical solution. However, an approximate analytical solution can be determined since equation (4.19) is equivalent to,

$$\frac{e^{x_o}}{x_o} = e ( 1 + \frac{g}{R_m} )^{\mu_r} \tag{4.20}$$

whilst in practice the ratio $\frac{g}{R_m} << 1$, and x lies in the interval $1 \leq x_o \leq 1.5$.

Taylor series expansions for the functions (ln x) and $e^{x_o}$ for $x_o \approx 1$ are:

$$e^{x_o} = e \sum_{n=0}^{\infty} \frac{( x_o - 1 )^n}{n !} \tag{4.21}$$

and

$$\ln x_o = \sum_{n=1}^{\infty} ( - 1 )^{n+1} \frac{( x_o - 1 )^n}{n} \tag{4.22}$$

Hence $e^{x_o}$ and $(\ln x_o)$ can be approximated by:

$$e^{x_o} \approx e \sum_{n=0}^{2} \frac{( x_o - 1)^n}{n !} = \frac{1}{2} e ( x_o^2 + 1 ) \leq e^{x_o} \tag{4.23}$$

and

$$\ln x_o \approx \sum_{n=1}^{2} (-1)^{n+1} \frac{( x_o - 1 )^n}{n} = \frac{x_o^2}{2} - 2 x_o + \frac{3}{2} \geq \ln x_o \tag{4.24}$$

From equations (4.19) and (4.24) an approximate analytical solution is obtained as:

$$x_o \approx x_1 = 1 + \sqrt{2 \mu_r \ln ( 1 + \frac{g}{R_m} )} \tag{4.25}$$

whilst from equations (4.20) and (4.23) an alternative approximate solution is obtained as:

$$x_o \approx x_e = \left(1 + \frac{g}{R_m}\right)^{\mu_r} + \sqrt{\left(1 + \frac{g}{R_m}\right)^{2\mu_r} - 1} \tag{4.24}$$

Since in the interval $1 \leq x_o \leq 1.5$ $e^{x_o}$ has been under-estimated in equation (4.23) whilst ($\ln x_o$) has been over-estimated in equation (4.24), $x_l \leq x_o \leq x_e$ , and a more accurate solution for x in equation (4.19) is:

$$x_o \approx \frac{x_l + x_e}{2} \tag{4.27}$$

Fig (4.2) compares the approximate analytical solution of equation (4.19) as given by equation (4.27) with the numerically determined solution for values of $g/R_m$ varying from 0 to 0.1.

### 4.2.3) Experimental validation and discussion

The magnet/airgap flux density distribution has been analysed for three slotless machines designated M1, M2 and M3, Fig (4.3). All three machines are equipped with radially magnetised anisotropic flexible ferrite magnets mounted on the surface of a cylindrical mild steel inner hub, the only difference being in the magnet thickness, Table (4.1). Furthermore, the magnet thickness in motor M2 has been chosen, using

Table (4.1) Parameters of test motors

| Motors | | M1 | M2 | M3 |
|---|---|---|---|---|
| airgap length | g (mm) | 0.5 | 0.5 | 0.5 |
| bore radius | $R_s$ (mm) | 20.8 | 20.8 | 20.8 |
| magnet thickness | $h_m$ (mm) | 2.0 | 4.0 | 6.0 |
| remanence | $B_r$ (T) | 0.23 | 0.23 | 0.23 |
| relative recoil permeability | $\mu_r$ | 1.04 | 1.04 | 1.04 |
| number of poles | 2p | 2 | 2 | 2 |
| pole-arc/pole-pitch | $\alpha_p$ | 1.0 | 1.0 | 1.0 |

equation (4.27), so as to produce the maximum flux density at the bore radius $R_s$, Fig (4.1a).

Fig (4.4) shows the calculated variation of the flux density along a magnet pole axis of the optimised motor M2, using Model A, Model B, and finite element analysis, whilst Fig (4.5) compares the flux density distribution at $r = R_s$, computed from model B, with measured results for all three machines. It will be noted that motor M2 exhibits the highest airgap flux density despite having less magnet material than motor M3.

Fig (4.6) compares computed and measured variations of the maximum flux density at the stator surface with magnet thickness. It can be seen that for this particular stator bore radius equation (4.1), which assumes a single magnet working point, becomes increasingly in error as the magnet thickness is increased beyond about 2 mm. Fig (4.7) shows predicted flux density distributions at $r = R_s$ together with corresponding flux plots for a range of magnet thicknesses, from which it will be seen that inter-pole leakage becomes more pronouced as the magnet thickness is increased, which explains the difference between predictions from Models A and B. The effect of inter-pole leakage is also evident in Fig (4.8), which shows the variation of the flux per pole with magnet thickness.

Figs (4.9), (4.10), and (4.11) show a comparison between predictions from Models A and B for the optimised motor M2, and further highlight the effect of inter-pole leakage as the number of pole pairs p, the pole-arc to pole-pitch ratio $\alpha_p$, and the airgap length g are varied. However, it will be noted that both models predict almost the same flux density for pole numbers up to 12, a pole-arc to pole-pitch ratio $\alpha_p \geq 0.25$, and airgap lengths up to 10 mm.

Finally, Fig (4.12) shows the computed variation of the airgap flux density at $r = R_s$ with magnet thickness in the machine topology of Fig (4.1b) when $R_s$ is assumed to

have the same dimension as in M1, M2 and M3. However, it will be noted that unlike the topology of Fig (4.1a) an increase in the magnet thickness always results in an increase of the magnetic loading at the airgap no matter how pronouced the flux focusing effect.

### 4.2.4) Effect of stator slotting

The stator slotting affects the airgap magnetic field in different ways. Firstly, the airgap flux is reduced. Secondly, the magnetic field distribution is distorted in both the magnet and the airgap, as it exhibits a minimum at the centre of a slot opening. The effect of slotting on the magnetic field distribution can be accounted for by using a relative permeance function, which can be determined by the conformal transformation method by applying unit magnetic potential between the stator and rotor iron surfaces with no magnet present [61]. The ratio $\beta(r) = \dfrac{B_{max}(r) - B_{min}(r)}{2\,B_{max}(r)}$ is then given by:

$$\beta(r) = \frac{1}{2}\left[1 - \frac{1}{\sqrt{1 + \left(\frac{b_o}{2g'}\right)^2 (1 + x^2)}}\right] \tag{4.28}$$

where $b_o$ and $g' = g + \dfrac{h_m}{\mu_r}$ are the slot opening and the effective airgap respectively, whilst x is determined from:

$$y\frac{\pi}{b_o} = \frac{1}{2}\ln\left(\frac{\sqrt{q^2 + x^2} + x}{\sqrt{q^2 + x^2} - x}\right) + \frac{2g'}{b_o}\arctan\left(\frac{2g'}{b_o}\left(\frac{x}{\sqrt{q^2 + x^2}}\right)\right) \tag{4.29}$$

where for machine topology of Fig (4.1a)

$$y = r - R_s + g' \tag{4.30a}$$

and for machine topology of Fig (4.1b)

$$y = R_s + g' - r \tag{4.30b}$$

and $q = \sqrt{1 + \left(\dfrac{2g'}{b_o}\right)^2}$.

The magnetic field distribution within the airgap is assumed to be affected by the stator slotting in a similar manner to that in a slotted induction machine, viz,

$$B(r,\theta)\begin{cases} B(r)\left(1-\beta(r)-\beta(r)\cos\left(\frac{\pi}{0.8\,\theta_o}\theta\right)\right) & \text{for } 0 \le \theta \le 0.8\,\theta_o \\ B(r) & \text{for } 0.8\,\theta_o \le \theta \le \frac{\theta_d}{2} \end{cases} \qquad (4.31)$$

where $\theta = 0$ coincides with the centre of a slot, $\theta_o = \frac{b_o}{R_s}$, $\theta_d = \frac{\tau_t}{R_s}$ and $\tau_t$ is the slot pitch.

### 4.2.5) Flux density waveform in tooth body

As the rotor rotates, the total flux in a tooth body remains essentially constant until an adjacent slot opening coincides with a transition between magnet poles, Fig (4.13a), after which it varies linearily until it changes polarity, ie. the flux waveform is trapezoidal, the extent of the flat-top depending on the number of slots $N_s$ as well as the number of pole pairs. However, for the usual cases of $N_s = 3p$ and $N_s = 6p$, the duration of the transition from flux of one polarity to the other is given by:

$$T_d = \frac{2\pi}{N_s} p \qquad (4.32)$$

The maximum flux in a tooth body occurs when the tooth axis coincides with the axis of a magnet pole, and is given by:

$$\varphi_{tmax} = 2\,R_s \int_0^{\frac{\theta_d}{2}} B\,(R_s,\theta)\,d\theta \qquad (4.33)$$

where $B\,(R_s,\theta)$is given by equation (4.31). Hence, from equations (4.31) and (4.33):

$$B_{tmax} = \frac{R_s\,B\,(R_s)}{W_t}\left(\frac{2\pi}{N_s} - 1.6\,\beta\,(R_s)\,\theta_o\right) \qquad (4.34)$$

where $W_t$ is the width of the tooth body.

### 4.2.6) Flux density waveforms in the stator back-iron

The flux density waveform in the stator back-iron also depends primarily on the number of stator slots and the number of pole-pairs. For example, when $N_s$ = 6p (ie. 1-slot/pole/phase), which usually corresponds to the stator carrying 'overlapping' windings, the flux waveform is essentially triangular, the maximum flux being:

$$\varphi_{ymax} = \frac{\varphi_p}{2} \tag{4.35}$$

whenever a stator slot opening coincides with an interpolar axis, when, the total flux per pole, is given by:

$$\varphi_p = 6\, R_s \int_0^{\frac{\theta_d}{2}} B\,(R_s,\theta)\, d\theta \tag{4.36}$$

and

$$B_{ymax} = \frac{3\, R_s\, B(R_s)}{W_{yk}} \left( \frac{2\,\pi}{N_s} - 1.6\, \beta(R_s)\, \theta_o \right) \tag{4.37}$$

where $W_{yk}$ is the thickness of the stator back-iron. On the other hand, when $N_s$=3p, which corresponds to a stator having 'non-overlapping' windings, the situation is slightly more complicated, since only one tooth per pole contributes to the flux carried by the stator back-iron at the instant when this is a maximum. However, the flux waveform can be approximated as piece-wise linear, using two values of flux, $\varphi_{ymax}$ and $\varphi_y$, corresponding to the instant when the axis of a stator slot and the axis of a stator tooth coincide with transitions between magnet poles, as shown in Fig (4.13b). If iron saturation is likely to be significant the fluxes can be calculated from the simple non-linear lumped model shown in Fig (4.14), in which reluctance 1 has an effective flux path length equal to twice that of reluctance 2. However, if saturation can be neglected the fluxes can be approximated simply as:

$$\varphi_{ymax} = \frac{2}{3}\, \varphi_{tm}, \text{ and } \varphi_{yc} = \frac{1}{3}\, \varphi_{tm} \tag{4.38}$$

where

$$\varphi_{tm} = R_s\, B\,(R_s)\,(\frac{2\pi}{N_s} - 0.8\,(\,1 + \beta\,(R_s))\,\theta_o\,) \qquad (4.39)$$

which neglects flux fringing into the slot opening which is coincident with a magnet pole transition.

### 4.2.7) Flux density waveforms in stator tooth tip

Various shapes of stator tooth tip are used, often being selected so as to minimise the effect of stator slotting on both the flux per-pole and the magnetic field distribution in the airgap. Further, in general the flux paths in the tooth tips are generally more complex than those in the tooth body. However, in machines in which the tooth tip is smaller than volume of the tooth body , the tooth tip can simply be assumed to be an extension to the tooth body, and to have a similar flux density waveform, the peak flux density being approximated by taking an average cross-section area. However, in machines in which the tooth tip volume is comparable to that of the tooth body, which is ususally the case in machines having a low number of slots, the flux density waveforms in the tooth tip region have to be analysed separately. In the following, a more or less typical tooth tip shape for 1slot/pole/phase and 1/2 slot/pole/phase brushless dc machines, Fig (4.15), is analysed.

The stator tooth tip can be divided into two regions, 1 and 2, as shown in Fig (4.15), in each of which the flux density waveforms are markedly different. In region 1, for example, the flux density will have both radial and circumferential components, ie. the flux density vector exhibits rotational behaviour, whilst in region 2 the flux density is more or less alternating. However, in both regions each of the two orthogonal alternating components can be analysed independently.

The maximum radial flux component in region 1 is assumed to be identical to that in the tooth body, and to be trapezoidal in waveform, although the effective maximum radial flux density is different, due to the variable cross-section of the region. However, the average peak flux density, can be approximated by:

$$B_{tr} = \frac{\varphi_{tmax}}{\left(\frac{2\,l_t + W_t}{2}\right)} \tag{4.40}$$

where $\frac{2\,l_t + W_t}{2}$ is the average cross-section area. The circumferentially directed flux component has a peak value when the axis of a tooth coincides with a transition between magnet poles, as shown in Fig (4.13), and decreases almost linearily to zero as the rotor rotates half a slot pitch. The maximum circumferential flux density can be approximated by:

$$B_{t\theta} = \frac{\varphi_{tmax}}{2\,l_t} \tag{4.41}$$

Assuming a perfect transition between magnet poles, the maximum flux entering region 2 is given by:

$$\varphi_{t2} = \frac{\varphi_{tmax}}{2} \tag{4.42}$$

and is essentially alternating with a trapezoidal waveform. The average maximum flux density can be deduced by the following expression:

$$B_{t2} = \frac{\varphi_t}{\left(\frac{l_t + \frac{\pi}{N_s} R_s\,(\,1 - 0.8\,\beta\,(R_s)\,\theta_o\,)}{2}\right)} \tag{4.43}$$

where $\frac{l_t + \frac{\pi}{N_s} R_s\,(\,1 - 0.8\,\beta\,(R_s)\,\theta_o\,)}{2}$ is an approximation of the effective average cross-section area, taking account of the magnetic field distribution in the airgap, with the transition angle from flux of one polarity to the other being approximated by:

$$T_t = \frac{g}{\mu_r h_m} \frac{\pi}{2} \tag{4.44}$$

## 4.3) Flux density waveforms on load

### 4.3.1) Drive system simulation

The voltage equations governing the dynamic performance of a 3-phase star-connected motor are given by:

$$\begin{cases} R\, i_a + L_p \dfrac{di_a}{dt} - M_p \left( \dfrac{di_b}{dt} + \dfrac{di_c}{dt} \right) + e_a = V_a \\ R\, i_b + L_p \dfrac{di_b}{dt} - M_p \left( \dfrac{di_c}{dt} + \dfrac{di_a}{dt} \right) + e_b = V_b \\ R\, i_c + L_p \dfrac{di_c}{dt} - M_p \left( \dfrac{di_a}{dt} + \dfrac{di_b}{dt} \right) + e_c = V_c \\ i_a + i_b + i_c = 0 \end{cases} \tag{4.45}$$

where R, $L_p$ and $M_p$ are the phase resistance, the phase self-inductance and the mutual inductance between two phases respectively, and $e_a$, $e_b$ and $e_c$ are the induced emfs in phases A, B and C respectively. For a brushless dc drive, Fig (4.16), $V_a$, $V_b$ and $V_c$ are functions of the dc supply, the characteristics of the electronic components in the path of the phase currents, viz transistors and diodes, and the commutation logic.

Ideally, in a brushless dc drive only two phases are simultaneously active, Fig (4.17), whilst under normal commutation a phase is commutated on $30^0$ elec. from the zero crossing of its induced emf. In practice, the inductive nature of the phase windings causes the phase current waveform to deviate from the ideal rectangular waveforms for two main reasons:

a) the electrical time constant, which prevents sudden current variations, and causes a dependence of the current waveforms on the motor speed.

b) the creation of 6 periods per electrical cycle, each of duration $\theta_c$ as shown in Fig (4.18), during which all three phases simultaneously conduct. However, since only two phases are commutated on, the stored magnetic energy in the third phase causes a circulating current through the free-wheel diode.

In addition, the back-emf waveform often deviates from the ideal trapezoid.

In general, the commutation of the current in particular phase is delayed by an angle $\gamma$ from the zero-crossing of its induced emf:

$$\gamma = \frac{\pi}{6} - \alpha_c \tag{4.46}$$

where $\alpha_c$ is the commutation angle, $\alpha_c < 0$ for retarded commutation, $\alpha_c = 0$ for normal commutation and $\alpha_c > 0$ for advanced commutation, as shown in Fig (4.19).

The numerical solution of equations (4.45) is performed using a time-stepping system simulation program "SIMNET" developed at the University of Sheffield under an EC funded BRITE (Basic Research in Industrial Technologies in Europe) project. The parameters required to model a brushless dc drive include :

- back-emf waveform
- phase resistance, self and mutuals inductances
- steady-state motor speed
- commutation angle

as well as the characteristics of the electronic components of the drive circuit,viz,

- constant voltage drops of the transistors and free-wheel diodes
- resistances of the transistors and free-wheel diodes.

is all contained in a the functional block "bldc3", as shown in Fig (4.20). In the analysis cogging is neglected and the rotor speed is assumed constant.

### 4.3.2) Relative positions of the open-circuit field and armature reaction Fields

Having calculated the phase current waveforms under a specified operating condition, before performing finite element analyses of the motor on load, it is necessary to determine the instantaneous position of the rotor relative to the current waveform. Assuming :

a) The axis of phase A as reference, Fig (4.22)

b) The reference polarity of current flowing in phase A such that a positive current creates a positive m.m.f, and similarly for the other two phases.

c) The phase sequence A,B and C such that the start conductor of phase B is $\frac{2\pi}{3}$ elec. from that of phase A, with the start conductor of phase C $\frac{2\pi}{3}$ elec. from that of conductor of phase B, in an anti-clockwise direction.

d) t=0 as the instant when phase A is commutated, as shown in Fig (4.21);

f) The rotor is rotating anti-clockwise at an angular speed $\omega_r$.

The relative instantaneous position of the permanent magnet field, with respect to the armature reaction field is then given by:

$$\alpha_{ma} = p\,\omega_r\,t - \alpha_c + \frac{\pi}{6} + \pi \qquad (4.47)$$

whilst at the instant when phase A is commutated on :

$$\alpha_{ma} = (2n+1)\,\pi - \alpha_c + \frac{\pi}{6} \qquad (4.48)$$

where n is an integer, as shown in Fig (4.22).

### 4.3.3) Calculation of the instantaneous field distribution

The first-order finite element magnetostatic field solver "MAGSTAT", which has been developed at the University of Sheffield, is used to predict the instantaneous field distribution at each motor position.

### 4.3.4) Post-processing

Given the amount of data to be handled, which corresponds to potential values at each node for each rotor position times the number of position over half an electrical cycle, a post-processor was developed, its main features being :

**A) Input**

- Vector magnetic potential data from MAGSTAT.
- Iron loss density constants for the particular steel laminations used for the stator core, from a single-sheet test.
- Steady-state rotational speed of rotor.
- Axial length of the stator lamination stack.

**B) Processing**

- Synthesis of the local flux density waveforms from the potential data.
- Harmonic analysis of local flux density waveforms.
- Calculation of the local iron loss densities.

**C) Output**

**C-1) Numerical output**

- Data file containing harmonic information of the synthesised local flux density waveforms.

- Data file containing local iron loss density components, viz, hysteresis, classical eddy current and excess eddy current.
- Total integrated iron loss.

**C-2) Graphical output**

- Screen plot of the finite element mesh.
- Screen plot of the harmonic distortion distribution throughout the stator core.
- Screen plot of the hysteresis loss density distribution throughout the stator core.
- Screen plot of total eddy current loss density distribution, viz, classical and excess, throughout the stator core.
- Screen plot of total iron loss density distribution throughout the stator core.
- Screen plot of flux density waveforms, ie to the circumferential and radial components, their respective Fourier spectrums, and the corresponding flux density loci, at 'mouse' selected elements from the finite element mesh plot.
- Screen print of the local iron loss density at mouse selected elements from the iron loss density distribution plot.
- Screen plot of the flux density waveform between two mouse selected nodes, again selected from the finite element mesh plot.

In addition, in order to ease the task of element and node selection as well as to provide the user with a enlarged view of a specified region, a zooming facility has been implemented which can be activated from any of the parameter distribution plots as well as from the finite element mesh plot. The use of the different output is controlled via a menu.

### 4.3.5) Harmonic analysis

The Fourier spectrum of a periodic waveform $B(\theta)$ defined at a discrete number $N_p$ of equis-paced rotor positions per cycle, is

$$B(\theta) = \sum_{n=1}^{\frac{N_p}{2}} ( a_n \cos (n\theta ) + b_n \sin ( n\theta ) ) \tag{4.48}$$

where

$$\begin{cases} a_n = Real ( \sum_{i=1}^{N_p} B(\theta_i) \times z^n ) \\ b_n = Imag ( \sum_{i=1}^{N_p} B(\theta_i) \times z^n ) \end{cases} \tag{4.49}$$

for $n \leq \frac{N_p}{2}$, and where the complex variable z is given by:

$$\theta_i = \frac{2\pi}{N_p} ( i - 1 ) \tag{4.50}$$

$$z = \cos ( \frac{2\pi}{N_p} ( i - 1 ) ) + j \sin ( \frac{2\pi}{N_p} ( i - 1 ) ) \tag{4.51}$$

where $j^2 = -1$.

### 4.4) Flux density waveforms in a prototype brushless dc motor

A prototype 150 W, 4-pole, 3-phase, 2000 rpm permanent magnet brushless dc motor equipped with flexible, surface-mounted, radially magnetized NdFeB magnets having a remanence of 0.48 T and a relative recoil permeability of 1.1, is shown in Fig (4.23). The stator lamination stack is made of the same material S3, which was characterised in Chapter 3. The motor was instrumented by wrapping search-coils around various parts of the stator core, ie the tooth body, the stator back-iron, each sides of a tooth tip, and through holes drilled in the back of a tooth in order to measure the radial and the circumferential components of flux, Fig (4.24).

### 4.4.1) Open-circuit operation

Figs (4.25) and (4.26) show a comparison between the computed and measured average flux density waveforms in the tooth body search coil A and the stator back-iron search coil B. It will be noted that whilst in both case a good agreement exists, using both analytical and numerical techniques, in the stator back-iron a slight asymmetry exists in the measured flux density waveform. The cause of the asymmetry is that flux sharing between the different sections of the back-iron in 1/2 slot/pole/phase motors is almost controlled entirely by the properties of lamination material. Hence, hysteresis plays an important role in determining the flux waveform. In order to investigate this further, measurements were made on a second 1/2 slot/pole/phase brushless dc motor having its stator lamination stack made from the non-annealed material, which again was characterised in Chapter 3. Since the material is non-annealed, it exhibits more hysteresis. Fig (4.27) compares the measured dc hysteresis loops of Samples of S1 and S3 at a maximum flux density of 1.5 T. It will be seen that sample S1 has a much wider hysteresis loop. As a consequence the measured stator back-iron flux density waveform of the motor with the stator lamination stack of S1 exhibits greater asymmetry, Fig (4.28).

Fig (4.29) compares measured and computed component flux density waveforms in the back of a tooth (search coils E and F), where it will be seen that the resultant flux density exhibits rotational behaviour. Further, due to the non-sinusoidal flux density components, the flux density loci is far from being either purely circular or elliptic.

Finally, Figs (4.30) and (4.31) show a comparison between computed and measured flux waveforms at both sides of a tooth tip (search coils C and D). It will be seen that the flux waveforms in both sides of a tooth tip are essentially identical.

### 4.4.2) On load operation

A load test was carried out on the prototype motor under rated load conditions, viz 2000 rpm, 150 W, 1.9 A rms phase current. Further, and in order to investigate the effect of the commutation strategy on iron losses, the motor was also tested at $20^{o}$advanced and $20^{o}$ retarded commutation, in both cases, the dc link voltage being adjusted and recorded to keep the rms phase current equal to 1.9 A at 2000 rpm. Fig (4.32) shows the measurement rig.

Figs (4.33), (4.34) and (4.35) show a comparison between measured and computed phase winding current waveforms for normal, $20^{o}$ advanced and $20^{o}$ retarded commutation, respectively. Clearly, the commutation strategy has a considerable effect on the phase winding current waveform.

Figs (4.36), (4.37) and (4.38) show a comparison between measured and computed average flux density waveforms in the tooth body under normal, $20^{o}$ advanced, and $20^{o}$ retarded commutation strategies, from which it will be seen that the commutation strategy also affects the flux waveform in the tooth body.

Figs (4.39), (4.40) and (4.41) show comparisons between measured and computed average flux density waveforms in the stator back-iron for normal, $20^{o}$ advanced and $20^{o}$ retarded commutation, where again the effect of the commutation strategy is clearly observed.

Further, Figs (4.42), (4.43) and (4.44) show a comparison between measured and computed flux density waveforms in the back of a tooth, for normal, $20^{o}$ advanced and $20^{o}$ retarded commutation. As with open-circuit operation the flux exhibits pronouced rotational behaviour.

Finally, Figs (4.45) and (4.46) show a comparison between computed and measured flux waveforms at both sides of a tooth tip under normal commutation, whilst Figs (4.47) and (4.48) show a comparison for $20^{o}$ advanced commutation, and Figs (4.49) and (4.50) show a comparison for $20^{o}$ retarded commutation. It will be seen that under a load condition, and no matter what the commutation strategy, the flux waveforms are not similar. An asymmetry with respect to the tooth axis always exists, and is caused by armature reaction. Fig (4.51) shows flux plots for different instants on open-circuit and on load operations.

### 4.4.3) Typical post-processor outputs

Fig (4.52) shows the finite element mesh which was used for the above calculations, whilst Fig (4.53) shows flux density waveforms and loci at selected sites in the stator core for open-circuit operation. Figs (4.54), (4.55) and (4.56) show corresponding flux density waveforms and locis at the same sites for rated load, for normal, $20^{o}$ advanced and $20^{o}$ retarded commutation respectively.

### 4.4.4) Discussion

In this section, it has been shown that the flux density waveforms in the stator core of a brushless dc motor are affected markedly by the load condition and the commutation strategy. Hence, it can be assumed that the iron loss will vary with load and commutation strategy. Numerical calculations indicate that this is the case as shown in the next chapter. It has also been shown that a more sophisticated analysis, which couples a drive system simulation to magnetostatic finite element analyses, enables the local flux density waveforms throughout a stator core to be predicted under any load conditon, and hence the iron loss and its variation with load can also be calculated.

## 4.5) Conclusions

In radial-field permanent magnet excited machines curvature can have a considerable effect on the calculation of the magnetic loading in the airgap. It has been shown that when the magnets are mounted adjacent to the airgap on an inner rotor an optimal magnet thickness exists for which the magnetic loading is a maximum, as has been confirmed by both finite element analysis and experiment. Further, and despite being very simple, an idealised analytical model can give very good results for the prediction of both the magnetic loading in the airgap and the spread of magnet working points.

A simple analytical technique for predicting flux density waveforms in the stator core of brushless dc motors on open-circuit operation has been presented, and confirmed by both finite element analysis and experiment. In addition, it has been shown that hysteresis in electrical steel laminations can affect the flux density waveforms in the stator back-iron.

The flux density waveforms throughout a stator core are affected significantly by the operating condition of the drive, ie the load and the commutation strategy. It has been shown that the flux density waveforms can be predicted under any operating condition by coupling a drive system simulation to magnetostatic finite element analyses. Further, the resultant field, ie comprising armature reaction and permanent magnet field components, distribution is unsymmetric about a tooth axis, as has been shown by predictions and experiments.

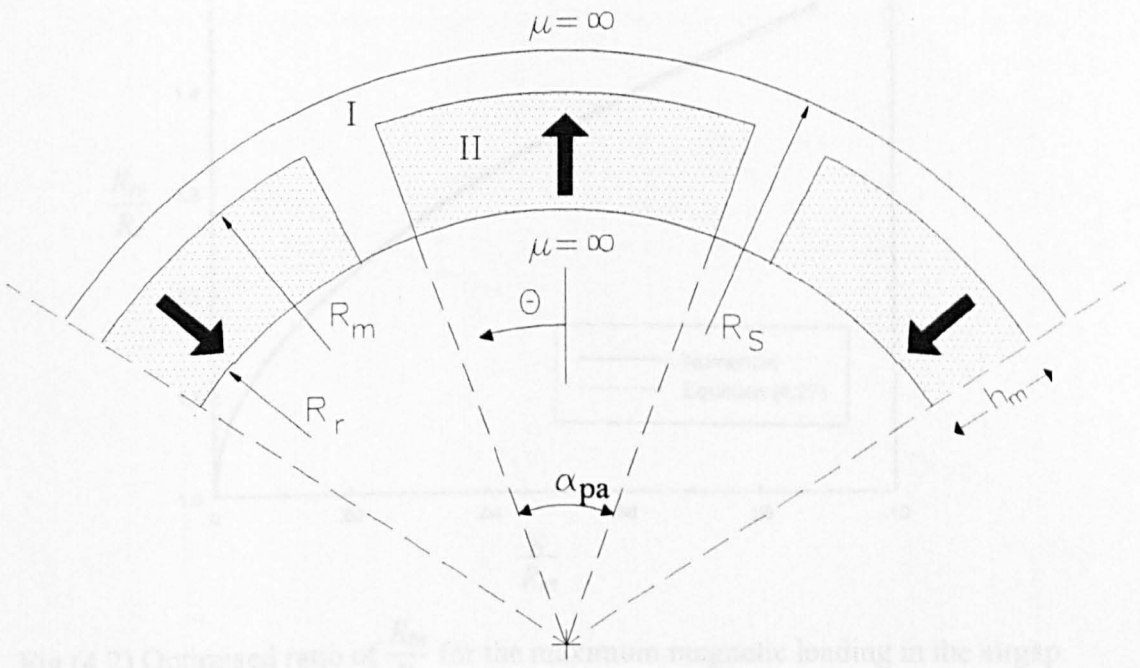


(a)

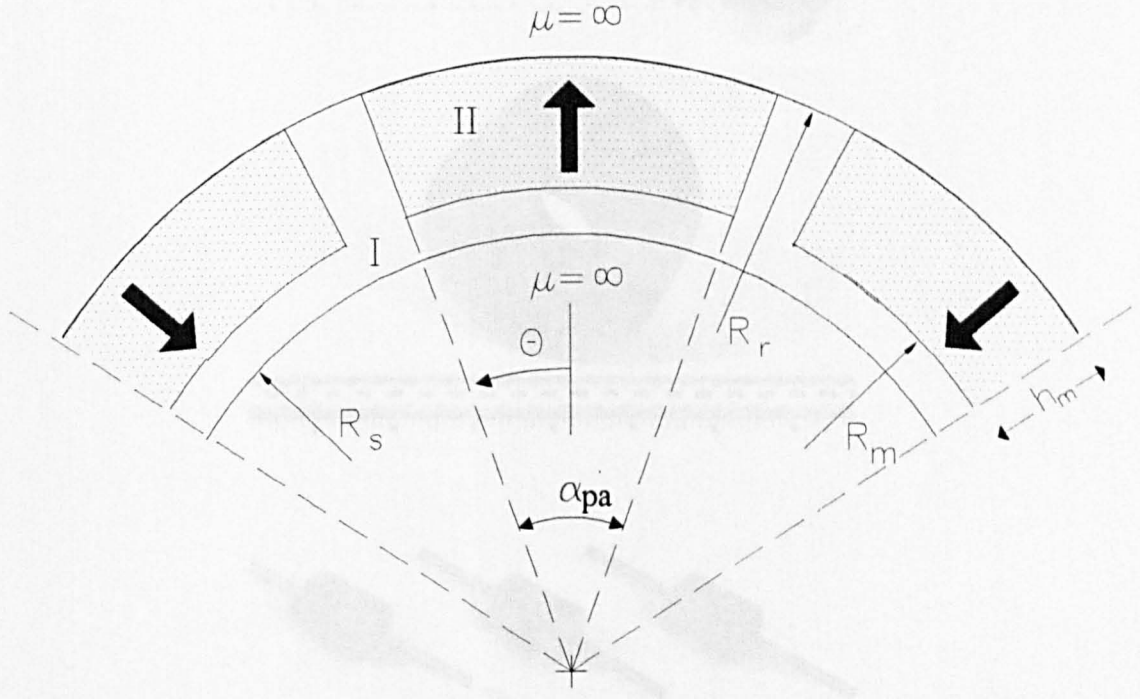


(b)

Fig (4.1) Alternative machine topologies.

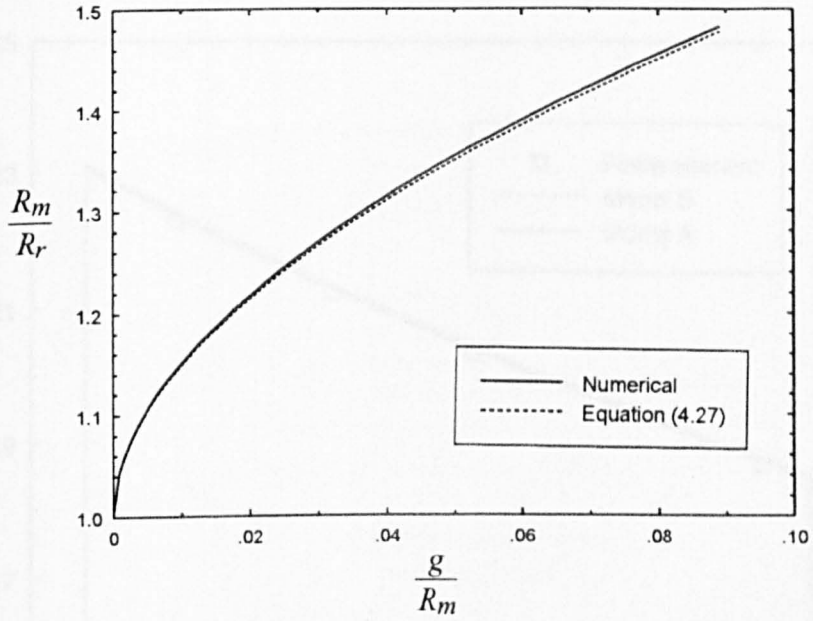


Fig (4.2) Optimised ratio of $\frac{R_m}{R_r}$ for the maximum magnetic loading in the airgap.

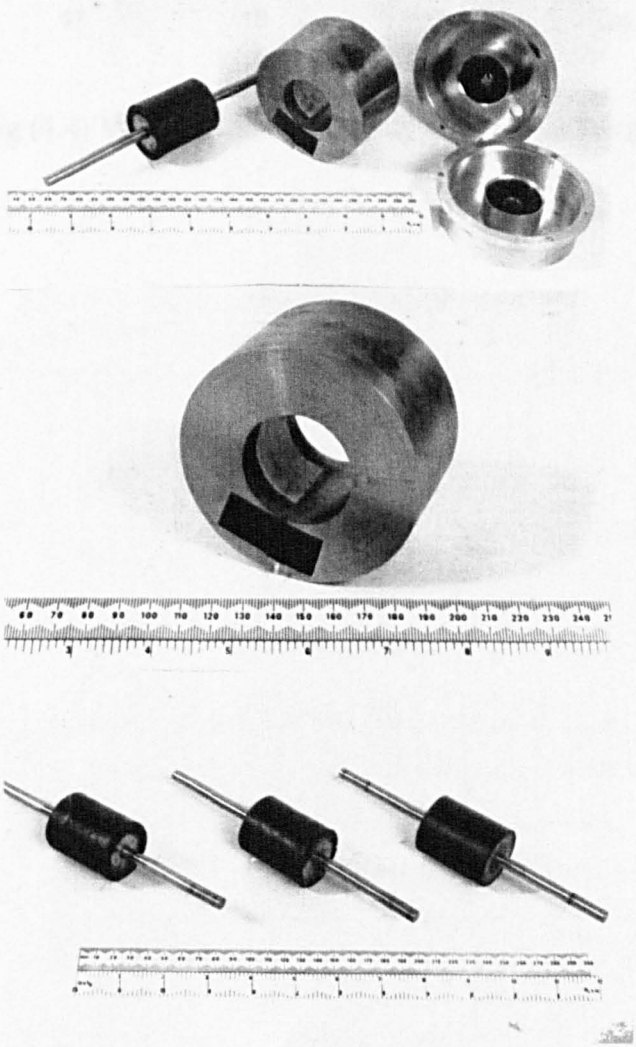

Fig (4.3) Prototype machines.

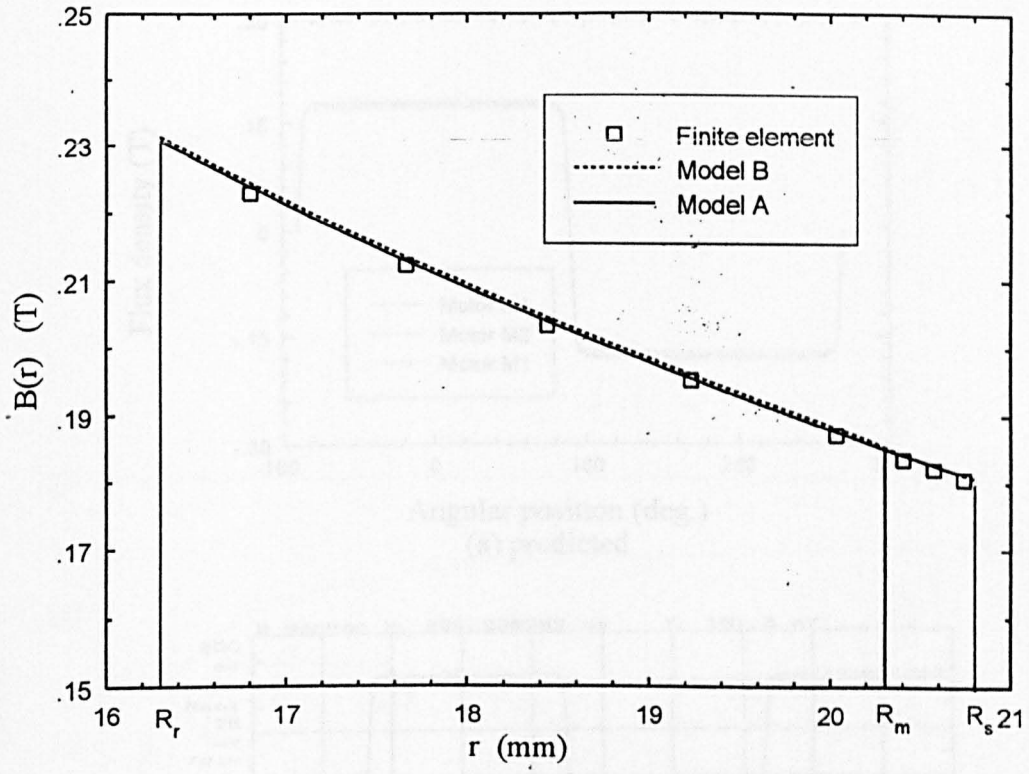


Fig (4.4) Variation of flux density with radius for motor M2.

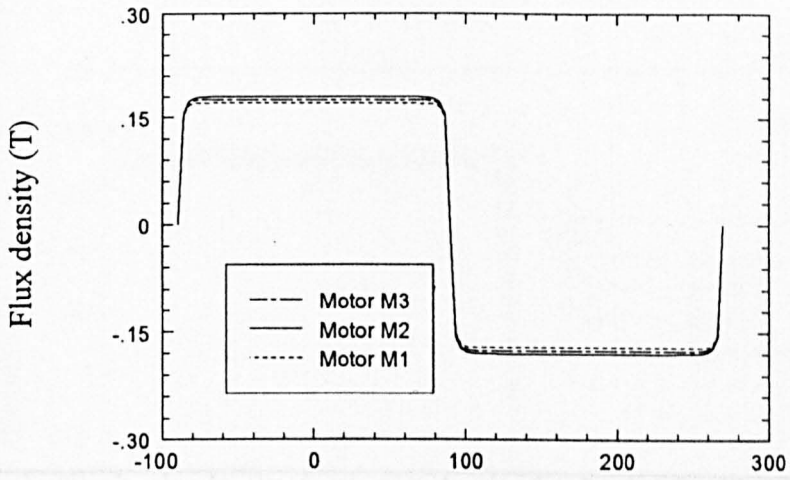


(a) predicted

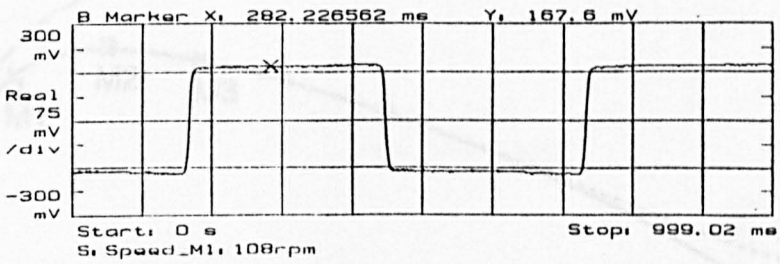


Motor M1

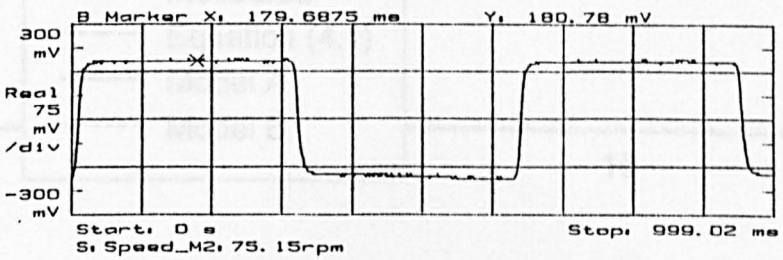


Motor M2

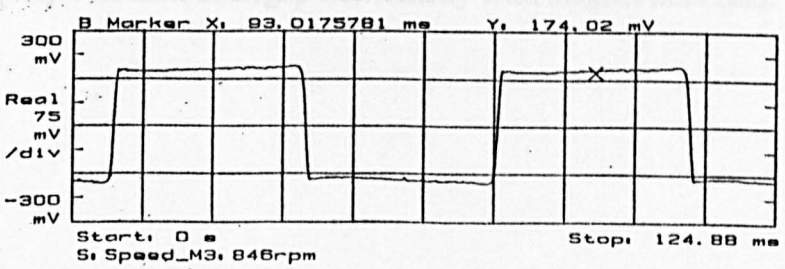


Motor M3

(b) measured (1V/T)

Fig (4.5) Comparison of flux density distributions.

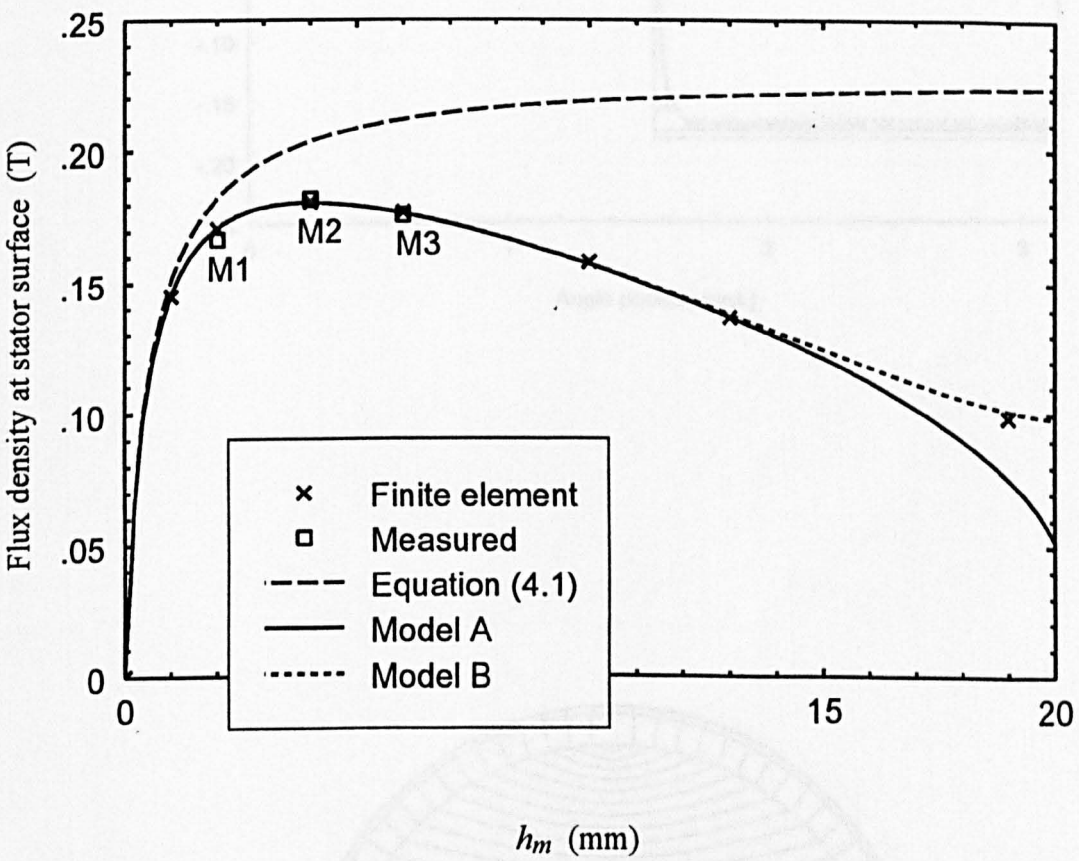


Fig (4.6) Variation of airgap flux density with magnet thickness.

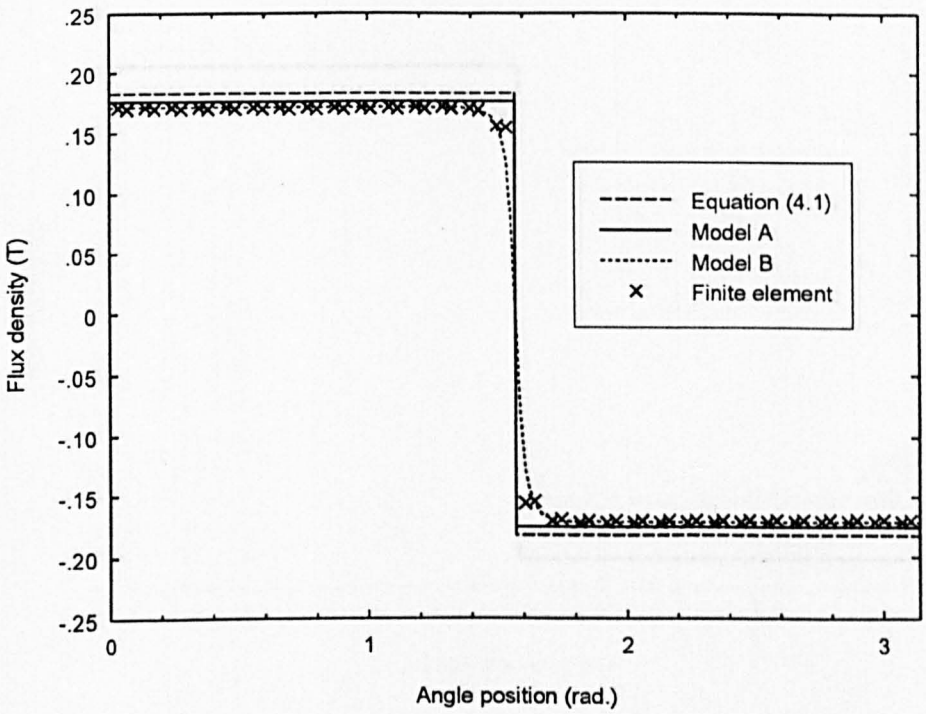
.25
.20
.15
.10
.05
0
-.05
-.10
-.15
-.20
-.25
Flux density (T)
0
1
2
3
Angle position (rad.)
Equation (4.1)
Model A
Model B
Finite element

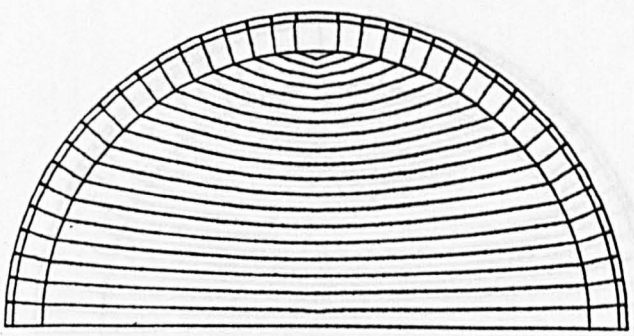

(a) $h_m = 2\ mm$

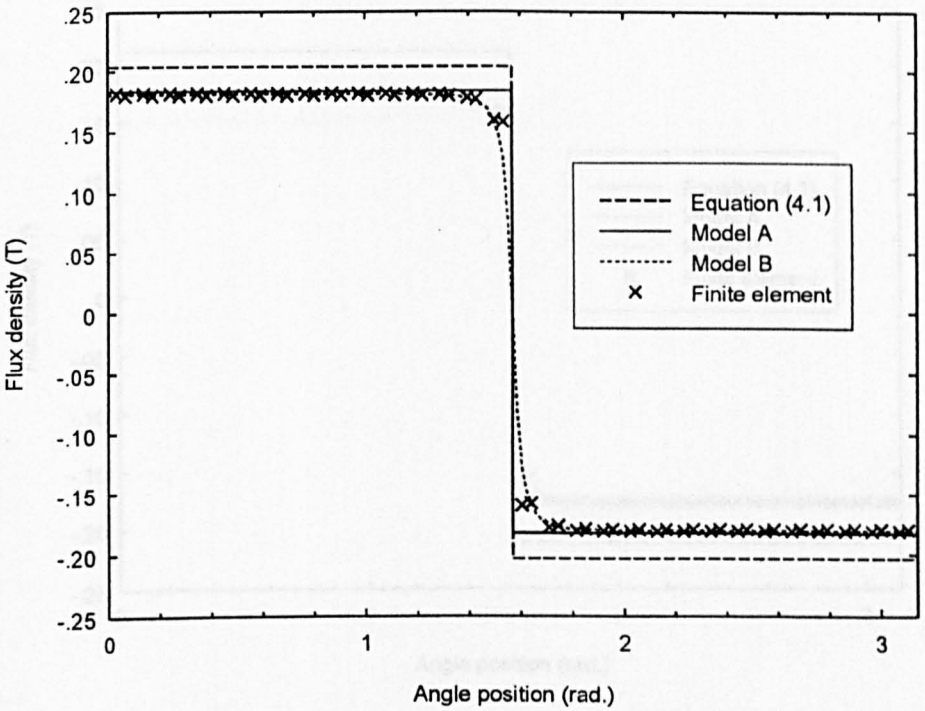
.25
.20
.15
.10
.05
0
-.05
-.10
-.15
-.20
-.25
0
1
2
3
Flux density (T)
Angle position (rad.)
Equation (4.1)
Model A
Model B
Finite element

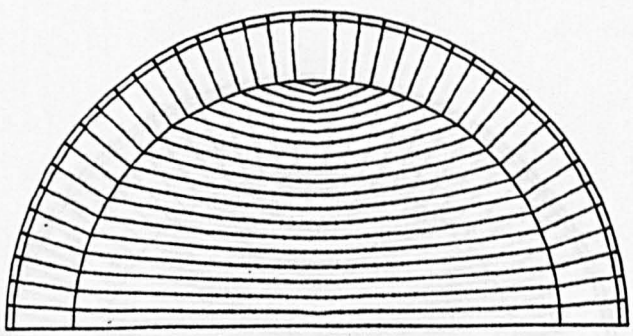

(b) $h_m = 4\ mm$

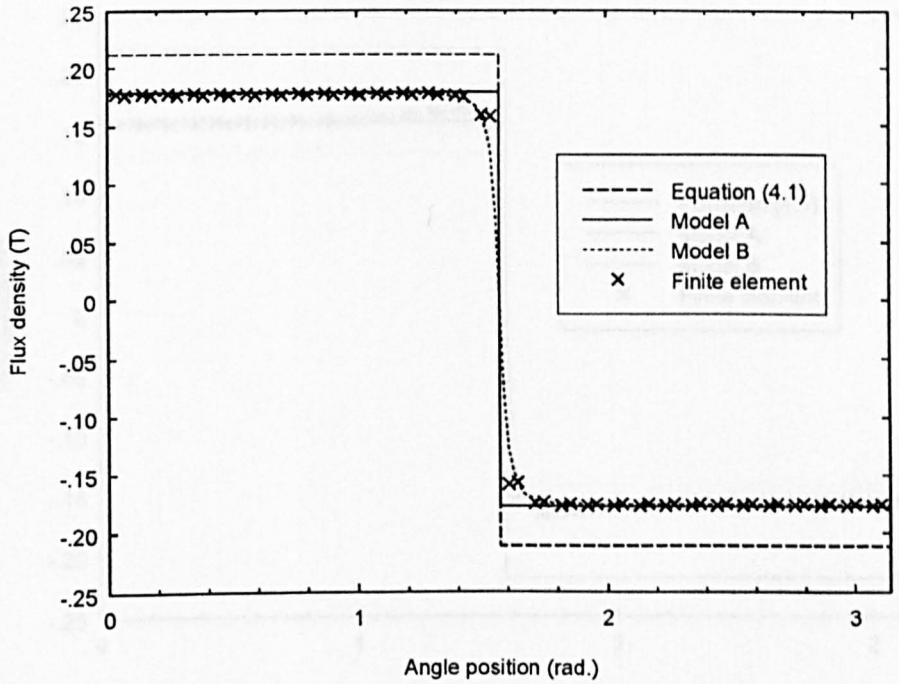
.25
.20
.15
.10
.05
0
-.05
-.10
-.15
-.20
-.25
Flux density (T)
0
1
2
3
Angle position (rad.)
Equation (4.1)
Model A
Model B
Finite element

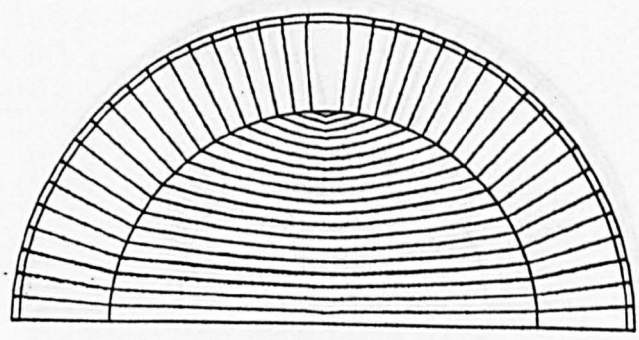

(c) $h_m = 6\ mm$

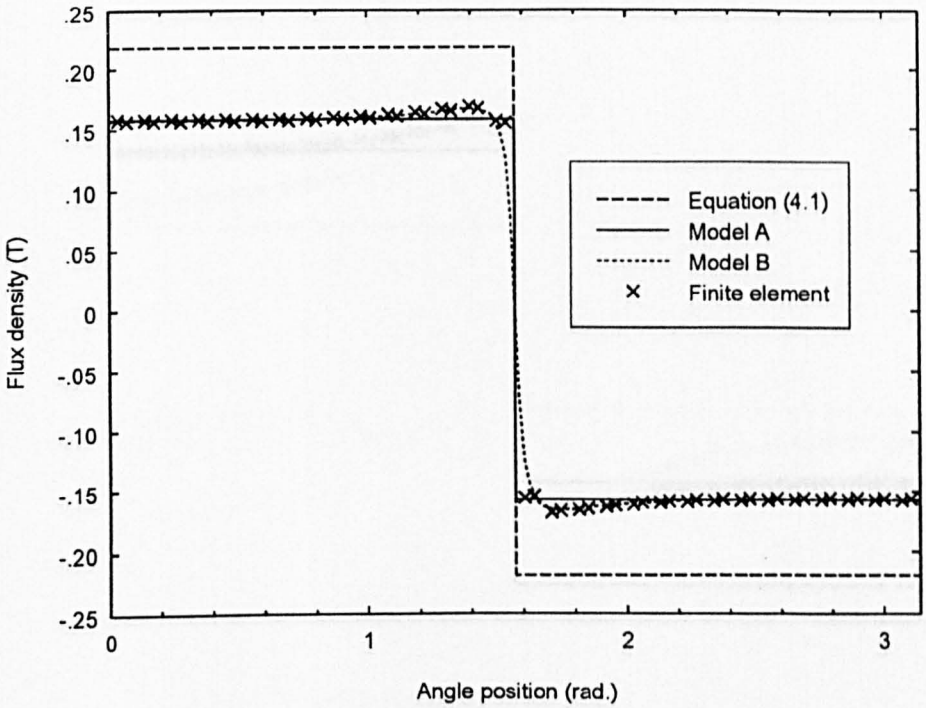
.25
.20
.15
.10
.05
0
-.05
-.10
-.15
-.20
-.25
0
1
2
3
Flux density (T)
Angle position (rad.)
Equation (4.1)
Model A
Model B
Finite element

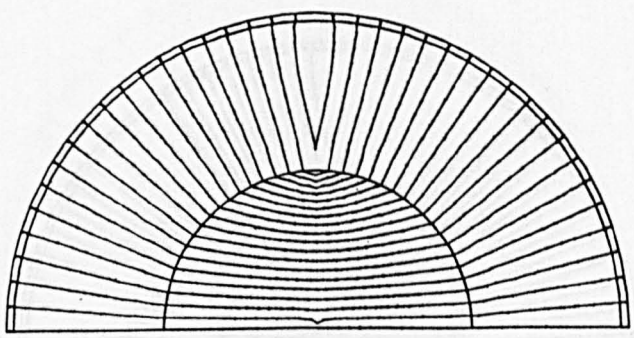

(d) $h_m = 10\ mm$

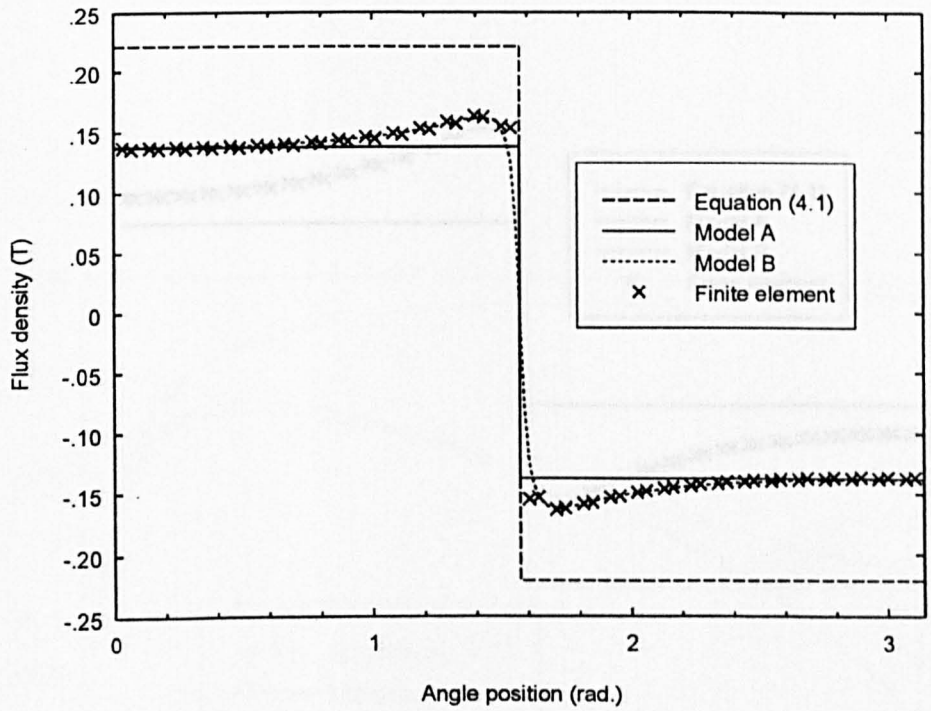
.25
.20
.15
.10
.05
0
-.05
-.10
-.15
-.20
-.25
Flux density (T)
0
1
2
3
Angle position (rad.)
Equation (4.1)
Model A
Model B
Finite element

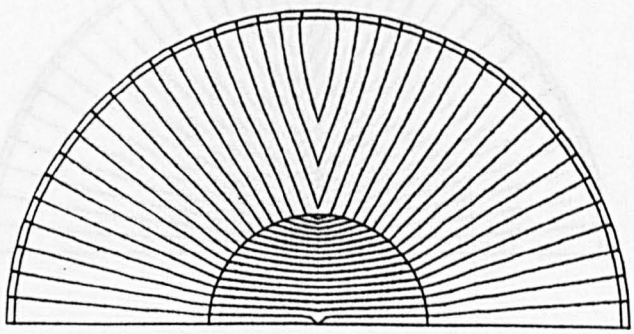

(e) $h_m = 13\ mm$

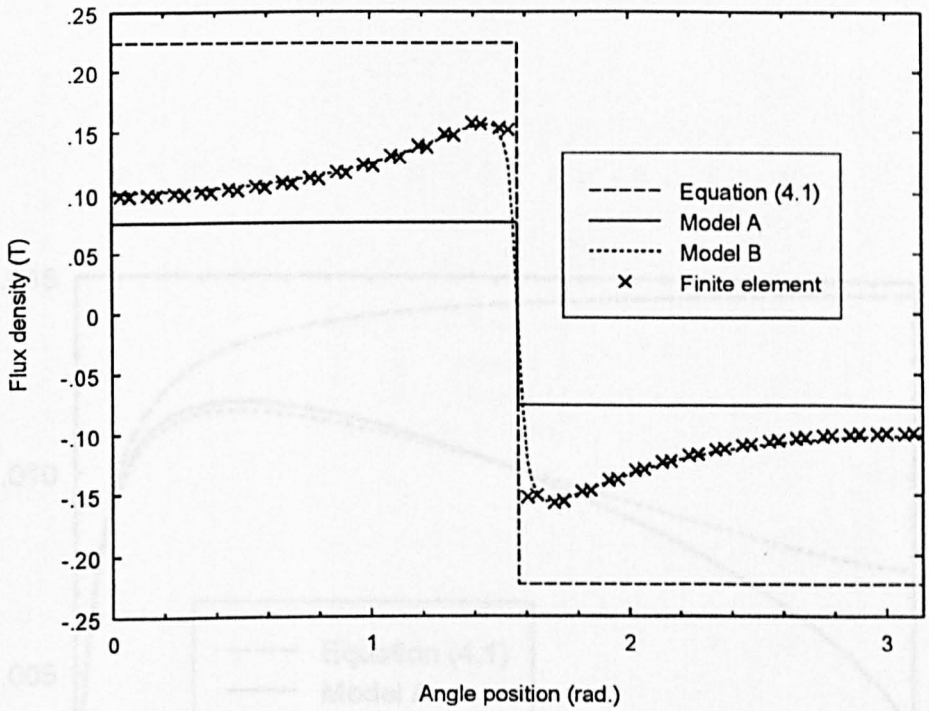


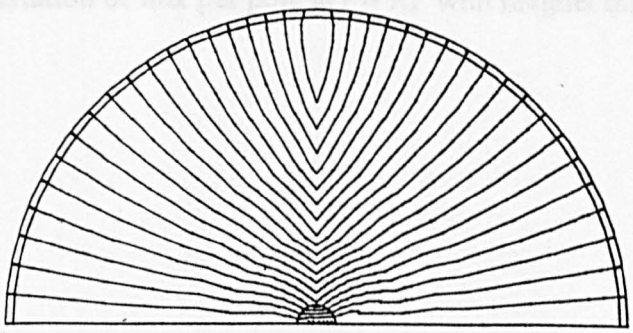

(f) $h_m = 19\ mm$

Fig (4.7) Flux density distributions at the stator surface and corresponding potential plots for different magnet thicknesses.

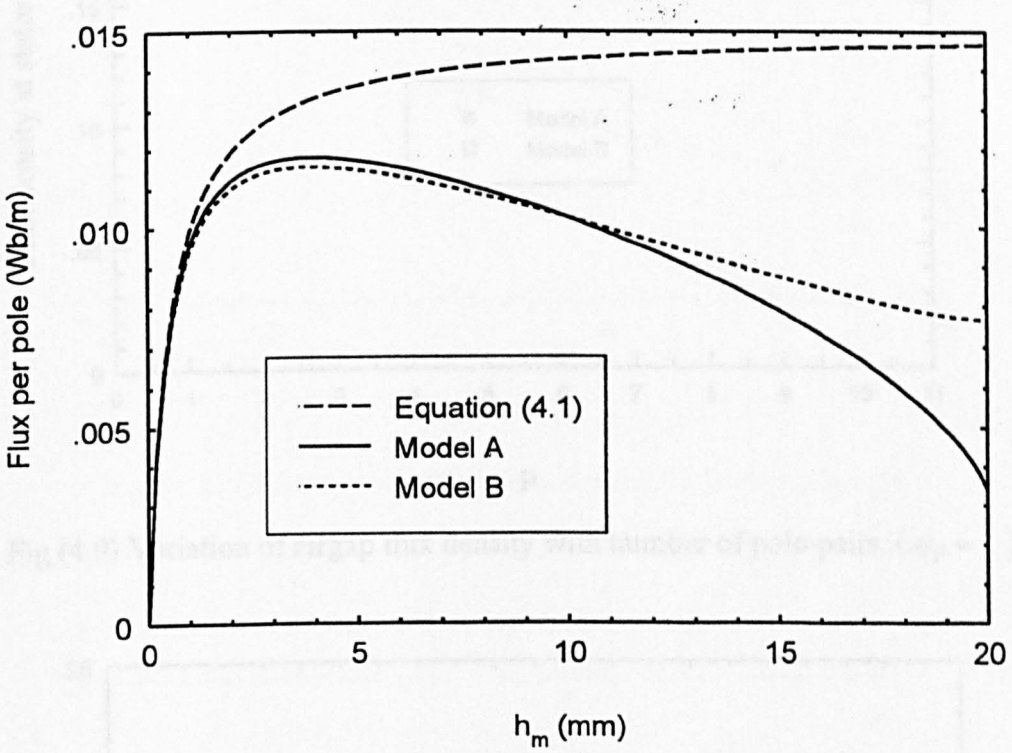


Fig (4.8) Variation of flux per pole at $r = R_s$ with magnet thickness.

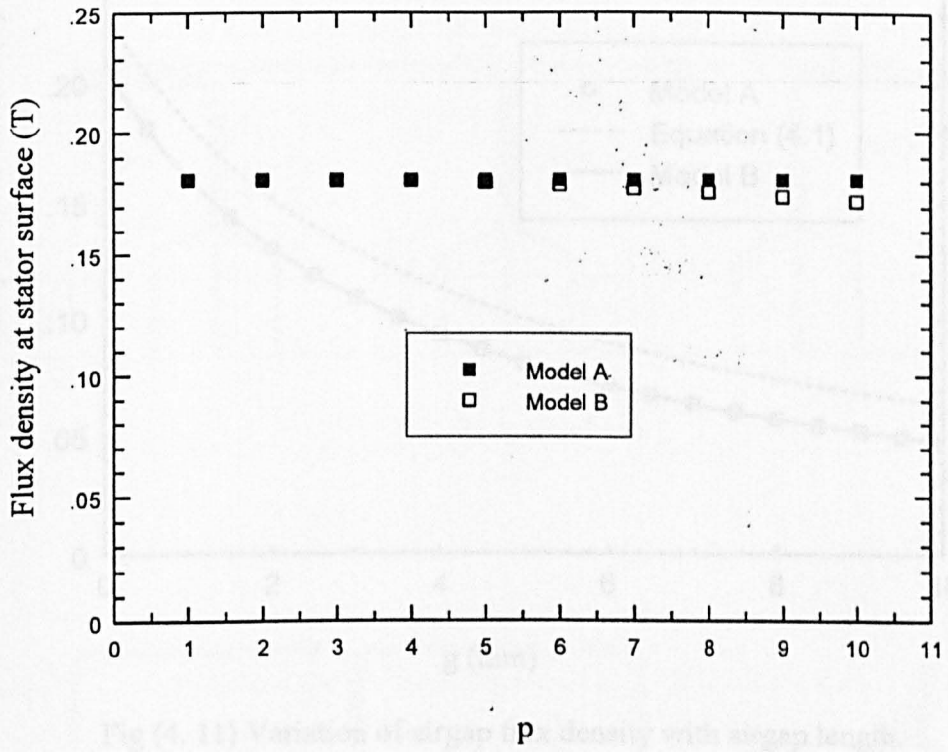


Fig (4.9) Variation of airgap flux density with number of pole-pairs. ( $\alpha_p = 1$ )

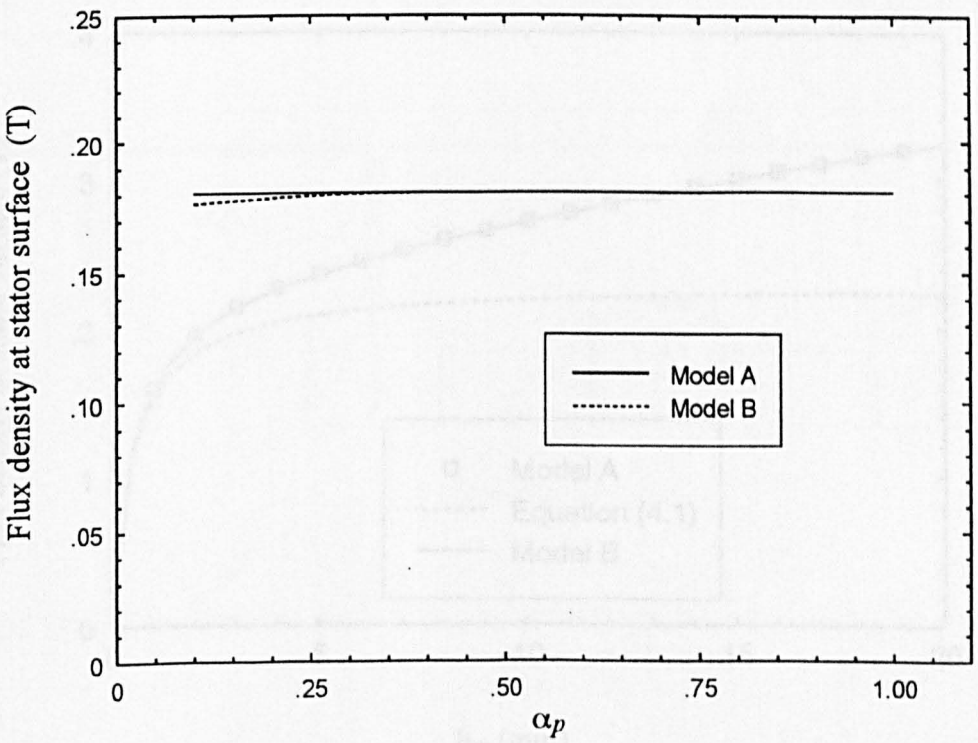


Fig (4.10) Variation of airgap flux density with pole-arc to pole-pitch ratio. ( $p = 1$ )

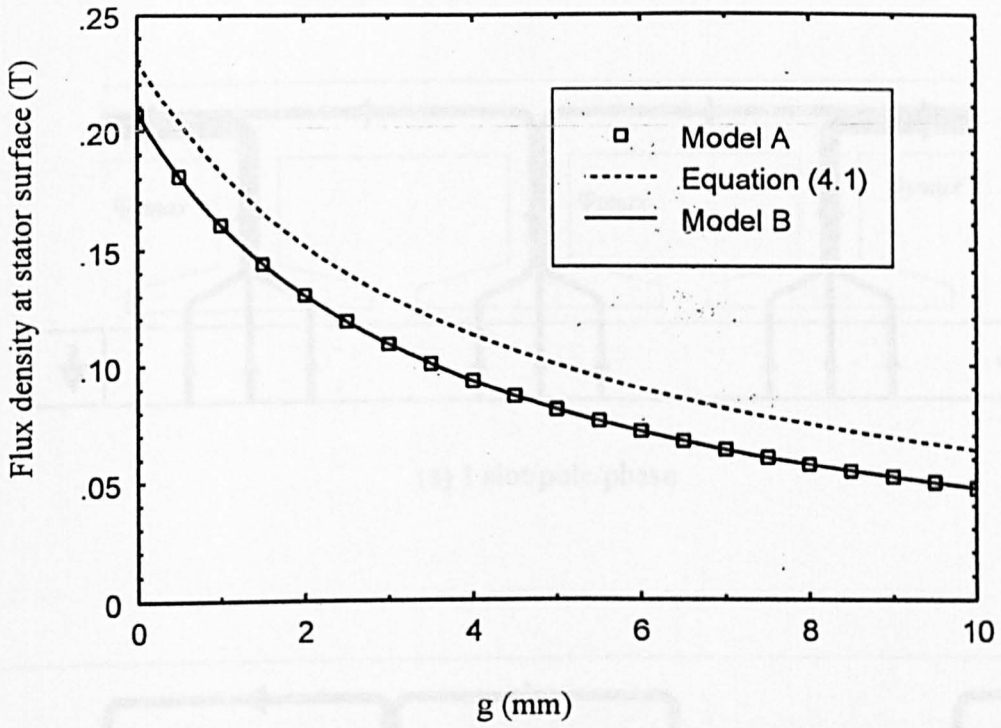


Fig (4. 11) Variation of airgap flux density with airgap length.

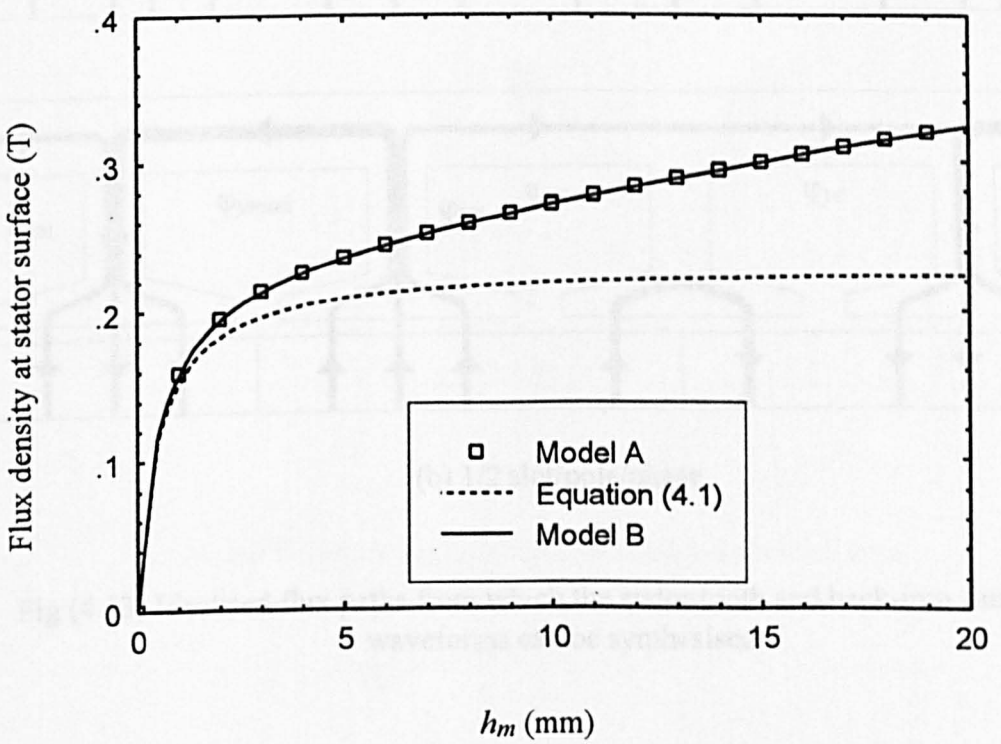


Fig (4.12) Variation of airgap flux density with magnet thickness for machine topology of Fig 1(b). ( $\alpha_p = 1$ , $p = 1$ )

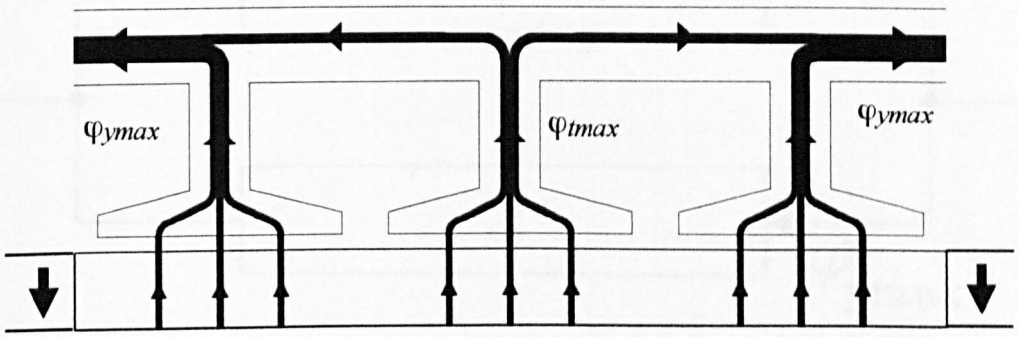


(a) 1 slot/pole/phase

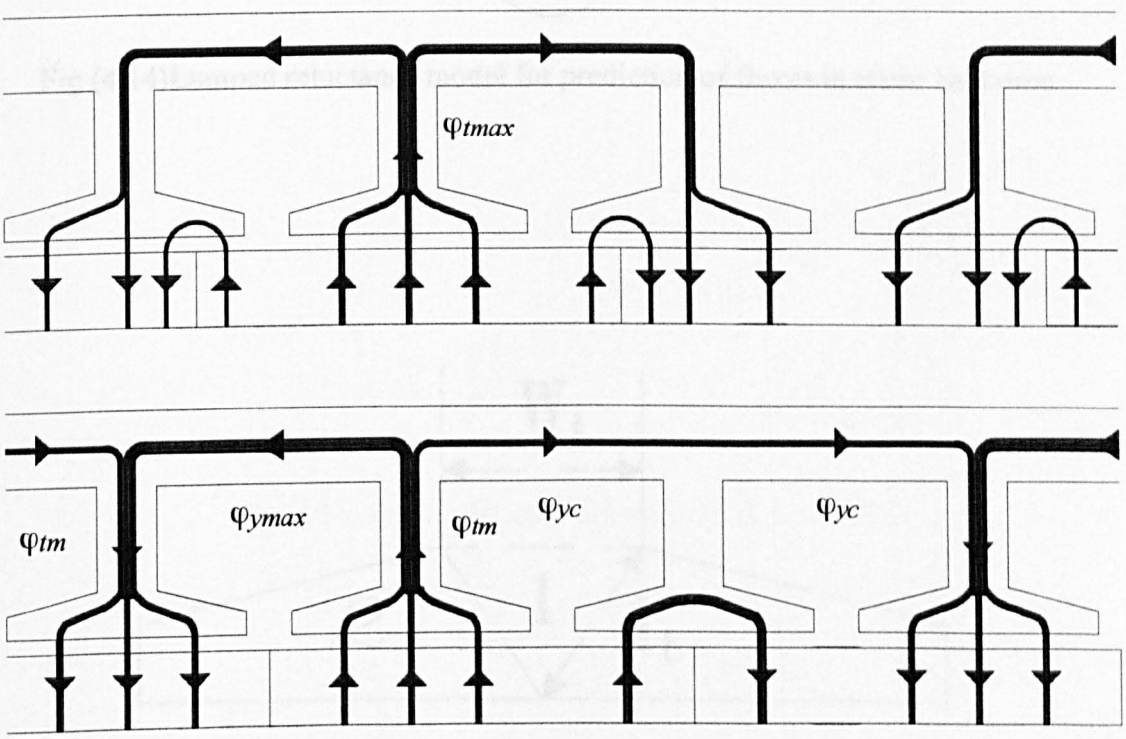


(b) 1/2 slot/pole/phase

Fig (4.13) Idealised flux paths from which the stator tooth and back-iron flux density waveforms can be synthesised.

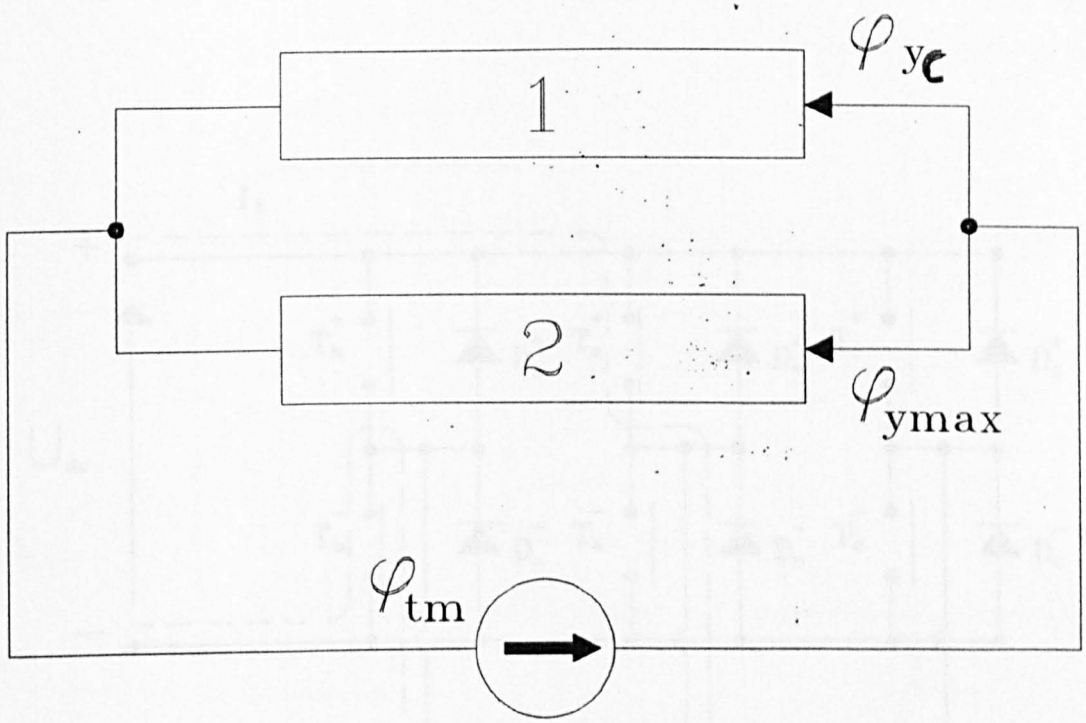


Fig (4.14)Lumped reluctance model for prediction of fluxes in stator back-iron.

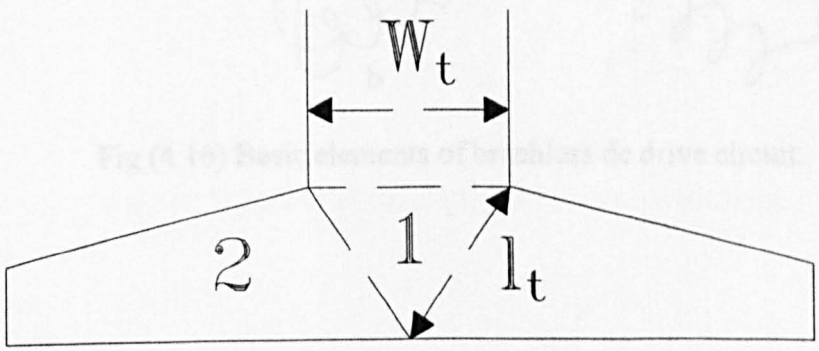


Fig (4.15) Different regions and cross-sections in the tooth-tip.

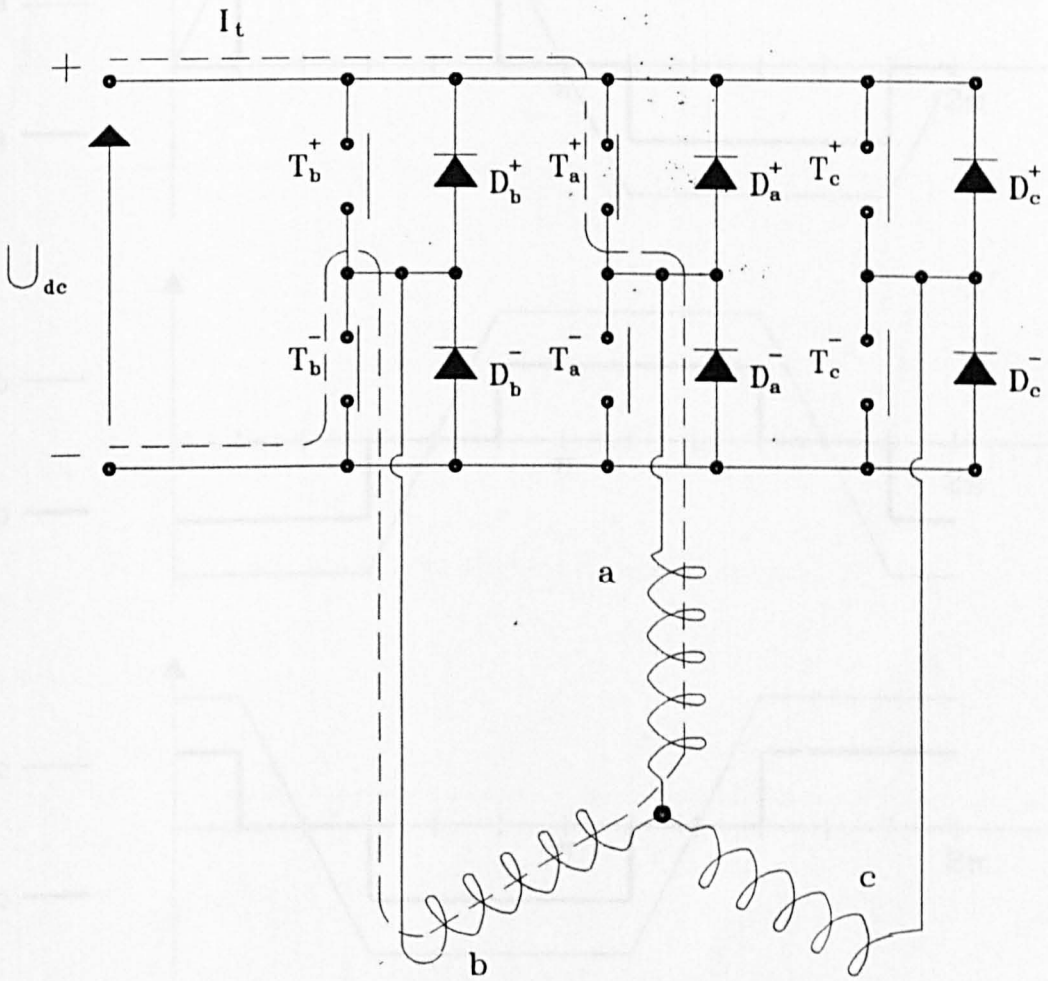


Fig (4.16) Basic elements of brushless dc drive circuit.

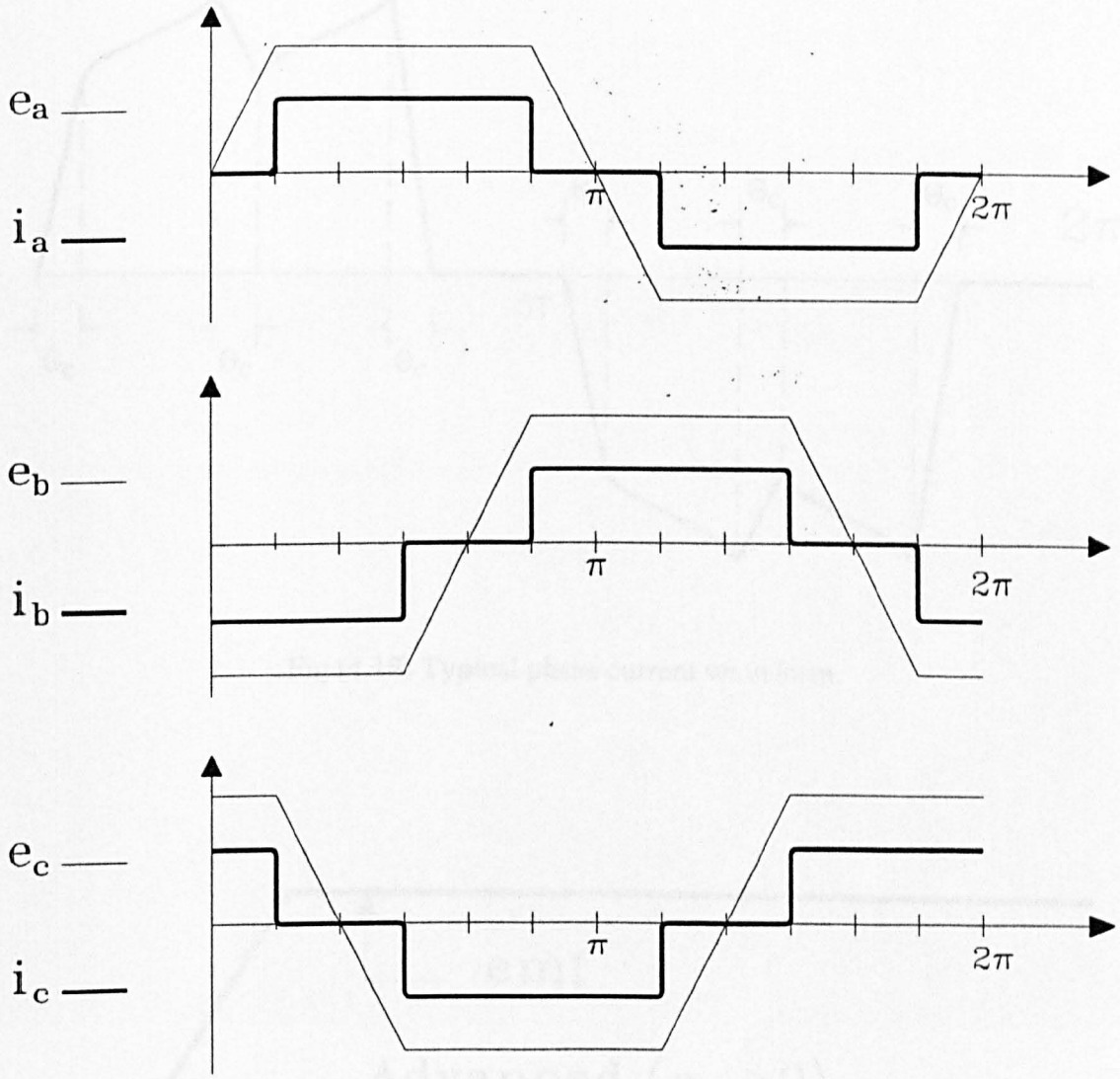


Fig (4.17) Idealised back-emf and current waveforms.

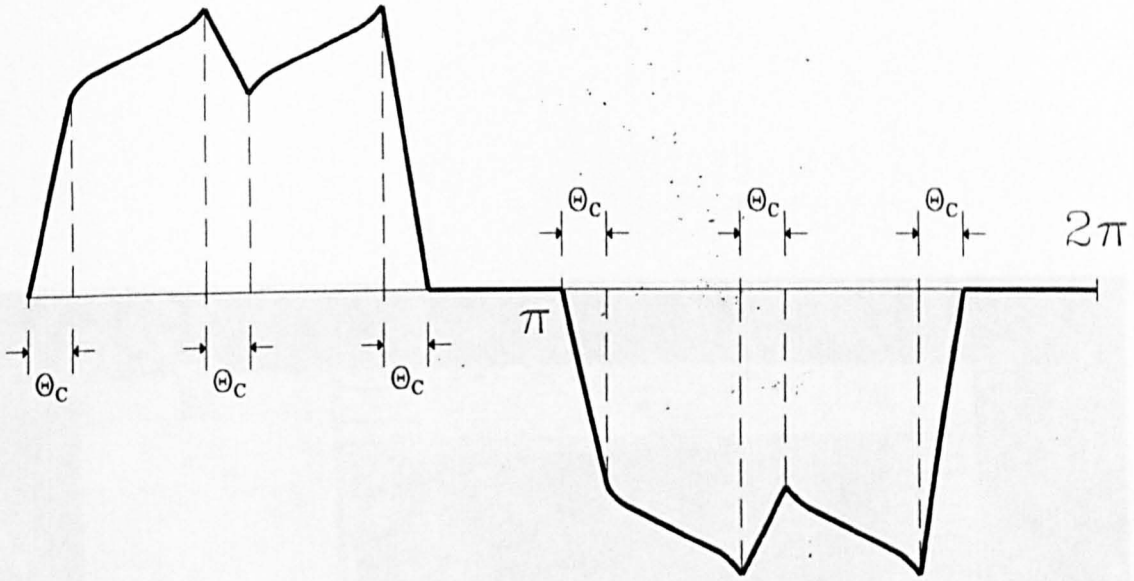


Fig (4.18) Typical phase current waveform.

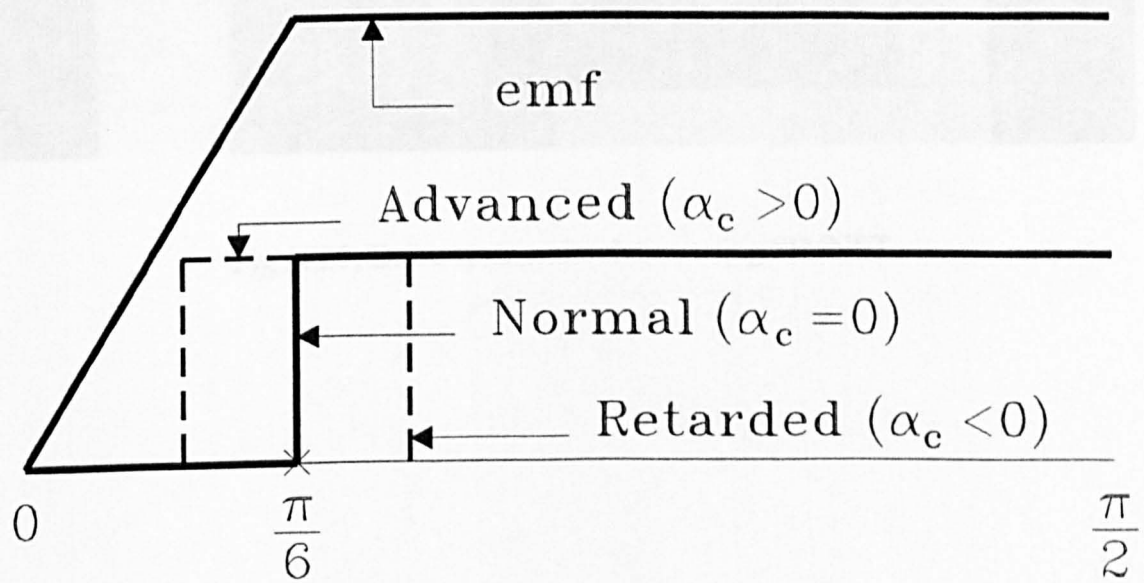


Fig (4.19) Definition of commutation angle.

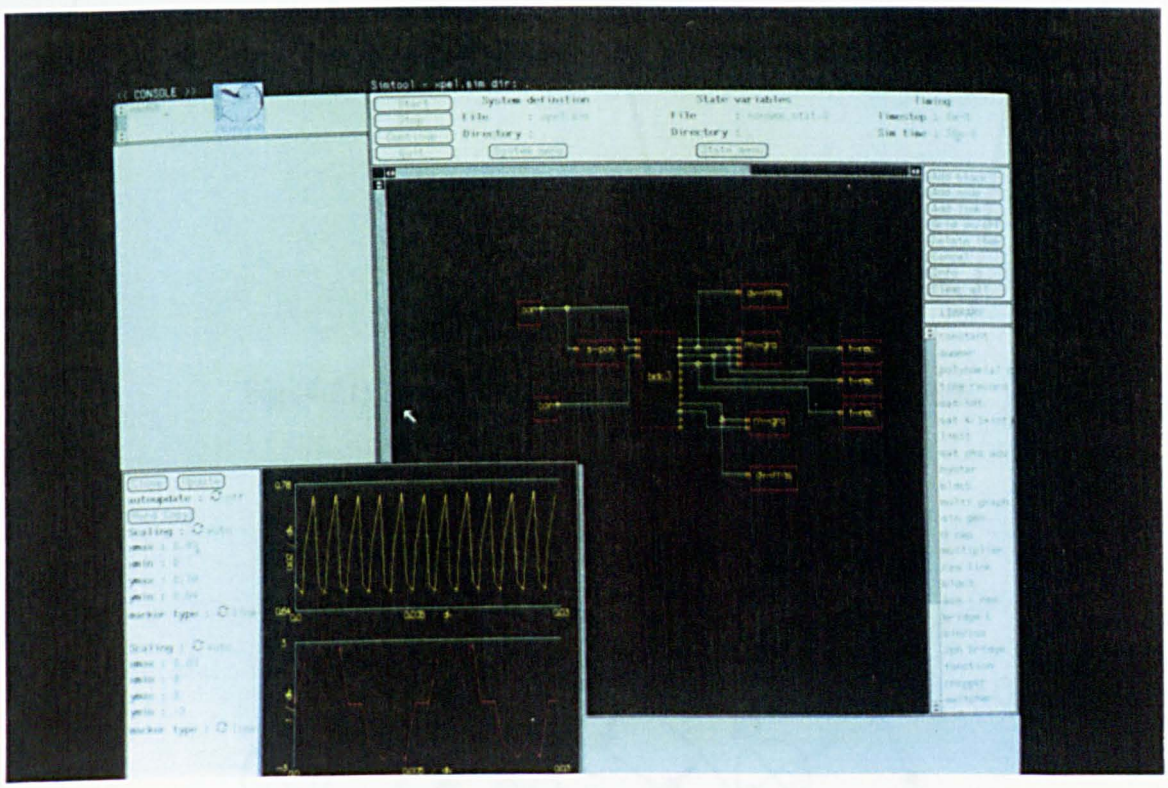

Fig (4.20) Drive system simulation using SIMNET.

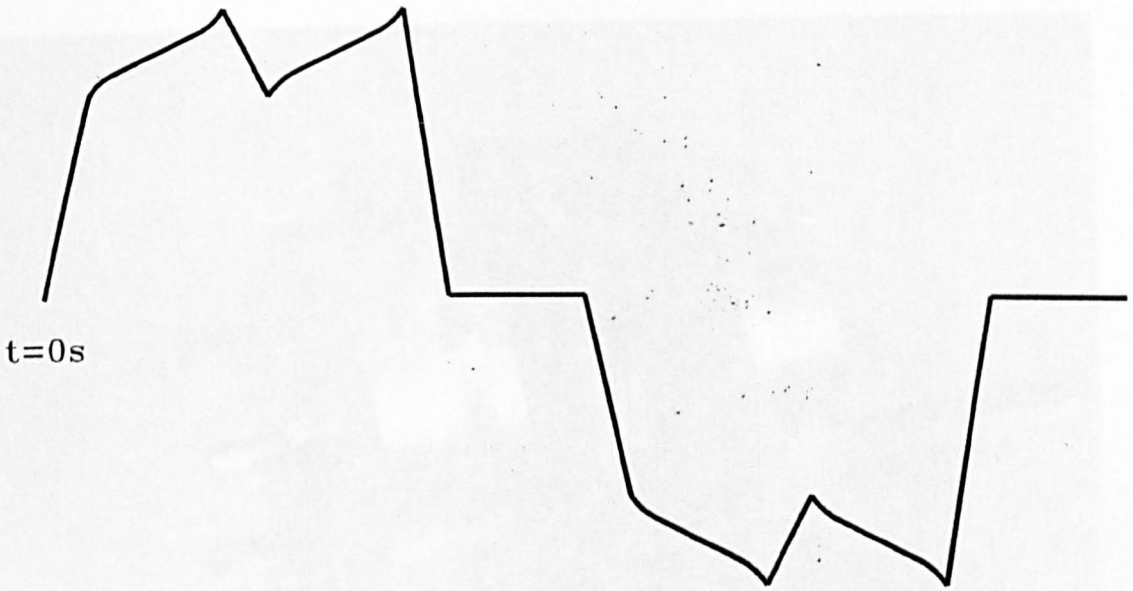


Fig (4.21) Definition of initial time for current waveform.

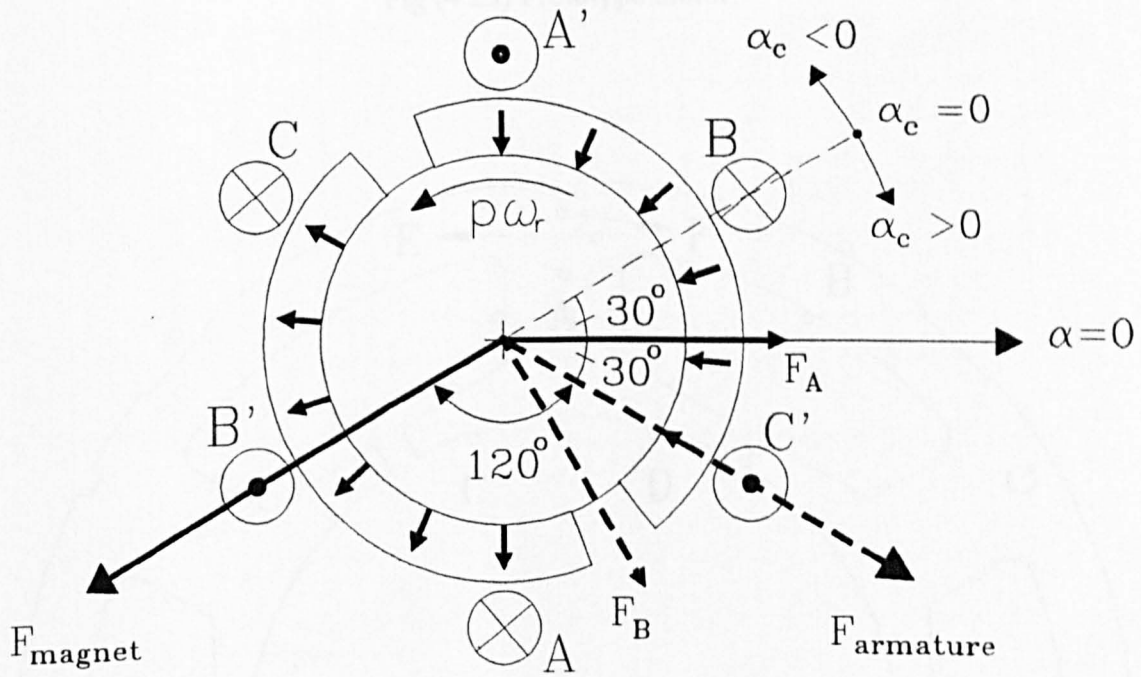


Fig (4.22) Initial rotor position.

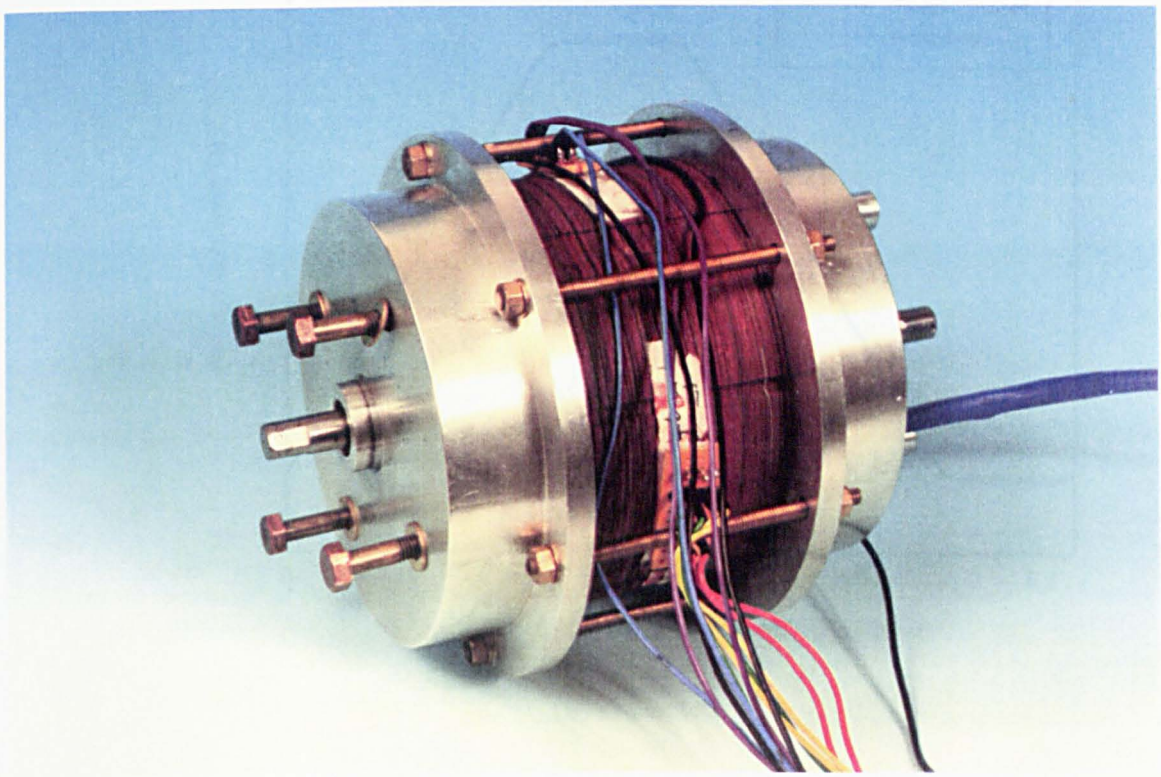

Fig (4.23) Prototype motor.

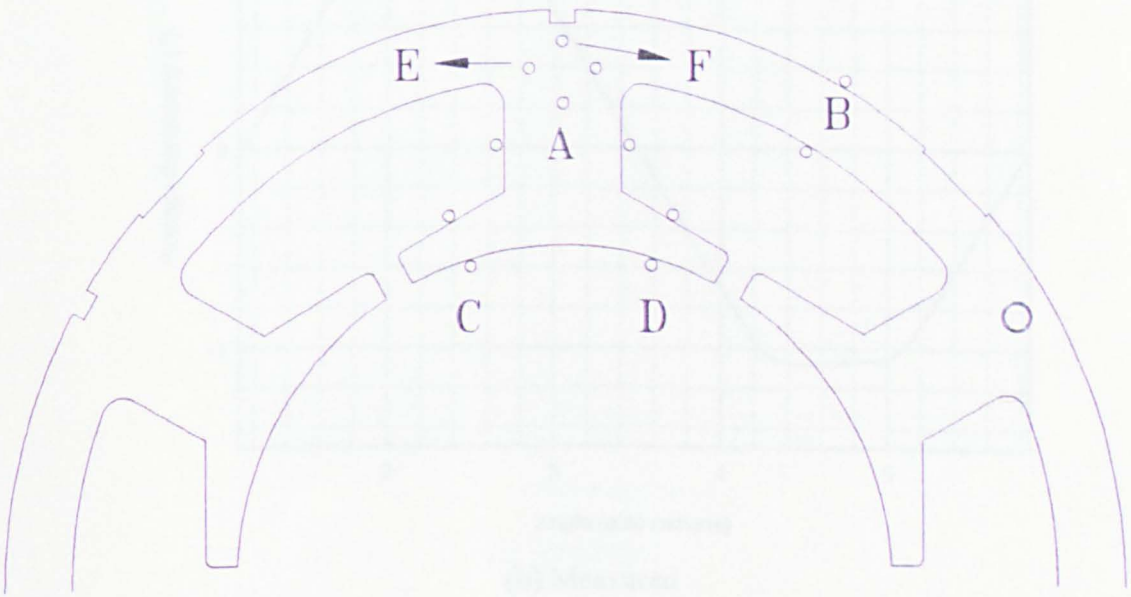


Fig (4.24) Positions of the search coils.

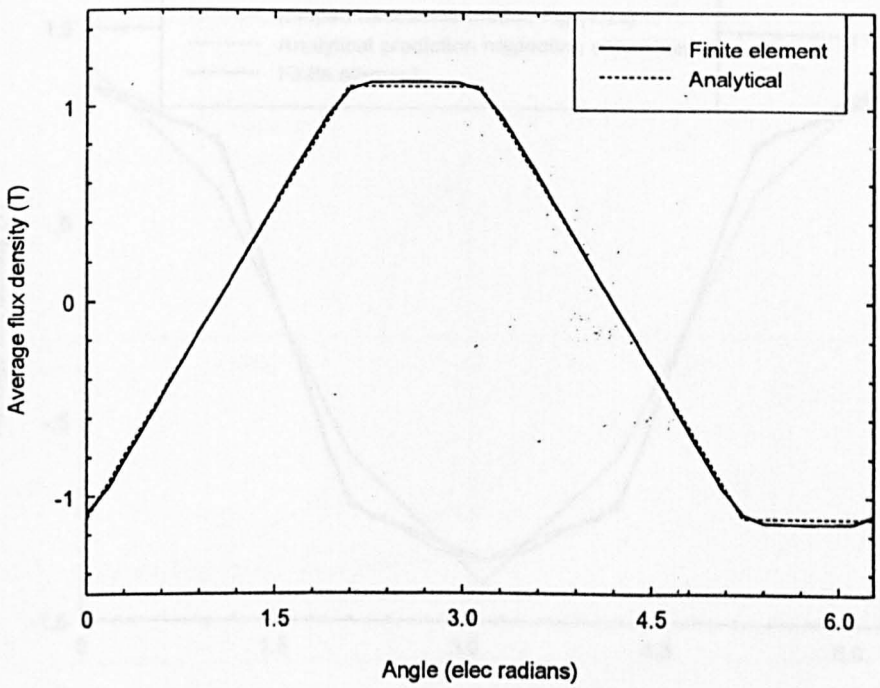


(a) Predicted

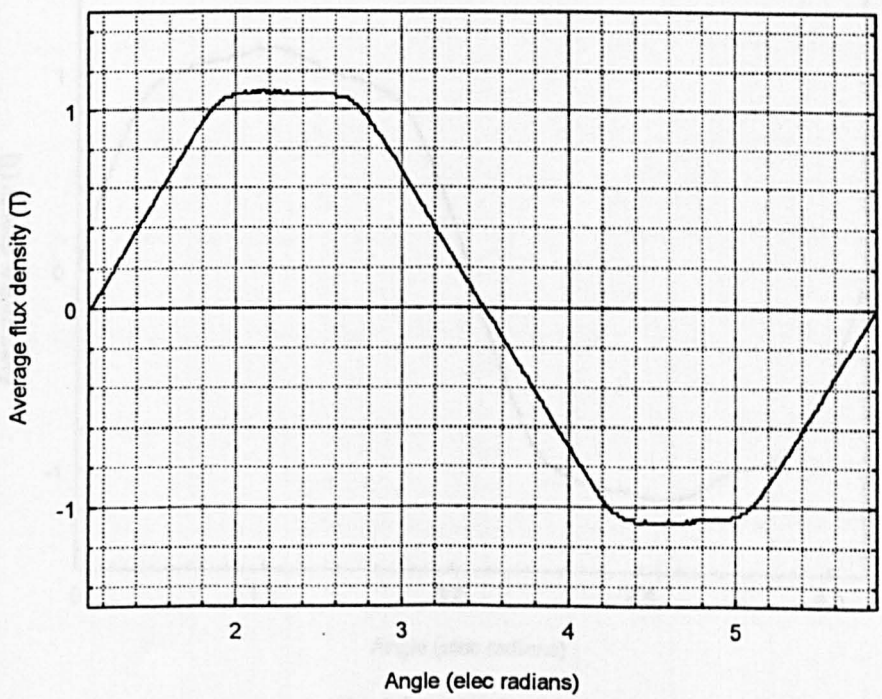


(b) Measured

Fig (4.25) Flux density waveform in the tooth body on open-circuit operation.

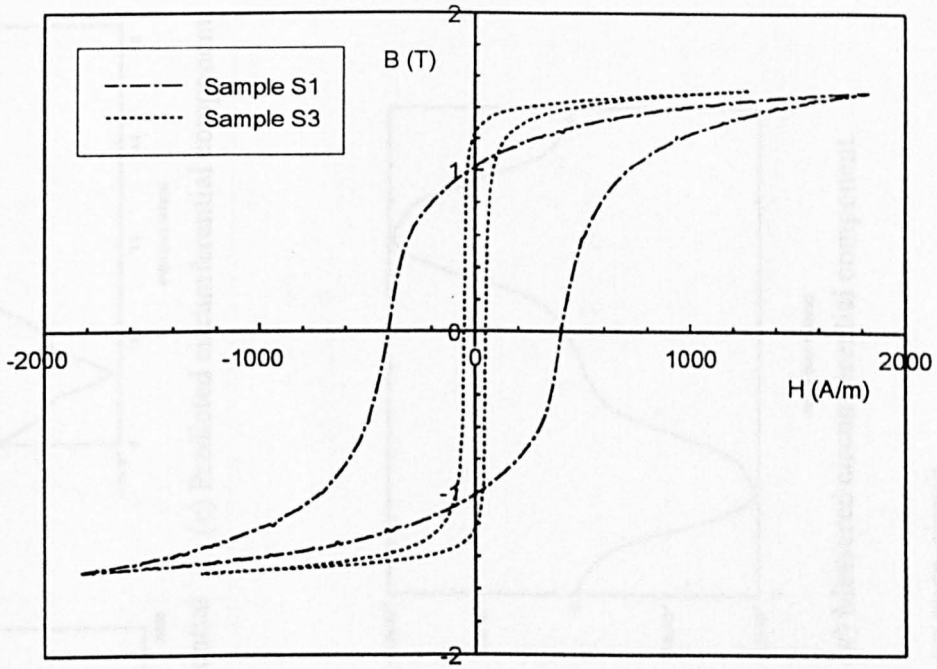


Fig (4.27) Measured dc hysteresis loops for samples S1 and S3. ( $B_{max} = 1.5\ T$ )

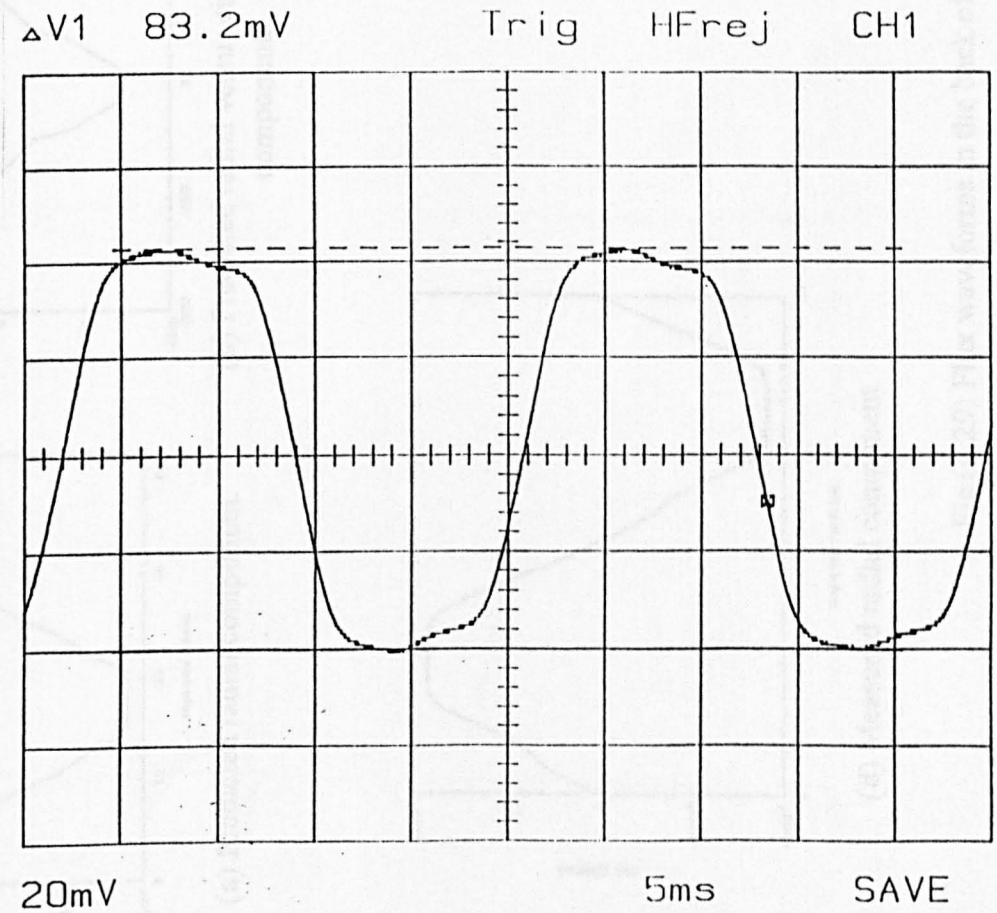


Fig (4.28) Measured flux density waveform in the stator back-iron of the second motor.

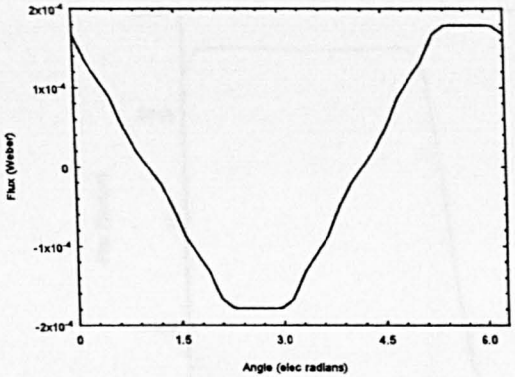


(a) Predicted radial component.

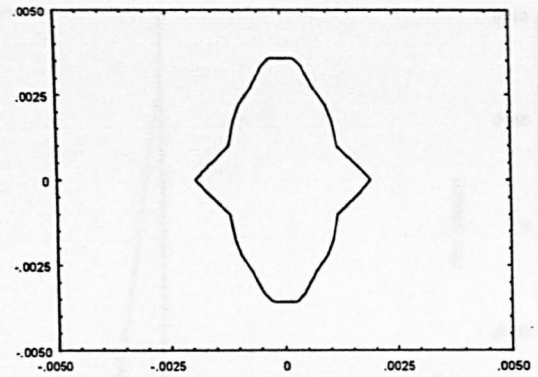


(b) Predicted radial versus circumferential components.

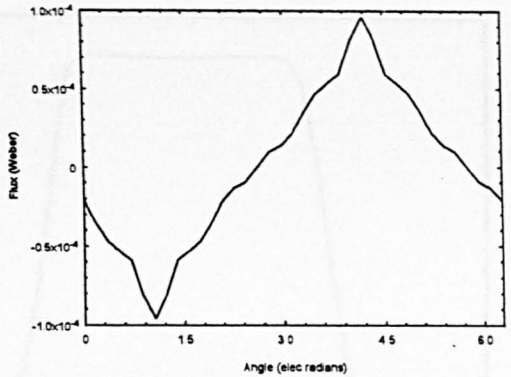


(c) Predicted circumferential component.

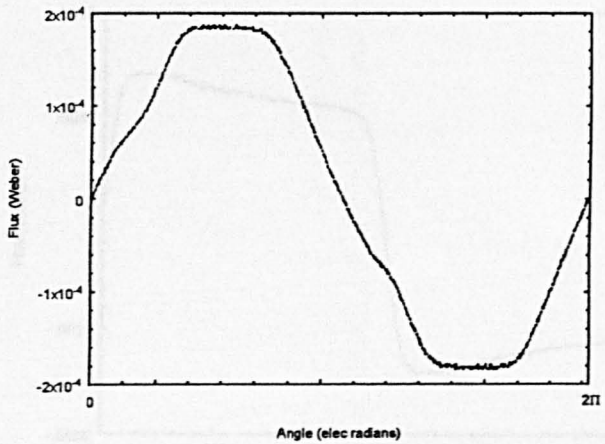


(d) Measured radial component.

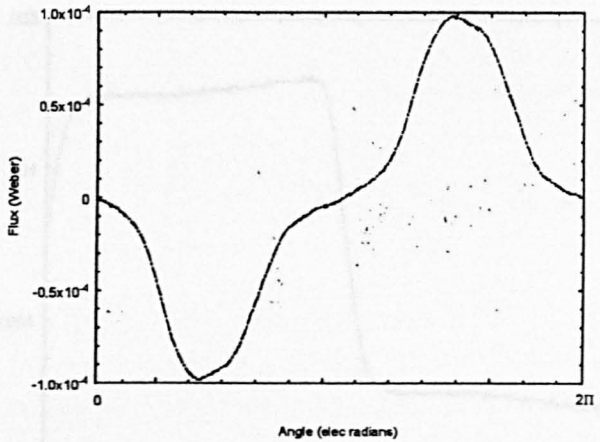


(e) Measured circumferential component.

Fig (4.29) Flux waveforms in the back of a tooth on open-circuit.

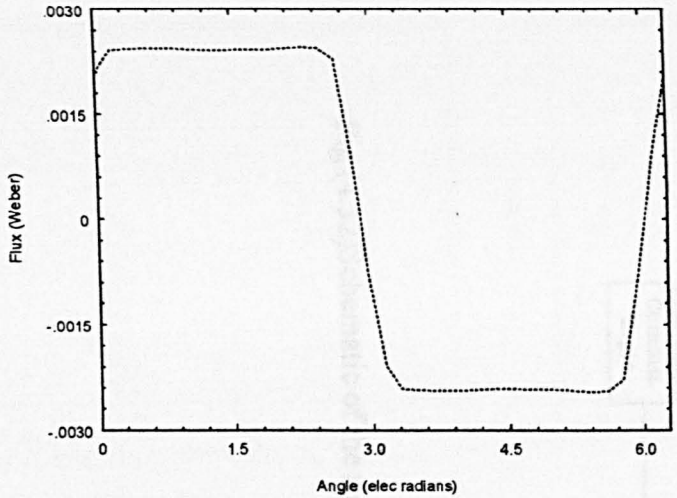


(a) Predicted .

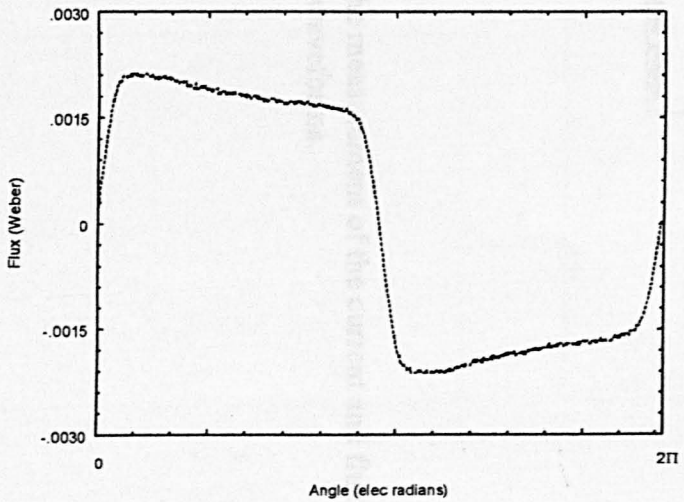


(b) Measured.

Fig (4.30) Flux waveforms in tooth tip C on open-circuit.

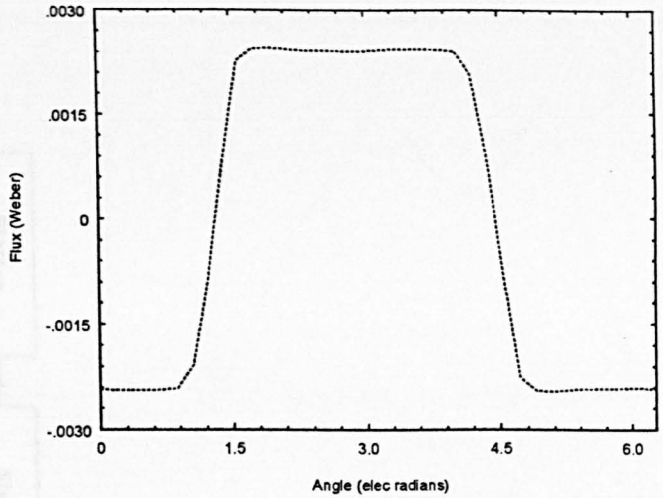


(a) Predicted .

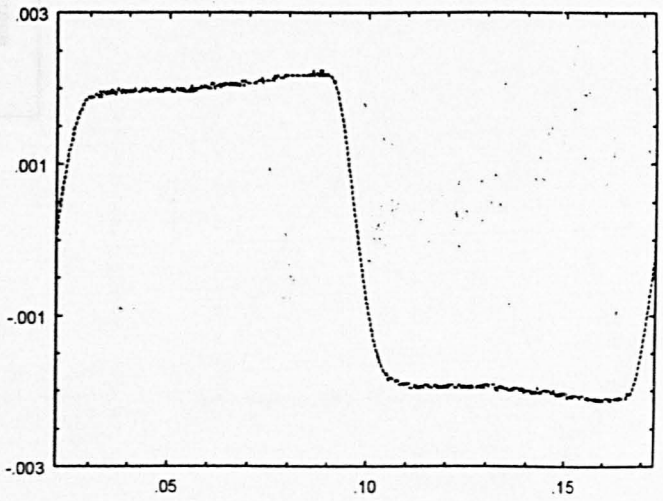


(b) Measured.

Fig (4.31) Flux waveforms in tooth tip D on open-circuit.

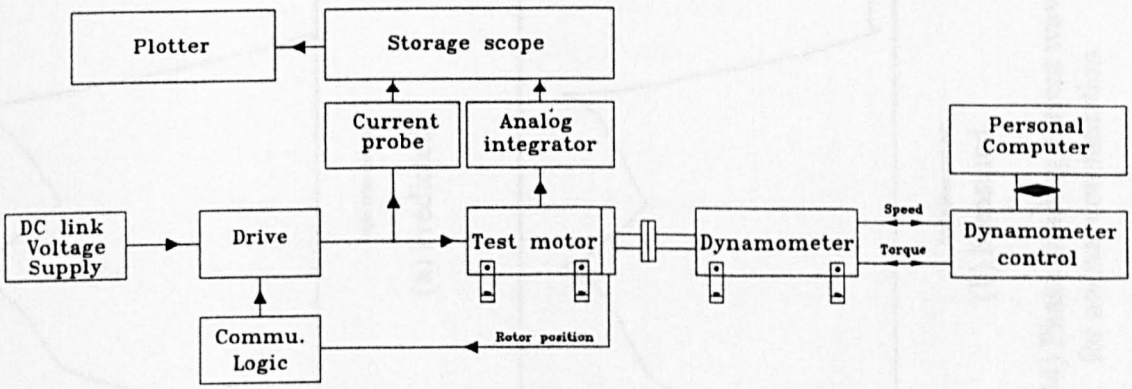


Fig (4.32)Schematic of the rig for the measurement of the current and flux density waveforms.

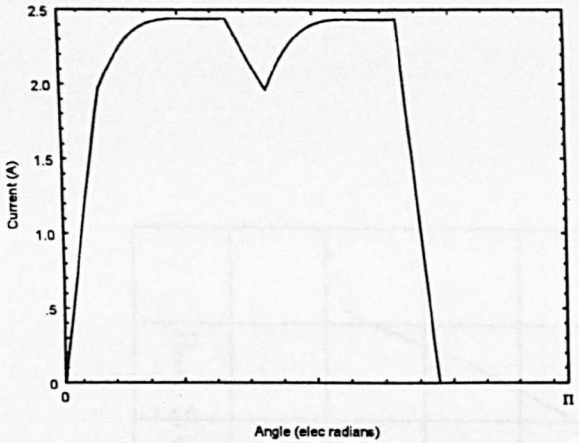


(a) Predicted.

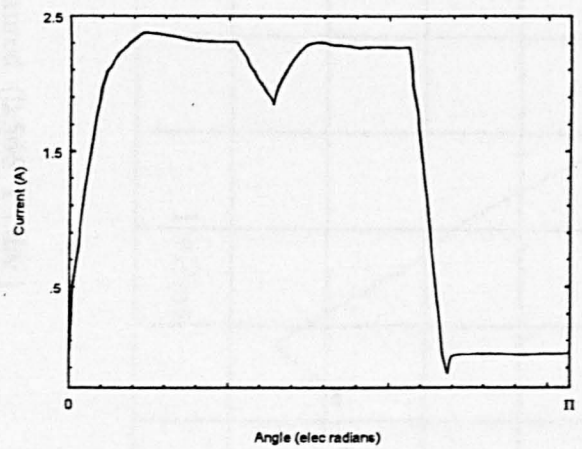


(b) Measured.

Fig (4.33) Phase winding current waveform for $20^{o}$ advanced commutation.

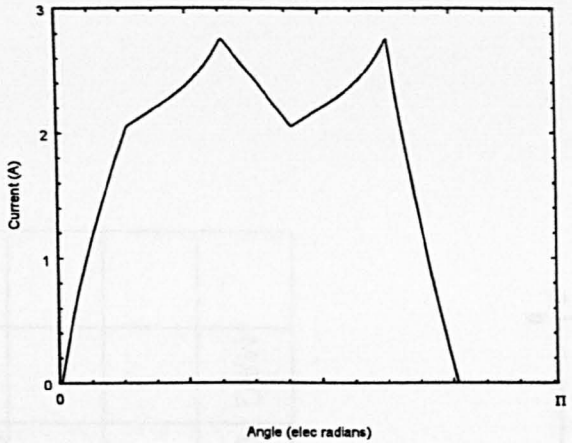


(a) Predicted.

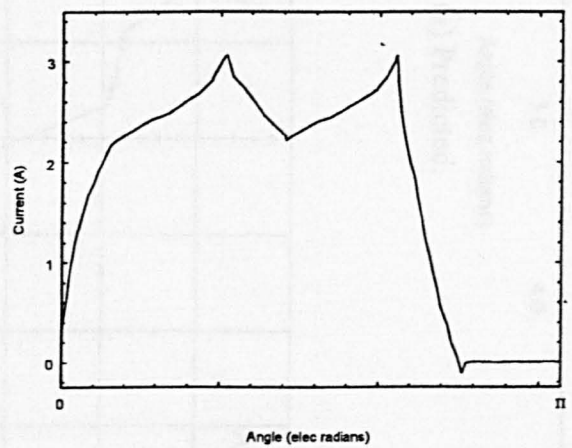


(b) Measured.

Fig (4.34) Phase winding current waveform for normal commutation.

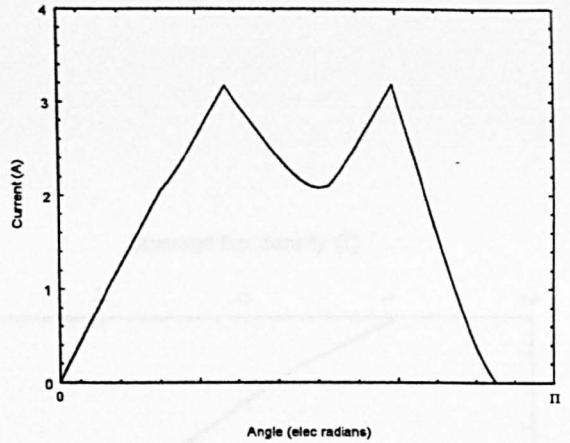


(a) Predicted.

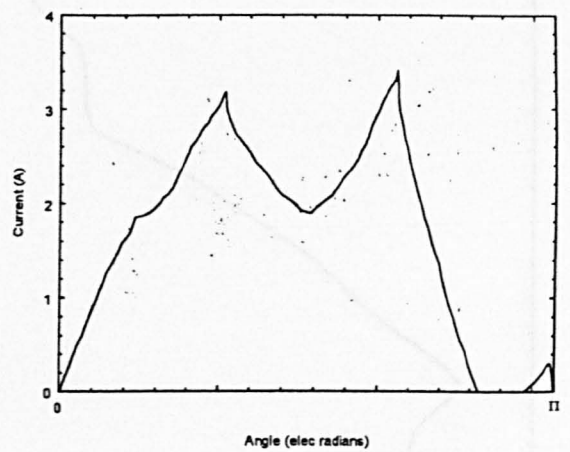


(b) Measured.

Fig (4.35) Phase winding current waveform for $20^{o}$ retarded commutation.

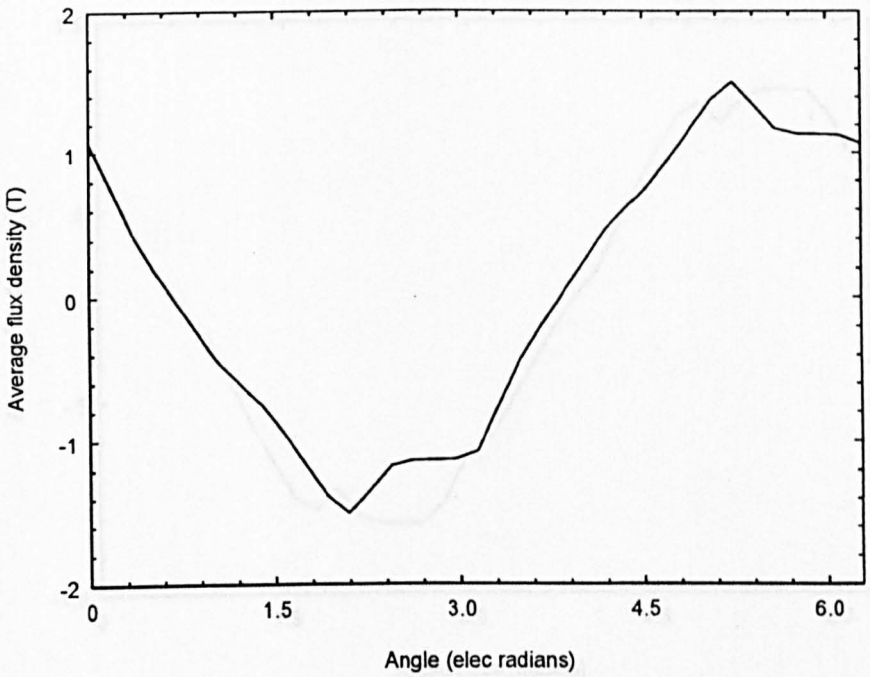


(a) Predicted.

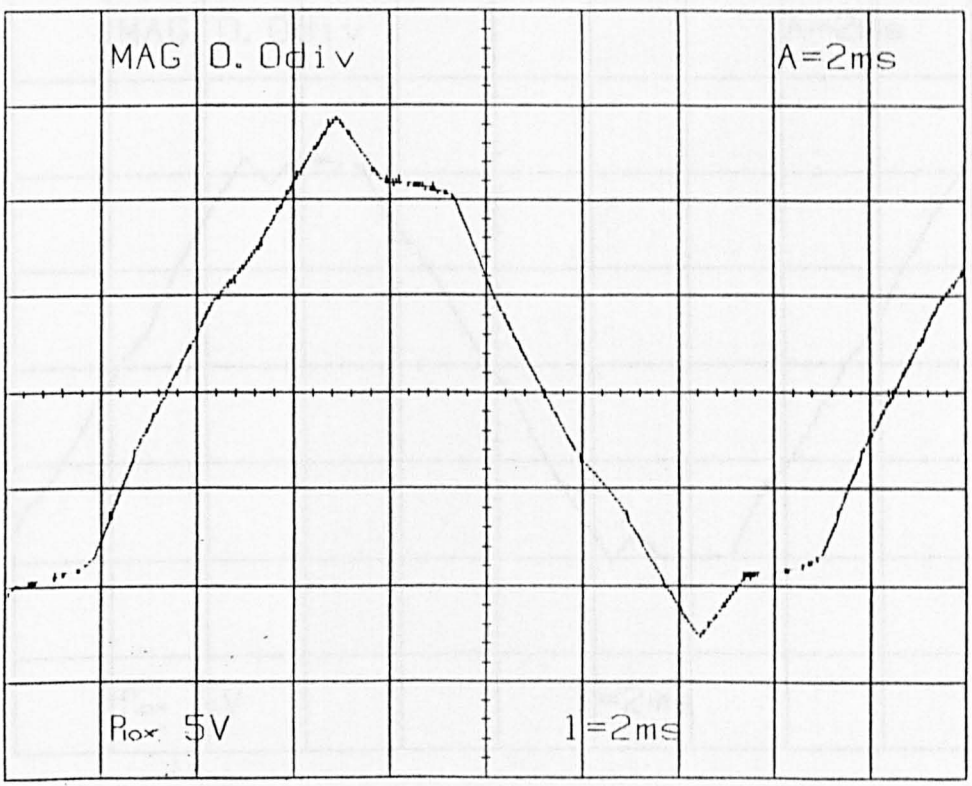


(b) Measured. (0.566 T / div )

Fig (4.36) Flux density waveform in the tooth body on rated load. (Normal commuation)

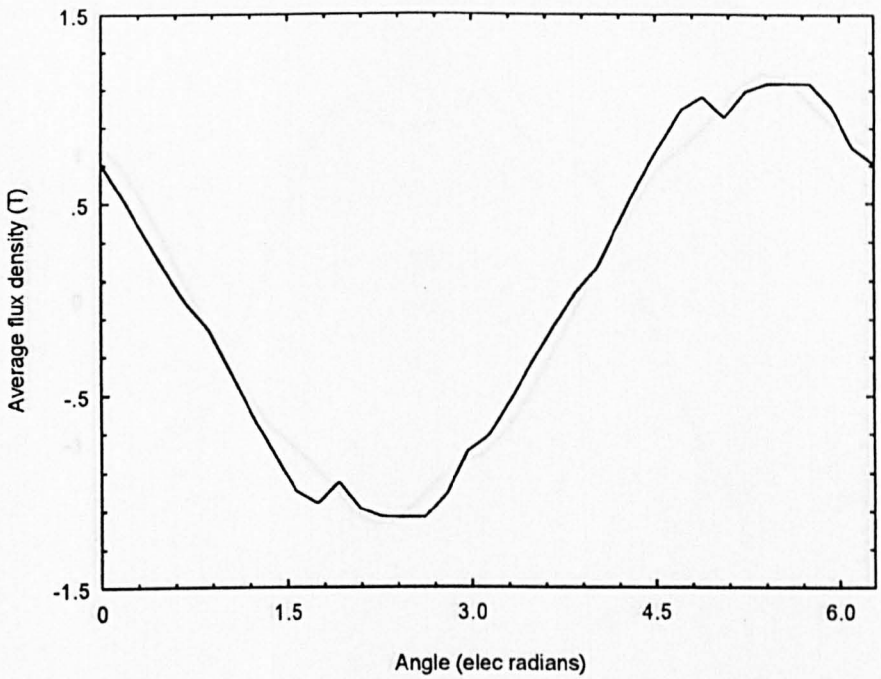


(a) Predicted.

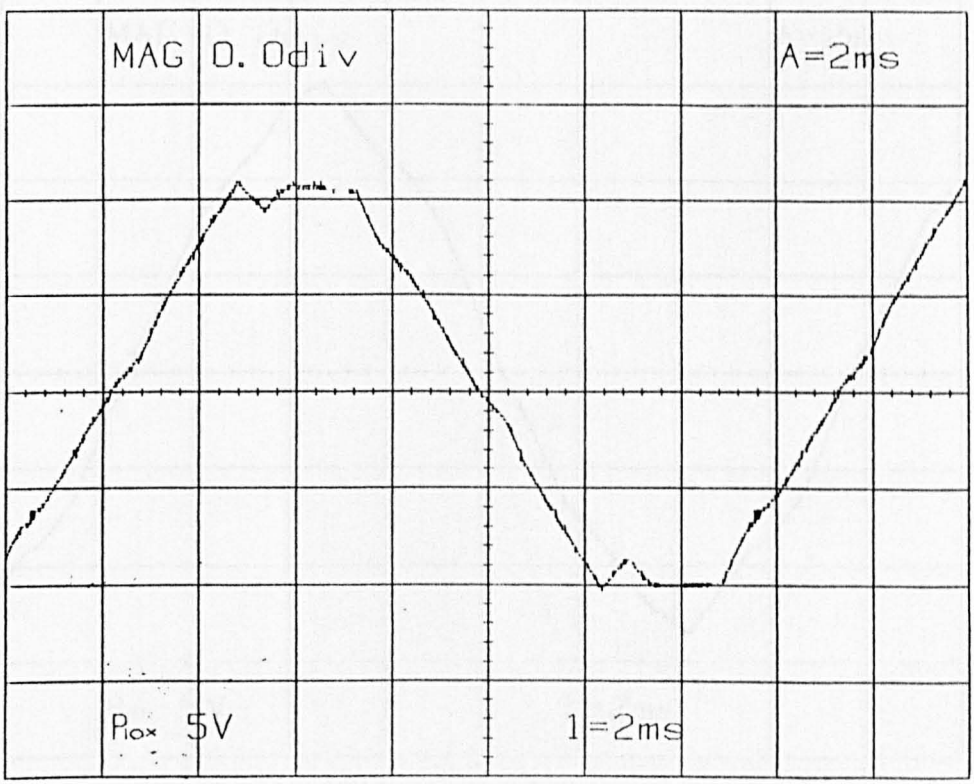


(b) Measured. (0.566 T / div)

Fig (4.37) Flux density waveform in the tooth body on load. ($20^{o}$ advanced commutation)

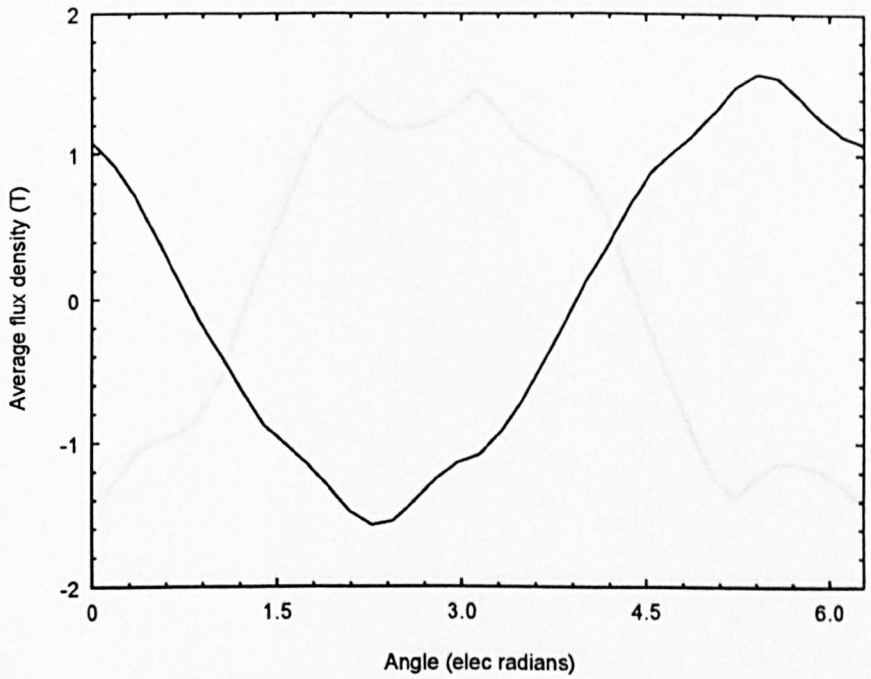


(a) Predicted.

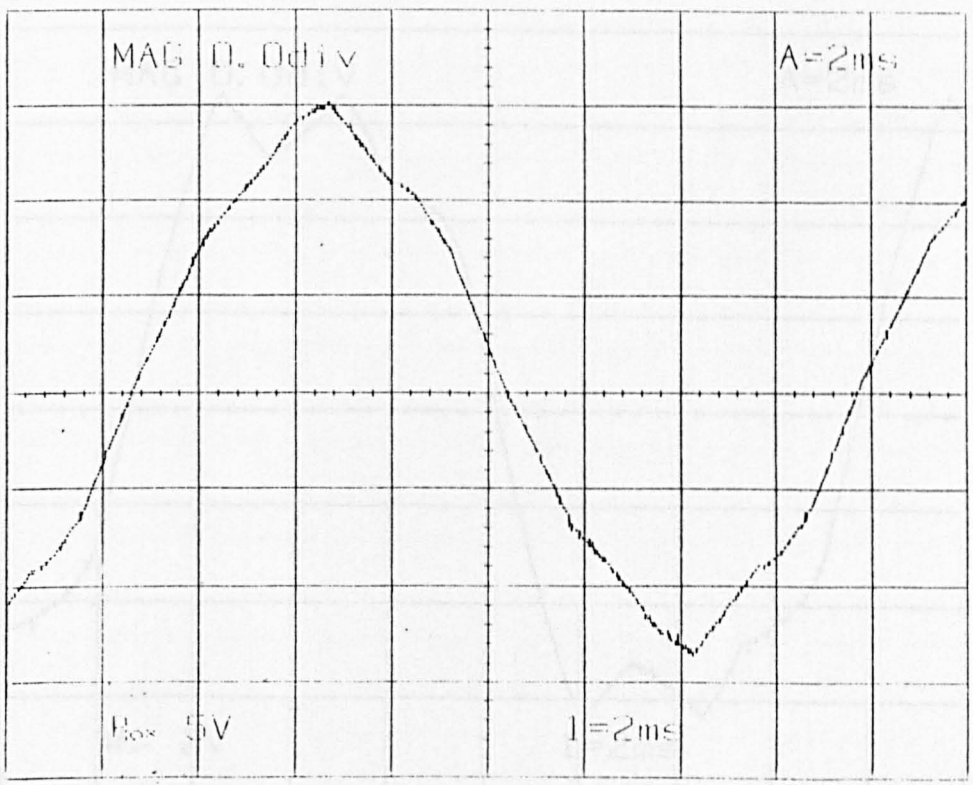


(b) Measured. (0.566 T / div)

Fig (4.38) Flux density waveform in the tooth body on load. ($20^{o}$ retarded commutation)

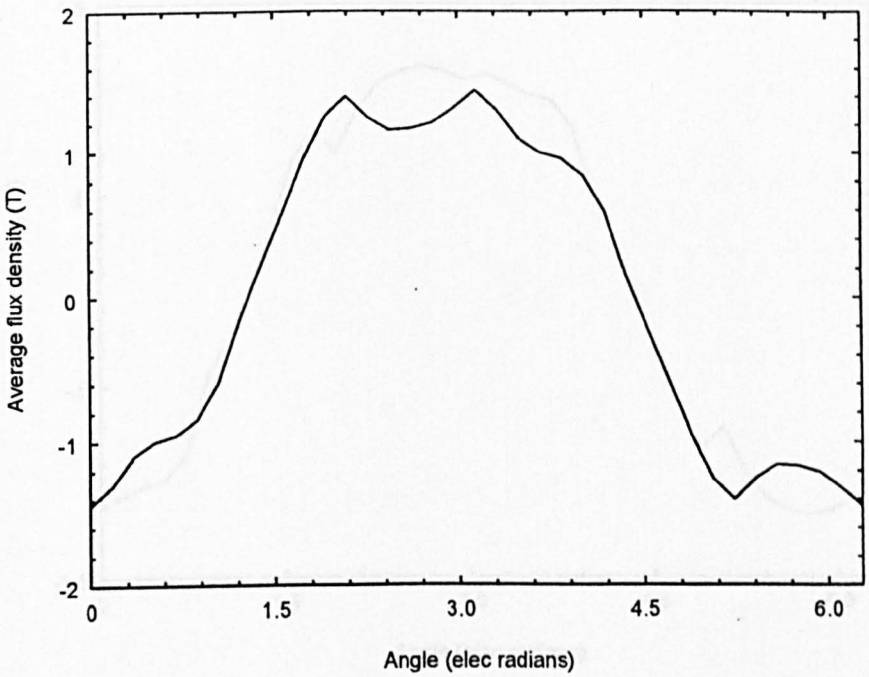


(a) Predicted.

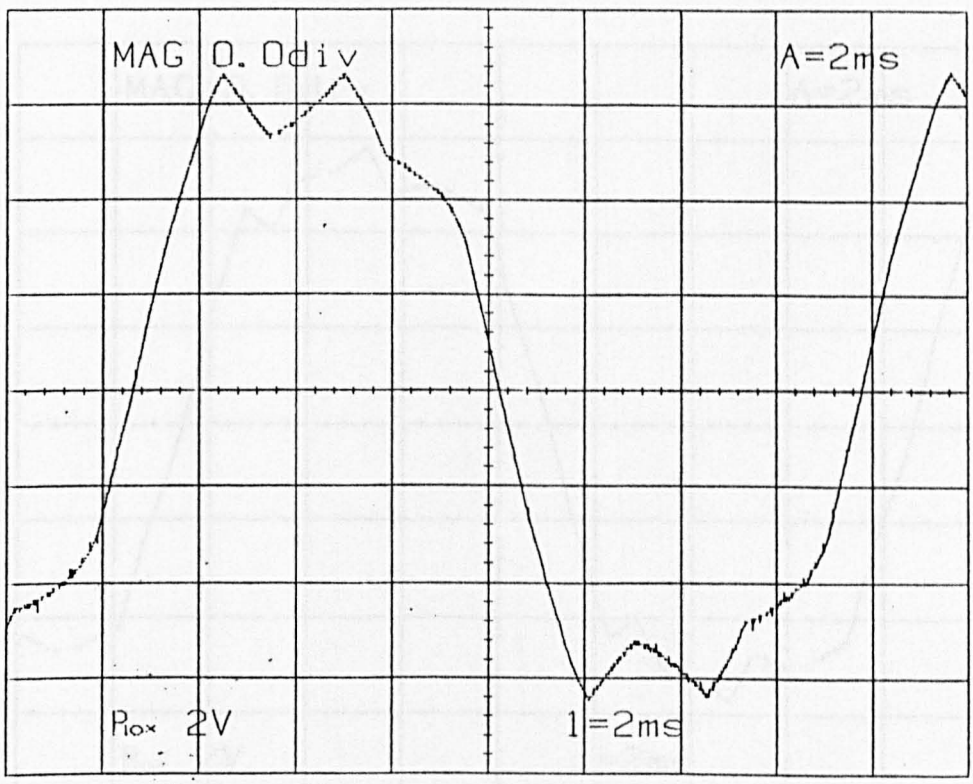


(b) Measured. (0.432 T / div )

Fig (4.39) Flux density waveform in the stator back-iron at rated load.
(Normal commutation)

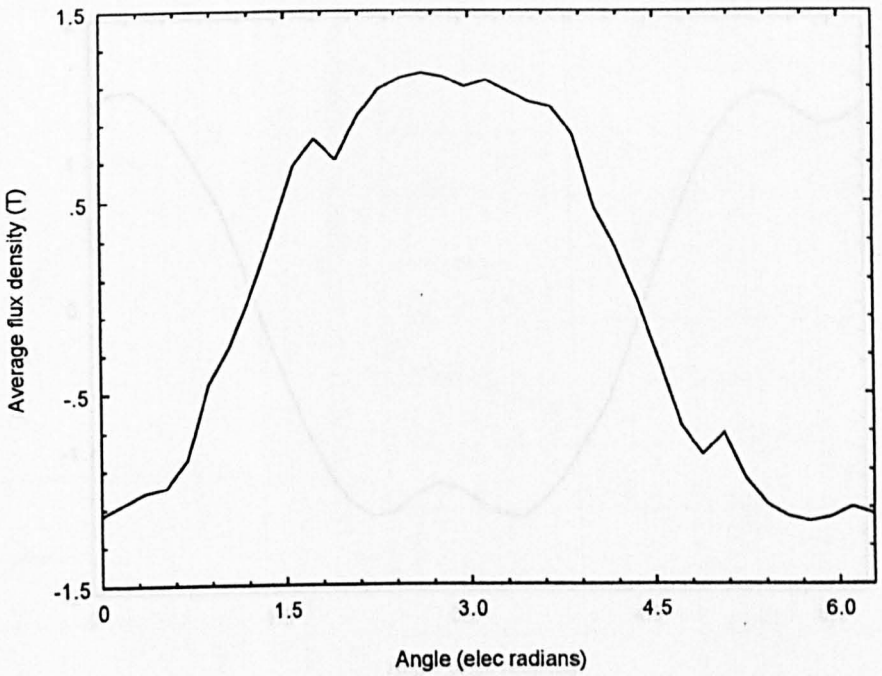


(a) Predicted.

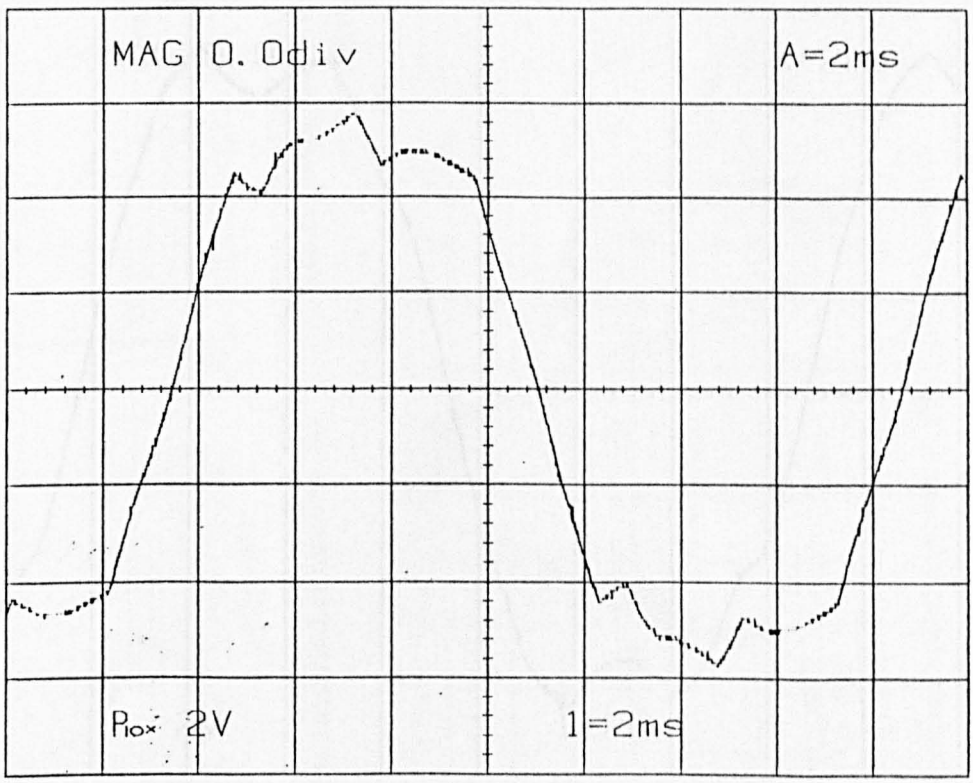


(b) Measured. ( 0.432 T / div )

Fig (4.40) Flux density waveform in the stator back-iron. ($20^{o}$ advanced commutation)

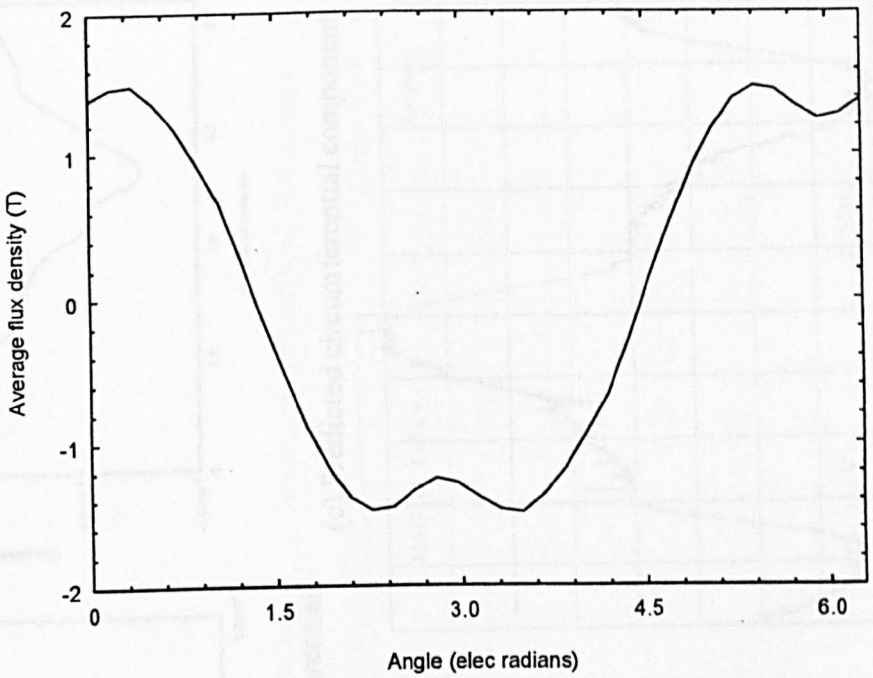


(a) Predicted.

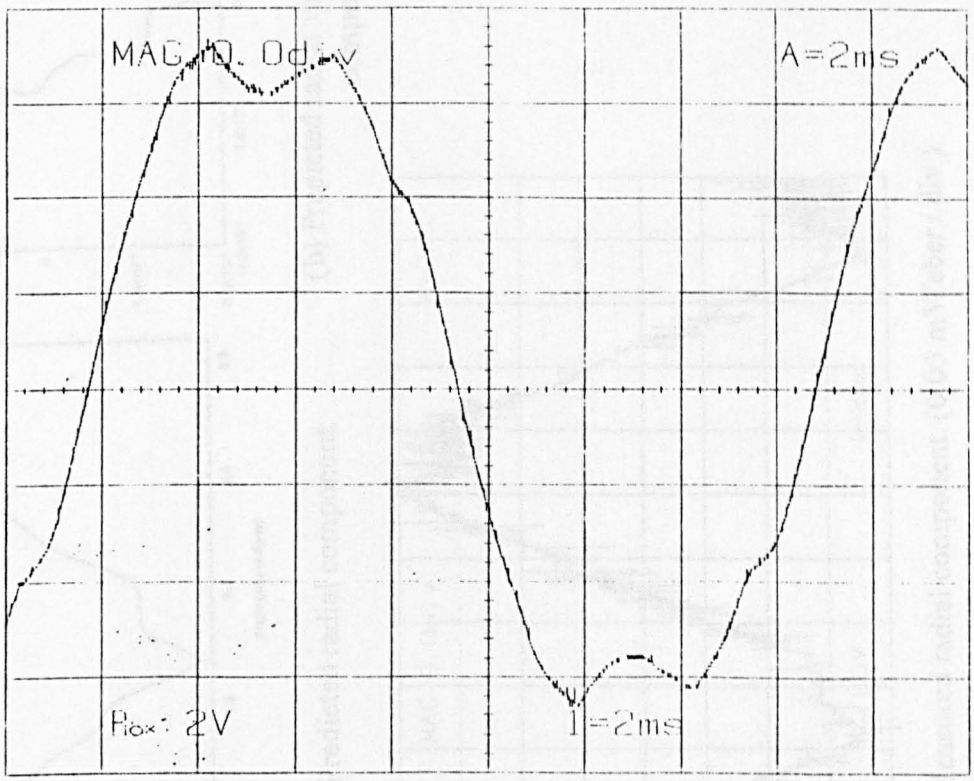


(b) Measured. ( 0.432 T / div )

Fig (4.41) Flux density waveform in the stator back-iron. ($20^{0}$ retarded commutation)

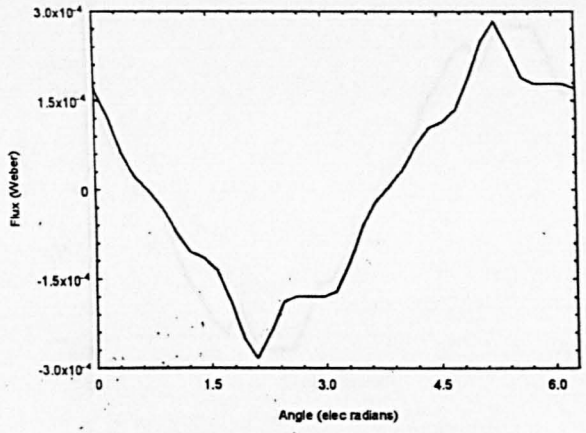


(a) Predicted radial component.

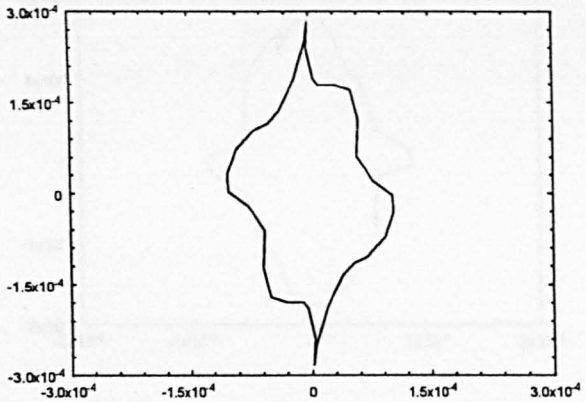


(b) Predicted radial versus circumferential components

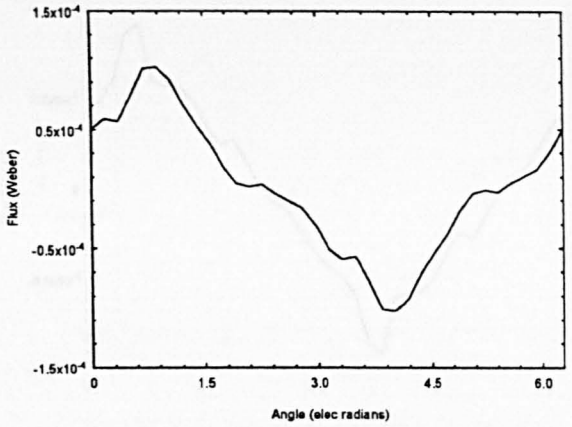


(c) Predicted circumferential component.

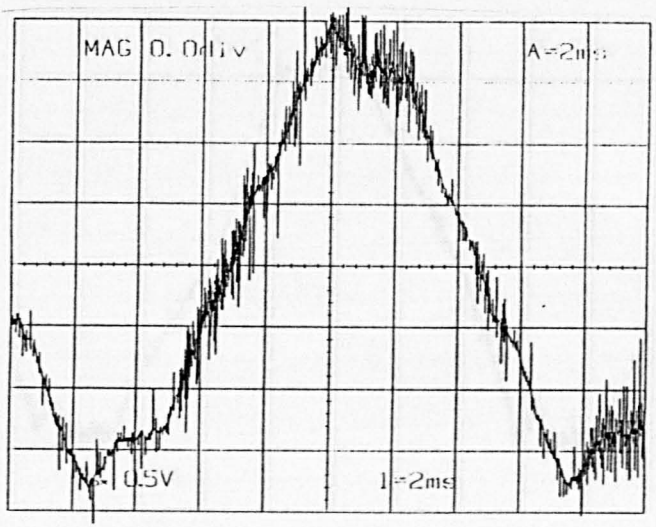


(d) Measured radial component. (0.05 mWeber / div )

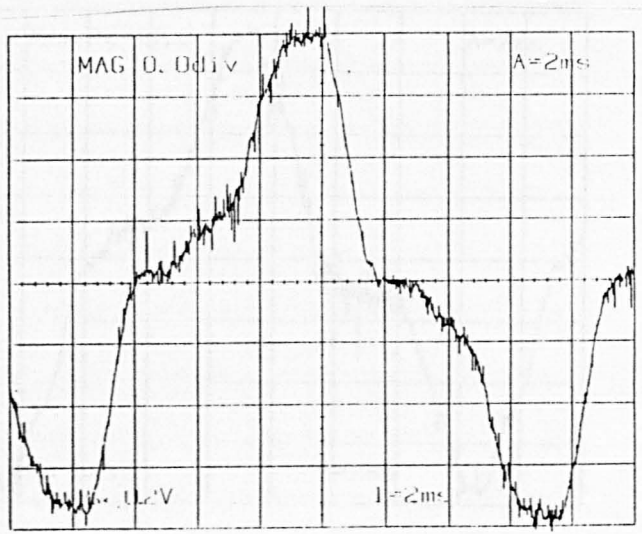


(e) Measured circumferential component. (0.02 mWeber / div )

Fig (4.42) Radial and tangential components of flux behind a tooth at rated load. ( Normal commutation)

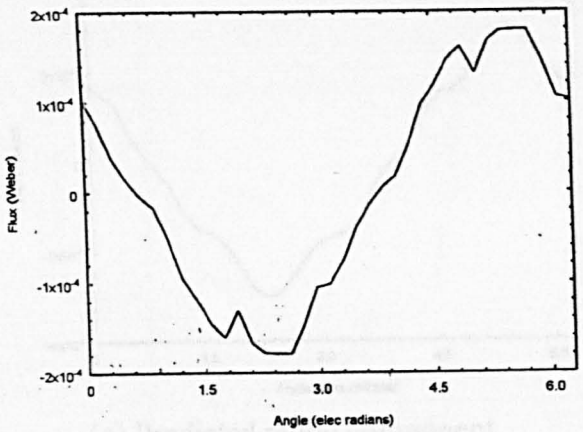


(a) Predicted radial component.

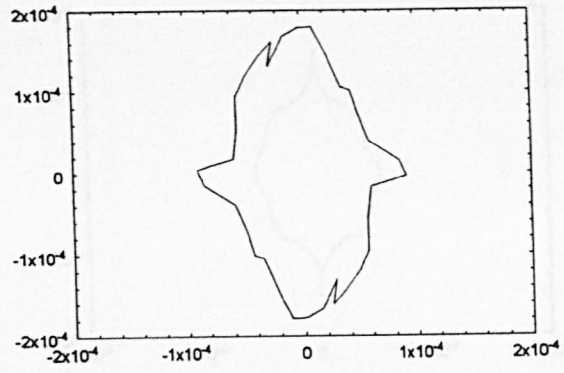


(b) Predicted radial versus circumferential components.

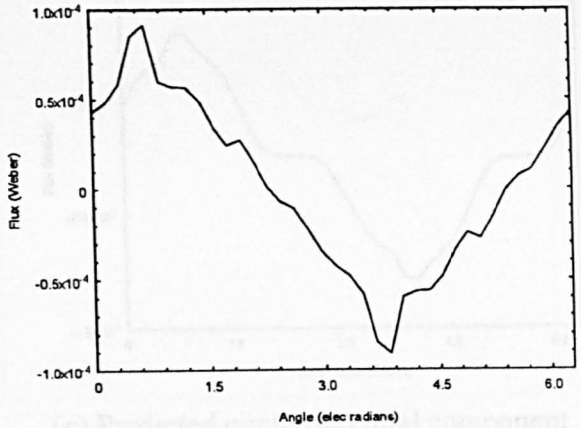


(c) Predicted circumferential component.

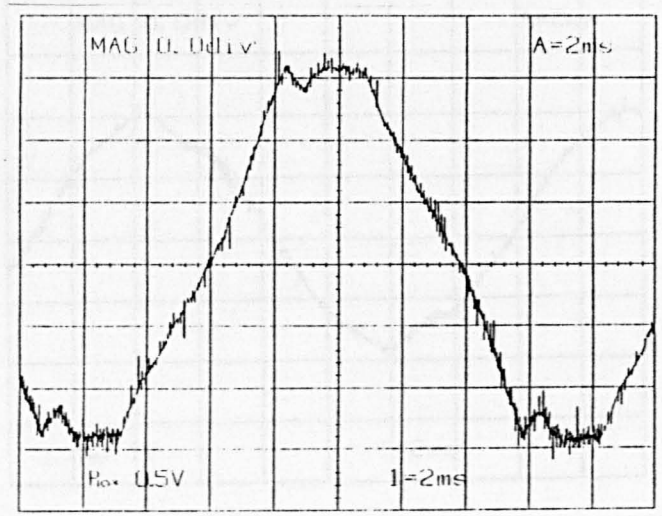


(d) Measured radial component. (0.05 mWeber / div)

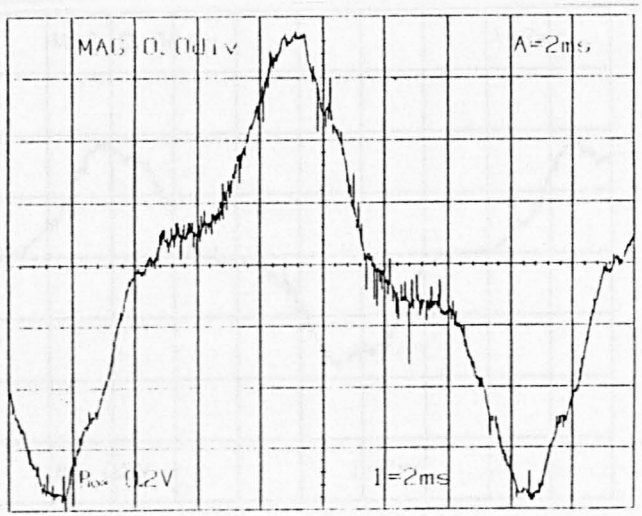


(e) Measured circumferential component. (0.02 mWeber / div)

Fig (4.43) Radial and tangential components of flux behind a tooth at rated load. ( $20^{o}$ advanced commutation)

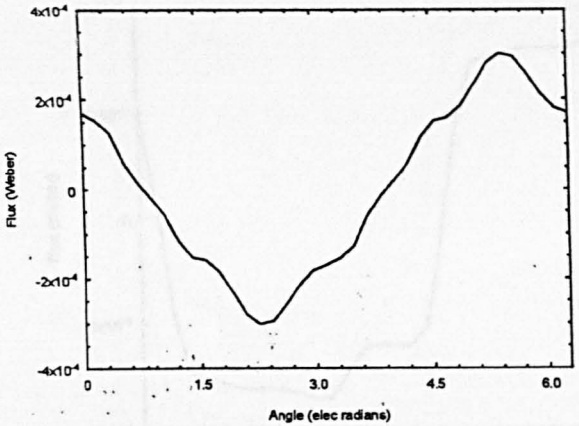


(a) Predicted radial component.

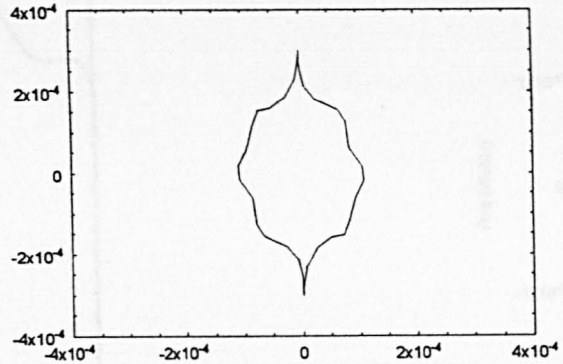


(b) Predicted radial versus circumferential components.

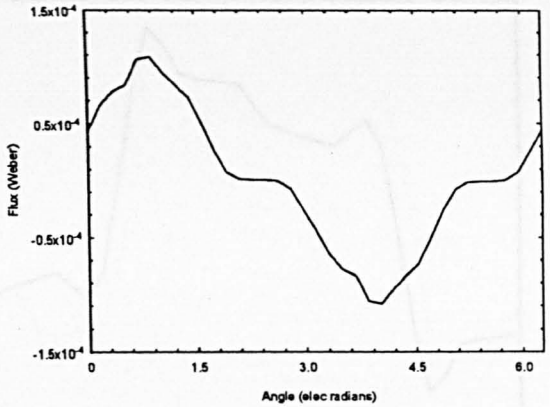


(c) Predicted circumferential component.

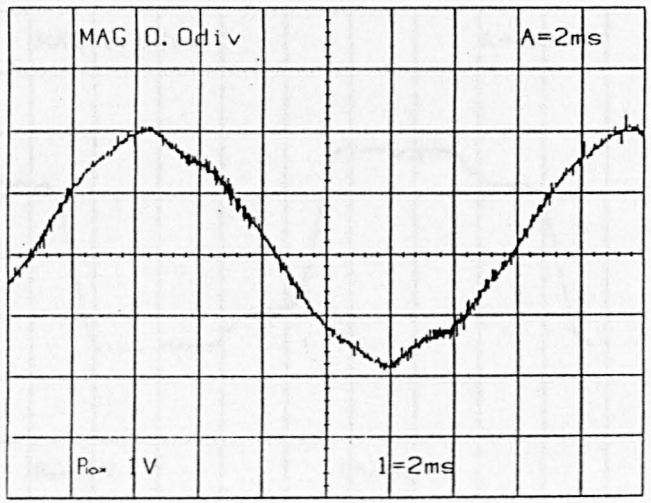


(d) Measured. (0.1 mWeber / div )

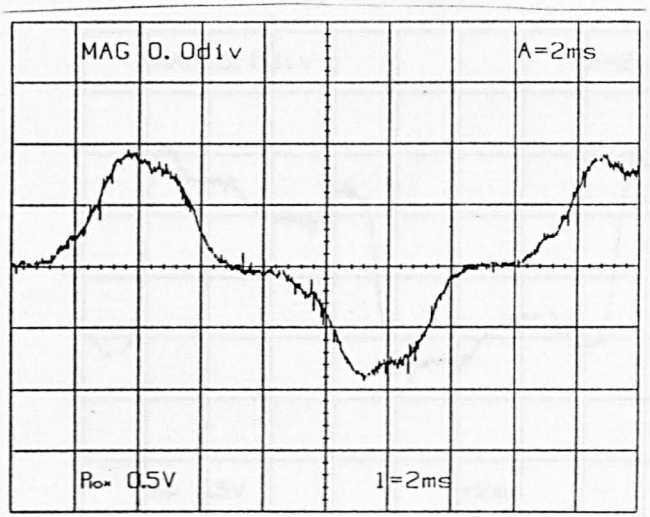


(e) Measured. (0.05 mWeber / div )

Fig (4.44) Radial and tangential components of flux behind a tooth at rated load. ( 20° retarded commutation)

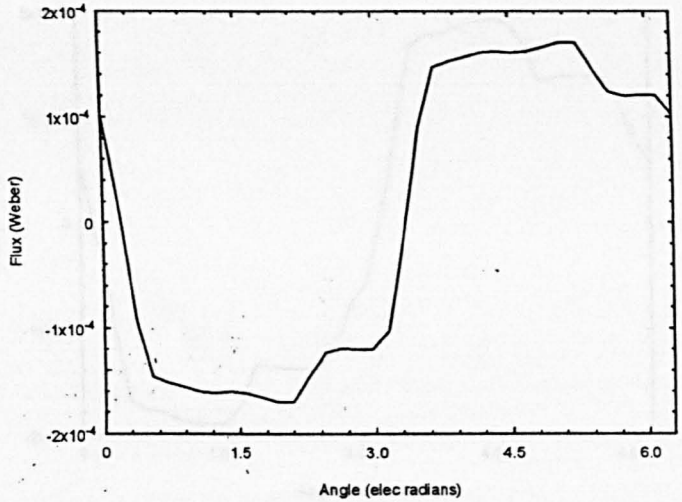


(a) Predicted.

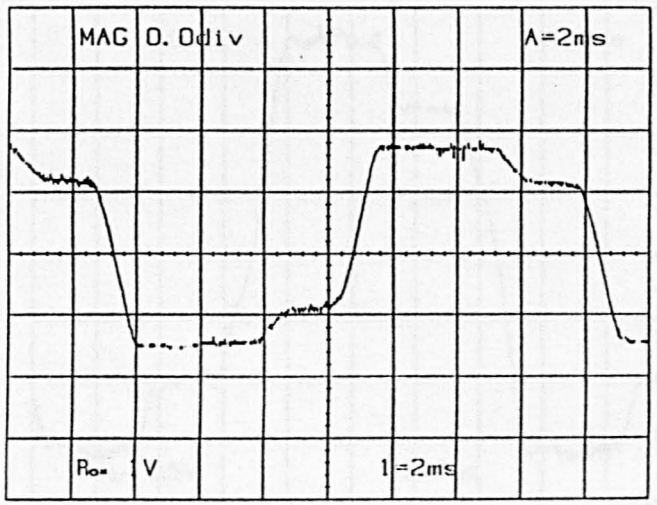


(b) Measured. ( 0.1 mWeber / div )

Fig (4.45) Flux waveform in tooth tip C at rated load.
(Normal commutation )

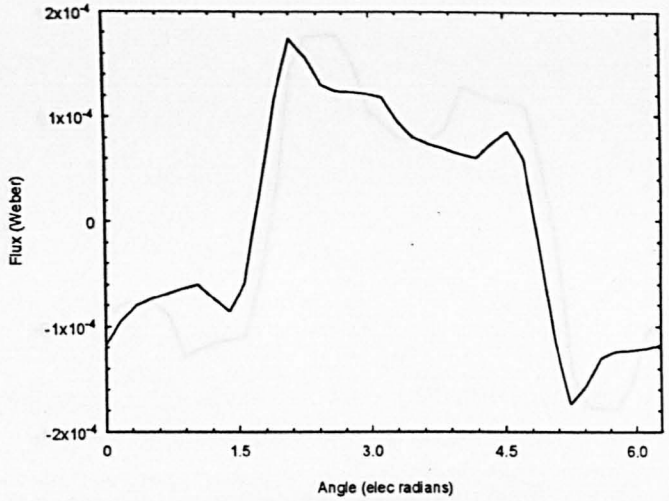


(a) Predicted.

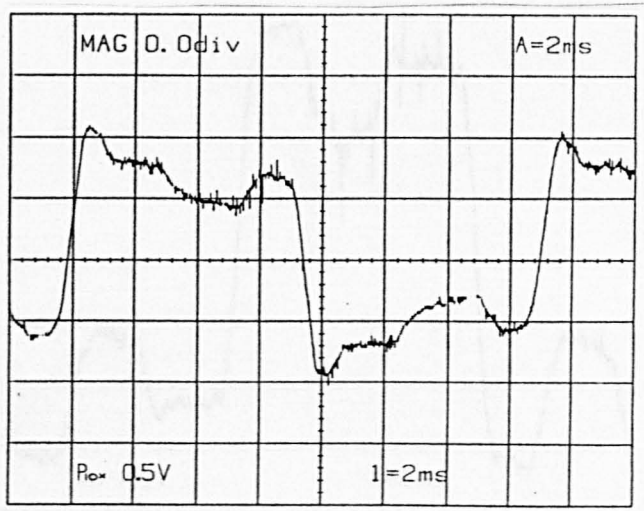


(b) Measured. ( 0.05 mWeber / div )

Fig (4.46) Flux waveform in tooth tip D at rated load.
(Normal commutation )

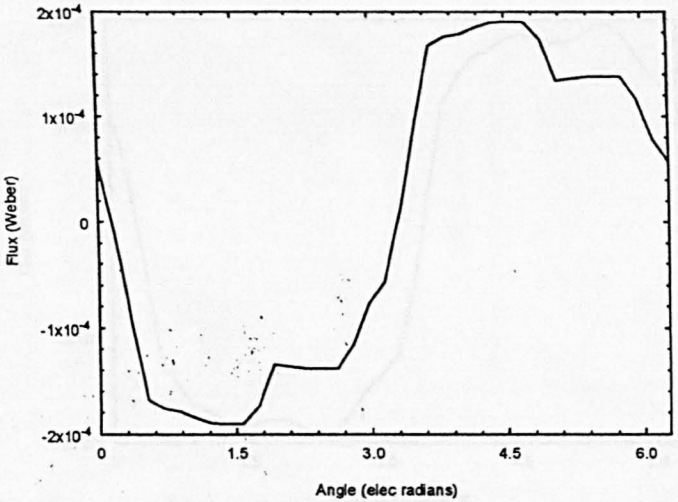


(a) Predicted.

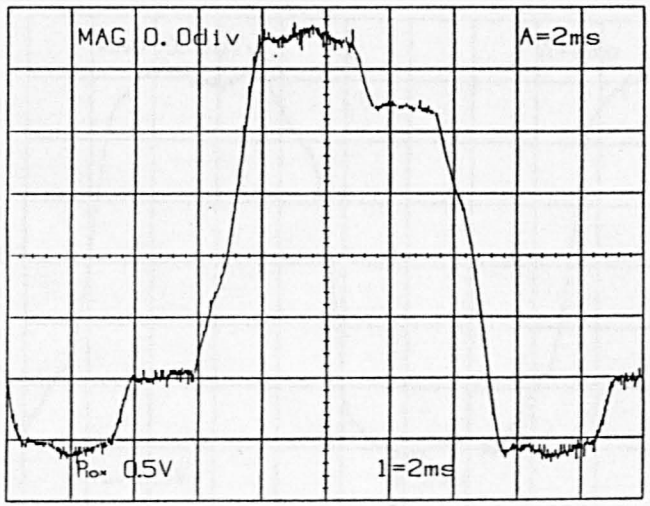


(b) Measured. (0.05 mWeber / div )

Fig (4.47) Flux waveform in tooth tip C at rated load.
(20° advanced commutation )

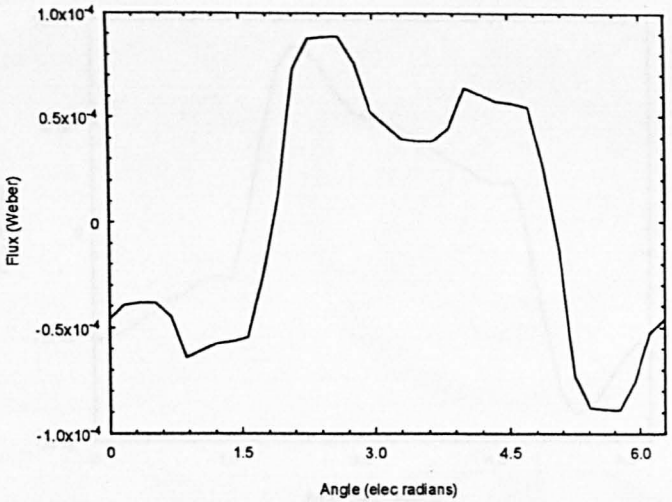


(a) Predicted.

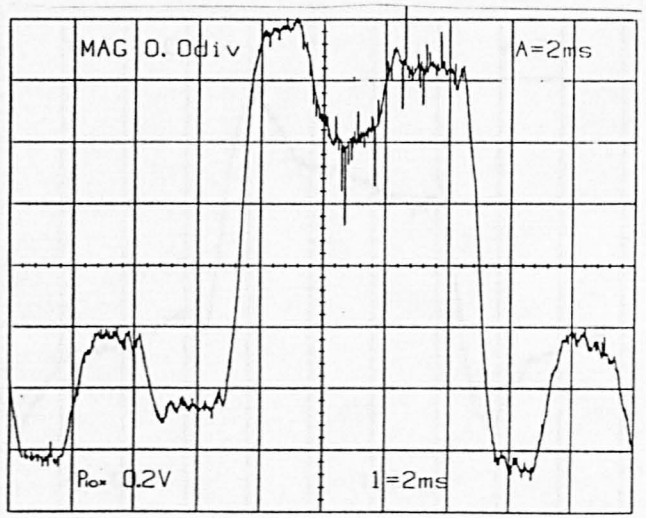


(b) Measured. (0.002 mWeber / div )

Fig (4.48) Flux waveform in tooth tip D at rated load.
(20° advanced commutation )

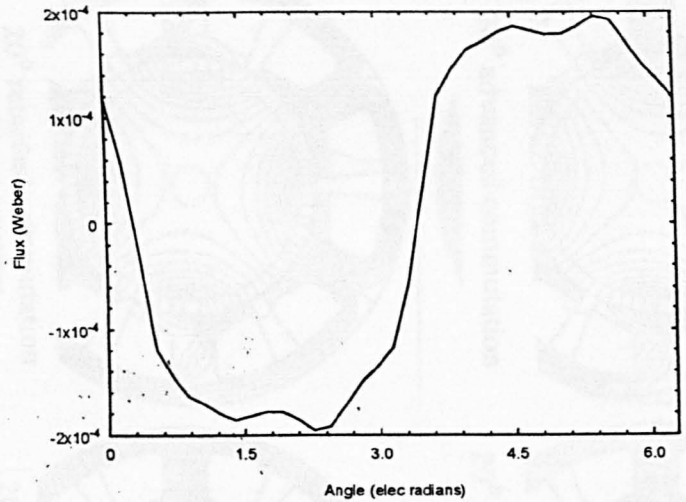


(a) Predicted.

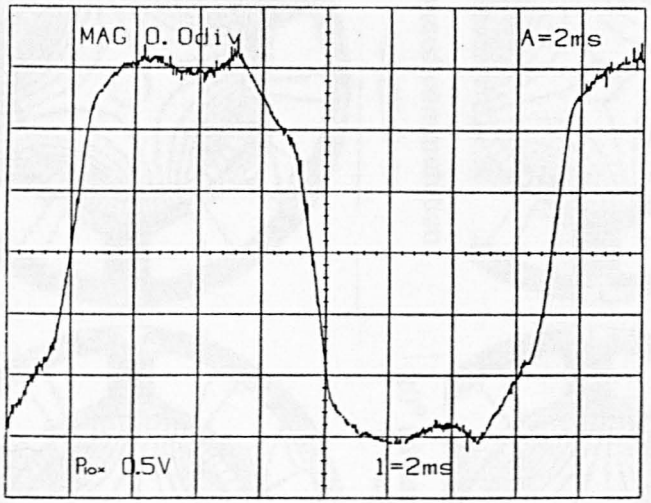


(b) Measured. (0.05 mWeber / div )

Fig (4.49) Flux waveform in tooth tip C at rated load.
($20^{o}$ retarded commutation )

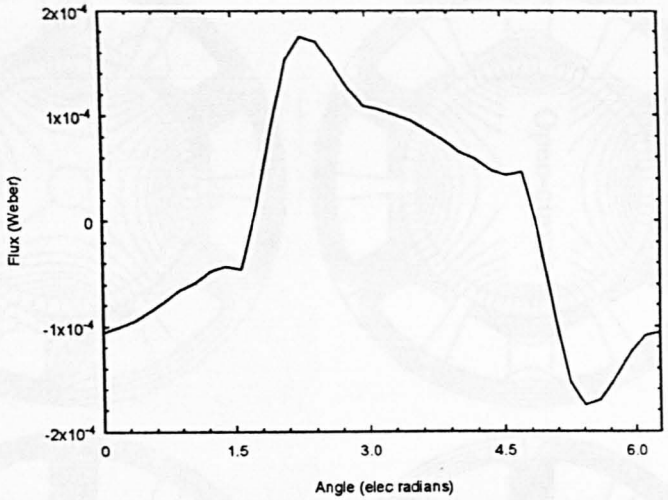


(a) Predicted.

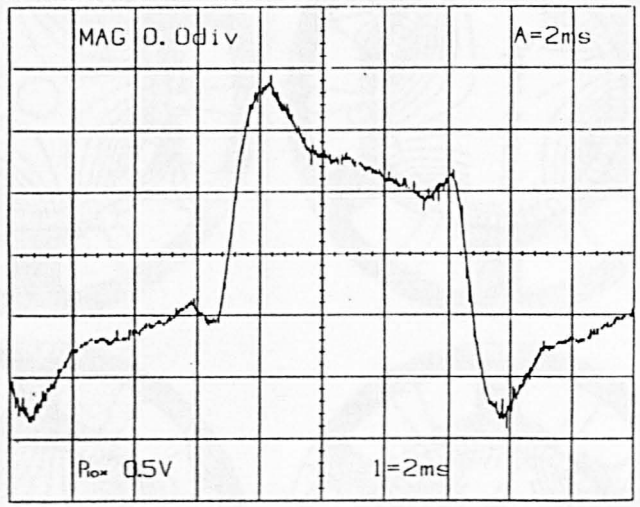


(b) Measured. (0.05 mWeber / div )

Fig (4.50) Flux waveform in tooth tip D at rated load.
($20^{o}$ retarded commutation )

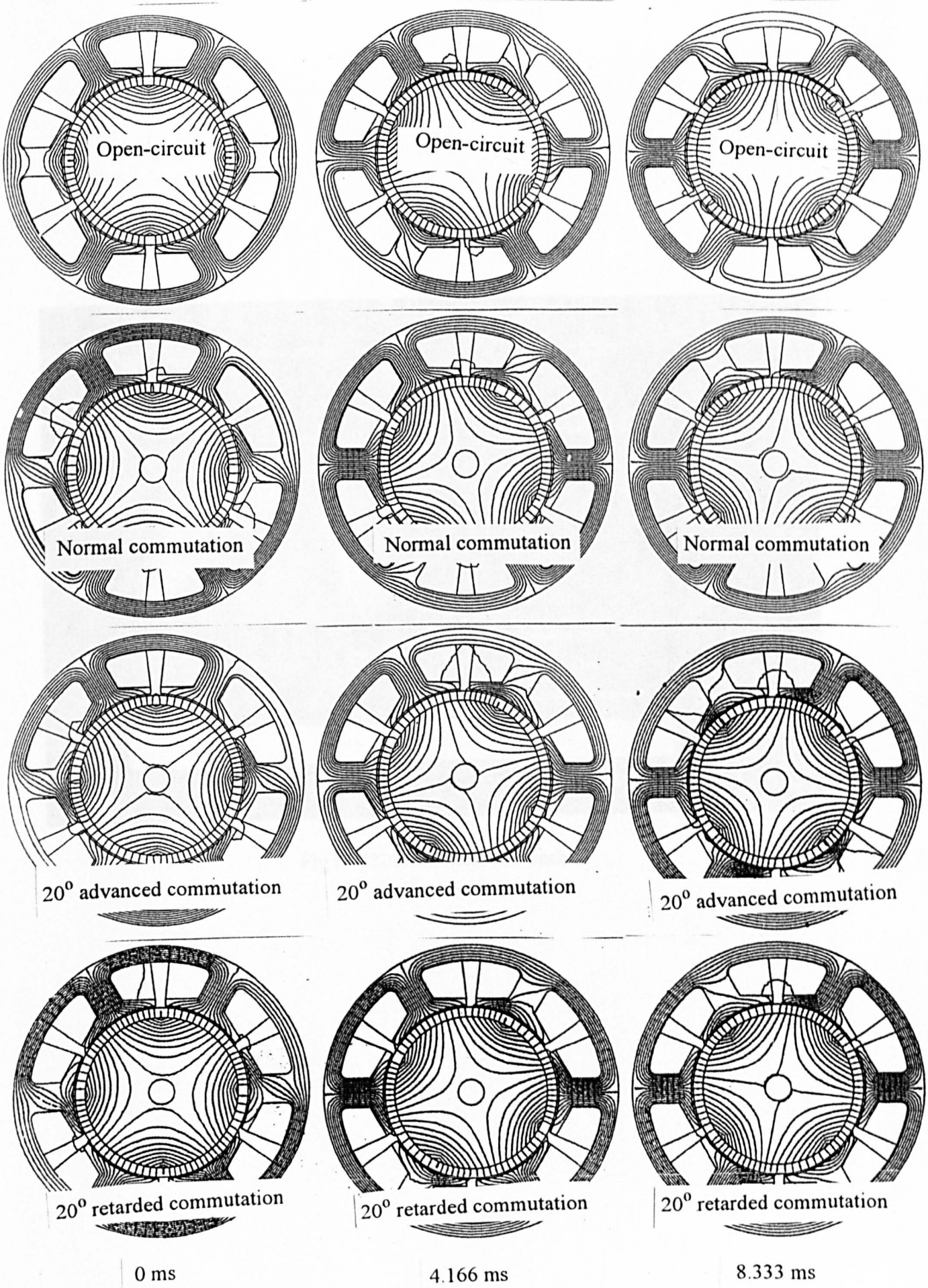


Fig (4.51) Flux plots for different instants.

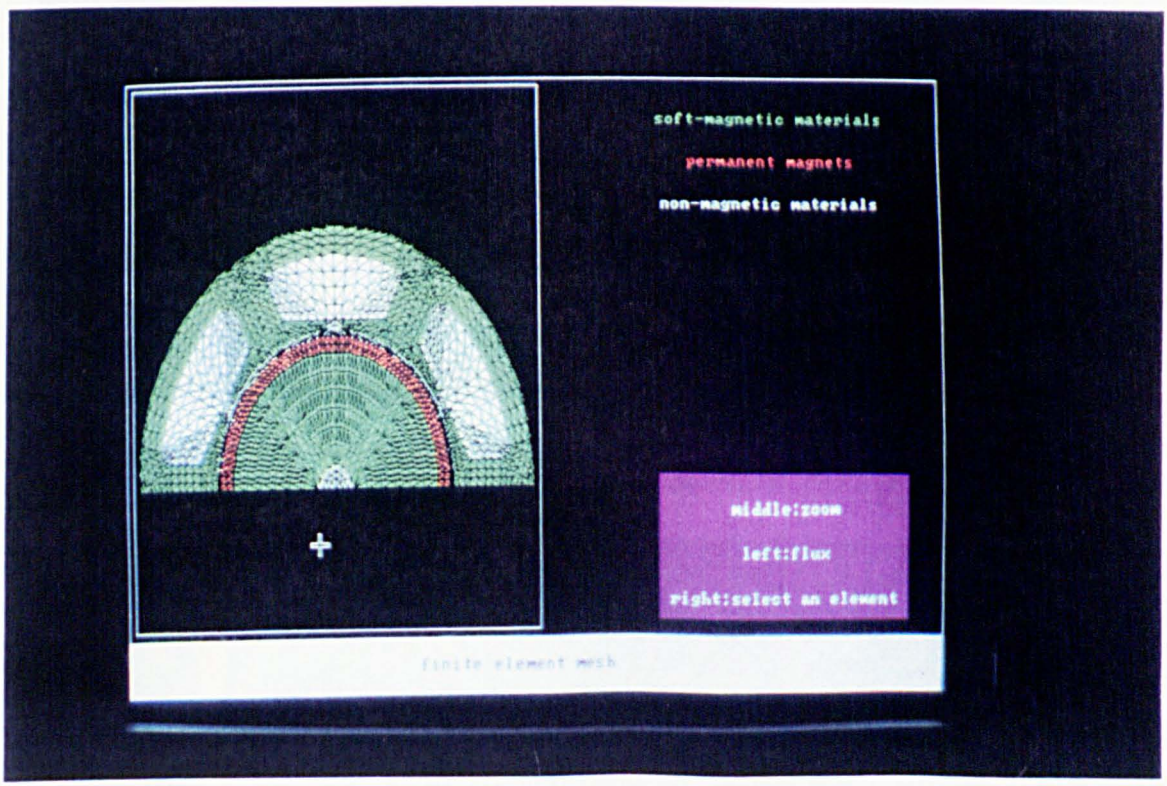


Fig (4.52) Finite element mesh.

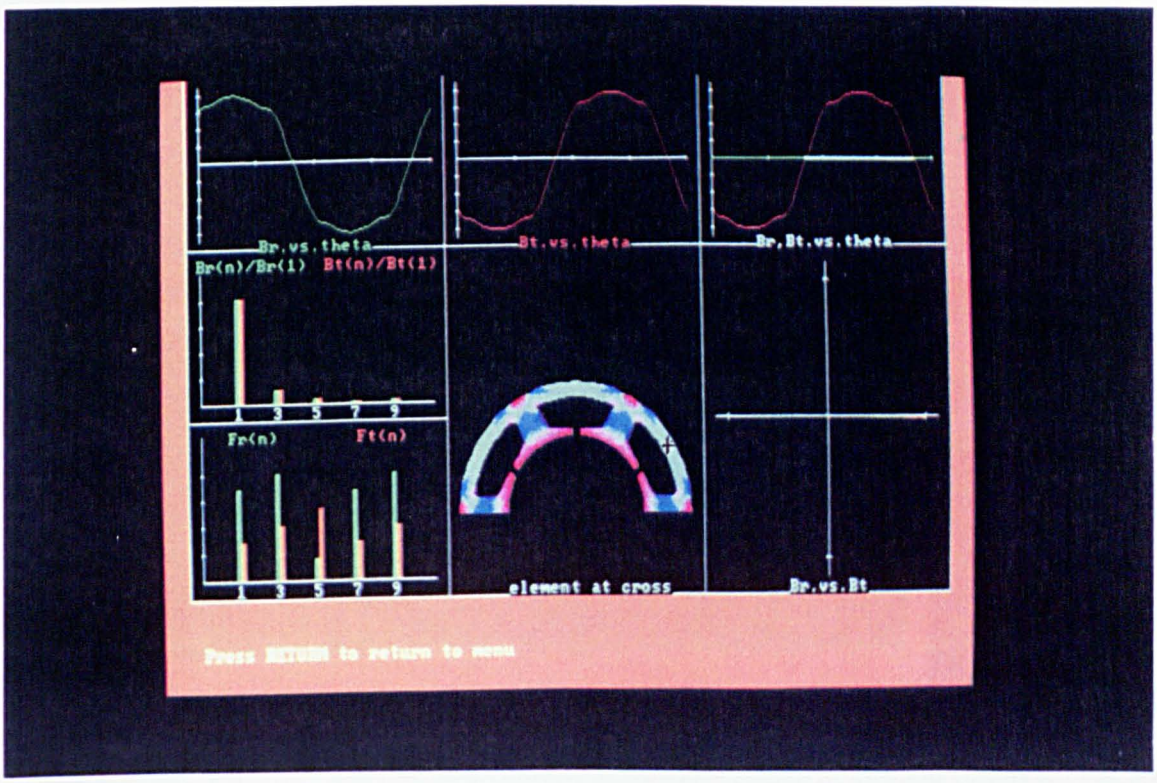


(a) Site 1.

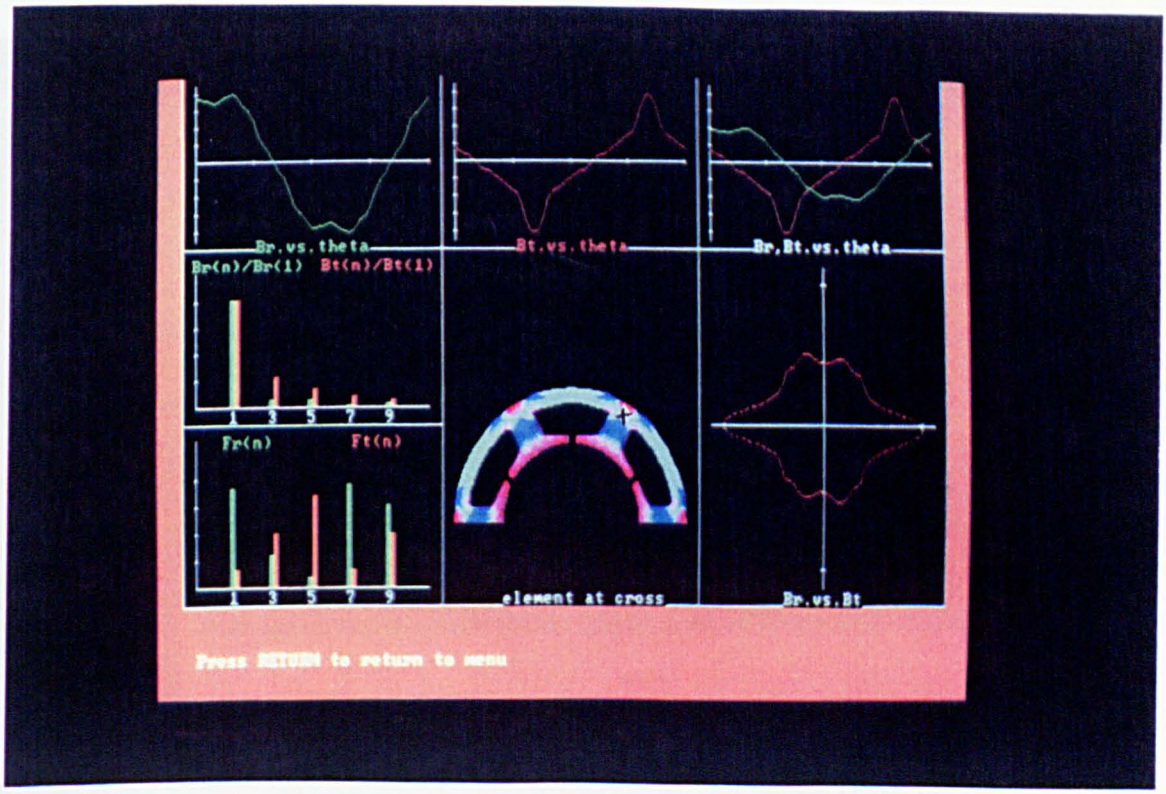


(b) Site 2.

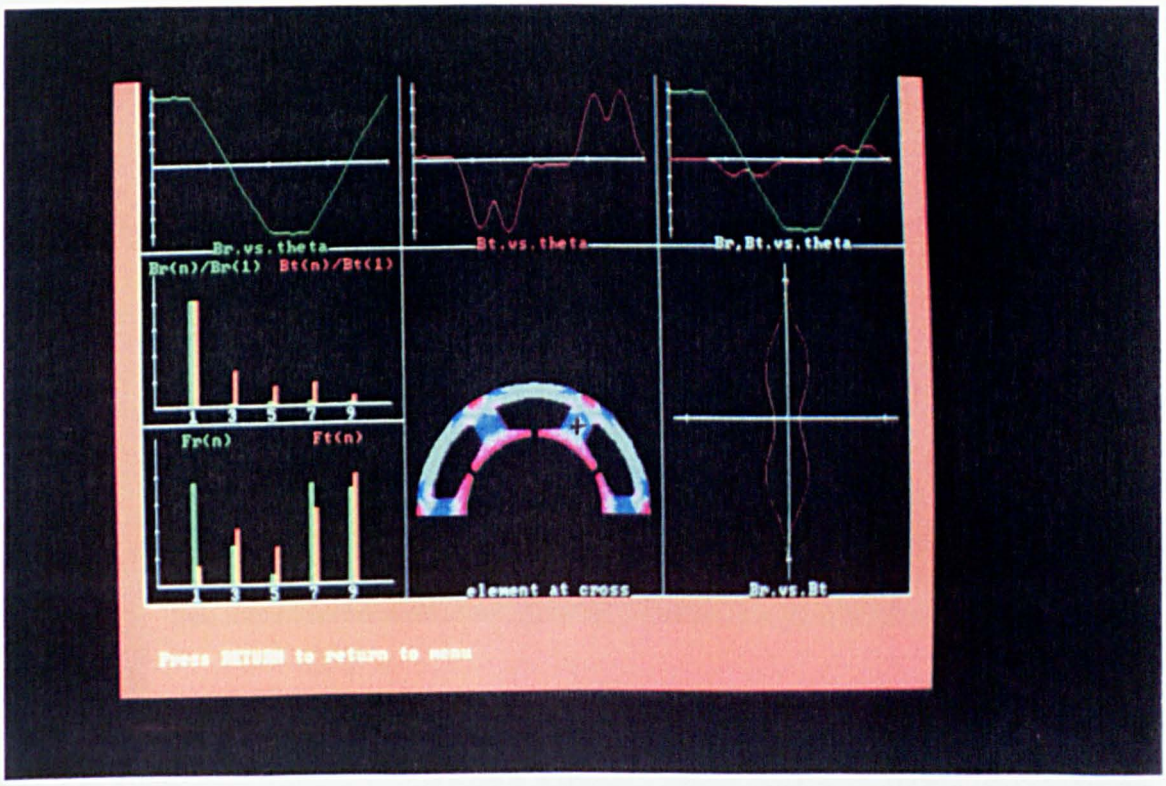


(c) Site 3.

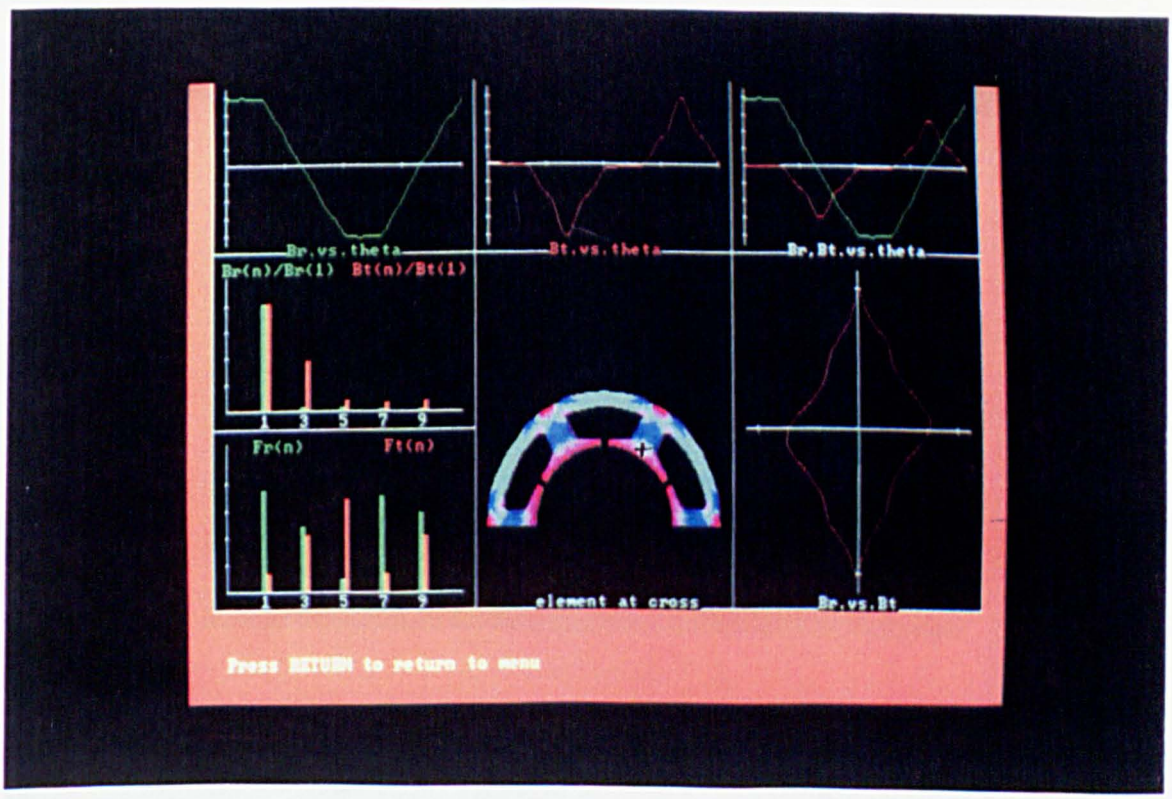


(d) Site 4.

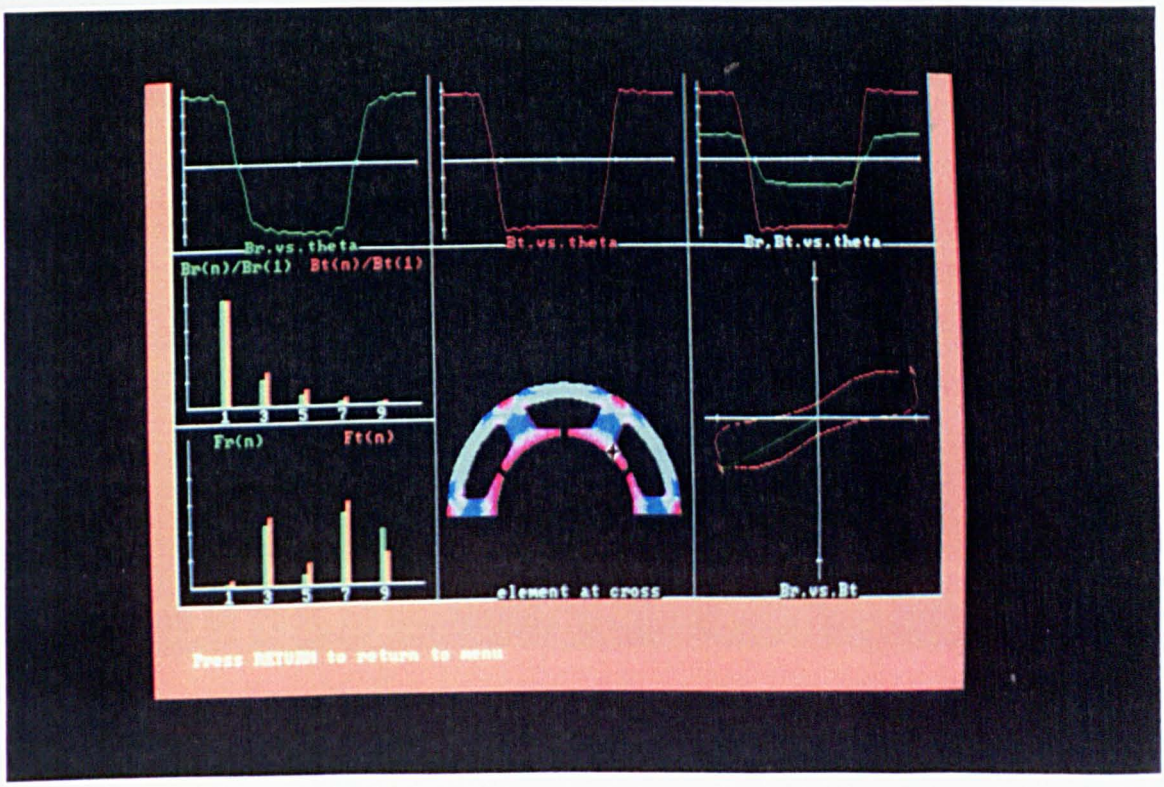


(e) Site 5.

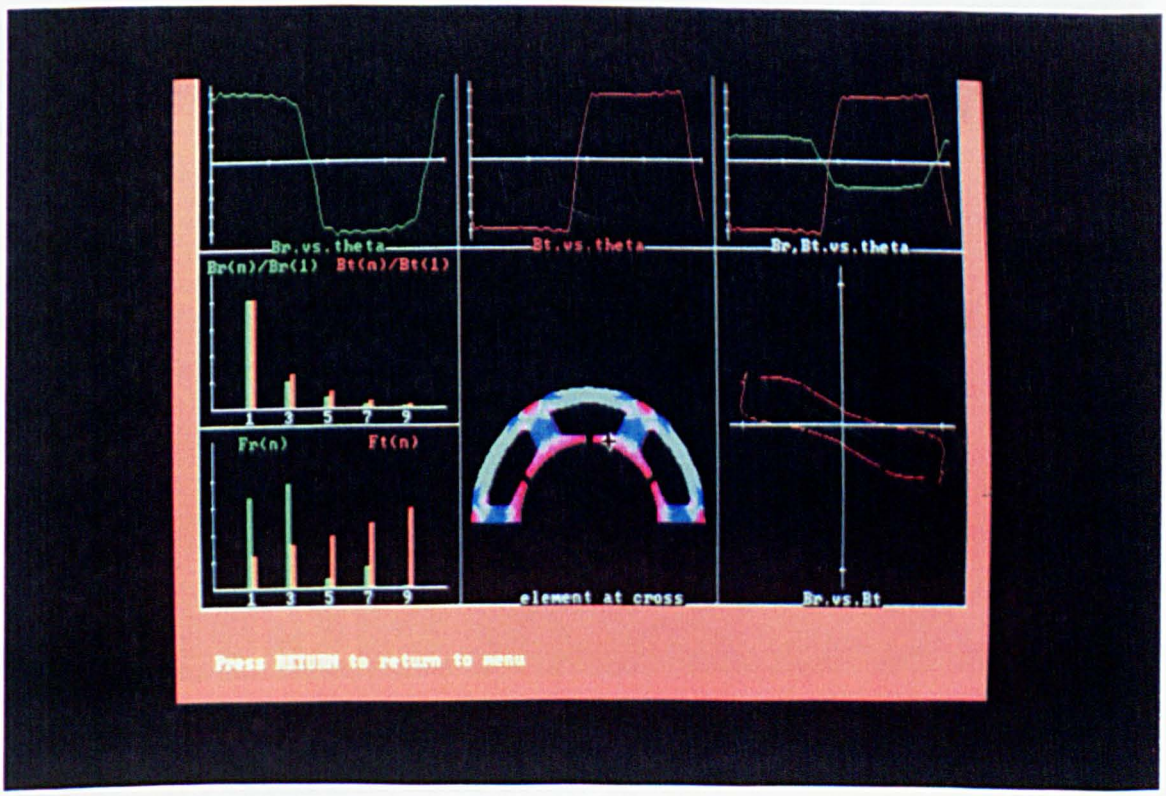


(f) Site 6.

Fig (4.53) Local flux density waveforms at selected sites on open-circuit operation.

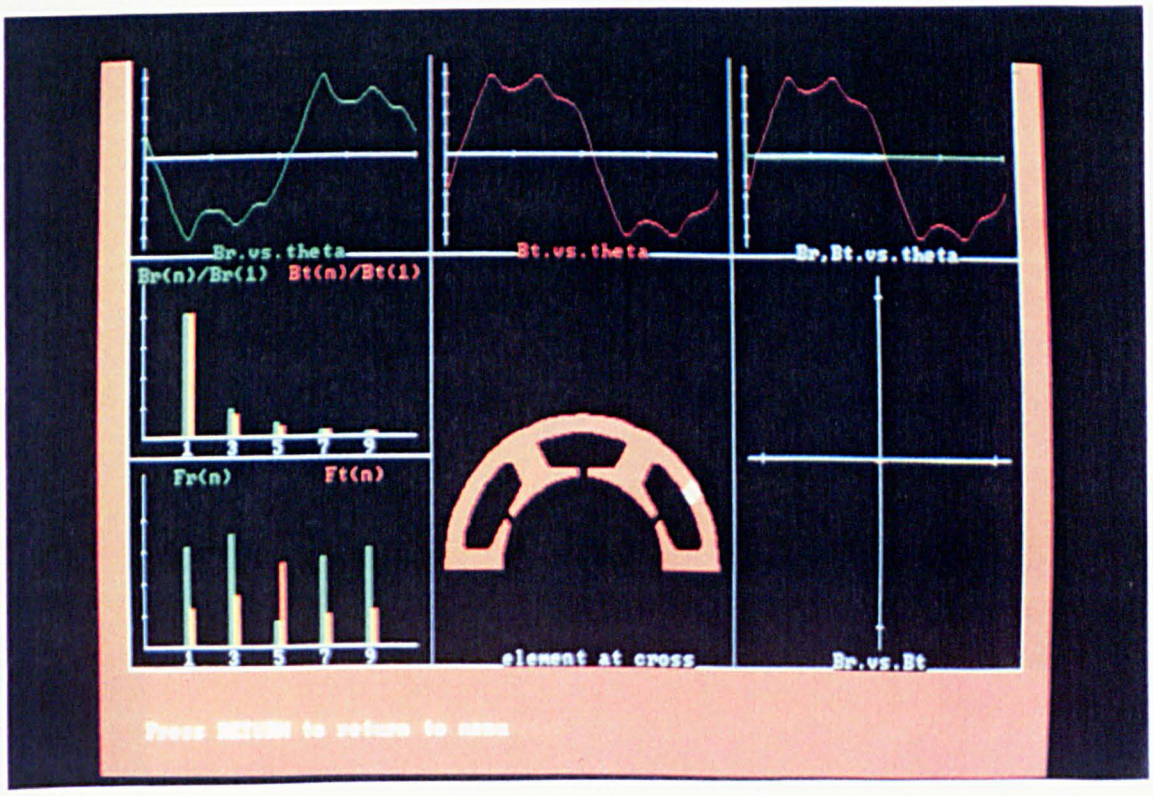


(a) Site 1.

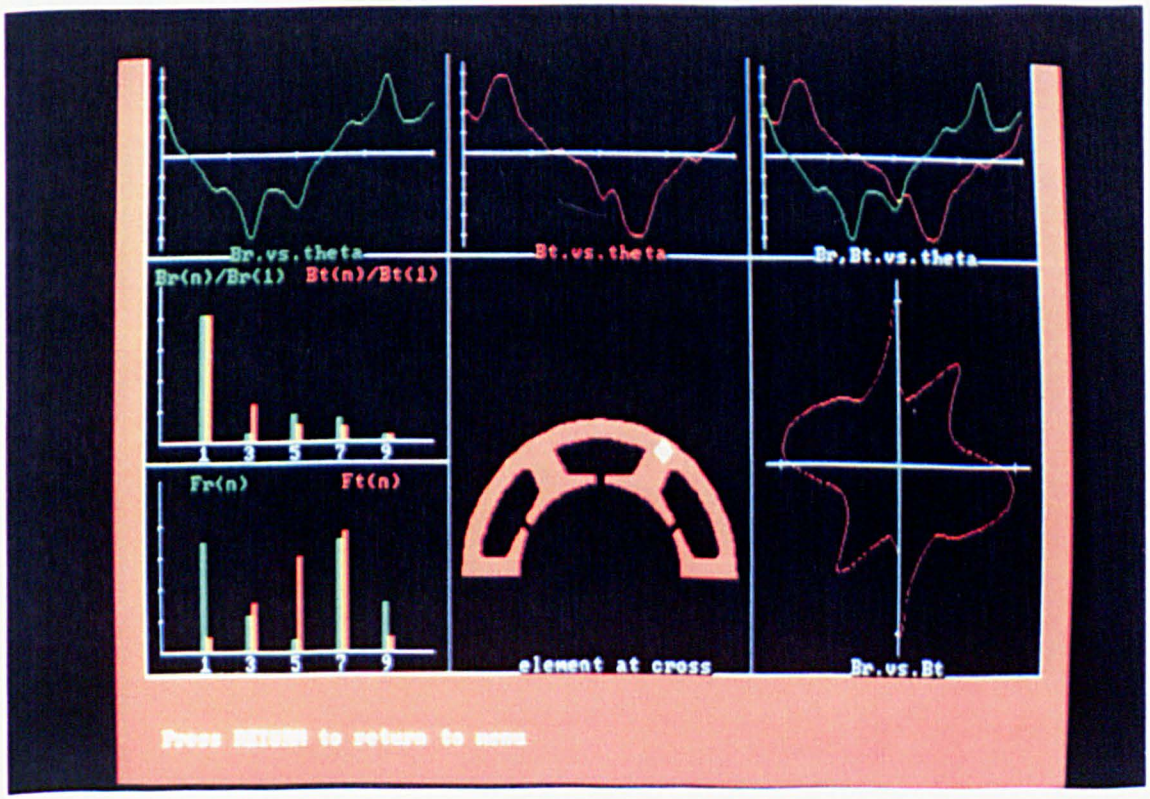


(b) Site 2.

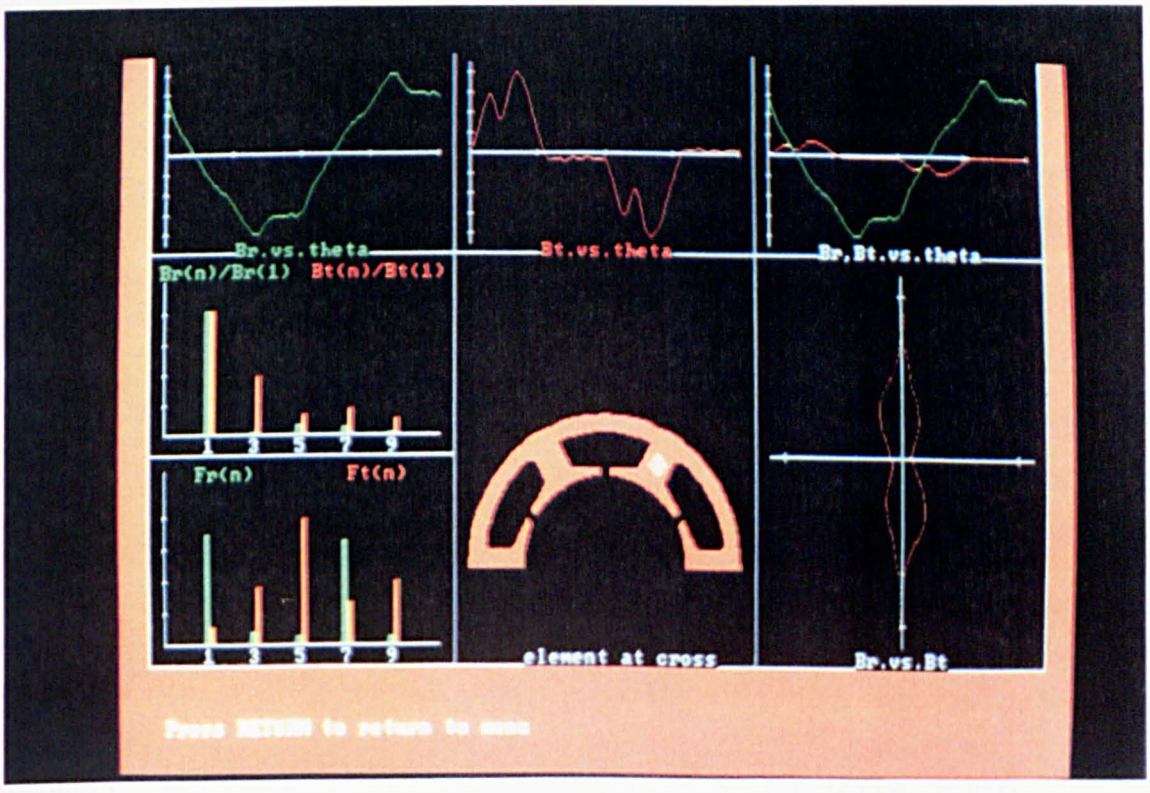


(c) Site 3.

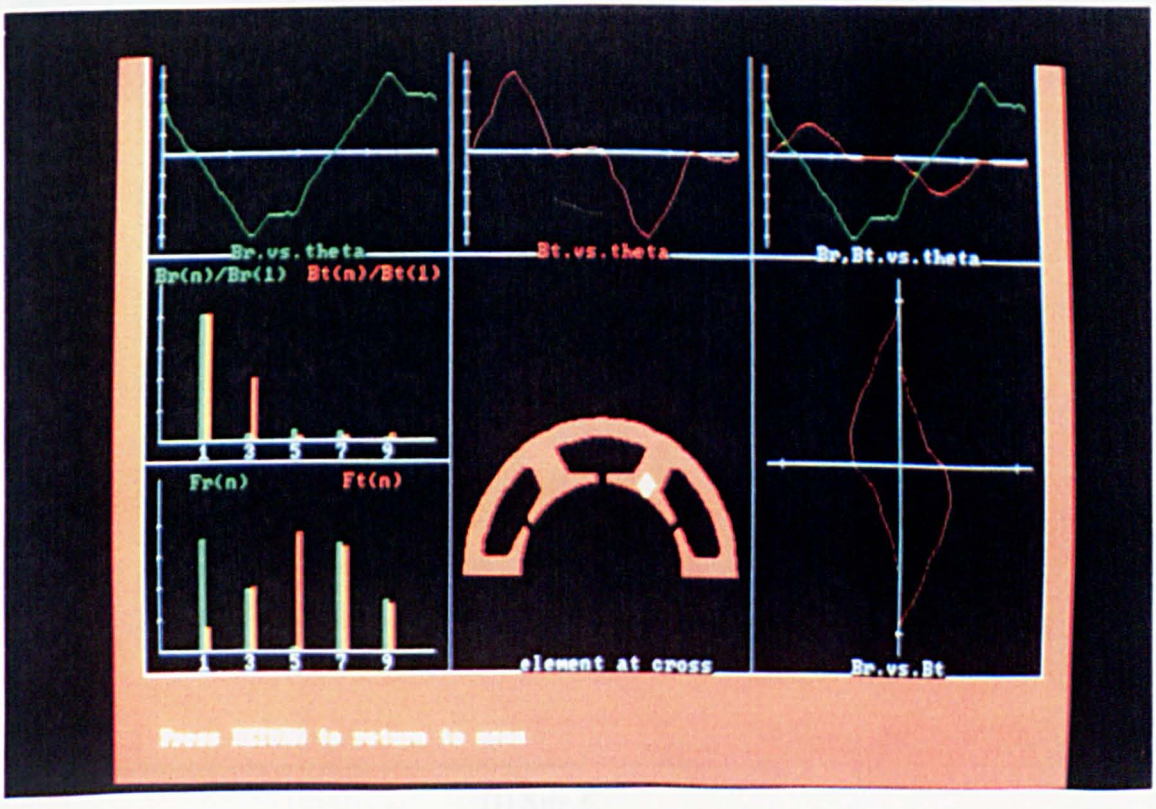


(d) Site 4.

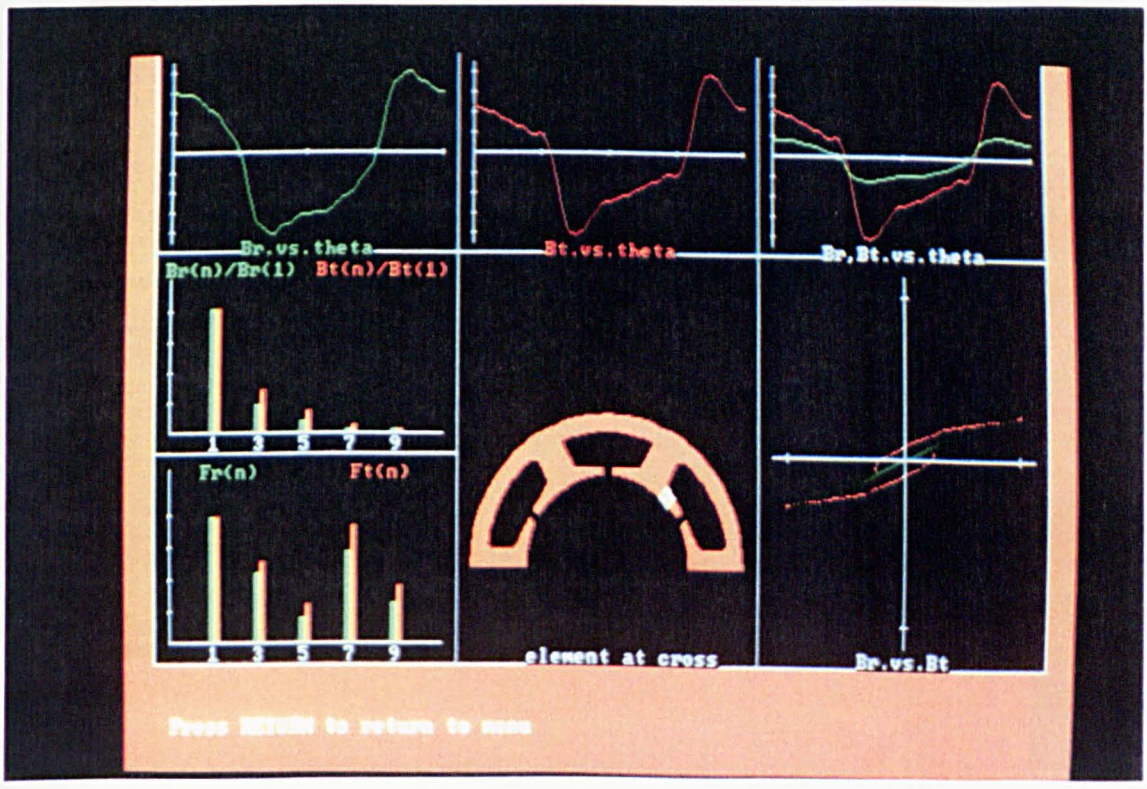


(e) Site 5.

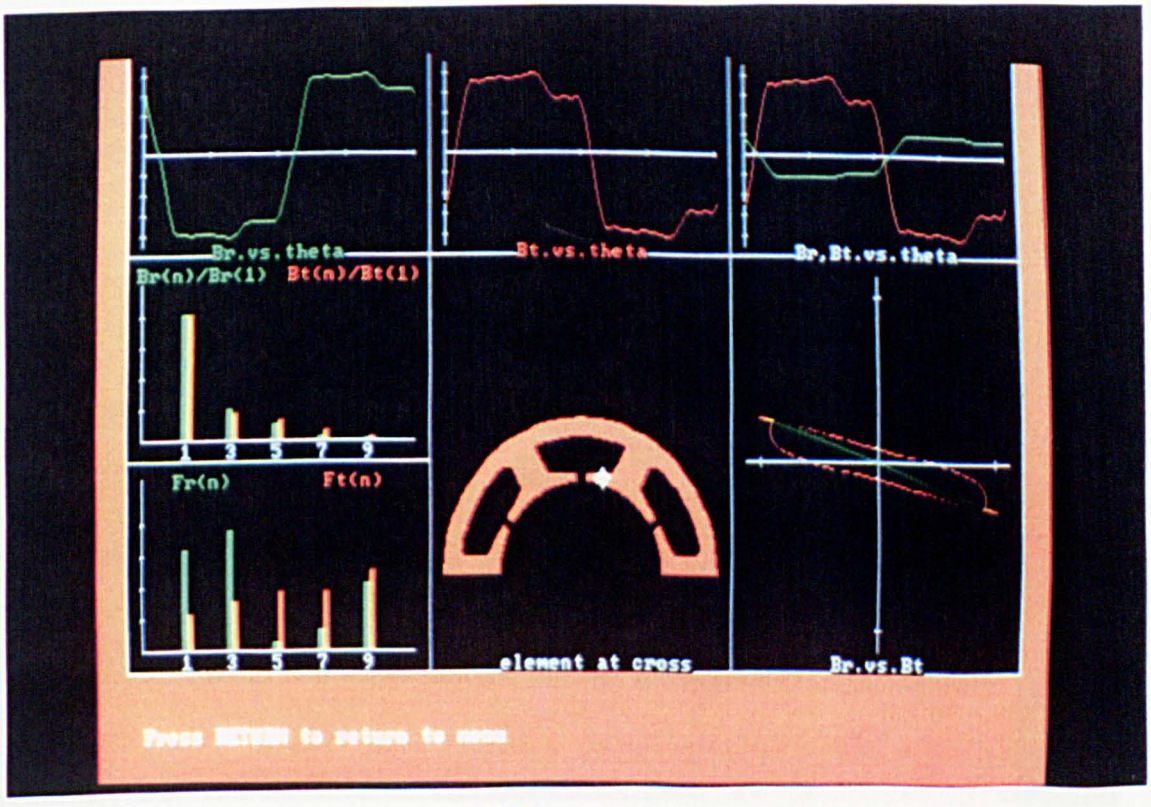


(f) Site 6.

Fig (4.54) Local flux density waveforms at selected sites on rated load. (Normal commutation)

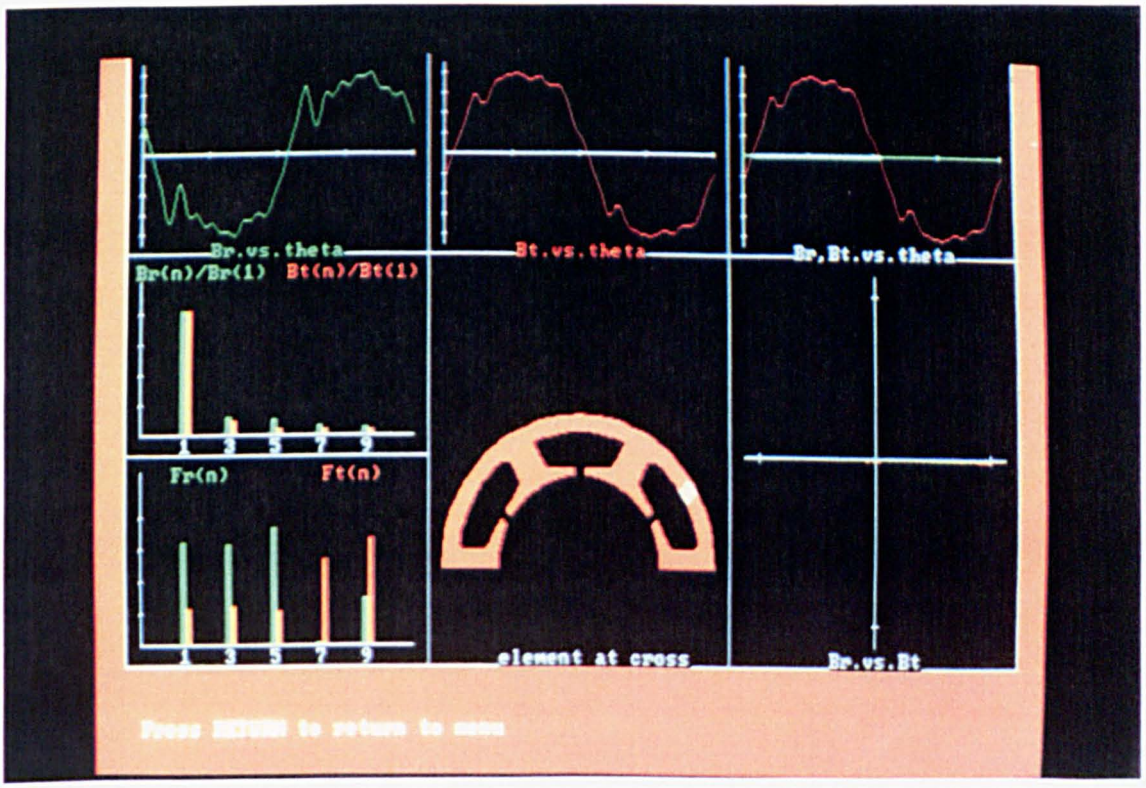


(a) Site1.

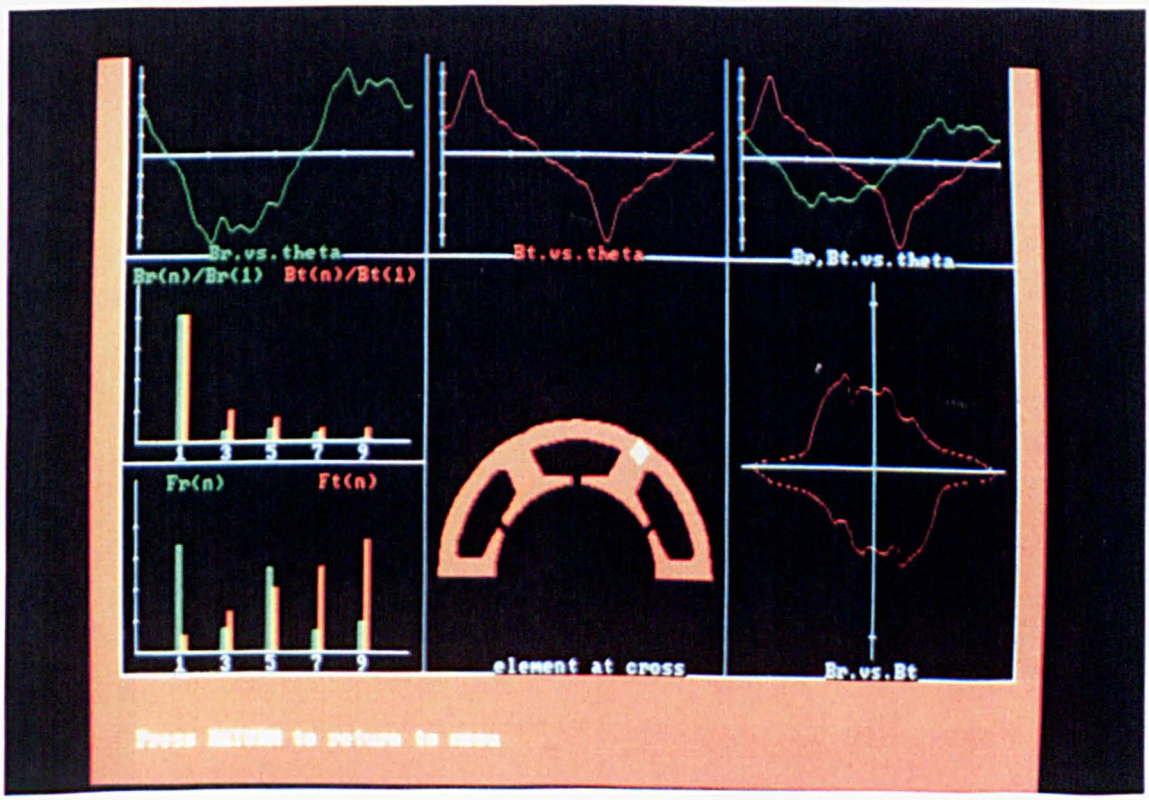


(b) Site 2.

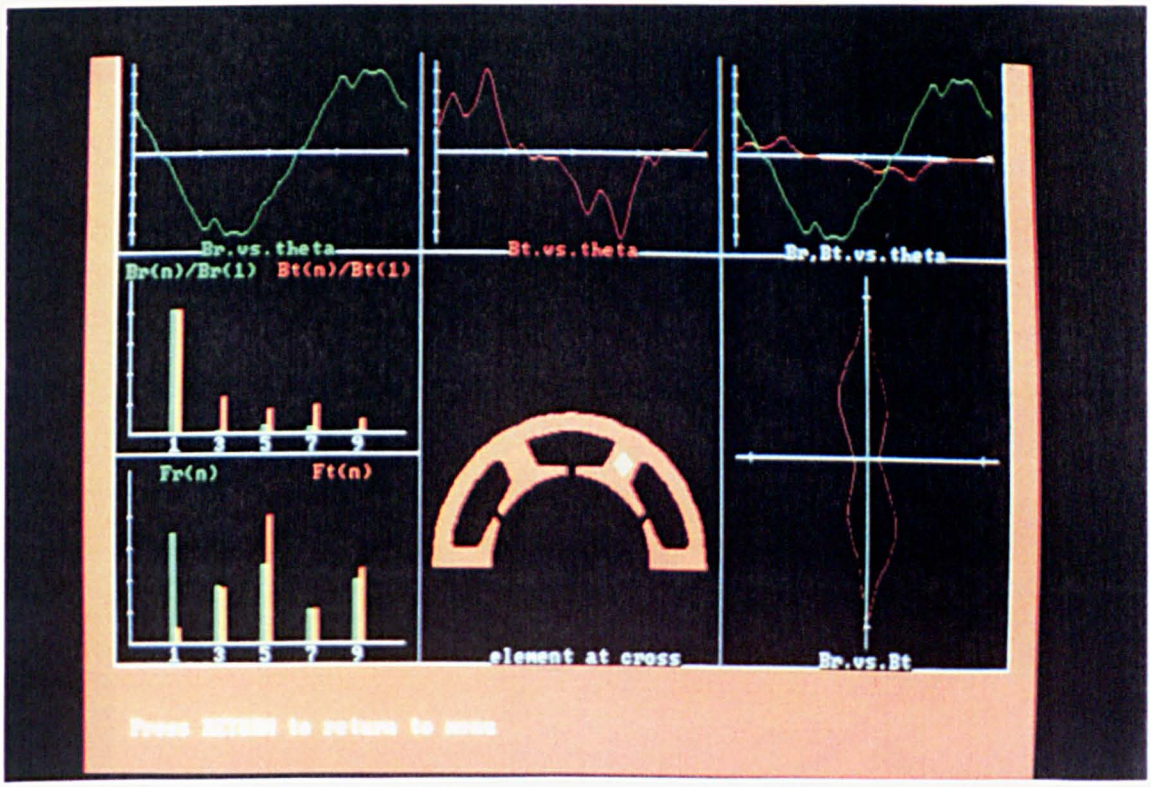


(c) Site 3.

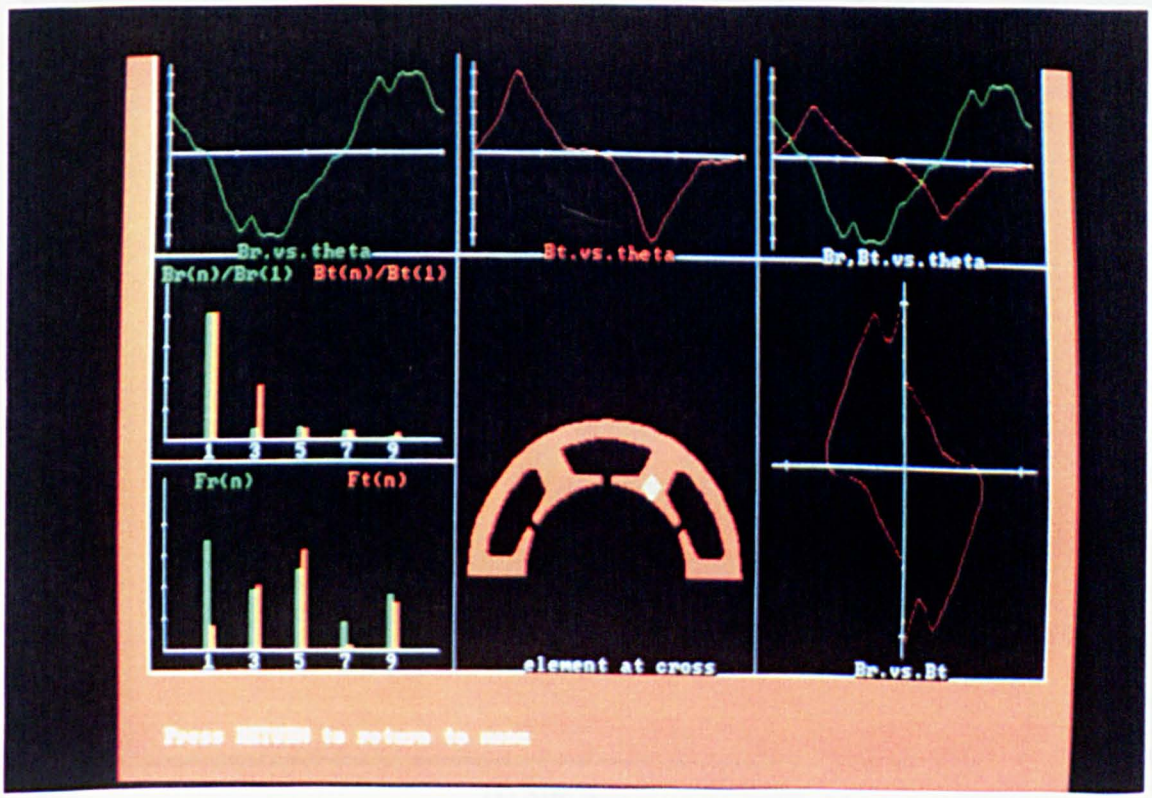


(d) Site 4.

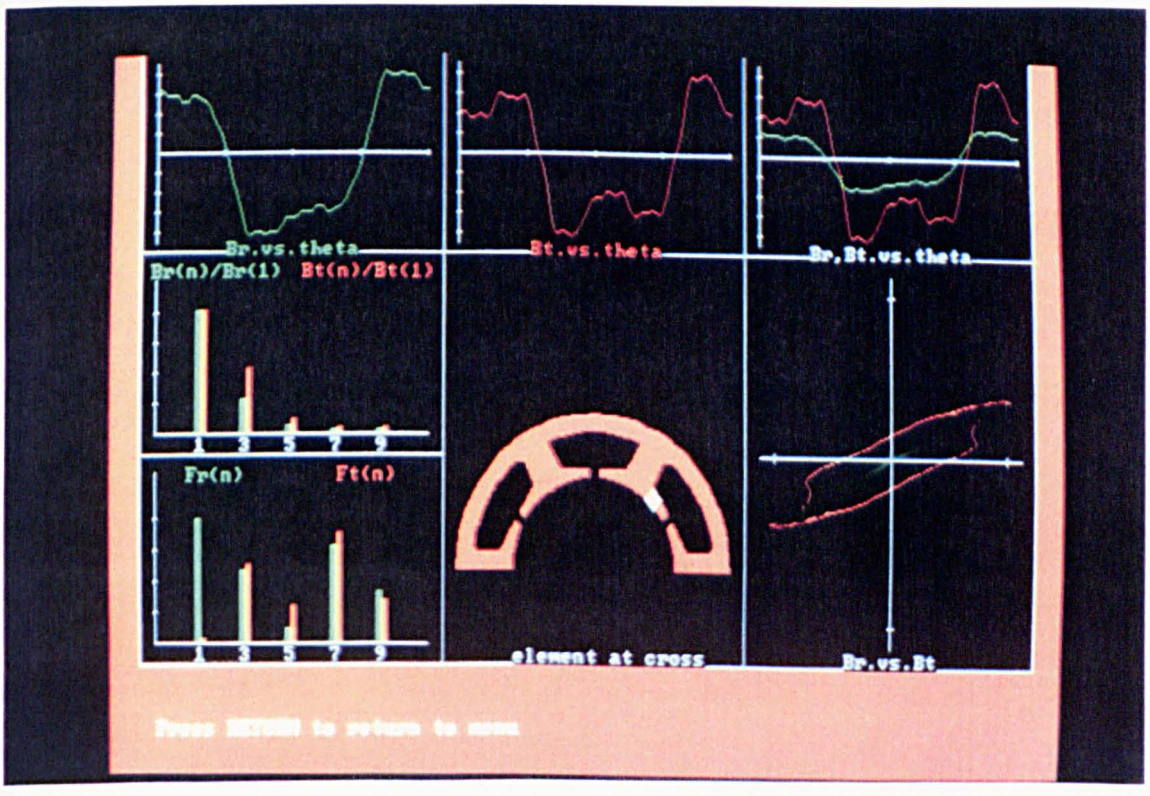


(e) Site 5.

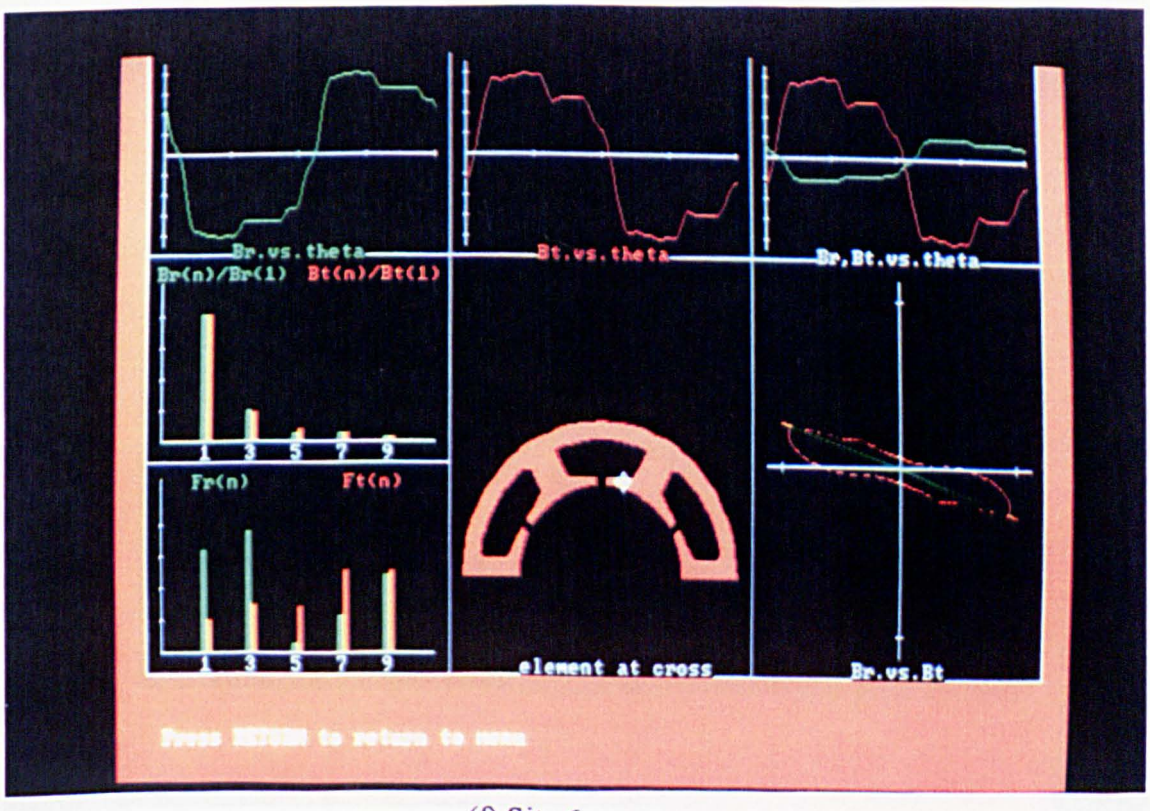


(f) Site 6.

Fig (4.55) Local flux density waveforms at selected sites at rated load. ($20^{o}$ advanced commutation)

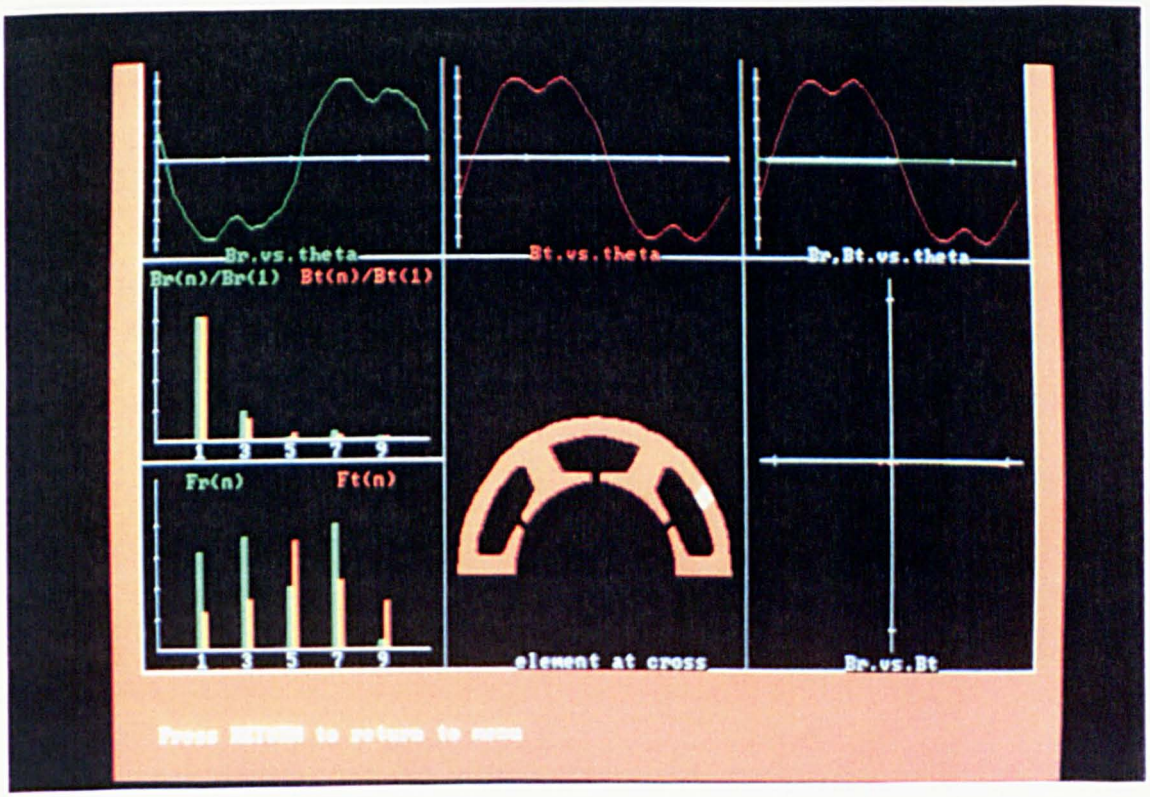


(a) Site 1.

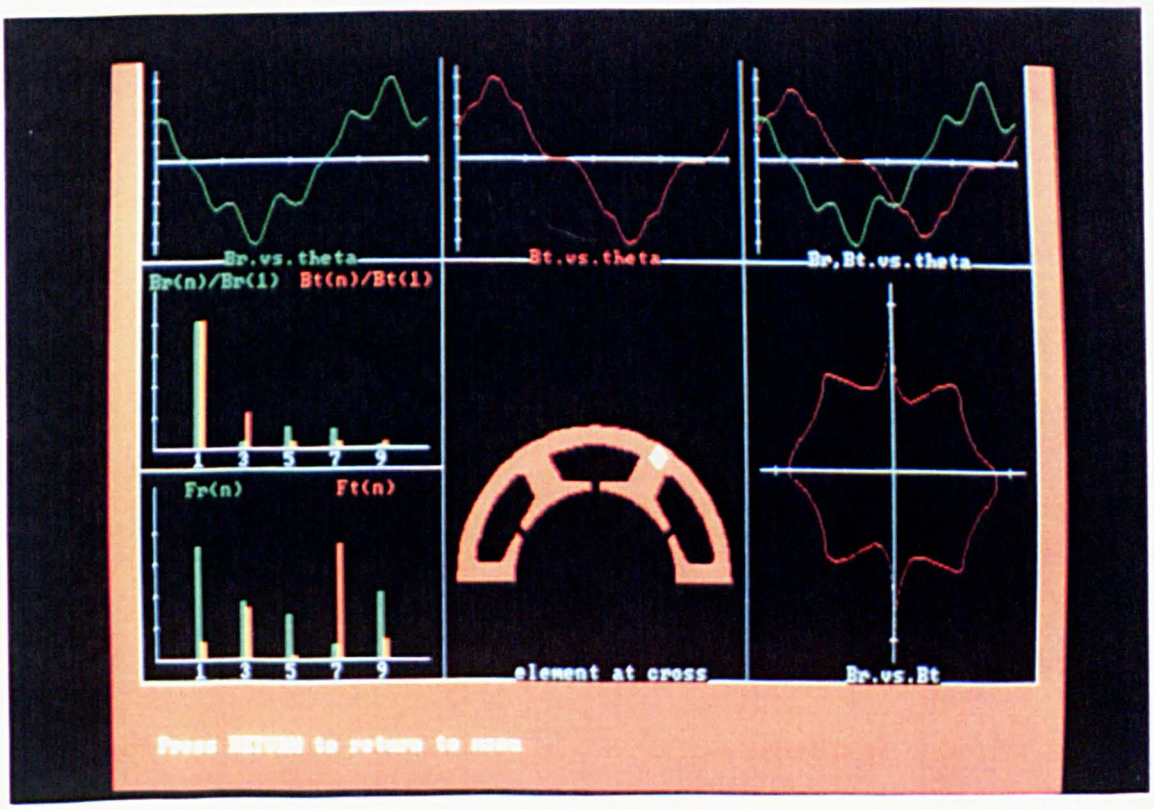


(b) Site 2.

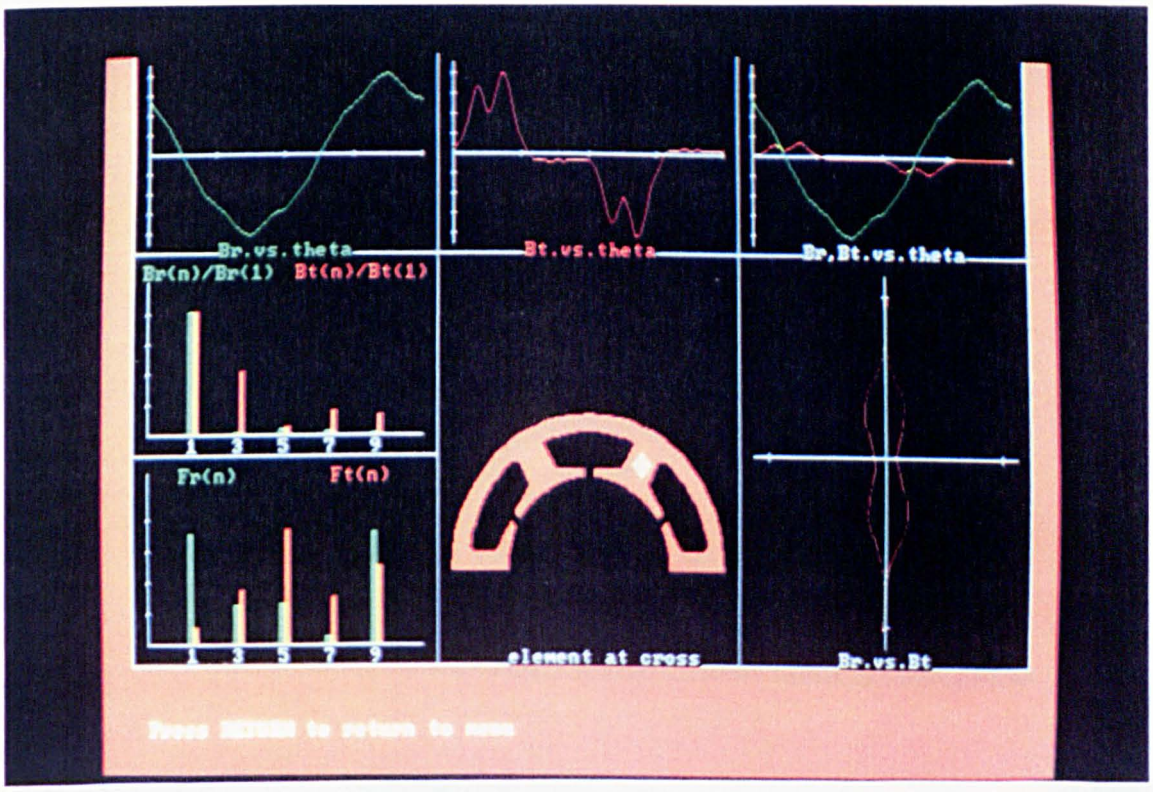


(c) Site 3.

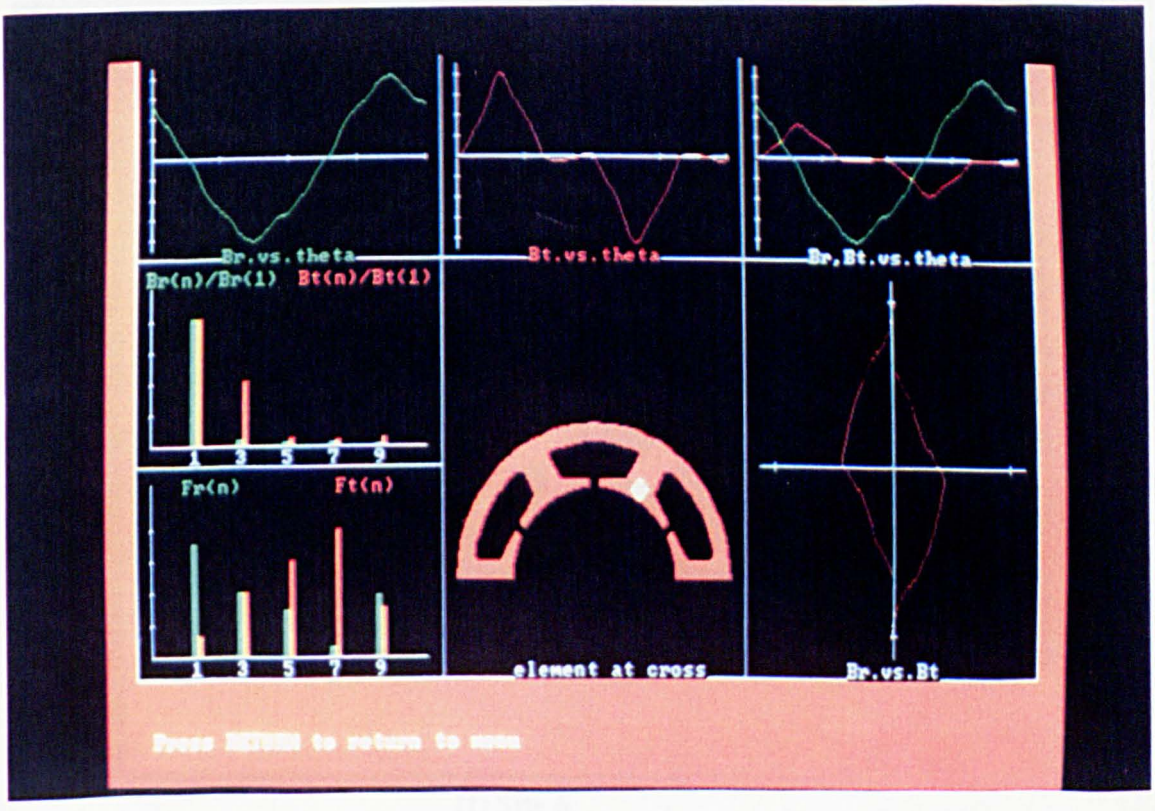


(d) Site 4.

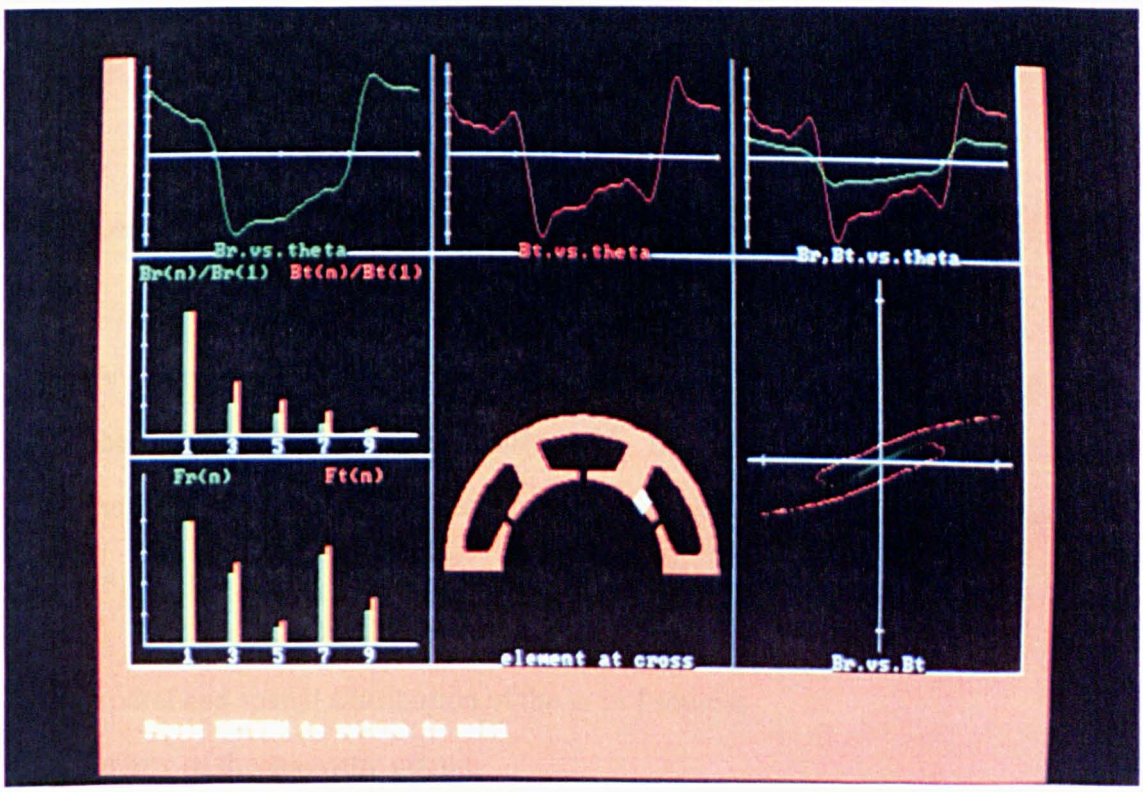


(e) Site 5.

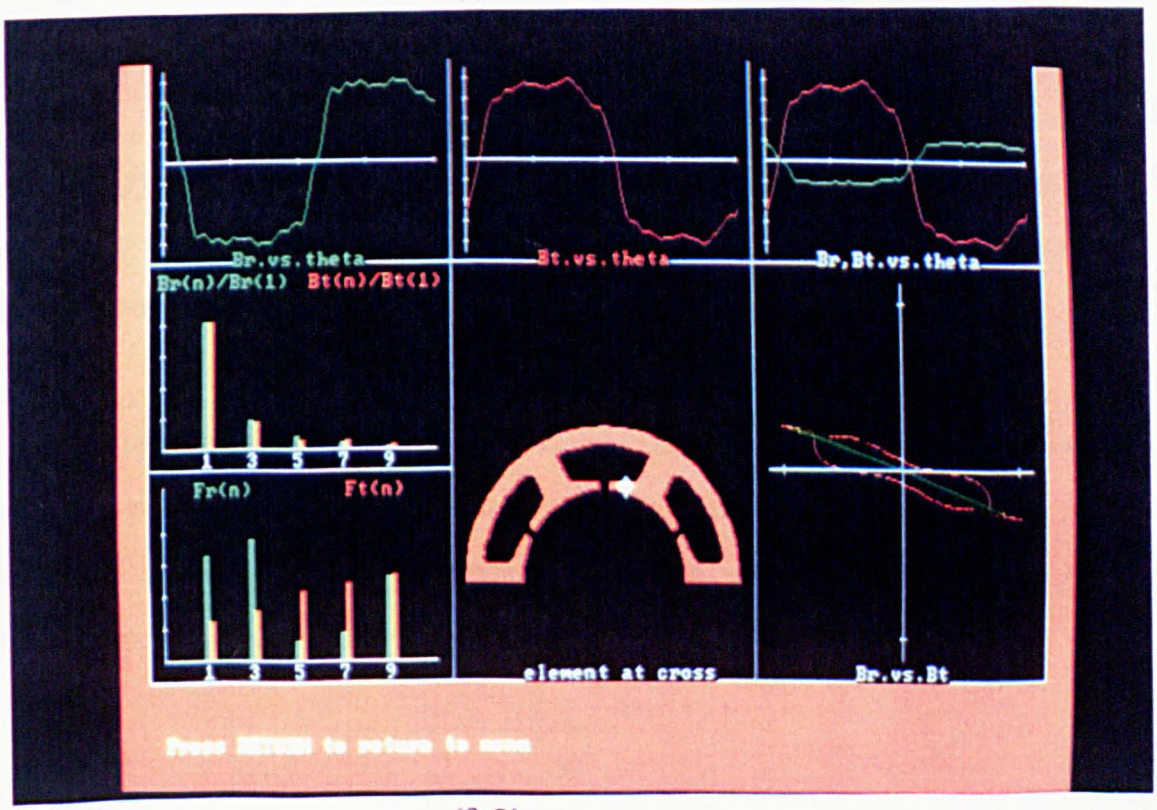


(f) Site 6.

Fig (4.56) Local flux density waveforms at selected sites at rated load. (20o retarded commutation)

# CHAPTER 5

# PREDICTION OF IRON LOSSES IN THE STATOR CORE OF BRUSHLESS DC MACHINES.

## 5.1) Introduction

Iron losses can represent a substantial portion of the total loss In electrical machines. Hence, they can influence considerably both the efficiency and the thermal performance. However, in all electrical machine topologies four fundamental parameters determine both the total iron loss and the iron loss density distribution, viz:

a. the temporal and spatial distribution of the m.m.f sources.
b. the geometry of the magnetic circuit.
c. the grade of the electrical steel laminations used for building the core.
d. the speed of the electrical machine.

Even though different machine topologies can be equipped with the same grade of laminations and run at the same speed, the temporal and spacial distribution of the m.m.fs and the shape of the magnetic circuit can make a major difference.

In this Chapter, two techniques, viz analytical and numerical, for the prediction of the iron loss in permanent magnet brushless dc motors are presented. However, whilst the application of the analytical technique is limited to open-circuit operation, the numerical techniqe caters for any load condition.

## 5.2) Iron losses on open-circuit operation

The prediction of the iron losses on open-circuit can be achieved either analytically or numerically. The analytical method is based on the technique described in Chapter 4 for prediction of the flux density waveforms in various parts of the stator core, whilst the numerical technique is based on finite element analysis for the prediction of the local flux density waveforms.

### 5.2.1) Analytical technique

In the analytical technique, the stator core is subdivided into 4 distinct regions, Fig (5.1), in each of which the flux density waveform is assumed to be the same throughout and is predicted using the technique described in Chapter 4. Since throughout the stator core, the flux density waveforms can be approximated as piece-wise linear, ie trapezoidal etc, the calculation of the hysteresis component of the stator core loss can be calculated using equation (3.1) or (3.33), according to the lamination material, whilst the eddy current loss component can be calculated using equations (3.37) and (3.38), for the classical and excess eddy current components respectively.

#### 5.2.1.1) Tooth body

In the tooth body the flux density waveform is essentially trapezoidal. Hence, the hysteresis component of the iron loss is given by:

$$P_{h\_t} = \frac{p\,\omega_r\,k_h\,B_{tmax}{}^{\alpha_h}\,V_t\,N_s\,\delta}{2\,\pi} \tag{5.1}$$

where $\omega_r$ and $V_t$ are the motor speed and the volume of the tooth body respectively. The classical eddy current component is given by:

$$P_{c\_t} = \frac{\sigma d^2}{12\,\pi^2} p\, N_s^2\, \omega_r^2\, B_{tmax}^2\, V_t \tag{5.2}$$

and the excess loss component is given by:

$$P_{e\_t} = \frac{2\, k_e\, p^{0.5}\, \omega_r^{1.5}\, N_s^{1.5}\, B_{tmax}^{1.5}}{\pi^{1.5}} V_t\, \delta \tag{5.3}$$

**5.2.1.2) Stator back-iron**

In the stator back-iron the flux density waveform is essentially triangular for 1 slot/pole/phase motors and piece-wise linear for 1/2 slot/pole/phase motors. In both cases, however, the hysteresis loss component is given by:

$$P_{h\_y} = \frac{p\, \omega_r\, k_h\, B_{ymax}^{\alpha_h}\, V_{yk}\, \delta}{2\,\pi} \tag{5.4}$$

where $V_{yk}$ is the volume of the stator back-iron. For the eddy current components, two cases are distinguished according to the number of slots/pole/phase, viz :

*a. 1/2 slot/pole/phase motors*

In this case, the classical eddy current component is given by:

$$P_{c\_y} = \frac{\sigma d^2}{\pi^2} \left[ B_{yc}^2 + \frac{(B_{ymax} - B_{yc})^2}{2} \right] p^2\, \omega_r^2\, V_{yk} \tag{5.5}$$

the excess eddy current component is given by:

$$P_{e\_y} = \frac{2\, k_e}{\pi^{1.5}} p^{1.5}\, \omega_r^{1.5} \left[ \sqrt{6}\, B_{yc}^{1.5} + (B_{ymax} - B_{yc})^{1.5} \sqrt{3} \right] V_{yk}\, \delta \tag{5.6}$$

*b. 1 slot/pole/phase motors*

The classical eddy current loss component is given by:

$$P_{c\_y} = \frac{\sigma d^2}{3\,\pi^2} p^2\, \omega_r^2\, B_{ymax}^2\, V_{yk} \tag{5.7}$$

whilst the excess eddy current component is

$$P_{c\_y} = \frac{2\sqrt{2}\, k_e}{\pi^{1.5}} p^{1.5}\, \omega_r{}^{1.5}\, B_{ymax}{}^{1.5}\, V_{yk}\, \delta \tag{5.8}$$

**5.2.1.3) Tooth tips**

It was shown In Chapter 4 that a tooth tip can be divided into two regions, ie viz regions 1 and 2 with reference to Fig (5.1). In region 1, the flux density has two orthogonal flux density components, viz radial and circumferential, for which associated losses have to be computed independently, whilst in region 2 the flux density is assumed to be unidirectional.

*a. Region 1*

The total hysteresis loss component is given by:

$$P_{h\_ttp1} = \frac{p\, \omega_r\, k_h\, V_{ttp1}\, N_s\, \delta}{2\pi} \left( B_{tr}{}^{\alpha_h} + B_{t\theta}{}^{\alpha_h} \right) \tag{5.9}$$

where $V_{ttp1}$ is the volume of region 1. The eddy current loss components are given by:

$$P_{c\_ttp1} = \frac{\sigma d^2}{6\pi^2} p\, N_s{}^2\, \omega_r{}^2\, V_{ttp1} \left( B_{tr}{}^2 + B_{t\theta}{}^2 \right) \tag{5.10}$$

and

$$P_{e\_ttp1} = \frac{2\, k_e}{\pi^{1.5}} p^{0.5}\, N_s{}^{1.5}\, \omega_r{}^{1.5}\, V_{ttp1}\, \delta \left( B_{tr}{}^{1.5} + B_{t\theta}{}^{1.5} \right) \tag{5.11}$$

*b. Region 2*

The hysteresis loss component is given by:

$$P_{h\_ttp2} = \frac{p\, \omega_r\, k_h\, V_{ttp2}\, N_s\, \delta}{2\pi} B_{t2}{}^{\alpha} \tag{5.12}$$

where $V_{ttp2}$ is the volume of region 2, whilst the classical eddy current component is given by:

$$P_{c\_ttp2} = \frac{\sigma d^2}{6\pi^2 g} p^2 \omega_r{}^2 \mu_r h_m N_s Vttp2 B_{t2}{}^2 \tag{5.13}$$

and the excess loss component by:

$$P_{e\_ttp2} = \frac{4 k_e}{\pi^{1.5} g^{0.5}} p^{1.5} \omega_r{}^{1.5} \mu_r{}^{0.5} h_m{}^{0.5} B_{t2}{}^{1.5} V_{ttp2} N_s \delta \tag{5.14}$$

**5.2.2) Numerical technique**

As was described in Chapter 4, the technique is based on the synthesis of local flux density waveforms from a series of magnetostatic finite element solutions, each of which corresponds to a descrete number of rotor positions, spanning half an electrical cycle. The different components of the local iron loss density are subsequently computed numerically by the following:

*a. Hysteresis loss component*

The hysteresis loss component is given by:

$$P_h = \frac{k_h B_m{}^{\alpha_h} \omega_r p}{2\pi} \tag{5.15}$$

*b. Classical eddy current component*

The classical eddy current component is given by :

$$P_c = \frac{\sigma d^2}{12\delta} \frac{1}{T} \int_T \left( \frac{dB}{dt} \right)^2 dt \tag{5.16}$$

or, in terms of the electrical angle $\theta$,

$$P_c = \frac{\sigma d^2}{24\pi\delta} p^2 \omega_r{}^2 \int_0^{2\pi} \left( \frac{dB}{d\theta} \right)^2 d\theta \tag{5.18}$$

*c. Excess eddy current loss component*

Similarly, in terms of the electrical angle, the excess eddy current loss component is given by:

$$P_e = \frac{k_e\, p^{1.5}\, \omega_r^{1.5}}{2\pi} \int_0^{2\pi} \left| \frac{dB}{d\theta} \right|^{1.5} d\theta \qquad (5.19)$$

The total iron loss at any specified speed is then given by:

$$P_{total} = l_{stk}\ \delta \sum_{n=1}^{N_e} [(\, P_h + P_c + P_e\,)\, A_n] \qquad (5.20)$$

where $l_{stk}$ is the axial length of the stator stack, $N_e$ is the number of elements in the finite element mesh, and $A_n$ the area of the $n^{th}$ finite element.

## 5.3) Iron losses on-load

The prediction of the iron loss on load follows simply from the technique, described in Chapter 4, which couples a drive system simulation to the finite element analyses. Local flux density waveforms are synthesised, and the local iron loss density distribution and the total loss are computed, exactly as for open-circuit operation.

## 5.3) Measurement technique

### 5.3.1) Open-circuit operation

The open-circuit stator iron losses are measured using the torque-speed method, ie the motor is driven with the stator windings on open-circuit up to the required speed by a second coupled motor. The total power loss on-open circuit is obtained from the loss torque and speed. However, since the open-circuit power loss also includes a

mechanical loss due to friction and windage, the measurement was repeated with the stator stack replaced by a non-magnetic non-conducting material. Fig (5.2) shows a schematic of the measurement rig.

### 5.3.2) On-load operation

Fig (5.3) shows a schematic of the test rig. The measurement is undertaken under closed-loop speed control. The input power of the machine is measured using a 3-phase power analyser, whilst the output power is obtained from the measured torque and speed. The iron loss is then determined from:

$$P_{iron} = P_{input} - P_{output} - P_{copper} - P_{mechanical} \tag{5.21}$$

The copper losses $P_{copper}$ are determined from:

$$P_{copper} = 3\,R\,I^2 \tag{5.22}$$

where R is the resistance per phase, and $I$ is the rms phase current. The winding resistance was measured, using a milli-ohmeter, immediately after switching off the motor, after the winding had attained its steady-state temperature rise.

## 5.4) Iron losses of prototype motor

The iron loss of the prototype 1/2 slot/pole/phase 150 W, 3-phase, 4-pole, 1.9 A rms, motor, which was used for the investigation of the flux waveforms in Chapter 4, has been measured and predicted both on open-circuit and on load.

### 5.4.1) Open-circuit iron loss

Fig (5.4) shows the measured windage and friction losses. Fig (5.5) shows a comparison between measured and predicted open-circuit iron loss, for which fairly good agreement can be seen. Further, Fig (5.6) shows the distribution of the total iron loss density throughout a cross-section of the stator core, whilst Figs (5.7) and (5.8) show distributions of the ratio of the hysteresis loss and the eddy current loss components to the total iron loss density respectively.

### 5.4.2) Iron loss at rated load

Three operating conditions have been considered, ie normal commutation, $20^{o}$ advanced commutation, and $20^{o}$ retarded commtation, which correspond to the conditions under which the flux waveforms were investigated in Chapter 4. Table (5.1) compares the computed total iron loss for each condition with both the measured and the open-circuit iron loss. It will be seen that, unlike the open-circuit operation, there is now a considerable discrepancy between the measured and computed results. The likely reason for this is that, firstly, the measurement technique employed inherently introduces significant error in the total loss measurement which could be eliminated only by employing a calibrated calorimetric technique. Secondly, because of the high quality of the steel used for the stator stack, in this motor the iron loss represents only about 15% of the total loss. Hence, any error in the measurement of the other loss components, ie copper and mechanical losses, will have a considerable effect on the accuracy of the iron loss measurement.

Nevertheless, from the computed and measured total iron losses, it can be seen that the operating condition has a considerable effect on the total iron loss. Further, it can be seen that advancing commutation results in the least change to the total iron loss.

Table (5.1) On-load iron loss of the prototype motor at 2000 rpm.

| | Computed | | Measured |
|---|---|---|---|
| | Numerical | Analytical | |
| Open-circuit | 2.01 | 1.87 | 1.97 |
| Normal commutation | 3.28 | - | 7.33 |
| $20^0$ advanced commutation | 2.26 | - | 6.66 |
| $20^0$ retarded commutation | 3.41 | - | 6.80 |

Fig (5.9) shows the distribution of the total iron loss density throughout the stator core for normal commutation, whilst Figs (5.10) and (5.11) show the corresponding distributions of the ratio of the hysteresis loss and the eddy current loss components to the total iron loss density respectively. Fig (5.12) shows the distribution of the total iron loss density throughout the stator core for $20^0$ advanced commutation, whilst Figs (5.13) and (5.14) show the corresponding distributions of the ratio of the hysteresis loss and the eddy current loss components to the total iron loss density respectively, whilst Figs (5.15), (5.16) and (5.17) show corresponding distributions for $20^0$ retarded commutation. It can be seen, that, as a consequence of the field asymmetry, the iron loss density on load is asymmetrical with regards to a tooth axis.

## 5.5) Conclusions

In this chapter, it has been shown that both the analytical and numerical techniques provide a fairly good estimate of the iron losses on open-circuit. Therefore, even though the analytical technique does not cater for the effects of load, and despite the fact that the iron loss changes with load it can be employed at an early stage in the design process if a quick estimation is required.

It has also been shown that both the iron loss density distribution and the total iron loss can be affected markedly by the operating condition of a brushless drive. However, this has to be predicted by a numerical technique, the utility of which has

been confirmed by experiment. Hence, the assumption that the iron loss remains more or less constant throughout the whole range of operating conditions can be very erroneous.

Finally, it has been emphasised that the torque-speed method for measuring the iron losses can be very unreliable. Hence, methods for their direct measurement, such as a the calorimetric method, are preferred. However, time precluded the development of such a method.

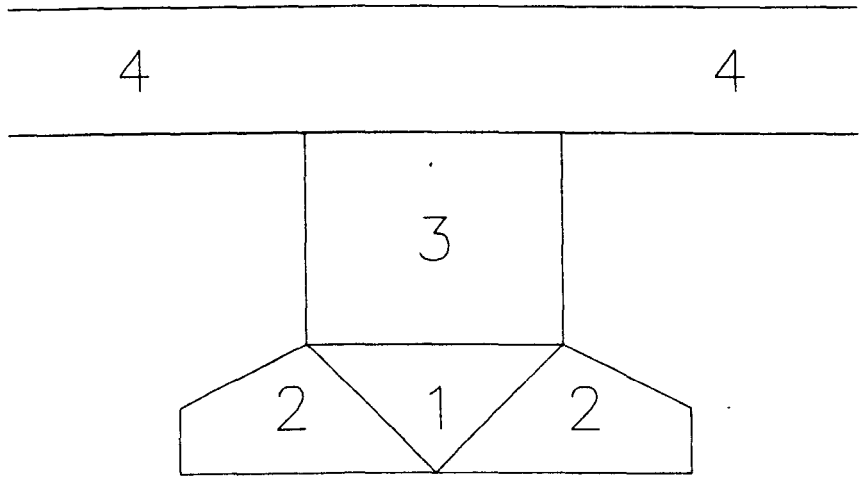


Fig (5.1) Different regions of the stator core.

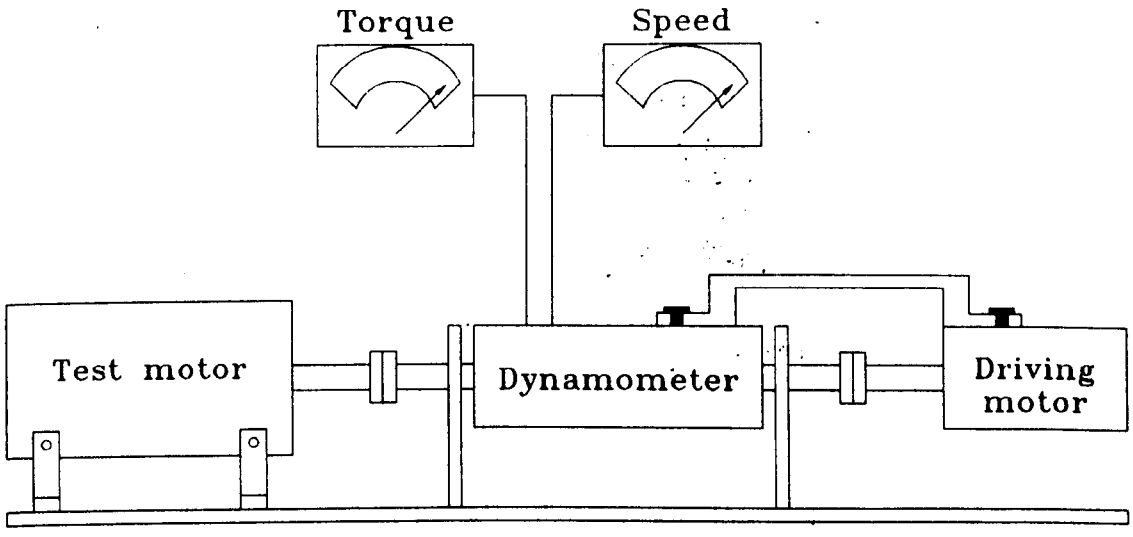


Fig (5.2) Schematic of the rig for the measurement of the mechanical losses and open-circuit iron loss.

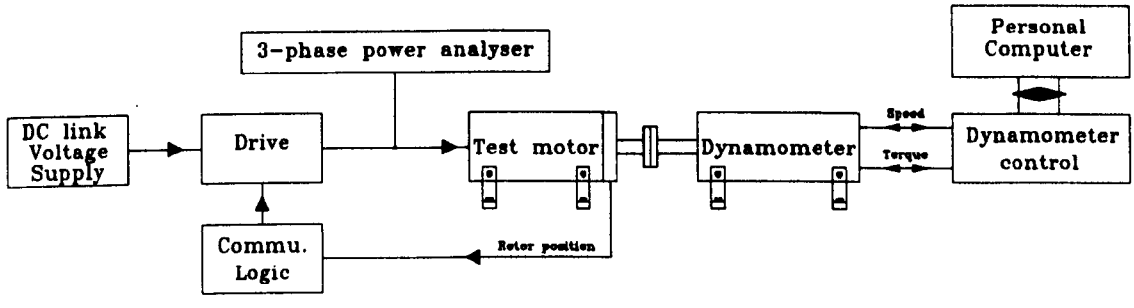


Fig (5.3) Schematic of the rig for the measurement of the on-load iron loss.

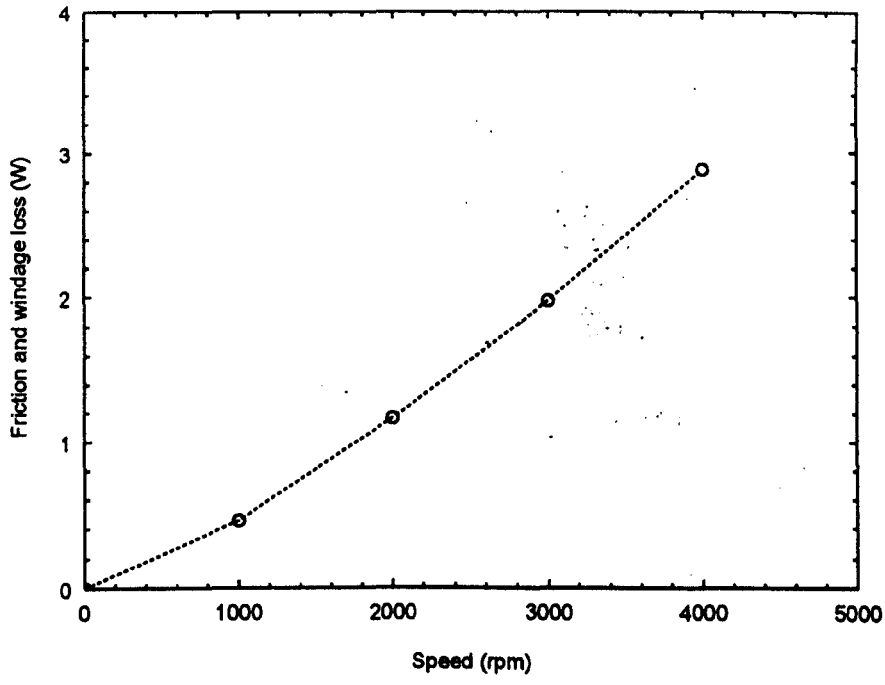


Fig (5.4) Measured windage and friction losses.

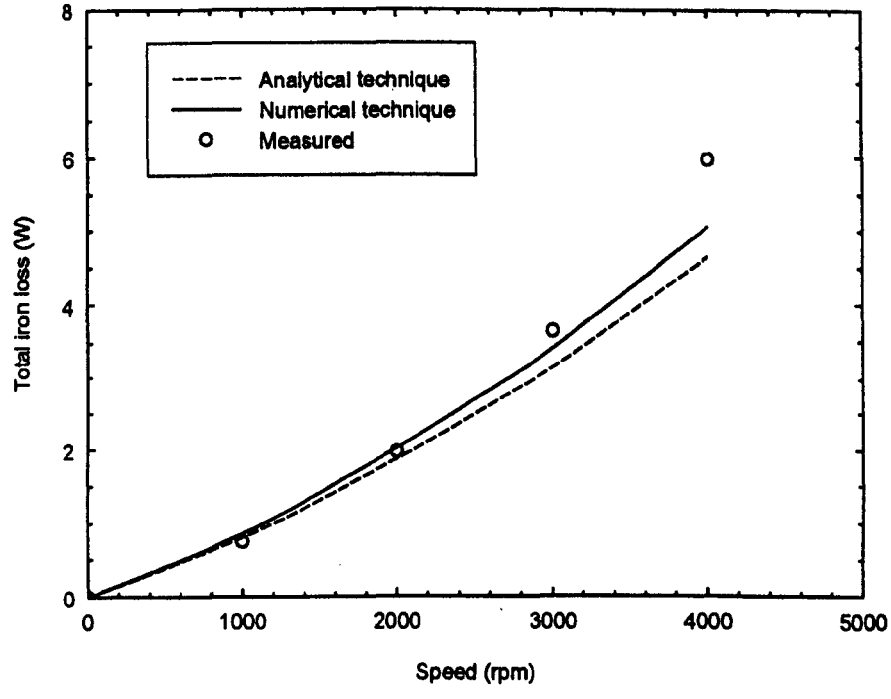


Fig (5.5) Comparison between measured and computed open-circuit iron loss.

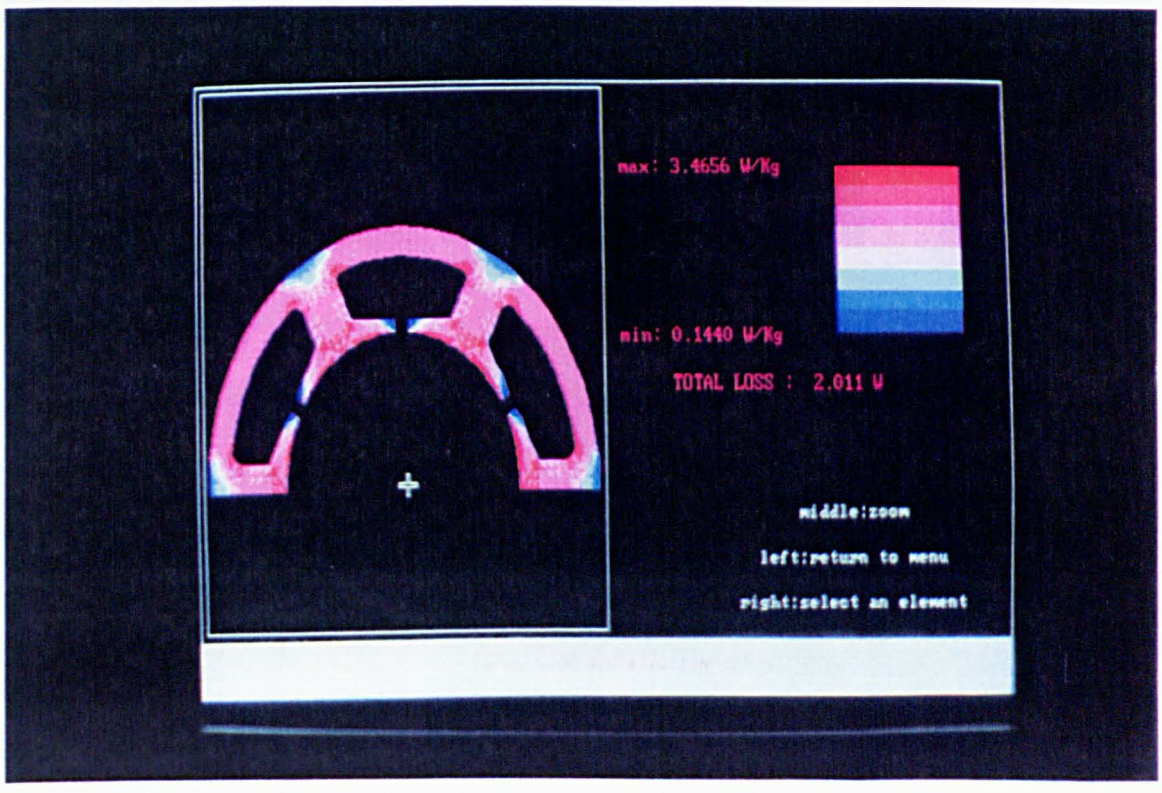


Fig (5.6) Total iron loss density distribution on open-circuit. (2000 rpm)

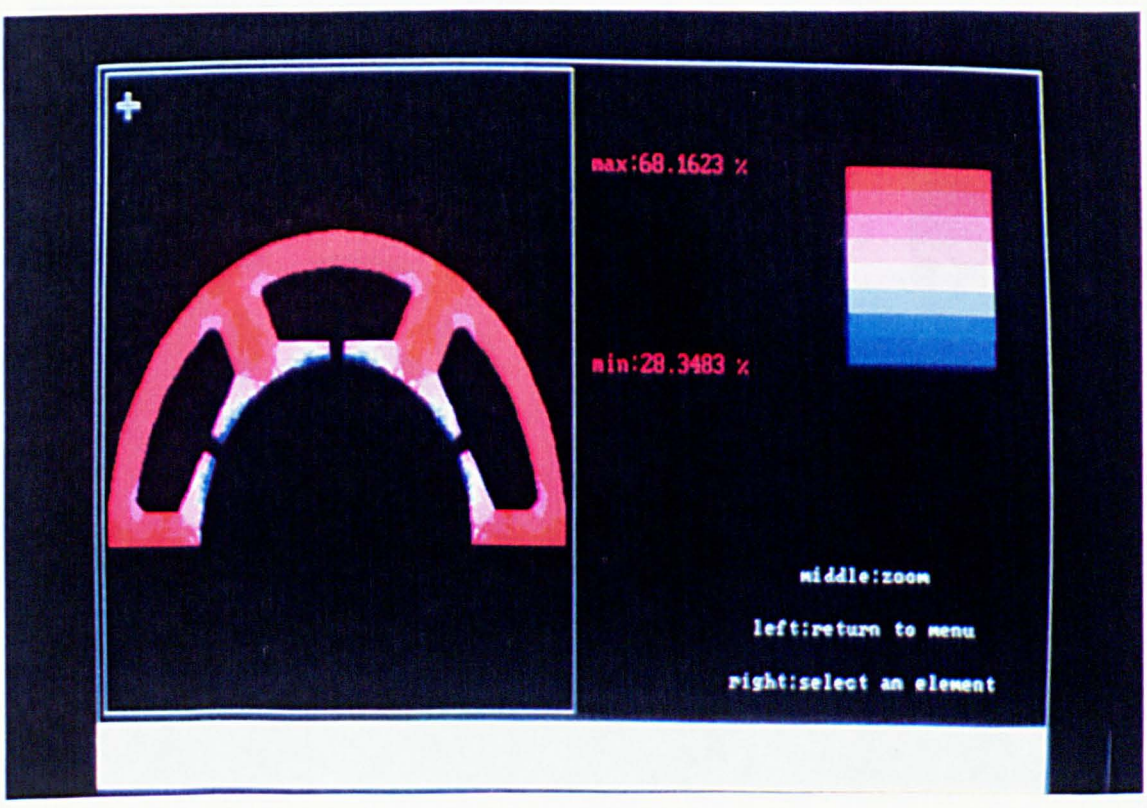


Fig (5.7) Hysteresis loss component distribution on-open circuit. (2000 rpm)

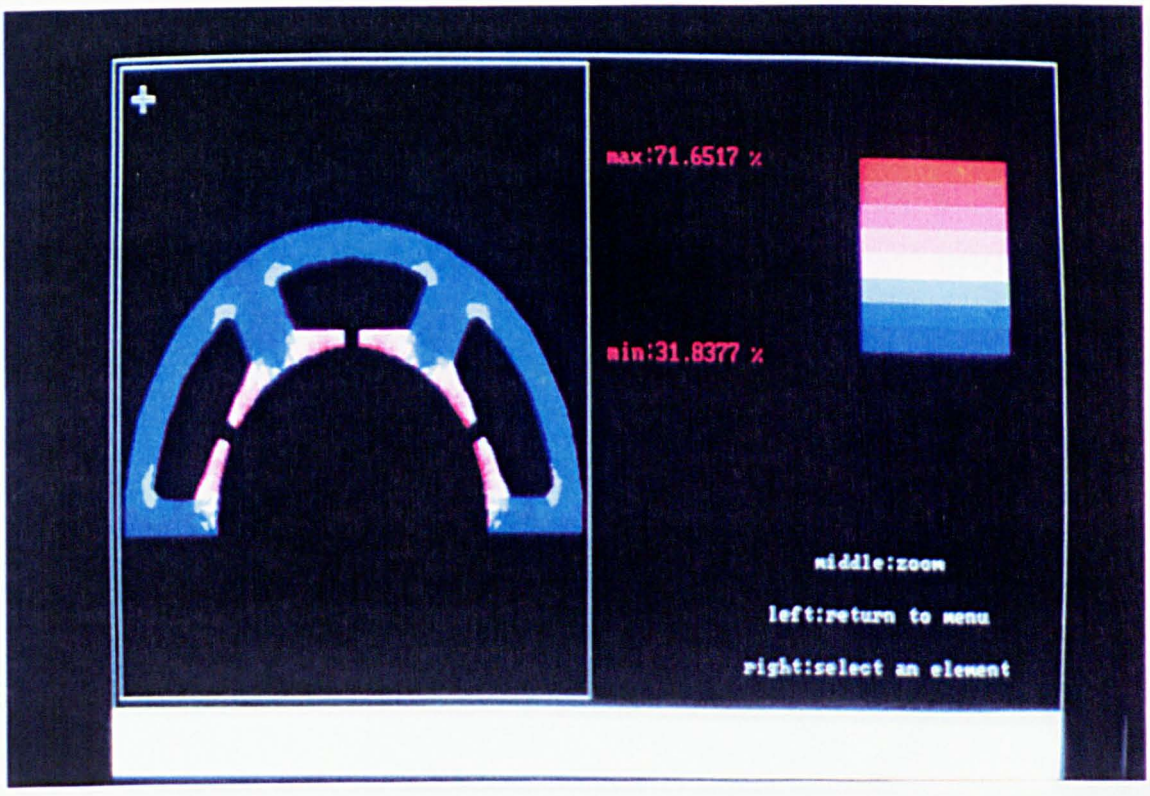


Fig (5.8) Eddy current loss component distribution on open-circuit. (2000 rpm)

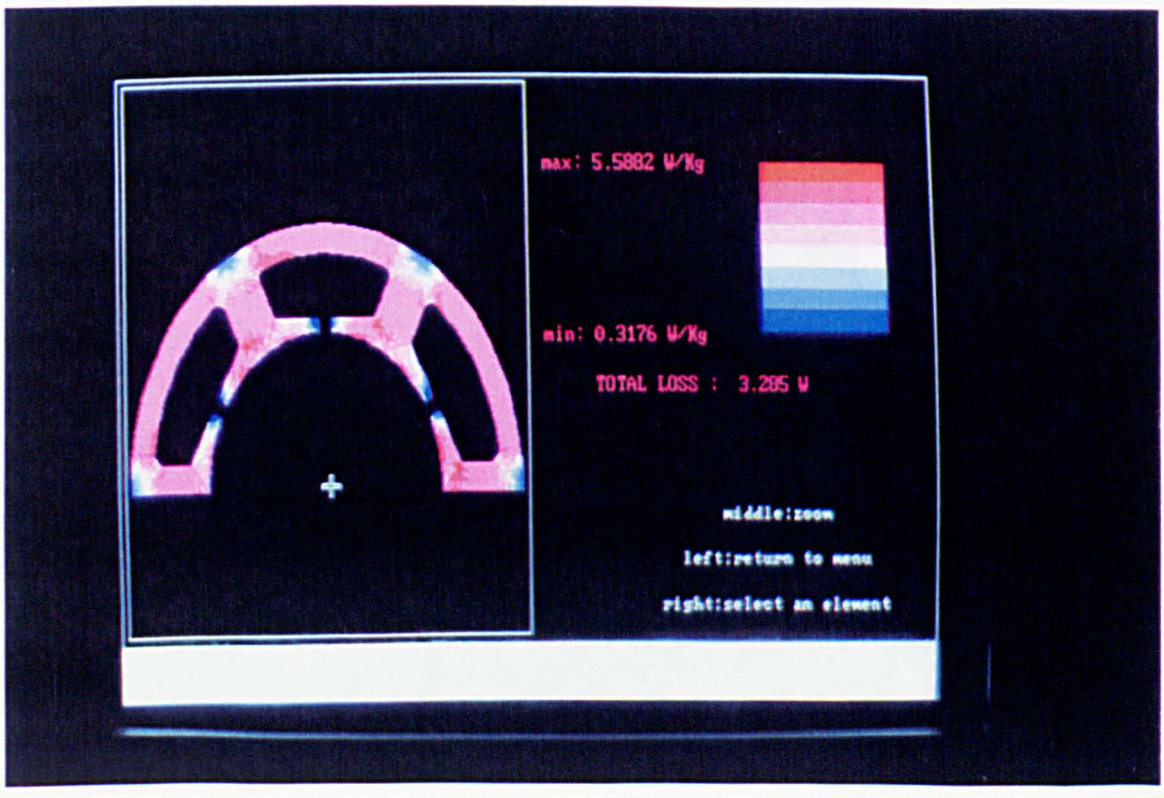


Fig (5.9)Total iron loss density distribution at rated load. (Normal commutation)


Fig (5.10) Hysteresis loss component distribution at rated load. (Normal commutation strategy)


Fig (5.11) Eddy current loss component distribution at rated load. (Normal commutation strategy)

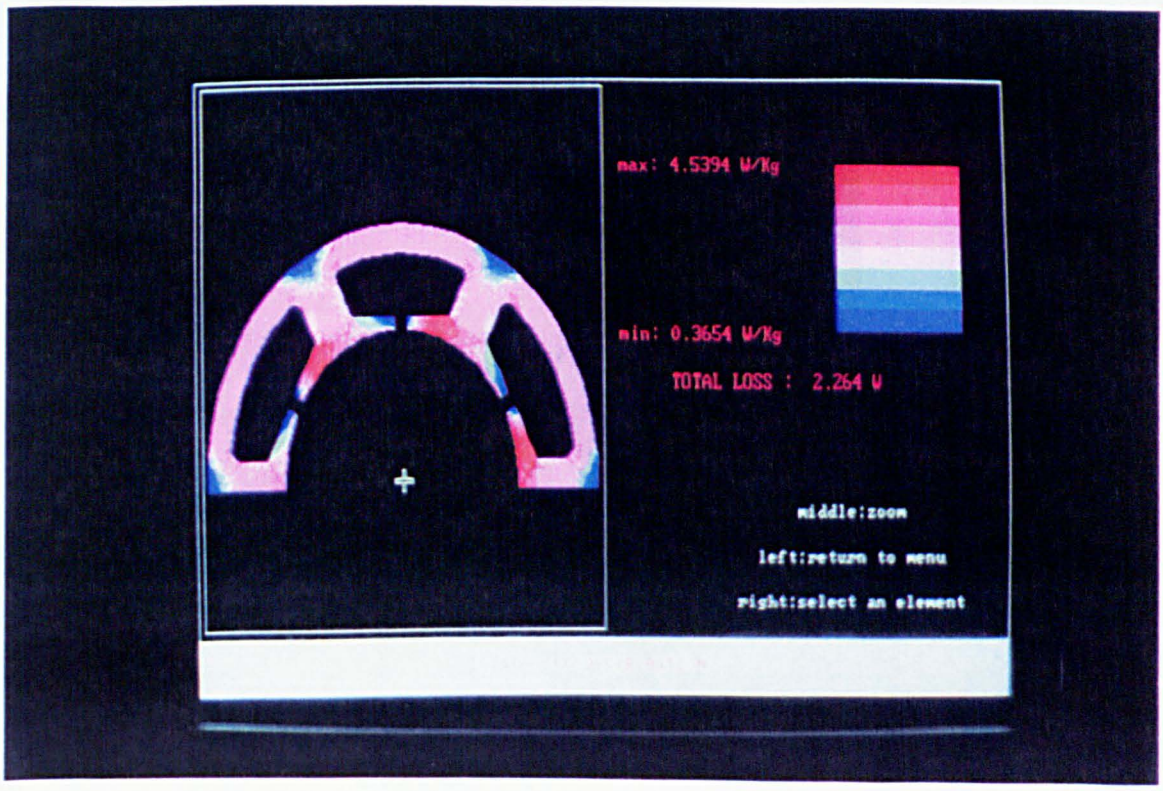


Fig (5.12) Total iron loss density distribution under advanced commutation strategy.


Fig (5.13) Hysteresis loss component distribution under advanced commutation strategy.

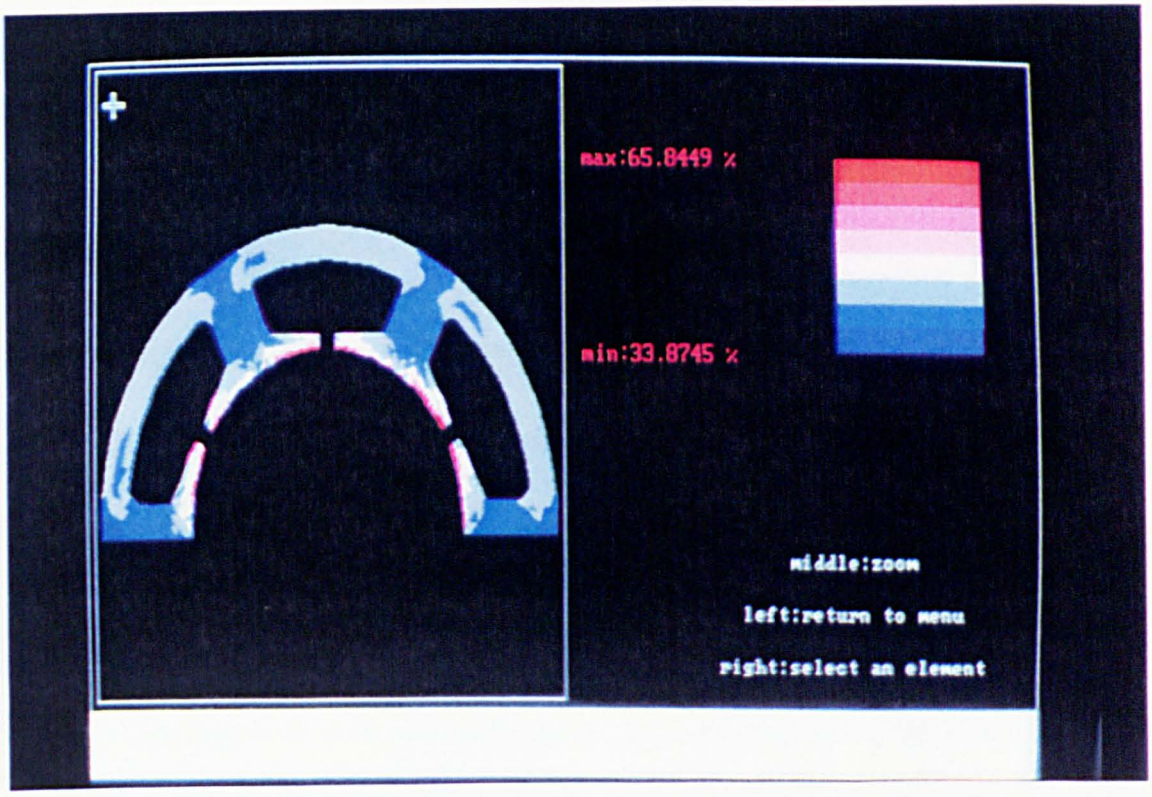


Fig (5.14) Eddy current loss component distribution under advanced commutation strategy.

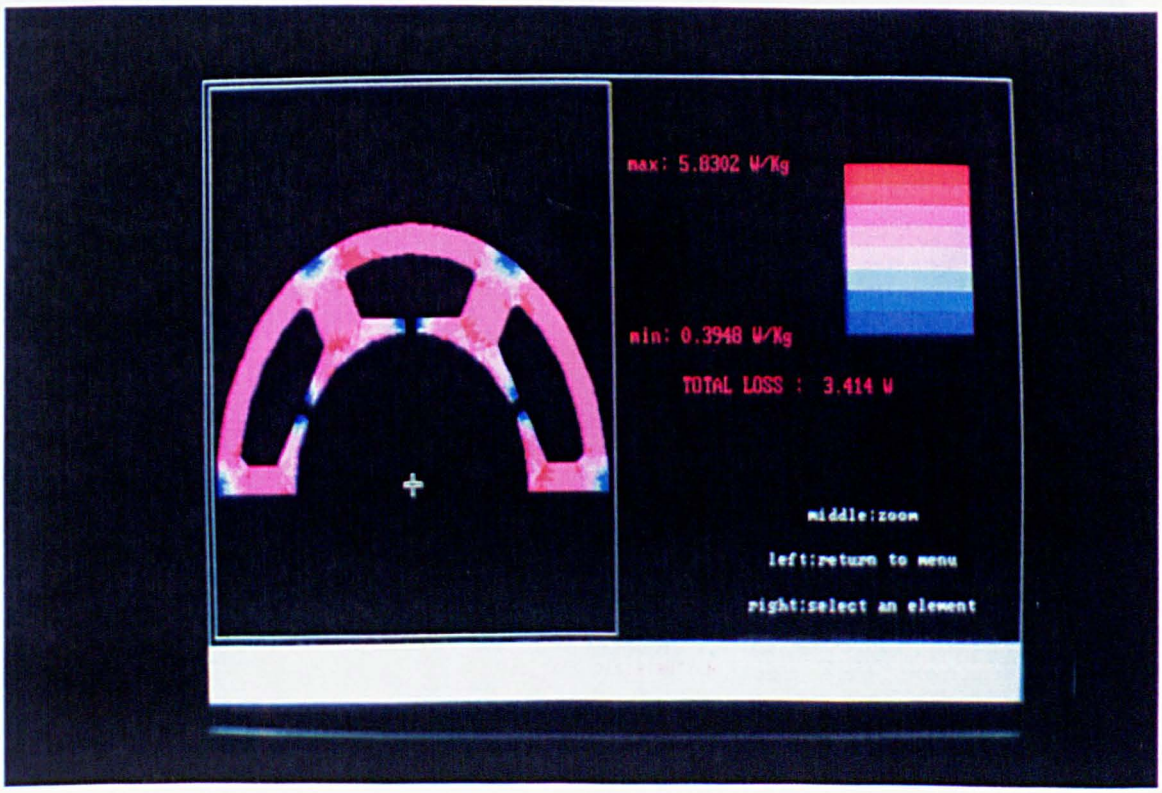


Fig (5.15) Total iron loss density distribution under retarded commutation strategy.


Fig (5.16) Hysteresis loss component distribution under retarded commutation.

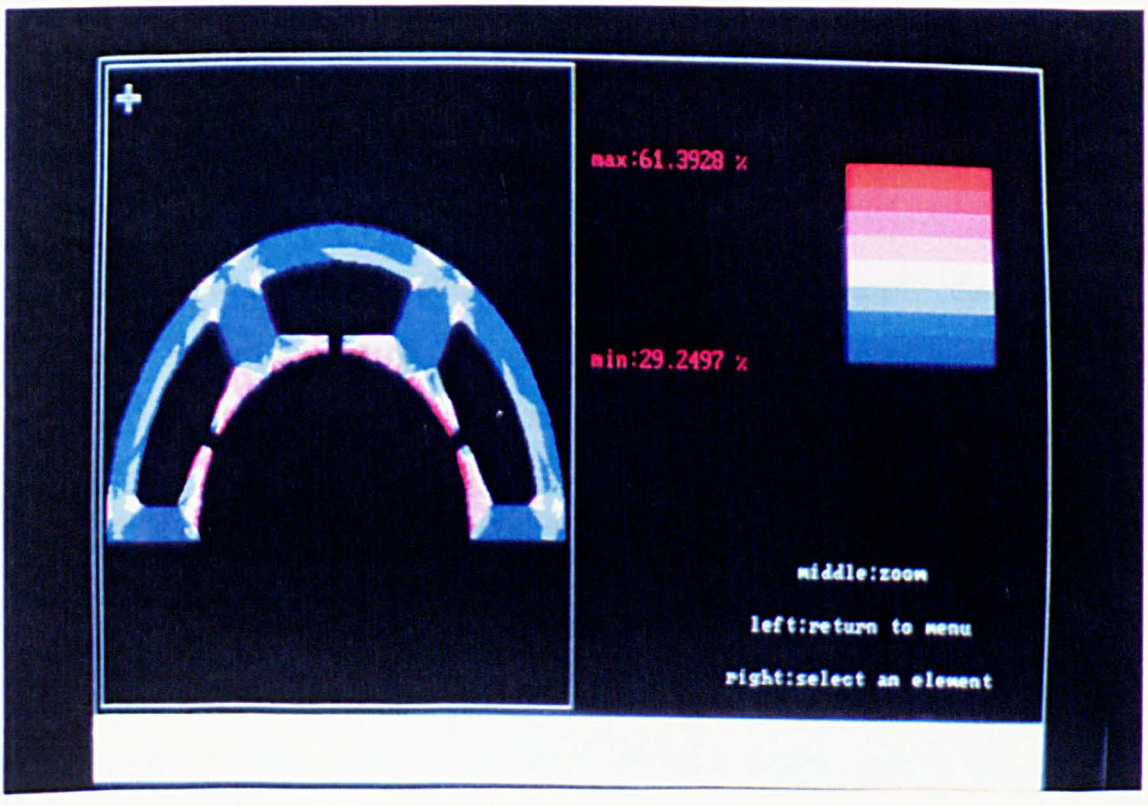


Fig (5.17) Eddy current loss component distribution under retarded commutation.

# CHAPTER 6

# CONCLUSIONS

## 6.1) Iron loss density in electrical steel laminations

It has been shown that a general model recently developed by Bertotti enables the accurate prediction of the excess eddy current iron loss density component under flux density waveforms typical of those encountered in the stator core of brushless permanent magnet dc motors. Thus, when used together with well established techniques for predicting the hysteresis and the classical eddy current iron loss density components, a reliable means for the prediction of iron losses in permanent magnet brushless dc motors is now available, albeit still being dependent upon the accurate characterisation of the lamination material. However, the characterisation requires parameters to be determined experimentally only under sinusoidal flux density waveforms. Although, a number of techniques are available in this investigation a computer-controlled single-sheet rig was developed, and used subsequently to validate the loss density calculation under a wide range of flux density waveforms.

Further, an exact expression for the calculation of the iron loss density component due to rotation under non-purely rotating flux conditions, from measured values of $\vec{H}$ and $\vec{B}$, has been derived. It has been shown that the instantaneous angular speed of the flux density vector is a necessary parameter for defining a rotating flux condition, and that only a flux condition defined by the flux density loci and the instantaneous angular speed of the flux density vector yields a unique iron loss density.

## 6.2) Curvature effects in radial field permanent magnet machines

It has been shown that curvature can have a considerable effect on the magnetic loading in the airgap of a permanent magnet excited machine. Indeed, in the machine topology of Fig (4.1a), which embraces interior rotor brushless dc machines, increasing the magnet thickness would not necessarily result in an increase of the magnetic loading in the airgap. In other words, an optimal magnet thickness exists for which the airgap flux density is a maximum. However, in machine topology of Fig (4.1b), which embraces external rotor brushless dc machines, an increase in the magnet thickness always leads to an increase of the magnetic loading in the airgap.

A simple model which caters for the effects of curvature has been developed. The model enables the prediction of both the magnetic loading in the airgap and the spread of magnet working points. Predictions have been validated against calculations using sophisticated analytical and numerical techniques as well as by experiment.

The impact of the effect of curvature extends beyond the accuracy of the magnetic field prediction. For example, the cost of the magnet material may be of particular importance, especially if high energy magnets are used, since they can amount to a considerable portion of the total cost of a machine. Thus, their optimal use requires attention to effects, such as those related to curvature.

## 6.3) Flux density waveforms in the stator core of permanent magnet brushless dc machines.

A simple analytical technique has been established to predict the flux density waveforms in various regions of the stator core of permanent magnet brushless dc

motors on open-circuit operation. The predictions have been shown to be fairly reliable by comparison with both finite element analysis and measurements.

A technique which couples a drive system simulation to the magnetostatic finite element analysis has also been developed to enable the prediction of the flux density waveforms in the stator core under any load/operating condition. Predictions, validated by experiment, have shown that the flux density waveforms can be affected markedly by the load condition. Besides having a marked effect on the actual waveforms, both their shape and magnitude, armature reaction causes an unsymmetric distribution with respect to the teeth axes.

### 6.4) Iron losses in the stator core of permanent magnet brushless dc motors

It has been shown that the open-circuit iron loss can be predicted fairly accurately using both the analytical and the numerical techniques. It has also been shown that the load condition has a marked effect on both the iron loss density distribution as well as the total iron loss. Indeed, as a result of the unsymmetric distribution of local flux density waveforms with respect to a tooth axis, the iron loss density distribution is also unsymmetric. Thus, the open-circuit iron loss, which is usually assumed to be the loss no matter what the operating condition, clearly cannot yield an accurate estimate of the loss on-load.

Finally, even though the difference between the measured and computed iron losses on load has been attributed mainly to experimental errors, other sources of error attributable to armature reaction effects in both the magnets/rotor and the stator end-region exist. However, at present there is no reliable method for estimating the contribution from these additional loss components.

## 6.5) Further work

A) More fundamental research concerning the iron loss density associated with rotating fluxes needs to be undertaken, since at present there is no available theoretical method for such a calculation. Therefore, a theoretical approach, based on the physical origins of the iron loss density is required, particularly since emerging drive/machine formats are giving rise to more complex flux conditions.

A test rig for the measurement of the iron loss density under rotating flux conditions is currently under development. Although fairly good success has been achieved using the initial rate of rise of temperature loss measuring method, the method based on the measured $\vec{H}$ and $\vec{B}$ is to be employed, since besides allowing the total iron loss density to be determined, it will enable the investigation of the iron loss density component due to rotation in non-purely rotating flux conditions. However, special care needs to be taken in designing and constructing the instrumentation, since small errors which are usually associated with the misalignement of the $\vec{B}$ and $\vec{H}$ sensing coils, can cause substantial errors in the measured iron loss density [18]. The test rig is to be used to study the iron loss density under rotating flux conditions, as well as to validate theoretical findings concerning the calculation of the iron loss density component in non-purely rotating flux conditions.

B) A thorough study of the effects of manufacturing conditions, such as stress, on the iron loss density in electrical steel laminations is required. A test rig which enables the measurement of the iron loss density under a compressive stress of up to 100 MPa is currently under development, and will be used to characterise materials under a stressed condition as well as to validate a proposed approach for the prediction of the iron loss density under stress conditions.

In Chapter 3, it has been shown that only three constants are required for the prediction of the iron loss density under any alternating flux density waveform. Hence, if the variation of these constants with stress is known, the iron loss density can be predicted under any stress level and flux density waveform. The total iron loss density is then written as :

$$P_i(s) = k_h(s) f B_m^{\alpha(s)} + \frac{\sigma d^2}{12\,\delta}\frac{1}{T}\int_T \left(\frac{dB}{dt}\right)^2 dt + \frac{k_e(s)}{T}\int_T \left|\frac{dB}{dt}\right|^{1.5} dt \qquad (6.1)$$

where s is the level of stress exerted on the lamination material. The variation of the hysteresis constants with stress needs to be determined from a set of measurements of the dc hysteresis loss for a reasonable range of stress levels, whilst the variation of the excess loss constant needs to be determined from tests under sinusoidal flux density waveforms for a similar range of stress levels. The classical eddy current component should not be affected by stress, since the material conductivity depends only on the alloy composition of the material.

The above approach avoids the use of correction factors, whose validity is usually limited to the conditions under which they have been determined. Further, the suggested technique can be easily incorporated into a C.A.D package for the prediction of iron losses in stressed machines.

C) The numerical technique which couples the drive system simulation to finite element analyses needs to be extended to cater for other drive/machine formats in order that the relative efficiencies of alternative drive systems can be compared, and improved. This can only be achieved in the context of the analysis of complete drive systems.

D) A more reliable technique for the direct measurement of loss needs to be developed. In this context a calorimetric method is currently under development at the University of Sheffield, Fig (6.1). The technique is based on the 'balance' method, the measurement procedure being as follows:

a. The temperature rise of the air flowing through the insulated enclosure is first measured with the test machine operating at a specified load.

b. The test is then repeated with the machine unexcited but still being rotated with the source of heat being resistance heaters, whose input power is adjusted until the same temperature rise is obtained.

c. Provided the air flow rate and incoming air temperature are unchanged the power supplied to the heaters will be equal to the loss dissipated by the test machine. Thus, only the power dissipated in the heaters needs to be accurately measured, and this can easily be achieved by using a standard laboratory watt meter.

E) A study of the proportion of rotor and end-region losses to the total iron loss should be undertaken. The rotor losses (in both the magnets and the rotor hub) are caused by the fact that the armature field rotates incrementally (ie the load angle effectively varies from $60^{o}$ to $120^{o}$) at each commutation. The relative motion between the field and the rotor causes eddy currents to be generated, which may cause the excessive heating, which may not only impact the mechanical integrity of the rotor but also cause the magnet properties to deteriorate. The use of laminated rotor hub [61] has been shown to significantly reduce the problem, whose severity depends on the supply converter. End-region losses are caused by stray fields generated by the end-windings as well as fringing at the airgap, and these have been the subject of much research in relation to turbo-generators. However, to the author's knowledge the issue of end-region effects in permanent magnet machines has not been addressed.

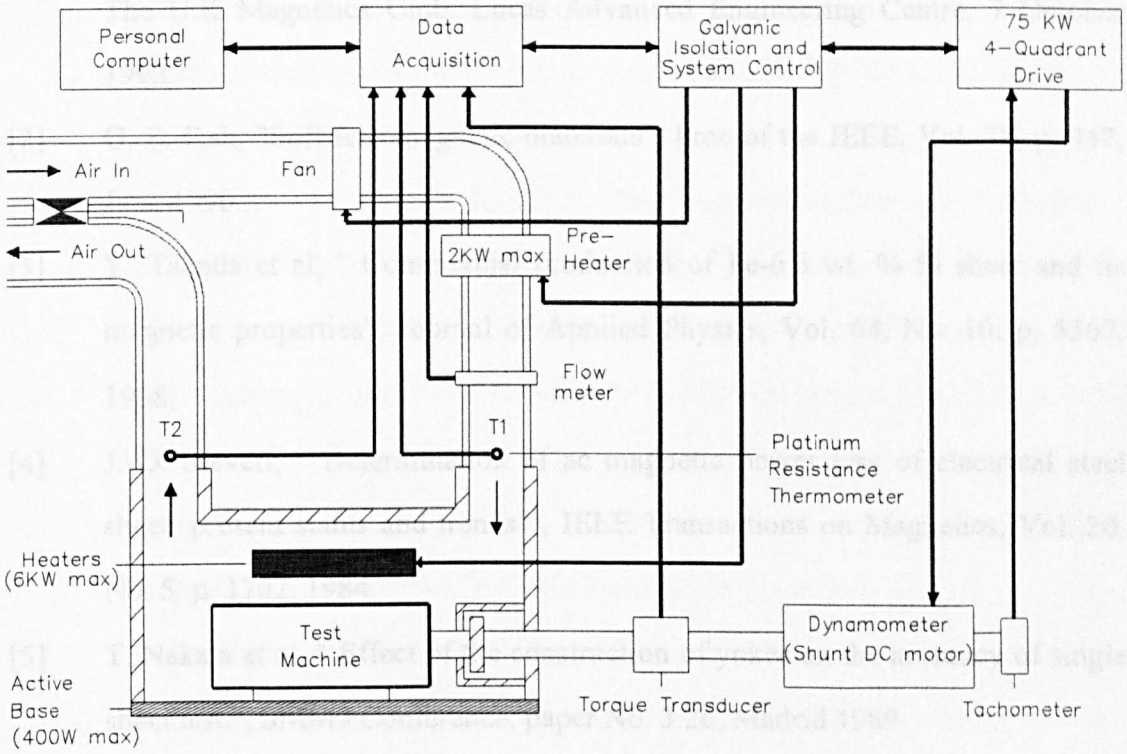


Fig (6.1) Schematic of the calorimetric test method.

## References


[1] A. J. Moses, " Soft magnetic materials for energy efficient rotating machines ", The U.K Magnetics Club, Lucas Advanced Engineering Centre, 7 October 1992.

[2] G. E. Fish, "Soft ferromagnetic materials", Proc of the IEEE, Vol. 78, p. 947, June 1990.

[3] Y. Takada et al, " Commercial production of Fe-6.5 wt. % Si sheet and its magnetic properties", Journal of Applied Physics, Vol. 64, No. 10, p. 5367, 1988.

[4] J. D. Sievert, " Determination of ac magnetic power loss of electrical steel sheet: present status and trends ", IEEE Transactions on Magnetics, Vol. 20, No. 5, p. 1702, 1984.

[5] T. Nakata et al, " Effect of the construction of yokes on the accuracy of single sheet test ", SMM9 Conference, paper No. 3.26, Madrid 1989.

[6] J. Sievert et al, " Experimental studies on single-sheet testers", SMM9 Conference, paper No. 2.17, Madrid 1989.

[7] T. Nakata et al, " Improvement of measuring accuracy of magnetic field strength in single-sheet testers by using two H-coils", IEEE Transactions on Magnetics, Vol. 23, No. 5, p. 2596, 1987.

[8] F. Brailsford, " Rotational hysteresis loss in electrical sheet steels", Proc Inst Elect Engrs, Vol. 38, p. 566, 1938.

[9] T. Yamagushi, K. Narita, " Rotational power loss in commercial Silicon-iron laminations ", Electrical Engineering in Japan, Vol. 96, No. 4, p. 15, 1976.

[10] A. Kaplan, " Magnetic core losses resulting from a rotating flux ", Journal of Applied Physics, Suppl 32, p. 370, 1961.

[11] M. Arabi, A. J. Moses, " An improved method for measuring rotational power loss in electrical steels ", Journal of magnetism and magnetic materials, Vol. 41, p. 227, 1984.

[12] W. Brix et al, " Method for the measurement of rotational power loss and related properties in electrical steel sheets ", IEEE Transactions on Magnetics, Vol. 18, p. 1469, 1982.

[13] W. Brix et al, " Improved method for the investigation of the rotational magnetization process in electrical steel sheets ", IEEE Transactions on Magnetics, Vol. 20, No. 5, p. 1708, 1984.

[14] A. Basak, A. J. Moses, " Influence of stress on rotational loss in Silicon iron ", Proc Inst Elect Engrs, Vol. 125, p. 165, 1978.

[15] M. Enokizono, J. D. Sievert, " Magnetic field and loss analysis in an apparatus for the determination of rotational loss ", Physica Scripta, Vol. 39, p. 356, 1989.

[16] M. Enokizono et al, " Rotational power loss of silicon steel sheet ", IEEE Transactions on Magnetics, Vol. 26, No. 5, p.2562, 1990.

[17] J. Sievert, " Recent advances in the one- and two-dimensional magnetic power loss ", IEEE Transactions on Magnetics, Vol. 26, No. 5, p.2553, 1990.

[18] J. Sievert et al, " Studies on the rotational power loss measurement problem", SMM9 Conference, paper No. 1.14, Madrid 1989.

[19] F. Preisach, " Uber die magnetische nachwirkung ", Z. Phys., Vol. 94, p. 277, 1935.

[20] G. Kadar, E. Della Torre, " Hysteresis modeling : I. non congruency ", IEEE Transactions on Magnetics, Vol. 23, No. 5, p.2820, 1987.

[21] R. M. Del Vecchio, "An efficient procedure for modeling complex hysteresis processes in ferromagnetic materials ", IEEE Transactions on Magnetics, Vol. 16, p. 809, 1980.

[22] G. Bertotti et al, " The prediction of power losses in soft ferromagnetic materials ", Journal de Physique, Colloque C8, Supplement au $n^{o}$ 12, Tome 49, p. 1915, 1988.

[23] G. Bertotti, " Principles of characterization and classification of power losses on soft metallic ferromagnetic materials ", Proceedings of the International Symposium on Physics of Magnetic Materials, p. 422, Sendai 1987.

[24] G. Bertotti et al, " Dependence of power losses on peak magnetization and frequency in grain-oriented 3% SiFe ", IEEE Transactions on Magnetics, Vol. 23, No. 5, p. 3520, 1987.

[25] R. H. Pry, C. P. Bean, " Calculation of the energy loss in magnetic sheet materials using a domain model ", Journal of applied physics, Vol. 29, p. 532, 1958.

[26] J. E. L. Bishop, " Mechanisms underlying eddy current loss in silicon iron and other materials ", SMM9 Conference, paper 4.01, Madrid 1989.

[27] G. Bertotti, " Space-time correlation properties of the magnetization process and eddy current losses : Theory ", Journal of Applied Physics, Vol. 54, p. 5293, 1983.

[28] G. Bertotti, " Space-time correlation properties of the magnetization process and eddy current losses : Applications. 1. fine wall spacing ", Journal of Applied Physics, Vol. 55, p. 4339, 1984.

[29] G. Bertotti, " A general statistical approach to the problem of eddy current losses ", Journal of Magnetism and Magnetic Materials, Vol. 41, p. 253, 1984.

[30] G. Bertotti, " Physical interpretation of eddy current losses in ferromagnetic materials. I. theoretical considerations ", Journal of Applied Physics, Vol. 57, p. 2110, 1985.

[31] G. Bertotti, " Physical interpretation of eddy current losses in ferromagnetic materials. II. analysis of experimental results ", Journal of Applied Physics, Vol. 57, p. 2118, 1985.

[32] B. Thomas, " A quantitative assessment of the change in magnetic properties of Co-Fe-V alloy when subjected to flux and stress conditions similar to those encountered in an aircraft generator ", IEEE Transactions on Magnetics, Vol. 16, No. 5, 1980.

[33] S. S. Grigoryan et al, " Influence of compression forces in the electromagnetic characteristics of stator cores ", Elektrotekhnika, No. 9, 1974.

[34] G. D. Kharlan, R. Z. Perel'man, " Magnetic properties of electrical steel during stamping and assembly of stator cores of induction motors", Elektrotekhnika, Vol. 61, No. 3, p. 11, 1990.

[35] P. M. Carlberg, B. Lewin, " The influence od edge effects and stress on losses", Proc. Modern Magnetic Materials, London, 20 June 1989.

[36] K. C. Pitman, " The influence of stress on ferromagnetic hysteresis ", IEEE Transactions on Magnetics, Vol. 26, No. 5, 1990.

[37] G. D. Kharlan et al, " Variation in magnetic properties of electrical steel during fabrication of asynchronous motor stator cores ", Elektrotekhnika, Vol. 59, No. 6, 1988.

[38] A. J. Taylor, " Advanced hard and soft magnetic materials: applications - specific measurements ", Proc of ICEM'92, Manchester, 15-17 Sept 1992.

[39] Y. Takada et al, " Application of 6.5 % Si steel to motor cores ", Intelligent motion proceedings, p. 408, 1989.

[40] M. Kostenko, L. Piotnovsky, " Electrical machines ", Vol 1, Mir Publishers, Moscow 1977.

[41] G. R. Slemon, X. Liu, " Core losses in permanent magnet motors", IEEE Transactions on Magnetics, Vol. 26, No. 5, p. 1653, 1990.

[42] C. E. Tindall, S. Brankin, " Finite element approach to iron and stray loss-at-source computation in salient pole alternators ", IEEE Transactions on Magnetics, Vol. 24, p. 487, 1988.

[43] M. K. Jamil, N. A. Demerdash, " Harmonics and core losses of permanent magnet dc motors controlled by chopper circuits ", IEEE Transactions on Energy Conversion, Vol. 5, No. 2, p. 408, 1990.

[44] R. S. Schiferl, T. A. Lipo, " Core loss in buried magnet permanent magnet synchronous motors ", IEEE Transactions on Energy Conversion, Vol. 4, No. 2, p. 279, 1989.

[45] A. Bertotti et al, " An improved estimation of iron losses in rotating electrical machines ", IEEE Transactions on Magntics, Vol. 27, No. 5, 1991.

[46] G. H. Shirkoohi, " Prediction of improvement of efficiency of induction machines by replacing the core materials using FEM techniques ", Journal of Magnetism and Magnetic Materials, Vol. 112, 1992.

[47] A. Boglietti et al, " Iron losses in magnetic materials with six-step ans PWM inverter supply ", IEEE Transactions on Magnetics, Vol. 27, No. 6, 1991.

[48] G. D. Kharlan et al, " Variation in magnetic properties of electrical steel during fabrication of asynchronous motor stator cores ", Elektrotekhnika, Vol. 59, No. 6, p. 15, 1988.

[49] N. G. Nikiyan, M. E. Iondem, " Influence of fabrication factors on magnetic stress in cores of asynchronous motors ", Elektrotekhnika, Vol. 59, No. 6, p. 19, 1988.

[50] V. V. Druzhinin, V. K. Chistyakov, " Influence of compressive stresses on the magnetic characteristics of electrical steel ", Elektrotekhnika, No. 1, 1973.

[51] S. V. Bronin et al, " Influence of technology for fabrication of stator laminations on the parameters of asynchronous motors ", Tr. VNIITelektromash, No. 10, 1972.

[52] Y. Borzyak et al, " Influence of technology factors on the electromagnetic characteristics of steel ", Izv. AN SSSR. Ser. fizicheskaya, Vol. 39, No. 7, 1975.

[53] R. I. Talyshinskii, " Effect of workhardness on electromagnetic characteristics of magnetic circuits ", Elektrotekhnika, No. 5, 1976.

[54] L. Rahf, J. D. Sievert, " Microprocessor-controlled test assembly for electrical steel sheets ", IEEE Transactions on Instrumentation and Measurement, Vol. IM-36, No. 3, 1987.

[55] A. M. Gumaidh et al, " Characterisation of magnetic materials under two-dimensional excitation ", Paper CD-06, Intermag'93.

[56] T. Nakata et al, " Iron losses of silicon steel produced by distorted flux ", Elec. Eng. in Japan, Vol. 90, Part 1, p. 10, 1970.

[57] J. D. Lavers et al, " A simple method of estimating the minor loops hysteresis in thin laminations ", IEEE Transactions on Magnetics, Vol. 14, No. 5, p. 386, 1978.

[58] H. J. Williams, W. Shockley, C. Kittel, " Studies of the propagation velocity of a ferromagnetic domain boundary ", Phys. Rev., Vol. 80, p. 1090, 1950.

[59] G. Bertotti, " General properties of power losses in soft ferromagnetic materials ", IEEE Transactions on Magnetics, Vol. 24, No. 1, p. 621, 1988.

[60] F. Fiorillo, A. Novikov, " Power losses under sinusoidal, trapezoidal, and distorted induction waveform ", IEEE Transactions on Magnetics, Vol. 26, No. 5, p. 2559, 1990.

[61] Z. Q. Zhu, " Electromagnetic performance of brushless permanent magnet dc motors - with particular reference to noise and vibration ", Ph.D thesis, University of Sheffield, 1991.

[62] N. Schofield, Private communication, University of Sheffield.

## PUBLICATIONS FROM RESEARCH IN THIS THESIS

* K. Atallah, Z. Q. Zhu, D. Howe, " An improved method for predicting iron losses in brushless dc drives ", IEEE Transactions on Magnetics, Vol 28, No 5, pp 2997-2999, 1992.
* K. Atallah, Z. Q. Zhu, D. Howe, " Flux waveforms and iron losses in brushless dc motors ", Proc of the $12^{th}$ Int Workshop on Rare-earth Magnets and their Applications, Camberra, Australia, pp 109-120, 16 July 1992.
* K. Atallah, Z. Q. Zhu, D. Howe, " The prediction of iron losses in brushless dc machines ", Proc of ICEM'92, Manchester, pp 1025-1029, 15-17 Sept 1992.
* K. Atallah, Z. Q. Zhu, J. K. Mitchell, D. Howe, " Curvature and flux focusing effects in cylindrical permanent magnet machines ", Proc of Int Workshop on Electric and Magnetic Fields, Liege, Belgium, pp 60.1-60.6, 28-30 Sept 1992.
* K. Atallah, Z. Q. Zhu, J. K. Mitchell, D. Howe, " Curvature effects in radial-field permanent magnet machines ", accepted for publication in Electric Machines and Power Systems.
* K. Atallah, D. Howe, " Calculation of the rotational power loss in electrical steel laminations from measured $\vec{H}$ and $\vec{B}$ ", accepted for publication in IEEE Transactions on Magnetics.